RIGA TECHNICAL
UNIVERSITY

Agija Stanke

OGLEKĻA OKSĪDU TERMOĶĪMISKA KONVERSIJA E-DEGVIELĀS UN TO PREKURSOROS

Promocijas darbs

THERMOCHEMICAL CONVERSION OF CARBON OXIDES INTO E-FUELS AND THEIR PRECURSORS

Doctoral Thesis

RTU Izdevniecība
RTU Press
Rīga 2026

RĪGAS TEHNISKĀ UNIVERSITĀTE
Dabaszinātņu un tehnoloģiju fakultāte
Ķīmijas un ķīmijas tehnoloģijas institūts

RIGA TECHNICAL UNIVERSITY
Faculty of Natural Sciences and Technology
Institute of Chemistry and Chemical Technology

Agija Stanke
Doktora studiju programmas “Ķīmija, materiālzinātne un tehnoloģijas” doktorante
Doctoral Student of the Study Programme “Chemistry, Materials Science and Engineering”

OGLEKĻA OKSĪDU TERMOĶĪMISKA KONVERSIJA E-DEGVIELĀS UN TO PREKURSOROS

Promocijas darbs

THERMOCHEMICAL CONVERSION OF CARBON OXIDES INTO E-FUELS AND THEIR PRECURSORS

Doctoral Thesis

Zinātniskās vadītājas / Scientific supervisors
Dr. chem. KRISTĪNE LAZDOVIČA
Dr. chem. SVETLANA ČORNAJA

RTU Izdevniecība / RTU Press
Rīga 2026 / Riga 2026

Stanke, A. Oglekļa oksīdu termoķīmiska konversija e-degvielās un to prekursoros. Promocijas darbs. Rīga: RTU Izdevniecība, 2026. 166 lpp.

Stanke, A. Thermochemical Conversion of Carbon Oxides into e-Fuels and Their Precursors. Doctoral Thesis. Riga: RTU Press, 2026. 166 p.

Publicēts saskaņā ar promocijas padomes “RTU P-01” 2026. gada 30. marta lēmumu, protokols Nr. 04030-9.1/81.

Published in accordance with the decision of the Promotion Council “RTU P-01” of 30 March 2026, Minutes No. 04030-9.1/81.

Vāka attēla autore – Agija Stanke
Cover image by Agija Stanke

PROMOCIJAS DARBS IZVIRZĪTS ZINĀTNES DOKTORA GRĀDA IEGŪŠANAI RĪGAS TEHNISKAJĀ UNIVERSITĀTĒ

Promocijas darbs zinātnes doktora (*Ph. D.*) grāda iegūšanai tiek publiski aizstāvēts 2026. gada 9. jūnijā Rīgas Tehniskās universitātes Dabaszinātņu un tehnoloģiju fakultātē, P. Valdena ielā 3, 272. auditorijā.

OFICIĀLIE RECENZENTI

Asociētais profesors *Dr. chem*. Artis Kinēns,
Latvijas Universitāte, Latvija

Asociētais profesors *Dr. chem*. Reinis Drunka,
Rīgas Tehniskā universitāte

Asociētais profesors *Ph. D. Hamid Reza Godini*,
Aalto Universitāte, Somija

APSTIPRINĀJUMS

Apstiprinu, ka esmu izstrādājusi šo promocijas darbu, kas iesniegts izskatīšanai Rīgas Tehniskajā universitātē zinātnes doktora (*Ph. D.*) grāda iegūšanai. Promocijas darbs zinātniskā grāda iegūšanai nav iesniegts nevienā citā universitātē.

Agija Stanke ……………………………. (paraksts)
Datums: ………………………

Promocijas darbs ir sagatavots kā tematiski vienotu zinātnisko publikāciju kopa ar kopsavilkumu latviešu un angļu valodā. Tajā ietverti pieci zinātniskie oriģinālraksti un viens raksta manuskripts. Publikācijas zinātniskajos žurnālos uzrakstītas angļu valodā.

SATURS

1. pielikums Stanke, A., Lazdovica, K., Laipniece, L. Evaluation of the Fischer-Tropsch synthesis product selectivity over iron-based silica-supported catalyst under mild temperatures. *Environmental Progress and Sustainable Energy*, **2024**, 43(3), e14335.

2. pielikums Stanke, A., Lazdovica, K., Gaile, A., Laipniece, L. Fischer-Tropsch synthesis product selectivity over silica-supported iron-based catalyst: Effect of K/Fe ratio. *Fuel*, **2025**, 387, 134399.

3. pielikums Stanke, A., Kampars, V. Agglomeration of Fe/SBA-15 with clays for Fischer-Tropsch synthesis. *Energy Reports*, **2022**, 8, 461-466.

4. pielikums	Abelniece, Z., Cutrufello, M. G., Rombi, E., Stanke, A., Piirsoo, H., Mändar, H., Tamm, A. The structure-activity interactions of Cu/Zn, In/Pd and Fe/K catalysts supported on mesoporous SBA-15 for carbon dioxide hydrogenation at low pressure. *Chemical Papers*, **2024**, 78, 5103-5112.
5. pielikums	Stanke, A., Lazdovica, K. The promotional effect of potassium on iron-based silica supported catalyst for CO_2 hydrogenation. No: *International Multidisciplinary Scientific GeoConference Surveying Geology and Mining Ecology Management, SGEM 2022: Conference Proceeding*, 22(4.1), pp. 161–166.
6. pielikums	Stanke, A., Abelniece, Z., Sutka, A., Berzins, A., Kõiv, M., Lazdovica, K. $NiFe_2O_4$ catalysts for CO_2 hydrogenation: Performance analysis and comparative life cycle assessment of catalyst synthesis routes. *Nepublicēti rezultāti.*
7. pielikums	Stanke, A., Berzins, A., Velasco, J. A., Sarsuns, K., Puurunen, R. L., Lazdovica, K. Cobalt-promoted Fe_3O_4 catalysts for CO_2 hydrogenation to C_{2+} hydrocarbons: Effect of pretreatment method and reaction temperature. *Fuel Processing Technology,* **2026,** 288, 108467.

LIETOTO SAĪSINĀJUMU SARAKSTS

BET	*Brunauer-Emmett-Teller* metode virsmas laukuma analīzei
BJH	*Barrett-Joyner-Halenda* poru izmēra sadalījuma analīzes metode
CO_2-FTS	uz CO_2 balstīta Fišera-Tropša sintēze
DME	dimetilēteris
FTIR	infrasarkanā Furjē spektroskopija
FTS	Fišera-Tropša sintēze
GC-TCD/FID	gāzu hromatogrāfs, kas aprīkots ar siltumvadītspējas un liesmas jonizācijas detektoriem
GC-MS	gāzu hromatogrāfs ar masspektrometru
HVO	hidrogenēta augu eļļa
KMR	kodolu magnētiskā rezonanse
RWGS	apgrieztā ūdens-gāzes maiņa (*reverse water-gas shift*)
SBA-15	*Santa Barbara Amorphous* mezoporains silīcija dioksīda materiāls
SEM-EDS	skenējošās elektronu mikroskopijas – enerģijas dispersijas rentgenstaru spektroskopija
WGS	ūdens-gāzes maiņa (*water-gas shift*)
XPS	rentgenstaru fotoelektronu spektroskopija
XRD	rentgenstaru difrakcija
XRF	rentgenstaru fluorescences spektroskopija

PROMOCIJAS DARBA VISPĀRĒJS RAKSTUROJUMS

Tēmas aktualitāte

Cilvēces attīstībā enerģijai ir būtiska loma, un fosilais kurināmais ir veicinājis līdz šim nepieredzētu rūpniecisko un sabiedrisko progresu. Tomēr fosilo resursu plašā izmantošana ir radījusi ievērojamas antropogēnās CO_2 emisijas, izjaucot dabisko oglekļa ciklu [1] un izraisot bioloģiskās daudzveidības samazināšanos, vides piesārņojumu un klimata pārmaiņas [2]. Kopš 2000. gada globālais enerģijas patēriņš ir pieaudzis aptuveni par vienu trešdaļu un paredzams, ka tas turpinās augt, turklāt fosilie energoresursi joprojām nodrošina gandrīz 80 % no kopējā pieprasījuma [3], [4]. Šī lielā atkarība no neatjaunojamajiem resursiem rada ilgtermiņa riskus gan klimata stabilitātei, gan enerģētiskajai drošībai [5].

Transports, kas ir visstraujāk augošais enerģiju patērējošais sektors, veido aptuveni vienu ceturtdaļu no globālā enerģijas patēriņa. Tā kā esošā degvielas ražošanas, sadales un uzglabāšanas infrastruktūra ir optimizēta ogļūdeņražu degvielai, strauja pāreja uz pilnīgi jauniem degvielas risinājumiem būtu dārga un laikietilpīga. Tādēļ ilgtspējīgas "*drop-in*" degvielas, kas ir saderīgas ar pašreizējo infrastruktūru un transportlīdzekļiem, piedāvā praktisku ceļu transporta dekarbonizācijai [6]. Šajā kontekstā elektrodegvielas kļūst par daudzsološu risinājumu pieaugošajam enerģijas pieprasījumam.

Elektrodegvielas jeb e-degvielas ir sintētisko degvielu klase, kuru ražošanas process ietver oglekļa monoksīda vai oglekļa dioksīda hidrogenēšanu, izmantojot ūdeņradi, kas iegūts ūdens elektrolīzes procesā [7]. Gan CO, gan CO_2 hidrogenēšana ir sarežģītu reakciju kopums, un tā rezultātā veidojas plašs produktu klāsts, kas atkarīgs no reakcijas apstākļiem un izmantotā katalizatora. CO un CO_2 var hidrogenēt par spirtiem un ogļūdeņražiem, izmantojot pārejas metālu katalizatorus.

CO katalītiskā hidrogenēšana par ogļūdeņražiem pazīstama kā Fišera-Tropša sintēze (FTS). FTS produktus var izmantot augstas kvalitātes dīzeļdegvielas, benzīna un aviācijas degvielas sintēzei. Reakcija parasti notiek paaugstinātā temperatūrā (200–350 °C) un spiedienā (10–20 bar). FTS ir reakcija, kurā no ūdeņraža un oglekļa monoksīda *in situ* veidotie produkti polimerizējas uz katalizatora virsmas [8]. Vispārīgi FTS var aprakstīt ar šādu vienādojumu:

$$2nH_2 + nCO \rightarrow \text{-}(CH_2)_n\text{-} + nH_2O, \qquad \Delta H_{298K} = -152\ \text{kJ/mol}. \qquad (1.1)$$

Produktu sastāvu nosaka līdzsvars starp virknes augšanas varbūtību uz katalizatora virsmas un virknes pārtraukšanas, hidrogenēšanas un iegūto savienojumu desorbcijas varbūtību. Galvenā FTS reakcija norit vienlaikus ar vairākām blakusreakcijām. Galvenie FTS produkti ir *n*-parafīni un 1-olefīni. Mazākos daudzumos var veidoties arī izomerizēti ogļūdeņraži, cikliski ogļūdeņraži, olefīni ar dubultsaiti pie otrā oglekļa atoma vai tālāk virknē, kā arī aldehīdi, ketoni, skābes un spirti, kas degvielas ražošanas kontekstā tiek uzskatīti par nevēlamiem produktiem [9], [10].

Parasti tiek piedāvāti divi galvenie mehānismi – karbīda mehānisms un CO iespiešanās mehānisms. Karbīda mehānismā CO disociē (tiešā vai H pavadīta disociācija) un uz katalizatora virsmas veido oglekļa savienojumus, kas tiek hidrogenēti un savienoti, veidojot C-C saites (1. att.).

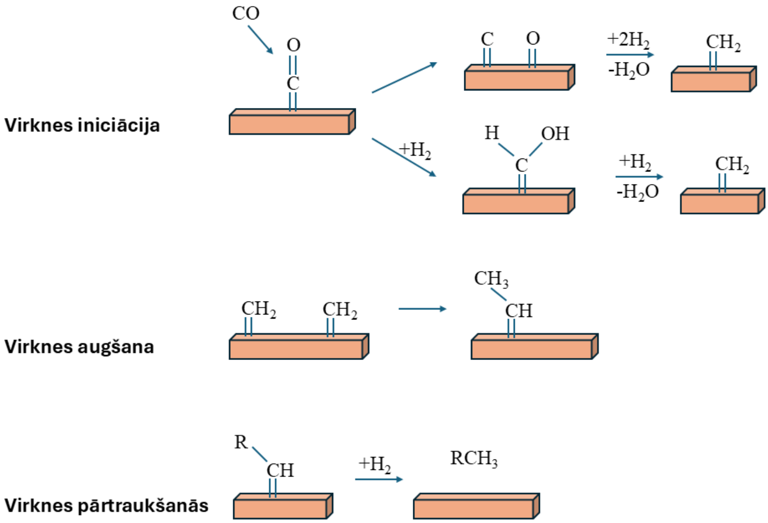

1. att. Karbīda mehānisma vienkāršots attēlojums. Pielāgots no [11], [12].

CO iespiešanās mehānismā tiek pieņemts, ka C-C virknes augšana notiek, CO monomēram iespraucoties starp virsmas-ūdeņraža (pirmā iniciācija) un ogļūdeņražu starpproduktu virsmas-oglekļa saiti (2. att.).

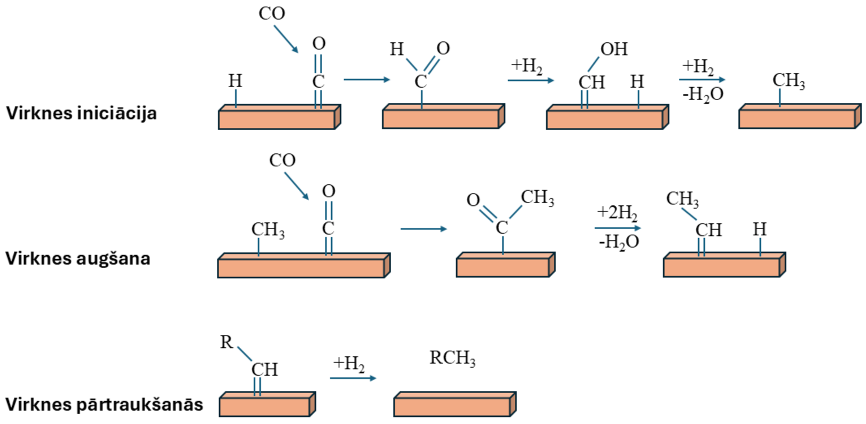

2. att. CO iespiešanās mehānisma vienkāršots attēlojums. Pielāgots no [11], [12].

FTS reakcijas laikā rodas liels daudzums ūdens, kas var paātrināt katalizatora deaktivāciju un izraisīt katalītiskās aktivitātes samazināšanos. FTS reakcijas apstākļos ūdens var piedalīties ūdens-gāzes maiņas reakcijā (*WGS*, *water-gas shift*), veidojot ūdeņradi un oglekļa dioksīdu:

$$CO + H_2O \rightleftarrows CO_2 + H_2, \qquad \Delta H_{298K} = -41{,}2 \text{ kJ/mol}. \tag{1.2}$$

WGS ietekmē CO, H_2, CO_2 un H_2O koncentrācijas (parciālos spiedienus) reakcijas sistēmā, tādējādi ietekmējot arī FTS primāro un sekundāro reakciju kinētiku un galaproduktu sadalījumu. Šī reakcija ir īpaši nozīmīga, izmantojot sintēzes gāzi (CO un H_2 maisījumu) ar nestehiometrisku ūdeņraža daudzumu (tipiski no biomasas iegūtai sintēzes gāzei).

CO_2 hidrogenēšana, atšķirībā no attīstītās CO hidrogenēšanas, izmantojot FTS, rada atšķirīgus un būtiskus fizikāli ķīmiskus izaicinājumus. Salīdzinot ar CO, CO_2 ir termodinamiski stabilāka molekula, jo ogleklis ir savā augstākajā oksidācijas pakāpē. Par spīti tam gan akadēmiskajos pētījumos, gan rūpnieciskajā praksē ir panākts ievērojams progress CO_2 konversijai produktos, kas satur vienu oglekļa atomu (oglekļa monoksīdā, metānā, metanolā, skudrskābē) [13]. Produktu ar vairākiem oglekļa atomiem (C_{2+}) sintēze ir sarežģītāka CO_2 inertuma, augstās C-C saites veidošanās enerģijas barjeras, konkurences ar CO_2 metanāciju un citu blakusreakciju dēļ.

Viens no daudzsološākajiem CO_2 valorizācijas risinājumiem ir uz CO_2 balstīta Fišera-Tropša sintēze (CO_2-FTS). CO_2-FTS procesā vispirms CO_2 apgrieztajā ūdens-gāzes maiņas (*RWGS*) reakcijā (1.3. vienādojums) tiek reducēts par CO, pēc tam CO piedalās FTS reakcijā (1.1. vienādojums) [14].

$$CO_2 + H_2 \rightleftarrows CO + H_2O, \qquad \Delta H_{298K} = 41{,}2\ \text{kJ/mol}. \qquad (1.3)$$

Tā kā CO_2 ir termodinamiski stabila molekula, konversijas uzlabošanai ir nepieciešamas augstāka sintēzes temperatūra. CO_2-FTS lielākoties tiek īstenota 280–350 °C temperatūrā un 15–25 bar spiedienā. Reakcijas temperatūrai ir divējāda nozīme CO_2 (un CO) hidrogenēšanas procesos. No vienas puses, paaugstināta temperatūra ir termodinamiski nepieciešama, lai aktivētu inerto CO_2 molekulu un veicinātu endotermisko *RWGS* reakciju; turklāt augstāka temperatūra eksponenciāli palielina reakcijas ātrumu. No otras puses, FTS ir eksotermisks process, kurā zemākas temperatūras veicina virknes augšanu. Līdz ar to pārāk augstas temperatūras neizbēgami novirza selektivitāti metāna un citu īsas virknes ogļūdeņražu veidošanās virzienā. Tādējādi rūpīga temperatūras optimizācija ir būtisks nosacījums, lai maksimalizētu vēlamo produktu (C_{2+} ogļūdeņražu) iznākumu.

Promocijas darbā apkopoti pētījumi par oglekļa oksīdu hidrogenēšanu, izmantojot dzelzs katalizatorus ar mērķi iegūt e-degvielas un to prekursorus. Katalizatoriem ir izšķiroša nozīme CO un CO_2 hidrogenēšanas procesos, jo tie ļauj aktivēt šīs termodinamiski stabilās molekulas un nosaka reakcijas selektivitāti par labu vēlamajiem ogļūdeņražiem vai skābekli saturošiem produktiem. Starp biežāk izmantotajiem aktīvajiem metāliem dzelzs katalizatori ir īpaši pievilcīgi to zemo izmaksu, plašās pieejamības un daudzfunkcionālo īpašību dēļ. Dzelzs katalizatori spēj vienlaikus katalizēt *WGS*/*RWGS* un FTS, kas padara tos īpaši piemērotus CO_2 hidrogenēšanai par ogļūdeņražiem. Turklāt to elastīgās oksidēšanās-reducēšanās un karbonizācijas īpašības ļauj pielāgot aktivitāti un selektivitāti, mainot katalizatora sastāvu, struktūru un pirmapstrādes veidu.

Dzelzs katalizatoru sintēzes rezultātā parasti veidojas oksīdu fāzes kā hematīts (Fe_2O_3), kas ir neaktīvas FTS procesā un kurām nepieciešama aktivēšana *in situ*, reducējot ar ūdeņradi, oglekļa monoksīdu vai sintēzes gāzi. Dzelzs katalizatori, bieži raksturoti kā "dzīvie katalizatori", darbojas kā dinamiskas sistēmas, kas no neaktīva oksīdu prekursora pārveidojas par kompleksu aktīvo fāžu sistēmu. Reducējošas vides ietekmē katalizatorā pakāpeniski notiek fāžu pārejas no oksīdiem uz metālisku dzelzi, kas karbonizējas, veidojot dzelzs karbīdus. Katalizatora veiktspēja ir atkarīga no sinerģiskas mijiedarbības starp šīm mainīgajām fāzēm – magnetīts (Fe_3O_4) tiek asociēts ar *WGS* reakcijām, metāliska dzelzs ir aktīva CO_2 disociācijā, savukārt dzelzs karbīdi, īpaši Hāga karbīds (Fe_5C_2), tiek uzskatīti par dominējošo aktīvo fāzi FTS norisei.

Promocijas darbs ietver divas nodaļas. Pirmajā nodaļā apkopoti dati, kas iegūti, sistemātiski analizējot FTS produktus, īpašu uzmanību pievēršot ogļūdeņražu frakcijām un ūdens fāzei. Lai nodrošinātu visaptverošu izpratni par CO hidrogenēšanu, izmantojot dzelzs katalizatorus, detalizēti izvērtēta temperatūras kā reakcijas parametra ietekme, kā arī SiO_2 kā katalizatora nesēja un kālija kā promotora loma produktu sadalījumā. Otrajā nodaļā apkopota sistemātiska CO_2-FTS analīze, īpašu uzmanību pievēršot temperatūras ietekmei kā reakcijas parametram un katalizatora sintēzes un pirmapstrādes metožu lomai produktu sadalījumā.

Pētījuma mērķi un uzdevumi

Promocijas darba mērķi ir e-degvielu un to prekursoru sintēze CO un CO_2 hidrogenēšanas reakcijās, izmantojot dzelzs katalizatorus, kā arī katalizatora raksturlielumu – katalītiskās veiktspējas un iegūto produktu sakarību izpēte.

Lai sasniegtu mērķus, tika definēti vairāki uzdevumi:

1) sintezēt dažāda veida dzelzi saturošus katalizatorus CO un CO_2 hidrogenēšanai un noteikt to raksturojumus;
2) veikt CO un CO_2 hidrogenēšanu dzelzs katalizatoru klātbūtnē un analizēt katalītisko veiktspēju un produktu selektivitāti;
3) izpētīt temperatūras ietekmi uz oglekļa oksīdu konversiju un to hidrogenēšanas produktu selektivitāti;
4) noskaidrot promotoru ietekmi uz dzelzs katalizatoru katalītisko veiktspēju CO un CO_2 hidrogenēšanā;
5) izvērtēt $NiFe_2O_4$ sintēzes metodes ietekmi uz katalizatora raksturlielumiem (fāžu tīrību, kristalītu izmēru) un katalītisko veiktspēju CO_2 hidrogenēšanā;
6) izvērtēt katalizatora prekursora ($Co(NO_3)_2/Fe_3O_4$) priekšapstrādes ietekmi uz katalītisko veiktspēju CO_2 hidrogenēšanā;
7) izvērtēt katalizatora ietekmi uz CO un CO_2 hidrogenēšanas procesos radušos ūdens fāzi un tās sastāvu.

Zinātniskā novitāte un galvenie rezultāti

Promocijas darbā ir sniegts visaptverošs pētījums par oglekļa oksīdu termoķīmisko konversiju, izmantojot FTS un CO_2-FTS procesus. Darba gaitā veikti sistemātiski pētījumi, lai padziļinātu fundamentālo izpratni par FTS un CO_2-FTS, īpaši izvērtējot, kā katalizatora īpašības ietekmē katalītisko veiktspēju oglekļa oksīdu termoķīmiskajā konversijā. Kopumā darbs veicina izpratni par sarežģītajām savstarpējajām attiecībām starp katalizatora struktūru/sastāvu, reakcijas apstākļiem un iegūto hidrogenēšanas produktu sastāvu un sadalījumu.

Darba struktūra un apjoms

Promocijas darbs ir sagatavots kā tematiski vienotu zinātnisko publikāciju kopa, kas apkopo pētījumus par oglekļa oksīdu konversiju e-degvielās un to prekursoros, izmantojot dzelzi saturošus katalizatorus. Promocijas darbs ietver piecas publikācijas *SCI* žurnālos un nepublicētus rezultātus (vienu raksta manuskriptu).

Darba aprobācija un publikācijas

Promocijas darba galvenie rezultāti publicēti piecos zinātniskajos oriģinālrakstos, kā arī sagatavots viens oriģinālpētījuma raksta manuskripts. Pētījumu rezultāti prezentēti trīs konferencēs.

Zinātniskās publikācijas

1) **Stanke, A.**, Bērziņš, A., Velasco, J. A., Saršūns, K., Puurunen, R. L., Lazdoviča, K. Cobalt-promoted Fe_3O_4 catalysts for CO_2 hydrogenation to C_{2+} hydrocarbons: Effect of pretreatment method and reaction temperature. *Fuel Processing Technology,* **2026**, 288, 108467. https://doi.org/10.1016/j.fuproc.2026.108467.
2) **Stanke, A.**, Ābelniece, Z., Šutka, A., Bērziņš, A., Kõiv, M., Lazdoviča, K. $NiFe_2O_4$ catalysts for CO_2 hydrogenation: Performance analysis and comparative life cycle assessment of catalyst synthesis routes. *Manuskripts iesniegts International Journal of Hydrogen Energy.* Patreizējais statuss – manuskriptis tiek recenzēts.
3) **Stanke, A.**, Lazdoviča, K., Gaile, A., Laipniece, L. Fischer-Tropsch synthesis product selectivity over silica-supported iron-based catalyst: Effect of K/Fe ratio. *Fuel*, **2025**, 387, 134399. https://doi.org/10.1016/j.fuel.2025.134399.
4) Ābelniece, Z., Cutrufello, M. G., Rombi, E., **Stanke, A.**, Piirsoo, H., Mändar, H., Tamm, A. The structure-activity interactions of Cu/Zn, In/Pd and Fe/K catalysts supported on mesoporous SBA-15 for carbon dioxide hydrogenation at low pressure. *Chemical Papers*, **2024**, 78, 5103-5112. https://doi.org/10.1007/s11696-024-03456-9.
5) **Stanke, A.**, Lazdoviča, K., Laipniece, L. Evaluation of the Fischer-Tropsch synthesis product selectivity over iron-based silica-supported catalyst under mild temperatures. *Environmental Progress and Sustainable Energy*, **2024**, 43 (3), e14335. https://doi.org/10.1002/ep.14335.
6) **Stanke, A.**, Kampars, V. Agglomeration of Fe/SBA-15 with clays for Fischer-Tropsch synthesis. *Energy Reports*, **2022**, 8, 461–466. https://doi.org/10.1016/j.egyr.2022.10.251.

Konferences, kurās publicēti pētījumu rezultāti

1) **Stanke, A**., Lazdoviča, K. The promotional effect of potassium on iron-based silica supported catalyst for CO_2 hydrogenation. No: *International Multidisciplinary Scientific GeoConference Surveying Geology and Mining Ecology Management, SGEM 2022: Conference Proceeding*, 22 (4.1), pp. 161–166. https://doi.org/10.5593/sgem2022/4.1/s17.21 Bulgārija, Albena, 4.–10. jūlijs, 2022.
2) **Stanke, A.** The effect of kaolin and hectorite clay on the Fischer-Tropsch synthesis condensed hydrocarbon products. No: *9th IUPAC International Conference on Green Chemistry: ICGC Book of Abstracts.,* Grieķija, Atēnas, 5.–9. septembris, 2022.
3) **Stanke, A**., Lazdoviča, K. The promotional effect of potassium on iron-based silica-supported catalyst for the hydrogenation of carbon oxides. No: *RTU 63. International Conference "Materials Science & Applied Chemistry": Program and Abstracts*, Latvija, Rīga, 21. oktobris, 2022.

PROMOCIJAS DARBA GALVENIE REZULTĀTI

Pēdējo gadu laikā strauji attīstās pētījumi par FTS un CO_2-FTS. Šo interesi ir veicinājis pieaugošais pieprasījums pēc enerģijas un steidzamā nepieciešamība mazināt siltumnīcas efektu izraisošo gāzu emisijas. Tomēr, neraugoties uz apjomīgajiem pētījumiem, zināšanās joprojām ir būtiskas nepilnības, jo FTS rezultātā veidojas sarežģīts daudzfāžu produktu maisījums, un tā selektivitāte, aktivitāte un blakusproduktu veidošanās ir ļoti atkarīga no katalizatora sastāva, promotoru satura, nesēja un reakcijas apstākļiem. Turklāt, lai gan FTS un CO_2-FTS procesos neizbēgami veidojas ievērojams ūdens daudzums, ūdens fāzes nozīme pētījumos bieži tiek ignorēta.

Eksperimentālo apstākļu un izmantoto katalizatoru atšķirības dažādos pētījumos ir radījušas savstarpēji pretrunīgus secinājumus, tādējādi akcentējot nepieciešamību pēc padziļinātas un standartizētas izpētes, kas sistemātiski sasaistītu katalizatora struktūru, tā sagatavošanas pieeju un darbības (reakcijas) apstākļus ar kopējo procesa veiktspēju.

Promocijas darba izstrādes gaitā veikti fundamentāli pētījumi, lai noskaidrotu katalizatora nesēja, promotora satura un reakcijas apstākļu ietekmi uz CO konversiju, ogļūdeņražu selektivitāti un skābekli saturošo savienojumu veidošanos FTS procesā. Turklāt pētīta arī reakcijas temperatūras, katalizatora sintēzes un priekšapstrādes metodes ietekme uz CO_2-FTS procesa veiktspēju.

Promocijas darbā izvērtēta dzelzs katalizatoru veiktspēja FTS un CO_2-FTS procesos, izmantojot nepārtrauktas plūsmas fiksētas katalizatora gultnes reaktoru (3. att.). Visos eksperimentos reaģentu gāzu plūsmas regulēšanai tika izmantoti atsevišķi masas plūsmas kontrolieri. N_2 aprēķinos tika izmantos kā iekšējais standarts. Reakcijas temperatūra tika mērīta, izmantojot K tipa termopāri, kas ievietots katalizatora slāņa centrā. Reakcijas efluents plūda caur vasku uztvērēju un gāzes/šķidruma/šķidruma separatoru. Kondensētie produkti tika analizēti *off-line*, izmantojot gāzu hromatogrāfu, kas savienots ar masspetrometru (GC-MS), kodolmagnētiskās rezonanses spektroskopiju (KMR) un Furjē transformācijas infrasarkano (FTIR) spektrometriju, savukārt gāzes fāze tika analizēta *on-line*, izmantojot gāzu hromatogrāfu, kas aprīkots ar siltumvadītspējas un liesmas jonizācijas detektoriem (GC-TCD/FID).

Katalizatoru pagatavošanai tika izmantotas vairākas metodes. Iegūtie heterogēnie katalizatori tika raksturoti, izmantojot šādas metodes: rentgenstaru difrakciju (*XRD*) kristāliskās fāzes un daļiņu izmēru noteikšanai; rentgenstaru fotoelektronu spektroskopiju (*XPS*) elektronisko stāvokļu izpētei; rentgenstaru fluorescences spektroskopiju (*XRF*) dzelzs koncentrācijas noteikšanai; skenējošo elektronu mikroskopiju (SEM) virsmas morfoloģijas attēlošanai; N_2 adsorcijas-desorbcijas mērījumus virsmas laukuma un poru izmēru sadalījuma noteikšanai. Gan pirms FTS, gan pirms CO_2-FTS procesa katalizatori tika reducēti *in situ* ar CO vai H_2, lai izveidotu katalītiski aktīvo fāzi. Šis reducēšanas process palielina pieejamo aktīvo vietu skaitu uz katalizatora virsmas un nodrošina efektīvu reaģējošo molekulu adsorbciju un aktivāciju.

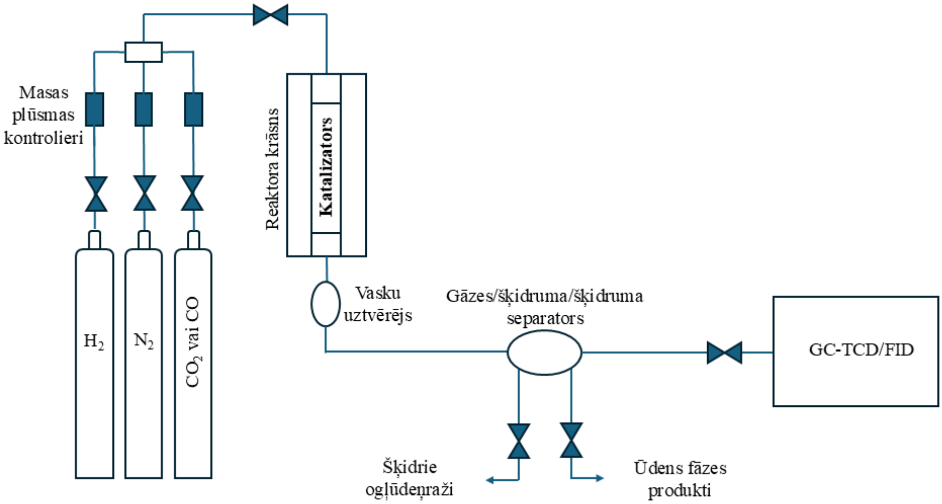

3. att. Eksperimentālās iekārtas shēma.

1. CO hidrogenēšana

1.1. Reakcijas temperatūras ietekme uz uznestu dzelzs katalizatoru FTS veiktspēju

Līdzšinējie pētījumi, kuros analizēta procesa apstākļu, katalizatora sastāva un struktūras ietekme uz produktu selektivitāti, galvenokārt ir koncentrējušies uz dzelzs katalizatoriem bez nesēja (*bulk catalysts*). Reakcijas temperatūras ietekme uz FTS veiktspēju būtiski atšķiras starp katalizatoriem bez nesēja un uznestiem katalizatoriem metāla dispersijas siltuma pārneses un fāžu stabilitātes dēļ. Katalizatori bez nesēja paaugstinātā temperatūrā mēdz piedzīvot izteiktas strukturālās un fāžu pārejas, kas būtiski ietekmē katalītisko aktivitāti un produktu selektivitāti. Savukārt uz nesēja uznestiem dzelzs katalizatoriem parasti piemīt augstāka termiskā stabilitāte un labāka siltumvadītspēja, nodrošinot kontrolētāku reakciju pret temperatūras izmaiņām [15].

Šajā promocijas darbā pētīta FTS reakcijas temperatūras ietekme diapazonā no 240 °C līdz 300 °C, izmantojot uz mezoporaina SiO_2 uznestu dzelzs katalizatoru. Katalizators tika pagatavots, impregnējot komerciālas SiO_2 granulas ar 0,8 M $Fe(NO_3)_3$ ūdens šķīdumu 50 °C temperatūrā piecas stundas. Pēc tam materiāls tika filtrēts, žāvēts 110 °C temperatūrā un piecas stundas izkarsēts gaisā 550 °C temperatūrā. Šī pagatavošanas procedūra nodrošināja vienmērīgu prekursora sadalījumu katalizatora porās, vienlaikus saglabājot granulu strukturālo integritāti un mehānisko stabilitāti.

Ar *XRF* noteiktais dzelzs saturs katalizatorā bija 11,4 masas %. *XRD* difratogrammā bija novērojami signāli, kas atbilda hematītam (α-Fe_2O_3). Platais pīķis pie $2\theta = 24$ ° (4. att.) ir saistīts ar amorfu SiO_2. Pēc Šrērera vienādojuma aprēķinātais vidējais Fe_2O_3 kristalītu izmērs bija 13 nm. Katalizatora nesēja un impregnētā katalizatora N_2 adsorbcijas-desorbcijas izotermas atbilda *IUPAC* IV tipa izotermai ar H1 histerēzes cilpu, kas raksturīga mezoporainiem materiāliem. SEM-EDS analīze apstiprināja vienmērīgu un homogēnu dzelzs oksīda sadalījumu uz katalizatora virsmas. Impregnētā katalizatora īpatnējais virsmas laukums (207 m^2/g)

saglabājās gandrīz neizmainīts, salīdzinot ar tīra katalizatora nesēja virsmas laukumu (213 m^2/g). Savukārt pēc impregnēšanas poru tilpums samazinājās no 0,88 cm^3/g līdz 0,79 cm^3/g, poru izmērs samazinājās no 16,5 nm līdz 15,3 nm, salīdzinot ar tīru katalizatora nesēju. Iegūtie raksturlielumi liecina, ka dzelzs daļiņas ir lokalizētas nesēja porās, tās nenosprostojot. Paredzams, ka šādas katalizatora īpašības būs priekšrocība FTS, jo tās var veicināt augstāku CO konversiju un C_{5+} ogļūdeņražu selektivitāti, salīdzinot ar literatūrā aprakstītajiem dzelzs katalizatoriem bez nesēja vai slikti dispergētiem dzelzs katalizatoriem [16].

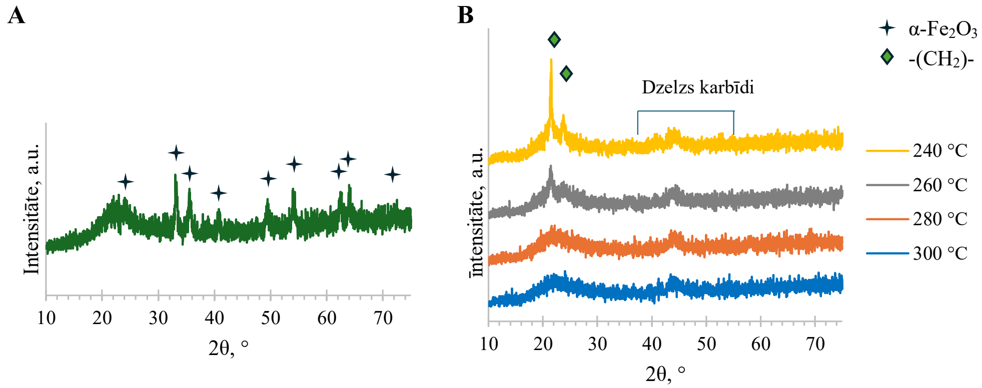

4. att. Izkarsēta katalizatora *XRD* pirms FTS (A) un izmantoto katalizatoru *XRD* pēc FTS (B).

Difrakcijas maksimumi visiem katalizatoriem pēc FTS redzami 2θ apgabalā no 35° līdz 52°. Tie ir identificējami kā dzelzs karbīdi, kas ir FTS aktīvās vietas (4. B att.). Katalizatoru difrakcijas ainās pēc reakcijām 240 °C un 260 °C temperatūrā redzami maksimumi arī pie $2\theta = 21{,}4°$ un 23,9°, kas atbilst vaskiem. Vasku uzkrāšanās uz katalizatora virsmas ir galvenais faktors, kas veicina novēroto katalizatora veiktspējas samazināšanos šajā temperatūrā.

Reakcijas temperatūras paaugstināšana no 240 °C līdz 280 °C izraisīja būtisku CO konversijas pieaugumu no 13,6 % līdz 34,2 %, kas liecina par labāku katalītisko aktivitāti (5. att.). Temperatūras paaugstināšana līdz 300 °C radīja tikai nelielu efektu, kas liecina, ka FTS reakcija tuvojas tās optimālajai kinētiskajai robežai. Gāzes fāze bija dominējošā visā temperatūru diapazonā, sasniedzot maksimumu 300 °C temperatūrā, savukārt šķidro ogļūdeņražu frakcija sasniedz maksimumu 280 °C temperatūrā, un tās daudzums strauji samazinājās, tālāk paaugstinot temperatūru. Turklāt arī ūdens fāzes daudzums pieauga, palielinot temperatūru līdz 280 °C, bet pie tālākas temperatūras palielināšanas tas samazinājās. Visā pētītajā temperatūras diapazonā vasku daudzums bija niecīgs; tas nedaudz pieauga 260 °C temperatūrā, bet augstākā temperatūrā samazinājās. Šie rezultāti norāda, ka 280 °C ir optimāla reakcijas temperatūra pētītajam katalizatoram, nodrošinot līdzsvaru starp CO konversiju un C_{5+} ogļūdeņražu selektivitāti. Augstākā temperatūrā sekundārās reakcijas un pastiprināta *WGS* aktivitāte veicināja īsas virknes ogļūdeņražu veidošanos. Savukārt zemākā temperatūrā tika novērota samazināta CO konversija un pastiprināta vasku uzkrāšanās, kas savukārt var veicināt katalizatora deaktivāciju.

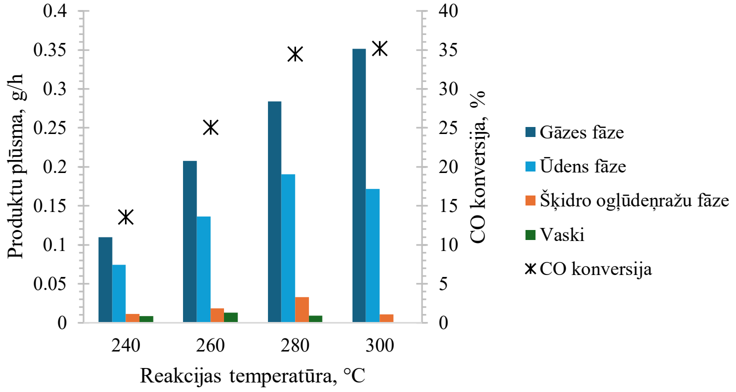

5. att. Reakcijas temperatūras ietekme uz CO konversiju un gāzes fāzes, šķidro ogļūdeņražu fāzes, vasku un ūdens fāzes produktu plūsmām.

Šķidro ogļūdeņražu frakcija tika analizēta, lai novērtētu tās potenciālu e-degvielu ražošanā. Oglekļa virknes garums analizētajos produktos bija no C_5 līdz C_{36}. Par īpaši vērtīgiem tiek uzskatīti ogļūdeņraži benzīna (C_5–C_{11}), petrolejas (C_{10}–C_{14}) un dīzeļdegvielas (C_{12}–C_{20}) diapazonos. Lielākajai daļai šķidro ogļūdeņražu produktu oglekļa virknes garums atbilda benzīna frakcijai (6. att.). Paaugstinot reakcijas temperatūru, benzīna frakcijas ogļūdeņražu īpatsvars pieauga no 54 % līdz 73 %. Vienlaikus petrolejas frakcijas īpatsvars samazinājās no 51 % līdz 38 %, savukārt dīzeļdegvielas – no 44 % līdz 26 %.

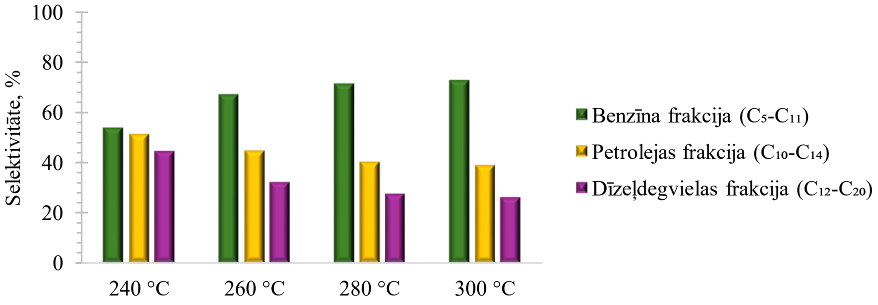

6. att. Benzīna frakcijas, petrolejas frakcijas un dīzeļdegvielas frakcijas ogļūdeņražu selektivitāte šķidrajā ogļūdeņražu fāzē.

Benzīna frakcija sastāvēja galvenokārt no *n*-parafīniem, dažādiem olefīniem, sazarotiem ogļūdeņražiem un vidēja garuma oglekļa virknes spirtiem (7. att.). Paaugstinot reakcijas temperatūru, samazinājās 1-olefīnu, bet pieauga *n*-parafīnu, sazarotu ogļūdeņražu un olefīnu ar dubultsaiti pie otrā oglekļa atoma vai tālāk virknē proporcija. Šī tendence liecina par 1-olefīnu iesaisti sekundārajās reakcijās, tostarp hidrogenēšanā un izomerizācijā. Prasības benzīnam, ko piegādā un tirgo Eiropas Savienībā, stingri regulē Eiropas benzīna standarts (*EN 228*). Tajā noteikts, ka maksimālais olefīnu saturs nedrīkst pārsniegt 18 tilpuma %, bet aromātisko savienojumu saturs – 35 tilpuma %. Salīdzinot iegūto benzīna frakciju ar *EN 228* noteiktajiem kritērijiem, redzams, ka olefīnu īpatsvars visos paraugos ir augstāks par atļauto. Tajā pat laikā izmantotais katalizators neveicina aromātisko savienojumu veidošanos.

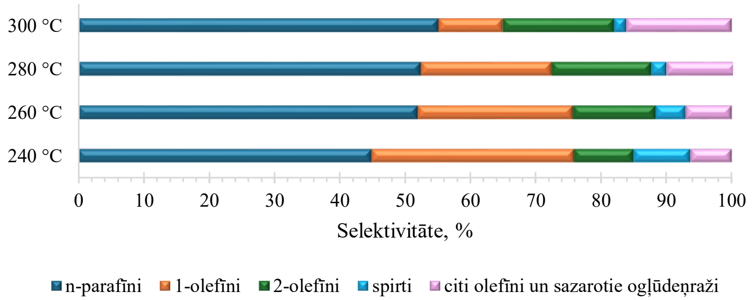

7. att. Reakcijas temperatūras ietekme uz benzīna frakcijas ogļūdeņražu sastāvu.

FTS laikā ogļūdeņražu virknes augšana notiek vienlaikus ar ūdens veidošanos. Reizē ar katras metilēngrupas ($-CH_2-$) pievienošanos augošajai ogļūdeņražu virknei veidojas viena ūdens molekula (1.1. vienādojums). Izveidojusies ūdens fāze satur dažādus skābekli saturošus savienojumus – spirtus, skābes, aldehīdus un ketonus. Šo savienojumu sadalījums starp ūdens fāzi un ogļūdeņražu fāzi ir atkarīgs no to virknes garuma un polaritātes. Skābekli saturošie savienojumi negatīvi ietekmē produktu selektivitāti, kā arī rada gan vides problēmas, gan ekonomiskus izaicinājumus.

Salīdzinājumā ar literatūrā aprakstītiem komerciālajiem katalizatoriem, kam ūdenī šķīstošo skābekli saturošo savienojumu īpatsvars sasniedz aptuveni 6 % no visiem produktiem [17], izmantotā katalizatora klātbūtnē ūdens fāzē izšķīdušie skābekli saturošie savienojumi veidoja relatīvi nelielu daļu no visiem FTS produktiem (2,4 % – 240 °C temparatūrā, 3,1 % – 260 °C temperatūrā, 3,6 % – 280 °C temperatūrā un 3,5 % – 300 °C temperatūrā).

Zinātniskajā literatūrā FTS pētījumi galvenokārt vērsti uz mērķa ogļūdeņražu produktu iegūšanu, savukārt ūdens fāzes ķīmiskais sastāvs bieži tiek uzskatīts par sekundāru aspektu. Rezultāti parādīja, ka, paaugstinot reakcijas temperatūru, palielinās skābekli saturošo savienojumu koncentrācija ūdens fāzē un būtiski mainās produktu proporcijas (8. att.). Metanols un etanols bija dominējošie skābekli saturošie savienojumi ūdens fāzē. Paaugstinot temperatūru no 240 °C līdz 300 °C, metanola tilpumdaļa palielinājās no 3,8 % līdz 10,4 %, etanola – no 3,5 % līdz 5,2 %. Citi identificētie produkti bija acetons un C_3–C_7 pirmējie spirti. Paaugstināta temperatūra kavēja garākas virknes spirtu veidošanos, taču tā veicināja karbonilsavienojumu rašanos. Šī tendence, visticamāk, ir saistīta ar 1-olefīnu sekundārajām reakcijām, kuru rezultātā rodas ketoni. Lai gan šis katalizators galvenokārt paredzēts ogļūdeņražu sintēzei, augstāka reakcijas temperatūra veicina tādas ūdens fāzes veidošanos, kas bagātināta ar atsevišķiem skābekli saturošiem savienojumiem, īpaši metanolu un etanolu. Šie abi spirti ir nozīmīgi gan kā nākotnes degvielu prekursori, gan kā "zaļās" piedevas benzīnam.

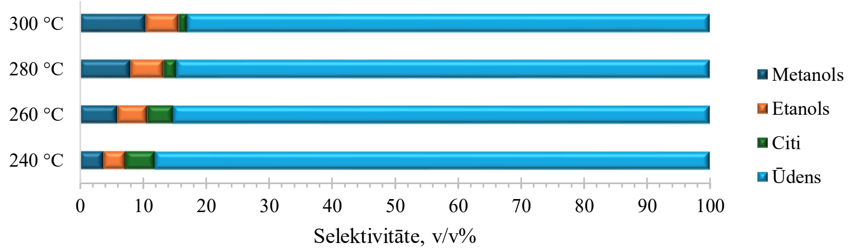

8. att. Reakcijas temperatūras ietekme uz ūdens fāzes sastāvu.

Eksperimentu rezultāti liecina, ka 280 °C ir optimāla reakcijas temperatūra uz mezoporaina SiO_2 uznestam dzelzs katalizatoram, jo tā nodrošina līdzsvaru starp augstu CO konversiju, paaugstinātu C_{5+} ogļūdeņražu selektivitāti un ierobežotu vasku veidošanos. Novirze no šīs temperatūras izraisīja vai nu samazinātu aktivitāti zemākā temperatūrā, vai arī palielinātu īsas oglekļa virknes ogļūdeņražu veidošanos augstākā temperatūrā.

Plašāks šajā nodaļā aprakstītā pētījuma izklāsts – oriģinālpublikācijā 1. pielikumā.

1.2. Promotora (kālija) satura ietekme uz uznestu dzelzs katalizatoru FTS veiktspēju

Starp dažādiem promotoriem kālijs ir viens no biežāk izmantotajiem dzelzs FTS katalizatoros, un tā ietekme uz katalītisko veiktspēju ir plaši pētīta. Tomēr tajā pat laikā zinātniskajā literatūrā aprakstītā ietekme uz katalītisko aktivitāti un skābekli saturošo savienojumu selektivitāti nav viennozīmīga un ietver pretrunīgus rezultātus. Šīs atšķirības galvenokārt skaidrojamas ar atšķirībām katalizatora sastāvā, promotora daudzumā un reakcijas apstākļos. Turklāt lielākā daļa līdzšinējo pētījumu veltīta katalizatoriem bez nesēja, savukārt sistemātiski pētījumi par uz nesēja uznestiem katalizatoriem ir salīdzinoši maz.

Kālijs FTS katalizatoru sastāvā nav metāliskā stāvoklī. Tas ir sastopams savienojumu veidā, piemēram, K_2O [18], KFe_xO_y [19], K_2CO_3, HCOOK [20], vai arī kā uz virsmas adsorbēts katjons (K^+), ko stabilizē skābekli saturoši anjoni [18], [21].

Kālija promotējošais efekts saistīts ar to, ka tas maina aktīvo vietu/centru elektronu blīvumu, tādējādi ietekmējot adsorbēto molekulu saistīšanās stiprumu [22]. Ir novērots, ka kālija klātbūtnē palielinās katalizatorā esošo dzelzs savienojumu elektronu blīvums [19], [22], [23]. Tas savukārt pastiprina CO adsorbciju un pavājina H_2 adsorbciju. Rezultātā uz katalizatora virsmas iegūtā zemākā H/C attiecība kavē hidrogenēšanas reakcijas un līdz ar to ierobežo CH_4 veidošanos, vienlaikus sekmējot ogļūdeņražu virknes augšanu un *WGS* reakcijas norisi.

Šajā promocijas darbā sistemātiski pētīta K/Fe attiecības ietekme uz FTS produktu selektivitāti, izmantojot uz mezoporaina SiO_2 uznestu dzelzs katalizatoru tādos reakcijas apstākļos, kas atbilst rūpnieciskajiem (P = 20 bar, T = 280 °C).

Uz mezoporaina SiO_2 uznests dzelzs katalizators (K-0) tika pagatavots pēc 1.1. nodaļā aprakstītās metodes. Katalizatori ar K/Fe molāro attiecību diapazonā no 0,02 līdz 0,06 tika sintezēti, impregnējot K-0 ar KNO_3 ūdens šķīdumu. Impregnēšanas šķīdumu koncentrācijas tika attiecīgi pielāgotas, lai nodrošinātu 0,02, 0,04 un 0,06 K/Fe molāro attiecību gatavajos katalizatoros. Pēc impregnēšanas paraugi tika žāvēti 110 °C temperatūrā divas stundas un izkarsēti gaisā 550 °C temperatūrā piecas stundas.

XRD difraktogrammās tika novēroti signāli, kas atbilda α-Fe_2O_3. Kālija pievienošana katalizatoriem neietekmēja hematīta kristālisko struktūru (9. A att.). Kālija savienojumus nebija iespējams detektēt ar *XRD*, visticamāk, to zemās koncentrācijas un augstās dispersijas dēļ. Pēc FTS procesa katalizatoru difrakcijas ainās redzami maksimumi pie 2θ = 21,4° un 23,9°, kas atbilst vaskiem. Vaski, kas uzkrājas uz katalizatora virsmas, samazina gan masas pārneses efektivitāti, gan katalizatora aktivitāti FTS procesā.

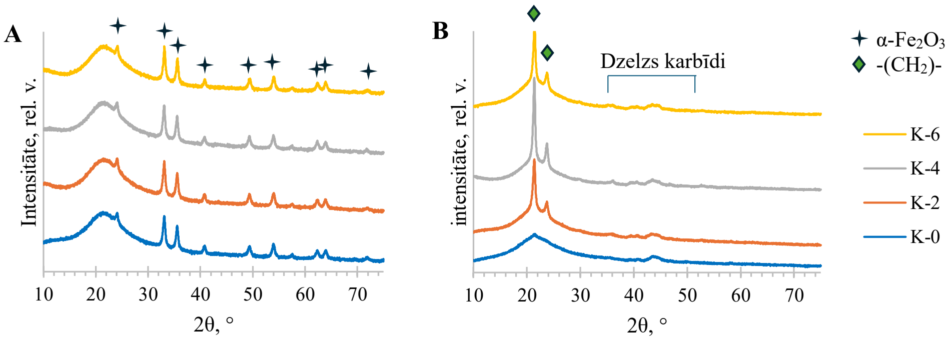

9. att. Katalizatoru *XRD* pirms FTS (A) un izmantotu katalizatoru *XRD* pēc FTS (B).

Katalizatoru teksturālie raksturojumi, kas apkopoti 1. tabulā, liecina, ka dzelzs un kālija savienojumi ir lokalizēti katalizatora nesēja porās. Turklāt rezultāti liecina, ka mazākās poras varētu būt bloķētas impregnēšanas procesā.

1. tabula

Katalizatora nesēja un ar kāliju promotēto katalizatoru teksturālie raksturlielumi

Paraugs	BET virsmas laukums, m^2/g	Kopējais poru tilpums, cm^3/g	Vidējais poru diametrs, nm
Nesējs (SiO_2)	213	0,88	16,5
K-0	207	0,79	15,3
K-2	200	0,78	15,4
K-4	197	0,76	15,5
K-6	194	0,76	15,7

FTS eksperimentos veidojās gāzes fāze, šķidro ogļūdeņražu fāze, vaski un ūdens fāze (10. att). Kālija pievienošana būtiski ietekmēja visu produktu fāzes, izņemot šķidro ogļūdeņražu fāzi. Vasku veidošanās procesā bija novērojama “vulkāna tipa” atkarība no kālija satura ar maksimumu pie K/Fe attiecības 0,02. Tajā pat laikā gāzes fāzes produktiem bija raksturīga paraboliska tendence ar minimumu pie K/Fe = 0,02. Šī tendence skaidrojama ar strauju CH_4 selektivitātes samazināšanos no 21,5 % līdz 8,5 % un vienlaikus CO_2 proporcijas pieaugumu no 12,3 % līdz 18,7 %, palielinoties K/Fe attiecībai. Turklāt ūdens fāzes daudzums pakāpeniski samazinājās, pieaugot K/Fe attiecībai. Samazinātā ūdens veidošanās kombinācijā ar augstāku CO_2 selektivitāti liecina par pastiprinātu *WGS* reakcijas aktivitāti ar kāliju promotētajiem katalizatoriem. Samazinātu vasku veidošanos pie lielāka kālija satura iespējams skaidrot ar lēnāku garas oglekļa virknes ogļūdeņražu difūziju katalizatora porās, kas izraisa ilgstošāku aktīvo vietu aizņemšanu. Arī CO konversija uzrādīja paraboliska rakstura atkarību no K/Fe attiecības, kas, visticamāk, saistīts ar līdzsvaru starp fizikālajiem difūzijas ierobežojumiem, ko rada vasku uzkrāšanās porās, un uzlabotu CO adsorbciju un disociāciju pie augstāka kālija satura. Pie K/Fe Fe = 0,02 ir novērojams minimums, kas iezīmē punktu, kurā vasku uzkrāšanās būtiski kavē reakciju. Tikai pie lielākas kālija koncentrācijas (K/Fe ≥ 0,04) uzlabotā virsmas kinētika spēj kompensēt difūzijas ierobežojumus.

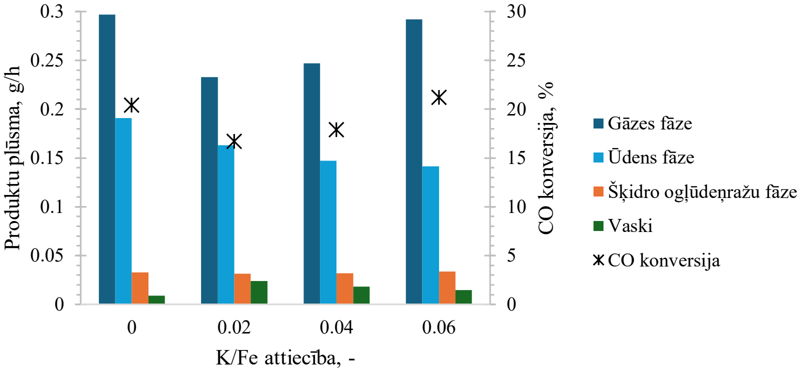

10. att. K/Fe attiecības ietekme uz CO konversiju un gāzes fāzes, šķidro ogļūdeņražu fāzes, vasku un ūdens fāzes produktu plūsmām.

Ņemot vērā to, ka šī promocijas darba mērķis ir e-degvielu un to prekursoru sintēze, īpaša uzmanība tika pievērsta K/Fe attiecības ietekmei uz šķidrās ogļūdeņražu fāzes produktiem. Šī fāze saturēja produktus ar oglekļa atomu virknes garumu no C_5 līdz C_{36}, tomēr lielākā daļa produktu bija ar oglekļa virknes garumu, kas atbilst benzīna frakcijai. Pretstatā reakcijas temperatūras ietekmei K/Fe attiecības palielināšana proporciju starp benzīna, petrolejas un dīzeļdegvielas frakcijām praktiski neizmainīja (11. att.).

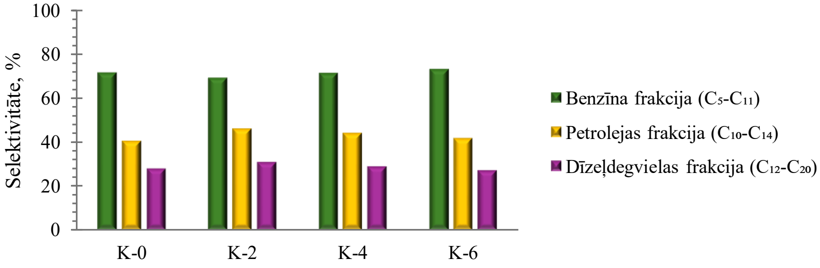

11. att. K/Fe attiecības ietekme uz benzīna, petrolejas un dīzeļdegvielas frakcijas ogļūdeņražu selektivitāti šķidrajā ogļūdeņražu fāzē.

Darba izstrādes gaitā tika izvērtēta K/Fe attiecības ietekme uz benzīna frakcijas ogļūdeņražu sastāvu. K/Fe attiecības palielināšana no 0 līdz 0,04 izraisīja būtiskas izmaiņas ogļūdeņražu sastāvā, savukārt turpmāka K/Fe attiecības palielināšana līdz 0,06 radīja tikai minimālu ietekmi (12. att.). Kālija promotora pievienošana samazināja katalizatora hidrogenēšanas aktivitāti. Rezultātā paraugos K-4 un K-6 katalizatoru klātbūtnē *n*-parafīnu saturs samazinājās vairāk nekā divas reizes, savukārt olefīnu saturs pieauga vairāk nekā divkārt, salīdzinot ar K-0. Tika novērots, ka kālija klātbūtne kavēja 1-olefīnu izomerizāciju par olefīniem ar dubultsaiti pie otrā oglekļa vai tālāk virknē. Rezultātā katalizatoriem ar lielāku kālija saturu bija augstāka 1-olefīnu attiecība pret olefīniem ar dubultsaiti molekulas vidū. Kālijs sekmēja arī oglekļa virknes augšanu, tādējādi veicinot garākas oglekļa virknes spirtu veidošanos. To zemās šķīdības ūdenī dēļ šie spirti uzkrājās šķidro ogļūdeņražu fāzē.

Iegūtās benzīna frakcijas salīdzinājums ar *EN 228* prasībām benzīnam liecina par krietni paaugstinātu olefīnu saturu paraugos. Šis rezultāts norāda, ka kālijs kā promotors nav piemērots tiešai e-degvielu ražošanai.

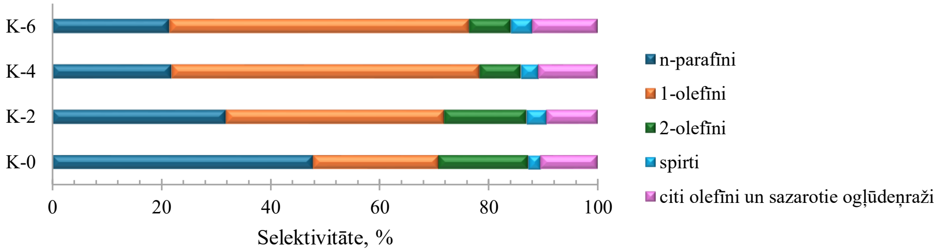

12. att. K/Fe attiecības ietekme uz benzīna frakcijas ogļūdeņražu sastāvu.

Kālijs nepalielināja ūdenī šķīstošo skābekli saturošo savienojumu īpatsvaru attiecībā pret visiem FTS produktiem; ūdenī šķīstošo skābekli saturošo savienojumu daudzums/selektivitāte samazinājās līdz aptuveni 2,1 % pie K/Fe attiecības 0,06. Tomēr kālijs būtiski mainīja ūdens fāzes ķīmisko sastāvu, izmainot atsevišķu skābekli saturošo savienojumu sadalījumu un koncentrāciju.

Kālija pievienošana veicināja oglekļa virknes augšanu, tādējādi mainot ūdens fāzes skābekli saturošo savienojumu profilu – nepromotētam katalizatoram dominējošais produkts bija metanols, savukārt ar kāliju promotētajiem katalizatoriem par dominējošo produktu kļuva etanols. Citi ūdens fāzē konstatētie produkti bija acetons un C_3–C_7 pirmējie spirti. Šo produktu proporcija, izņemot *n*-propanolu, palielinājās, pieaugot K/Fe attiecībai. Kopējā skābekli saturošo savienojumu selektivitāte uzrādīja parabolisku tendenci ar zemāko skābekli saturošo savienojumu saturu K-4 katalizatora klātbūtnē (13. att.). Šī tendence izskaidrojama ar diviem faktoriem: (1) kālijs nomāc katalizatora hidrogenēšanas aktivitāti, veicinot garākas oglekļa virknes un mazāk polāru produktu veidošanos; (2) kālijs pastiprina CO adsorbciju, tādējādi veicinot skābekli saturošu savienojumu veidošanos caur CO iespiešanās mehānismu.

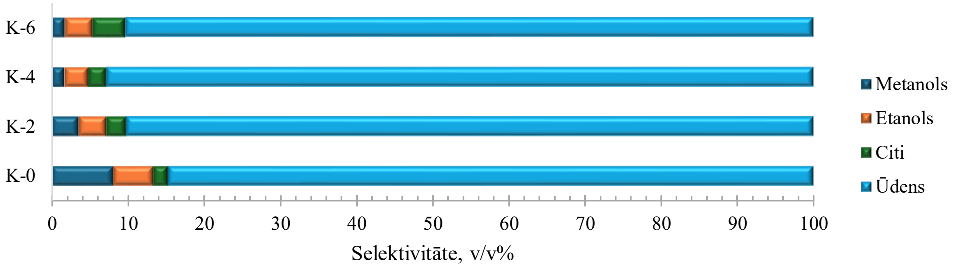

13. att. K/Fe attiecības ietekme uz ūdens fāzes sastāvu.

Eksperimentālie rezultāti liecina, ka K/Fe attiecības palielināšana būtiski ietekmē katalizatoru selektivitāti, kavējot metāna veidošanos un veicinot olefīnu, garas oglekļa virknes ogļūdeņražu un skābekli saturošu savienojumu veidošanos. Vienlaikus palielināta K/Fe attiecība veicina nepiesātinātu produktu veidošanos, kas ierobežo ar kāliju promotētu katalizatoru tiešu lietojumu e-degvielu sintēzē augstā benzīna frakcijas olefīnu satura dēļ.

Sīkāks šajā nodaļā aprakstītā pētījuma izklāsts – oriģinālpublikācijā 2. pielikumā.

1.3. Uz SBA-15 uznesta dzelzs katalizatora FTS veiktspēja

FTS procesā CO konversiju un produktu selektivitāti ietekmē gan promotori, gan katalizatora nesēji. Ieteicams izmantot inertu nesēju ar šauru poru izmēra sadalījumu un augstu termisko stabilitāti. Turklāt nesējam jābūt ar pietiekami liela diametra porām, lai tajās varētu izvietoties dzelzs oksīda kristāli, tādējādi novēršot to migrāciju uz ārējo virsmu katalizatora aktivācijas laikā [24]. SBA-15 ir piesaistījis uzmanību kā katalizatoru nesējs, piedāvājot ievērojamas priekšrocības, salīdzinot ar tradicionālo amorfo silīcija dioksīdu, pateicoties tā ļoti sakārtotajai sešstūrainajai periodiskajai struktūrai ar divdimensiju poru kanāliem un biezām silīcija dioksīda sienām. Šīs īpašības nodrošina augstu hidrotermisko stabilitāti, kas nepieciešama, lai izturētu FTS procesam raksturīgo augsto ūdens parciālo spiedienu. Salīdzinot ar iepriekš apskatītajiem nesējiem, SBA-15 poras ir mazākas (5–9 nm), bet tā virsmas laukums ir lielāks (parasti 500–1000 m^2/g). Šīs īpašības veicina augstāku dzelzs aktīvās fāzes dispersiju [25].

Šajā promocijas darbā tika pētīta FTS produktu selektivitāte, izmantojot arī uz SBA-15 uznestu dzelzs katalizatoru. Lai gan iepriekšējās nodaļās aprakstītajai nesēja matricai ir tādas priekšrocības kā komerciāla pieejamība, zemas izmaksas un praktiska granulveida forma, to stipri ierobežo maksimālais iespējamais uznestā dzelzs daudzums (< 12 masas %). Šī iemesla dēļ SBA-15 tika pētīts kā alternatīvs nesējs ar lielu virsmas laukumu.

Fe/SBA-15 pulveris tika sagatavots, izmantojot tiešās sintēzes metodi, kas adaptēta no *Zhao et al.* aprakstītās vispārīgās SBA-15 sintēzes procedūras [26]. Šāda pieeja ļāva vairāk nekā divkārt palielināt dzelzs saturu (28 masas %), neizjaucot sakārtoto mezoporaino struktūru un neizraisot poru nosprostošanos. Iegūtā katalizatora īpatnējais virsmas laukums bija 572 m^2/g liels, un tā vidējais poru diametrs bija 7 nm. Maza leņķa *XRD* difraktogrammās bija redzami difrakcijas signāli, kas attiecināmi uz (100), (110) un (200) plaknēm, tādējādi apstiprinot divdimensionālo heksagonālo SBA-15 mezoporu struktūru, savukārt plaša leņķa *XRD* liecināja par to, ka dzelzs katalizatorā galvenokārt bija α-Fe_2O_3 veidā (14. att.).

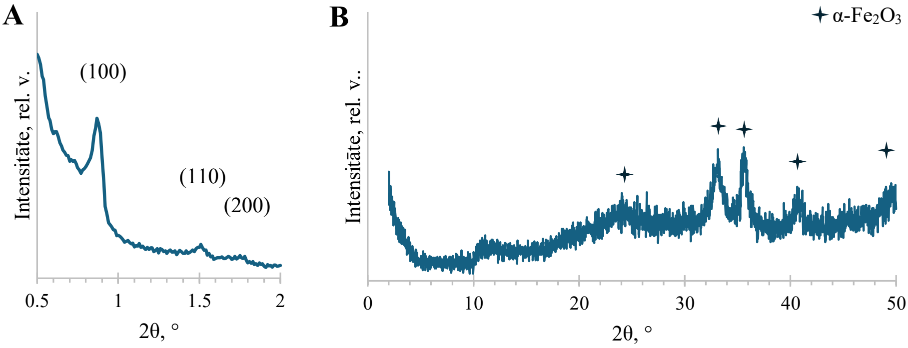

14. att. Fe/SBA-15 katalizatora maza leņķa (A) un plaša leņķa (B) *XRD* ainas.

Lai gan palielināts dzelzs saturs katalizatorā parasti palielina aktīvo centru skaitu, tas ne vienmēr korelē ar uzlabotu FTS veiktspēju. Literatūras dati liecina, ka dzelzs saturs primāri ietekmē CO konversiju un CO_2 selektivitāti, savukārt tā ietekme uz ogļūdeņražu selektivitāti ir salīdzinoši neliela. Ogļūdeņražu selektivitāti daudz lielākā mērā ietekmē izvēlētais katalizatora nesējs [24], [27].

Rezultāti, kas apkopoti 2. tabulā, liecina, ka augstā CO konversija un CO_2 selektivitāte, kas novērojama Fe/SBA-15 gadījumā, var tikt skaidrota ar palielināto dzelzs saturu katalizatorā. Katalītiskie testi apliecināja, ka poru raksturlielumiem ir būtiska nozīme uz silīcija dioksīda uznestu katalizatoru izmantošanai FTS reakcijā. Tomēr tajā pat laikā šie raksturlielumi neuzlabo mērķa produktu selektivitāti. C_{5+} ogļūdeņražu iznākums bija aptuveni uz pusi mazāks, nekā izmantojot 1.1. nodaļā analizēto uz SiO_2 uznesto katalizatoru. Fe/SBA-15 demonstrēja uzlabotu katalītisko aktivitāti un veicināja gāzveida ogļūdeņražu rašanos, kas liecina par šī katalizatora piemērotību efektīvai īsas virknes ogļūdeņražu ražošanai.

2. tabula

Fe/SiO_2 un Fe/SBA-15 katalītiskās veiktspējas salīdzinājums 280 °C un 20 bar

Katalizators	CO konversija, %	Selektivitāte, %			
		CO_2	CH_4	C_2-C_4	C_{5+}
Fe/SiO_2	34	8	11	12	69
Fe/SBA-15	54	19	17	30	34

Šķidro ogļūdeņražu fāzi veidoja produkti, kuru oglekļa virknes garums bija no C_5 līdz C_{36}. No tiem vairāk nekā 80 % bija ar oglekļa virknes garumu, kas atbilst benzīna frakcijai (3. tab.). Mazās SBA-15 mezoporas darbojas kā fiziski filtri ogļūdeņražu virkņu augšanai, ierobežojot garas virknes ogļūdeņražu difūziju uz ārpusi. Šis palielinātais uzturēšanās laiks porās var veicināt hidrokrekinga kā sekundāras reakcijas norisi, tādējādi veicinot īsākas oglekļa virknes produktu veidošanos [28].

3. tabula

Fe/SiO_2 un Fe/SBA-15 katalizatoru šķidro ogļūdeņražu fāzes selektivitātes salīdzinājums

	Fe/SiO_2	Fe/SBA-15
Benzīna frakcijas (C_5–C_{11}) selektivitāte, %	72	82
Petrolejas frakcijas (C_{10}–C_{14}) selektivitāte, %	40	30
Dīzeļdegvielas frakcijas (C_{12}–C_{20}) selektivitāte, %	28	17
Benzīna frakcijas ogļūdeņražu sastāvs		
n-parafīnu selektivitāte, %	52	48
1-olefīnu selektivitāte, %	20	8
2-olefīnu selektivitāte, %	15	18
n-spirtu selektivitāte, %	2	1
Citu olefīnu un sazarotu ogļūdeņražu selektivitāte, %	11	26

Fe/SBA-15 klātbūtnē iegūtās benzīna frakcijas *n*-parafīnu saturs bija tuvs tam, kāds tika iegūts ar iepriekš aprakstīto uz mezoporaina SiO_2 uznesto dzelzs katalizatoru. Savukārt 1-olefīnu īpatsvars samazinājās, bet sazaroto ogļūdeņražu un olefīnu, kam dubultsaite atrodas pie otrā oglekļa atoma vai tālāk virknē, īpatsvars palielinājās. FTS reakcijas apstākļos 1-olefīni ir reaģētspējīgi. To atkārtota adsorbcija virknes augšanas aktīvajos centros var radīt papildu/citus primāros produktus, savukārt adsorbcija citos centros un sekojošās sekundārās reakcijas var veicināt sazarotu ogļūdeņražu veidošanos izmantojot alkilidēna mehānismu [29], [30] vai izraisīt izomerizāciju, notiekot dubultsaites pārbīdei [31]. Šie rezultāti norāda, ka Fe/SBA-15, visticamāk, mazā poru izmēra dēļ veicina sekundārās reakcijas.

Fe/SBA-15 izmantošana samazināja skābekli saturošo savienojumu saturu ūdens fāzē, salīdzinot ar Fe/SiO_2. Galvenie identificētie skābekli saturošie savienojumi bija metanols (3,8 tilpuma %) un etanols (4,4 tilpuma %). Bez C_3–C_7 *n*-spirtiem un acetona tika konstatēta arī etiķskābe. Etiķskābes veidošanos iespējams skaidrot ar vairākiem mehānismiem. Uzlabotas virsmas īpašības var mainīt reakcijas ceļu sadalījumu starp hidrogenēšanu, CO iespiešanos un ogļūdeņražu veidošanos. Turklāt SBA-15 satur daudz silanola grupu (≡Si-OH), kas var ietekmēt šo reakcijas ceļu dinamiku un paaugstināt skābekli saturošo savienojumu, tostarp etiķskābes, selektivitāti.

Apkopojot rezultātus, secināms, ka SBA-15, pateicoties lielajam virsmas laukumam un sakārtotajai mezoporainajai struktūrai, kā katalizatora nesējs paaugstina CO konversiju. Tomēr tā mazās poras veicina sekundāras reakcijas un ierobežo garas virknes ogļūdeņražu veidošanos, un tā rezultātā, salīdzinot ar uz SiO_2 uznesto katalizatoru, veidojās vairāk gāzveida produktu un ir zemāks C_{5+} produktu īpatsvars. Tas padara uz SBA-15 uznesto katalizatoru piemērotāku īsas virknes ogļūdeņražu, nevis šķidras degvielas sintēzei.

Sīkāks šajā nodaļā aprakstītā pētījuma izklāsts – oriģinālpublikācijā 3. pielikumā.

2. CO_2 hidrogenēšana

2.1. Ar kāliju promotēti uz silīcija dioksīda uznesti katalizatori spirtu sintēzei

Spirtu sintēze aizvien ir nozīmīgs pētniecības virziens CO_2 hidrogenēšanā. Īsas oglekļa virknes spirti, kā metanols un etanols, ieņem nozīmīgu vietu ilgtspējīgās enerģētikas sistēmā – tie kalpo gan kā efektīvas degvielas, gan nozīmīgi ķīmiskie starpprodukti. Kā benzīna piedevas šie spirti uzlabo degšanas procesa efektivitāti un samazina emisijas. Papildus tiešajam lietojumam šie spirti ir svarīgs izejmateriāls spirts-par-X (*alcohol-to-X*) pārveides procesos, kuros dehidratācijas un oligomerizācijas reakciju rezultātā tie tiek pārveidoti par aviācijas degvielai un dīzeļdegvielai piemērotiem ogļūdeņražiem. Tādējādi tiek nodrošināta pāreja no mazmolekulāriem skābekli saturošiem savienojumiem uz enerģētiski blīviem ogļūdeņražiem [32].

Rūpnieciski metanolu galvenokārt ražo no fosilas izcelsmes sintēzes gāzes, izmantojot $Cu/ZnO/Al_2O_3$ katalizatorus. Reakcija notiek paaugstinātā spiedienā (50–100 bar) un temperatūrā (200–300 °C) [33]. Dažādi metālu un metālu oksīdu katalizatori tiek pētīti CO_2 pārveidei par metanolu. Visplašāk pētītas ir varu saturošas katalītiskās sistēmas, tām seko indija oksīda katalizatori un pallādija katalizatori [34]. CO_2 katalītiska pārveide par augstākiem spirtiem savukārt ir mazāk attīstīta. Pēdējā laikā dzelzs katalizatori tiek minēti kā daudzsološs risinājums metanola un augstāku spirtu sintēzei no CO_2 [35]–[37]. Pētījumos norādīts, ka sārmu promotora sinerģiskā iedarbība dzelzs katalizatoros veicina spirtu veidošanos [37], [38].

Šajā promocijas darbā, izmantojot ar kāliju promotētus uz silīcija dioksīda uznestus dzelzs katalizators, tika pētīta CO_2 hidrogenēšana par spirtiem. Katalizatori tika pagatavoti, ar $Fe(NO_3)_3$ un KNO_3 ūdens šķīdumiem impregnējot komerciālus silīcija dioksīda katalizatoru nesējus (SiO_2 granulas un SBA-15 pulveri). Iegūtie katalizatori tika žāvēti un izkarsēti gaisā. Uz SiO_2 uznestajiem katalizatoriem dzelzs saturs bija 10 %, savukārt uz SBA-15 uznestajam katalizatoram – 20 %. K/Fe attiecība uz SiO_2 uznestajiem katalizatoriem bija 0/100, 2/100 un 5/100, bet uz SBA-15 uznestajam katalizatoram – 5/100. Katalizatori tika attiecīgi apzīmēti kā Fe/SiO_2, $2K/Fe/SiO_2$, $5K/Fe/SiO_2$ un 5K/Fe/SBA-15.

Visos katalizatoros dzelzs galvenokārt bija α-Fe_2O_3 veidā, un kālija pievienošana neietekmēja hematīta kristālisko fāzi. Kālija savienojumus nebija iespējams detektēt ar *XRD* to zemās koncentrācijas un augstās dispersijas dēļ. Katalizatoru teksturālās īpašības apkopotas 4. tabulā.

4. tabula

Katalizatoru teksturālie raksturlielumi

Katalizators	BET virsmas laukums, m^2/g	Kopējais poru tilpums, cm^3/g	Vidējais poru diametrs, nm
Fe/SiO_2	207	0,79	15,3
$2K/Fe/SiO_2$	201	0,78	15,5
$5K/Fe/SiO_2$	195	0,76	15,6
5K/Fe/SBA-15	318	0,77	7,9

Palielinoties kālija saturam, uz SiO_2 uznesto katalizatoru virsmas laukums un poru tilpums samazinājās, savukārt vidējais poru diametrs nedaudz palielinājās. Šie rezultāti liecina, ka kālijs, iespējams, nosprosto mazākās poras. Uz SBA-15 uznestajam katalizatoram bija vislielākais virsmas laukums un vismazākais vidējais poru diametrs.

Vidējā CO_2 konversija uz SiO_2 uznestajiem katalizatoriem bija aptuveni 10 %, savukārt uz SBA-15 uznestā katalizatora vidējā CO_2 konversija bija tikai 1 %. Iepriekš publicētos pētījumos ziņots, ka uz silīcija dioksīda uznestos dzelzs katalizatoros dzelzs dispersiju un daļiņu izmēru ietekmē nesēja poru izmērs. Nesēji ar mazāku poru izmēru, piemēram, SBA-15, var veicināt grūti reducējamu dzelzs silikātu veidošanos [39]. Turklāt mazākas dzelzs savienojumu daļiņas parasti ir grūtāk reducējamas un karbonizējamas. Šie faktori, visticamāk, ir iemesls 5K/Fe/SBA-15 sliktajai katalītiskajai veiktspējai.

Produktu sadalījums, gāzes fāzē neiekļaujot CO selektivitāti, redzams 15. attēlā. Visiem katalizatoriem CH_4 bija dominējošais organiskais savienojums, kas tika konstatēts gāzes fāzē. Vienīgais identificētais spirts bija metanols, savukārt DME tika identificēts, tikai izmantojot 5K/Fe/SBA-15 katalizatoru. DME veidojas metanola dehidratācijas reakcijā, un šai reakcijai parasti nepieciešams katalizators ar skābām aktīvajām vietām [40]. Tikai no silīcija dioksīda sastāvošu SBA-15 materiālu virsma satur vienīgi silanola grupas, kam raksturīgas vāju skābju īpašības un kas ir katalītiski neaktīvas [41]. Virsmas skābes īpašības iespējams palielināt, dopējot SBA-15 ar dažādiem metāliem, tostarp dzelzi. Ir ziņots, ka dzelzs pievienošana palielina SBA-15 virsmas skābumu, veidojot Luisa skābei atbilstošus centrus [42]. 5K/Fe/SBA-15 katalizatora lielā virsmas laukuma un uznestā dzelzs daudzuma kombinācija, visticamāk, radīja pietiekamu virsmas skābumu, lai katalizētu DME veidošanos.

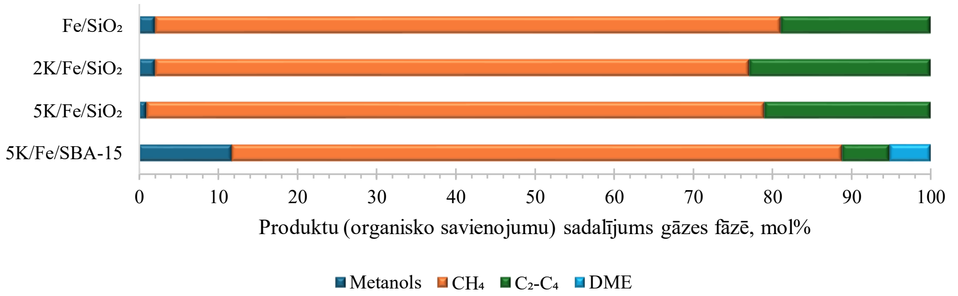

15. att. Organisko savienojumu sadalījums gāzes fāzē.

No testētajiem katalizatoriem 5K/Fe/SBA-15 uzrādīja visaugstāko metanola selektivitāti. Aprēķinātais metanola iznākums šim katalizatoram bija 3 mg/h·g_{cat}. Savukārt uz SiO_2 uznestajiem katalizatoriem metanola iznākums pieauga no 1,3 mg/h·g_{cat} Fe/SiO_2 līdz 2,7 mg/h·g_{cat}, izmantojot 2K/Fe/SiO_2, bet pēc tam būtiski samazinājās līdz 0,3 mg/h·g_{cat} 5K/Fe/SiO_2 katalizatora klātbūtnē.

Iegūtie metanola iznākumi šo katalizatoru klātbūtnē ir vairāk nekā 50 reižu zemāki par literatūrā aprakstītajiem iznākumiem, kas iegūti, izmantojot vara vai indija oksīda katalizatorus

[43]–[45]. Rezultāti liecina, ka pētītajos apstākļos ar kāliju promotētiem uz silīcija dioksīda uznestiem dzelzs katalizatoriem ir ierobežota CO_2 hidrogenēšanas aktivitāte.

Plašāka informācija par šajā nodaļā aprakstītajiem pētījumiem – oriģinālpublikācijā 4. pielikumā un konferences rakstā 5. pielikumā.

2.2. Sintēzes metodes ietekme uz $NiFe_2O_4$ struktūru un katalītisko veiktspēju e-CH_4 iegūšanā

E-metāns, kas sintezēts no CO_2, izmantojot enerģija-par-gāzi (*Power-to-Gas*) tehnoloģiju, tiek uzskatīts par daudzsološu nākotnes energoresursu, īpaši klimata pārmaiņu mazināšanas un ilgtspējīgas enerģētikas kontekstā. Atšķirībā no biometāna, kura ražošanu ierobežo lauksaimniecības vai bioloģisko atkritumu pieejamība, e-metāns nav atkarīgs no zemes izmantošanas un nekonkurē ar pārtikas ražošanu.

Augsta CH_4 selektivitāte un CO_2 konversija, izmantojot niķeļa katalizatorus, Sabatjē reakcijā parasti tiek sasniegta temperatūras diapazonā no 350 °C līdz 500 °C. Temperatūrā virs 400 °C pieaug nevēlamu blakusreakciju īpatsvars, tiek novērota oglekļa nogulsnēšanās uz katalizatora virsmas un niķeļa daļiņu saķepšana. Savukārt zemākā temperatūrā procesa efektivitāti ierobežo nepieciešamība pēc ļoti aktīviem katalizatoriem [46].

Bimetāliski katalizatori, salīdzinot ar tradicionālajiem katalizatoriem, var nodrošināt būtiskas priekšrocības, galvenokārt pateicoties unikālajai sinerģiskajai mijiedarbībai starp to komponentiem. Šīs mijiedarbības, uzlabotās dispersijas un efektīvākas aktīvo centru izmantošanas rezultātā daudzkomponentu katalizatori bieži demonstrē augstāku katalītisko aktivitāti. Neseni pētījumi CO_2-FTS jomā apliecina šo sinerģiju priekšrocības, parādot, ka tās var būtiski samazināt aktivācijas barjeras un uzlabot kopējo procesa efektivitāti [47], [48].

Niķeļa ferīts ($NiFe_2O_4$) ir špineļa tipa oksīda materiāls, kas piesaistījis uzmanību kā perspektīvs materiāls katalīzē, pateicoties savām unikālajām strukturālajām īpašībām, termiskajai stabilitātei un sastāva regulēšanas iespējām. $NiFe_2O_4$ špineļa kristālrežģī vienlaikus esošie niķeļa un dzelzs joni piešķir materiālam izteiktas oksidēšanās-reducēšanās īpašības, padarot to par daudzsološu materiālu dažādu ķīmisko reakciju, tostarp CO_2 konversijas procesu, katalizēšanai. Atšķirībā no vienkāršiem metālu oksīdu maisījumiem špineļa tipa struktūras parasti nodrošina šaurāku daļiņu izmēru sadalījumu, precīzāku stehiometriskā sastāva kontroli un līdz ar to lielāku katalītiski aktīvās virsmas laukumu [49].

Bimetālisko oksīdu katalizatoru veiktspēju ietekmē vairāki faktori, tostarp sintēzes process, kas nosaka špineļa oksīdu struktūru, morfoloģiju un vispārējās īpašības [50], [51]. Fāzes ziņā tīra, homogēna un ar kontrolētu daļiņu izmēru špineļa $NiFe_2O_4$ sintēze joprojām ir būtisks izaicinājums. Sintēzes apstākļu variācijas bieži noved pie sekundāro fāžu vai piemaisījumu veidošanās, kas maina kristālisko struktūru un līdz ar to ietekmē katalītiskos ceļus un kopējo efektivitāti. Neraugoties uz dažādu sintēzes metožu izpēti, universāla un reproducējama metode augstas tīrības, monodispersu špineļa ferītu daļiņu iegūšanai līdz šim nav izstrādāta [52].

Šajā promocijas darbā tika pētīta $NiFe_2O_4$ sintēzes metodes ietekme uz katalizatora raksturlielumiem un CO_2-FTS veiktspēju. $NiFe_2O_4$ nanodaļiņas tika sintezētas, izmantojot trīs dažādas metodes – sonoķīmisko, sola-gela pašsadegšanas un reducētāja asistētu izgulsnēšanu (16. att.). Četri paraugi tika sintezēti, izmantojot sonoķīmisko metodi. Iegūtās nanodaļiņas tika apzīmētas kā $NiFe_2O_4$-sono-X, kur X apzīmē reakcijas pH līmeni (X = 8, X = 9, X = 10, X = 11). Divi paraugi tika sintezēti pēc sola-gela pašsadegšanas metodes, kā degvielu izmantojot citronskābi ($NiFe_2O_4$-Citric) vai citronskābi un etanolu ($NiFe_2O_4$-C-E). Savukārt paraugs -Prec tika sintezēts, izmantojot reducētāja asistētas izgulsnēšanas metodi.

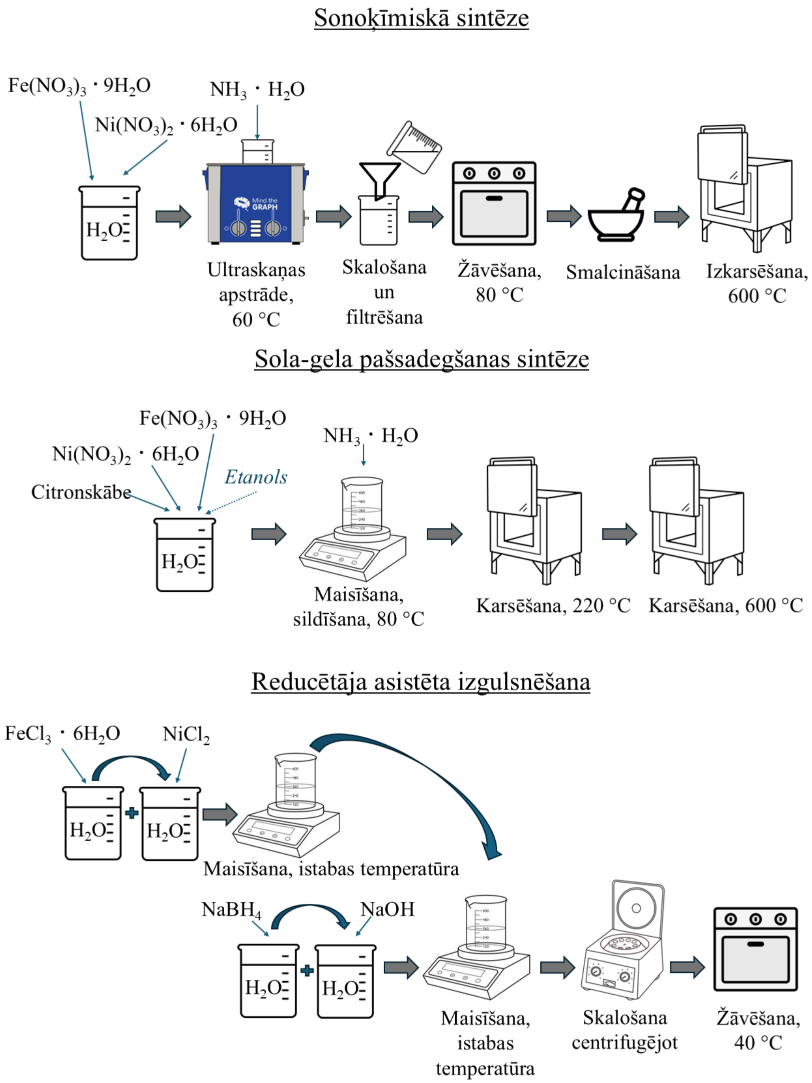

16. att. Shematisks sonoķīmiskās, sola-gela pašsadegšanas un reducētāja asistētas izgulsnēšanas sintēzes metožu attēlojums.

Dati par sintezēto $NiFe_2O_4$ nanodaļiņu fāžu sastāvu un kristalītu izmēriem apkopoti 5. tabulā. Paaugstināts pH līmenis samazināja $NiFe_2O_4$ fāzes veidošanās efektivitāti un palielināja Fe_2O_3 piemaisījumu klātbūtni paraugos. Turklāt, palielinoties pH līmenim, $NiFe_2O_4$

kristalītu izmērs samazinājās, kas liecina par paātrinātu nukleāciju. Rezultāti rāda, ka optimālais sonoķīmiskās sintēzes pH līmenis ir 8, nodrošinot augstu $NiFe_2O_4$ saturu (98 masas %) un mazu katalizatora daļiņu izmēru (~ 26 nm). Ar sola-gela pašsadegšanas metodi tika iegūti paraugi ar samazinātu $NiFe_2O_4$ saturu un paaugstinātu sekundāro fāžu (Fe_2O_3 un NiO) piemaisījumu daudzumu. Izmantojot citronskābi kā vienīgo degvielu, tika iegūts paraugs ar augstāku $NiFe_2O_4$ fāzes tīrību (76 masas %), salīdzinot ar metodi, kurā kā degviela tika izmantota gan citronskābe, gan etanols. Paraugam $NiFe_2O_4$-Citric tika novērots lielākais $NiFe_2O_4$ kristalītu izmērs (~73 nm), salīdzinot visus analizējamos paraugus. Reducētāja asistēta izgulsnēšana ļāva iegūt fāzes ziņā tīru $NiFe_2O_4$ ar mazu daļiņu izmēru.

5. tabula

Paraugu fāžu sastāvs un kristalītu izmēri

Paraugs	Kristāliskā fāze, masas %	$NiFe_2O_4$ kristalītu izmērs, nm	Fe_2O_3 kristalītu izmērs, nm	NiO kristalītu izmērs, nm
$NiFe_2O_4$-sono-8	$NiFe_2O_4$:Fe_2O_3, 98:2	25,6 ± 0,4	76 ± 21	–
$NiFe_2O_4$-sono-9	$NiFe_2O_4$:Fe_2O_3, 94:6	20,5 ± 0,3	70 ± 6	–
$NiFe_2O_4$-sono-10	$NiFe_2O_4$:Fe_2O_3, 60:40	15,6 ± 0,3	80 ± 1	–
$NiFe_2O_4$-sono-11	$NiFe_2O_4$:Fe_2O_3, 37:63	13,9 ± 0,5	44,7 ± 0,6	–
$NiFe_2O_4$-C-E	$NiFe_2O_4$:Fe_2O_3:NiO, 33:48:19	42,4 ± 1,6	85,9 ± 5,2	42,4 ± 3,9
$NiFe_2O_4$-Citric	$NiFe_2O_4$:Fe_2O_3:NiO, 76:18:6	73,3 ± 1,1	143 ± 16	50,9 ± 5,6
$NiFe_2O_4$-Prec	$NiFe_2O_4$, 100	12,0 ± 0,3	–	–

No katras attiecīgās sintēzes metodes viens augstākās tīrības $NiFe_2O_4$ paraugs ($NiFe_2O_4$-sono-8, $NiFe_2O_4$-Citric, $NiFe_2O_4$-Prec) tika papildus raksturots, izmantojot N_2 adsorbcijas-desorbcijas analīzi un SEM. Visi analizētie paraugi uzrādīja mezoporainiem materiāliem raksturīgas *IUPAC* IV tipa izotermas ar histerēzes cilpu (17. att.).

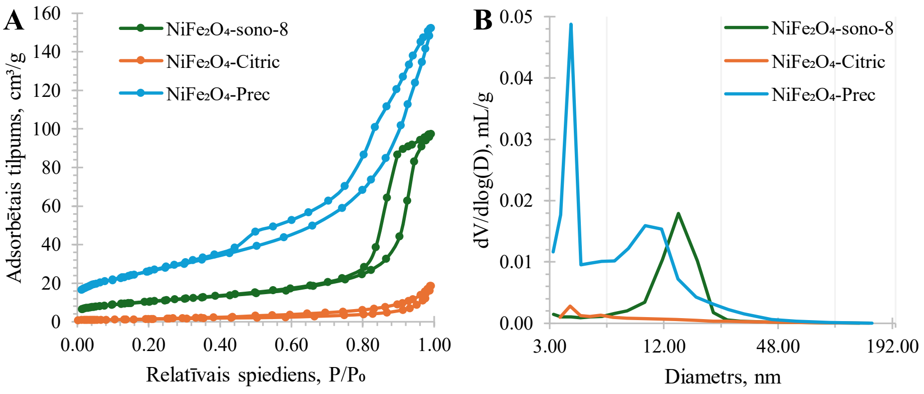

17. att. Augstākās tīrības pakāpes $NiFe_2O_4$ paraugu N_2 adsorbcijas-desorbcijas izotermas (A) un BJH poru izmēra sadalījuma līknes (B).

Starp visiem testētajiem paraugiem $NiFe_2O_4$-Prec bija vislielākais BET īpatnējās virsmas laukums, bet $NiFe_2O_4$-sono-8 bija visšaurākais poru izmēru sadalījums, par ko liecina minimālā atšķirība starp vidējo un mediāno poru diametru. $NiFe_2O_4$-Citric turpretim bija vismazākais virsmas laukums un visplašākais poru izmēru sadalījums, kas liecina par būtisku strukturālo heterogenitāti (6. tab.).

6. tabula

Paraugu teksturālie raksturojumi

Paraugs	BET virsmas laukums, m^2/g	Kopējais poru tilpums, cm^3/g	Vidējais poru diametrs ,nm	Mediānais poru diametrs, nm
$NiFe_2O_4$-sono-8	36,82	0,151	16,39	14,34
$NiFe_2O_4$-Citric	5,20	0,029	22,15	3,85
$NiFe_2O_4$-Prec	93,77	0,236	10,06	3,88

[a] Noteikts, izmantojot BJH desorbcijas metodi.

SEM attēli atklāja, ka $NiFe_2O_4$-sono-8 un $NiFe_2O_4$-Prec veido sfērisku daļiņu agregāti, savukārt $NiFe_2O_4$-Citric gadījumā bija redzamas daļiņas, kas salipušas kopā aglomerātu saķepšanas (*sintering*) rezultātā (18. att.).

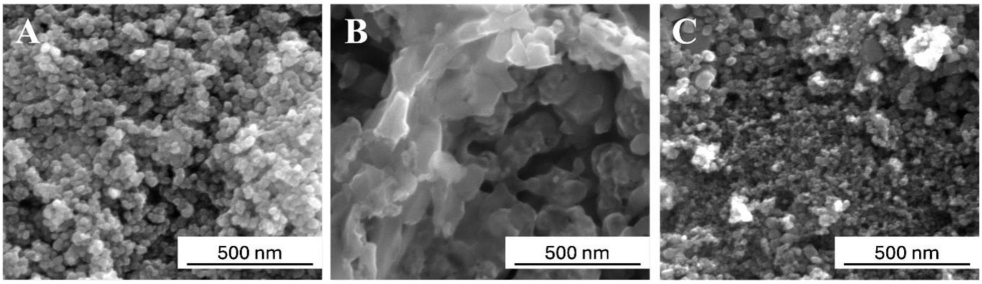

18. att. $NiFe_2O_4$-sono-8 (A), $NiFe_2O_4$-Citric (B) un $NiFe_2O_4$-Prec (C) SEM attēli.

CO_2-FTS testi tika veikti, kā katalizatorus izmantojot $NiFe_2O_4$-sono-8, $NiFe_2O_4$-Citric un $NiFe_2O_4$-Prec. Šo paraugu FTS veiktspēja 280 °C temperatūrā un 20 bar spiedienā ir apkopota 19. attēlā. Par spīti izteiktajai nehomogenitātei un mazajam virsmas laukumam $NiFe_2O_4$-Citric uzrādīja augstāko CO_2 konversiju (23,7 %). Visdrīzāk, tas bija pateicoties atšķirīgajam fāžu sastāvam un lielajiem kristālu izmēriem, kas atvieglo gan reducēšanu, gan karbonizāciju.

Katalizatoru augstās hidrogenēšanas aktivitātes dēļ galvenais ogļūdeņražu produkts visos gadījumos bija CH_4. Šķidrā ogļūdeņražu fāze neveidojās pietiekamā daudzumā, lai to varētu atgūt. Turklāt daļa C_{5+} produktu palika gāzveida stāvoklī un tika aizvadīta kopā ar gāzu plūsmu. Starp testētajiem paraugiem $NiFe_2O_4$-Prec uzrādīja visaugstāko hidrogenēšanas aktivitāti; tā klātbūtne deva vismazāko C_{5+} ogļūdeņražu proporciju. $NiFe_2O_4$-sono-8 savukārt veicināja augstāko CO iznākumu. Tā kā $NiFe_2O_4$-sono-8 un $NiFe_2O_4$-Prec katalizatori ir gandrīz identiski fāžu tīrības ziņā (5. tab.), atšķirības šo divu katalizatoru darbībā var skaidrot ar daļiņu izmēra ietekmi. Rezultāti liecina, ka mazāks daļiņu izmērs veicina CH_4 veidošanos, savukārt lielākas daļiņas veicina CO un C_{5+} proporcijas palielināšanos. Tas ir tāpēc, ka katalizatori ar lielāku daļiņu izmēru ir vieglāk karbonizējami, bet mazākām daļiņām ir mazāka tieksme karbonizēties, veidojot χ-Fe_5C_2. Līdz ar to mazākas daļiņas varētu saglabāt lielāku to fāžu īpatsvaru, kas veicina hidrogenēšanu, nevis virknes augšanu [39], [53].

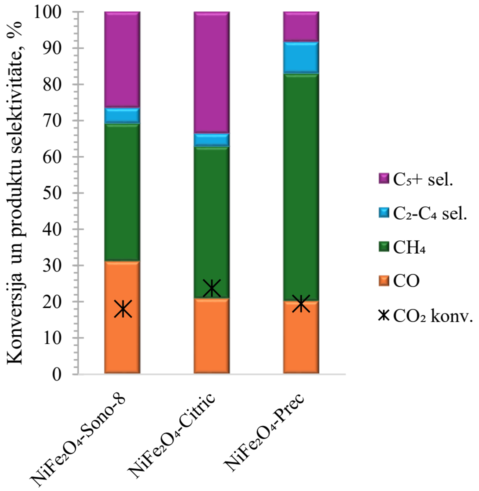

19. att. $NiFe_2O_4$ katalizatoru katalītiskā veiktspēja CO_2 hidrogenēšanā.

Visiem analizētajiem katalizatoriem skābekli saturošo savienojumu daudzums ūdens fāzē bija mazāks par 1 tilpuma %. Līdz ar to skābekli saturošo savienojumu izgūšana no ūdens fāzes nav pamatota, un ūdens fāze ir jāuztver kā notekūdeņi. $NiFe_2O_4$-Prec ūdens fāze bija vistīrākā; salīdzinot ar citiem katalizatoriem, šis katalizators uzrādīja viszemāko spirtu selektivitāti un līdz ar to bija selektīvāks pret ogļūdeņražu veidošanos. Savukārt $NiFe_2O_4$-sono-8 ūdens fāze saturēja vislielāko spirtu un vismazāko skābju daudzumu.

Novērotais metāna selektivitātes pieaugums apvienojumā ar zemo C_{5+} produktu iznākumu un samazināto skābekli saturošo savienojumu veidošanos liecina, ka $NiFe_2O_4$-Prec piemīt visaugstākā hidrogenēšanas aktivitāte starp analizētajiem katalizatoriem. Šīs īpašības apliecina tā lietošanas potenciālu e-metāna sintēzē.

Detalizētāks šajā nodaļā aprakstītā pētījuma izklāsts – manuskriptā 6. pielikumā.

2.3. Priekšapstrādes metodes un reakcijas temperatūras ietekme uz ar kobaltu promotēta Fe_3O_4 veiktspēju CO_2-FTS

E-degviela, kas tiek sintezēta no CO_2, izmantojot enerģija-par-šķidrumu (*Power-to-Liquid*) pārstrādes tehnoloģiju, tiek uzskatīta par vienu no daudzsološākajiem risinājumiem pārejā uz ekonomiku bez fosilajiem energoresursiem. Gan e-degvielas, gan hidrogenēta augu eļļa (*HVO*) ir praktiski izmantojamas alternatīvas, jo abas var integrēt esošajā degvielas piegādes infrastruktūrā un lietot iekšdedzes dzinējos bez būtiskām tehniskām modifikācijām. E-degvielām, kuru sintēzes process apvieno atjaunojamo elektroenerģiju ar uztvertā CO_2 pārveidi šķidrā degvielā, ir lielāks ilgtermiņa dekarbonizācijas potenciāls. E-degvielu ražošanu atšķirībā no *HVO* neierobežo biomasas pieejamība vai zemes izmantošanas ierobežojumi.

Turklāt tās ļauj efektīvi izmantot un uzkrāt pārpalikušo atjaunojamo elektroenerģiju, tādējādi sekmējot elastīgas un klimatneitrālas energosistēmas attīstību [54].

Lai uzlabotu katalītisko veiktspēju un palielinātu C_{2+} ogļūdeņražu selektivitāti, dzelzi saturošiem CO_2-FTS katalizatoriem parasti pievieno promotorus. Vairākos pētījumos norādīts, ka neliels kobalta daudzums var būtiski palielināt C_{5+} ogļūdeņražu selektivitāti, vienlaikus samazinot CO veidošanos [55], [56]. Pētījumi arī liecina, ka kobalta iekļaušana katalizatora sastāvā veicina arī augstāku CO_2 konversiju, kā arī sekmē dzelzs oksīdu reducēšanos [57].

Lai gan promotoru ietekme uz dzelzs katalizatoriem CO_2 hidrogenēšanai ir plaši pētīta [58], trūkst sistemātisku pētījumu par to, kā sintēzes ceļi un priekšapstrādes stratēģijas ietekmē katalizatoru veiktspēju. Katalizatora sintēze priekšapstrādei un aktivēšanas procedūrām ir svarīga loma aktīvās fāzes sastāva, daļiņu izmēra un kristāliskās struktūras noteikšanā. Pirms CO_2-FTS procesa dzelzs katalizatori parasti tiek aktivēti ar H_2, CO vai sintēzes gāzi [59], [60], savukārt kobalta katalizatori parasti tiek aktivēti H_2 atmosfērā [61]. Katalizatora fāžu sastāvs pirms reducēšanas būtiski ietekmē pēc tam izveidojušos aktīvo fāžu raksturu, jo dažādām prekursoru fāzēm raksturīga atšķirīga reducējamība, transformācijas ceļi un termodinamiskā stabilitāte.

Izkarsēšanas atmosfēra ir kritisks parametrs, kas ietekmē metāla dispersiju, katalizatora oksidācijas pakāpi un reducējamību. Šie faktori nosaka aktīvo daļiņu sadalījumu un reakcijas ceļus [62]. Neraugoties uz tās nozīmību, izkarsēšanas atmosfēras loma CO_2-FTS dzelzs katalizatoru kontekstā ir maz pētīta.

Dzelzs katalizatoru katalītisko veiktspēju būtiski ietekmē ne tikai promotoru un nesēju klātbūtne, bet arī dinamiskās fāžu transformācijas reakcijas apstākļos. CO_2-FTS procesā ogļūdeņražu sintēze sākas ar CO_2 reducēšanu līdz CO endotermiskajā *RWGS* reakcijā (1.3. vienādojums), kam seko ogļūdeņražu virkņu augšana eksotermiskajā FTS procesā (1.1. vienādojums). Dzelzs katalizatori ir aktīvi abās reakcijās – Fe_3O_4 ir aktīvā fāze *RWGS* procesam, savukārt dzelzs karbīdi – FTS procesam. Reakcijas temperatūra nosaka dzelzs oksīdu reducēšanās un karbonizēšanās intensitāti – augstākā temperatūrā tiek veicināta metāliskas dzelzs un dzelzs karbīdu veidošanās, bet zemāka temperatūra stabilizē oksīdu fāzes [63]. No otras puses, temperatūra ietekmē *RWGS* un FTS reakciju ātrumu un tādējādi arī CO_2, H_2, CO un H_2O parciālos spiedienus. Paaugstināts CO parciālais spiediens sekmē dzelzs karbīdu veidošanos, savukārt augsts CO_2 un H_2O parciālais spiediens kavē reducēšanos un veicina atkārtotu oksidēšanos. Lielāks H_2 parciālais spiediens savukārt paātrina oksīdu reducēšanos un karbīdu veidošanos [64].

Šajā promocijas darbā tika pētīta ar kobaltu promotēta Fe_3O_4 katalizatora priekšapstrādes procedūras ietekme, kā arī izvērtēta reakcijas temperatūras ietekme 280–320 °C diapazonā, izmantojot gan nepromotētu, gan ar kobaltu promotētu Fe_3O_4 nanopulvera katalizatorus.

Pētījumi par Fe_3O_4 morfoloģijas ietekmi uz FTS aktivitāti liecina, ka Fe_3O_4 nanosfēras nodrošina labāku dzelzs dispersiju un atvieglo dzelzs savienojumu reducēšanos un karbonizāciju, kā rezultātā palielinās aktīvo centru blīvums un uzlabojas C_{5+} ogļūdeņražu selektivitāte [65].

Ar kobaltu promotēts Fe_3O_4 katalizatora prekursors tika pagatavots, impregnējot Fe_3O_4 ar $Co(NO_3)_2$ ūdens šķīdumu. Impregnēšanas šķīduma koncentrācija tika aprēķināta tā, lai nodrošinātu Co : Fe molāro attiecību 5 : 100. Iegūtais katalizatora prekursors tika sadalīts trīs daļās un attiecīgi apzīmēts kā Co/Fe_3O_4, Co/Fe_3O_4-N un Co/Fe_3O_4-A. Katram paraugam tika piemērota atšķirīga priekšapstrādes procedūra – Co/Fe_3O_4 tika reducēts H_2 atmosfērā; Co/Fe_3O_4-N tika izkarsēts N_2 atmosfērā un pēc tam reducēts H_2 atmosfērā; savukārt Co/Fe_3O_4-A tika izkarsēts gaisā un pēc tam reducēts H_2 atmosfērā. Kā references katalizators tika izmantots nepromotēts Fe_3O_4, kas pirms CO_2-FTS tika reducēts H_2 atmosfērā. Katalizatoru sastāvs tika analizēts ar *XRD* un *XPS* metodēm gan pēc izkarsēšanas, gan pēc reducēšanas.

XRD rezultāti parādīja, ka pēc reducēšanas H_2 atmosfērā Co/Fe_3O_4 paraugā dominējošā kristāliskā fāze bija α-Fe. Co/Fe_3O_4-N paraugā pēc izkarsēšanas N_2 atmosfērā dzelzs galvenokārt bija kā Fe_3O_4, no kā pēc reducēšanas H_2 atmosfērā veidojās α-Fe. Savukārt Co/Fe_3O_4-A pēc izkarsēšanas gaisā saturēja maghemītu (γ-Fe_2O_3), bet pēc reducēšanas tika konstatētas γ-Fe_2O_3, γ-Fe_2O_3 un α-Fe fāzes. Zemās koncentrācijas dēļ ar *XRD* kobalta savienojumus detektēt nebija iespējams (20. att.).

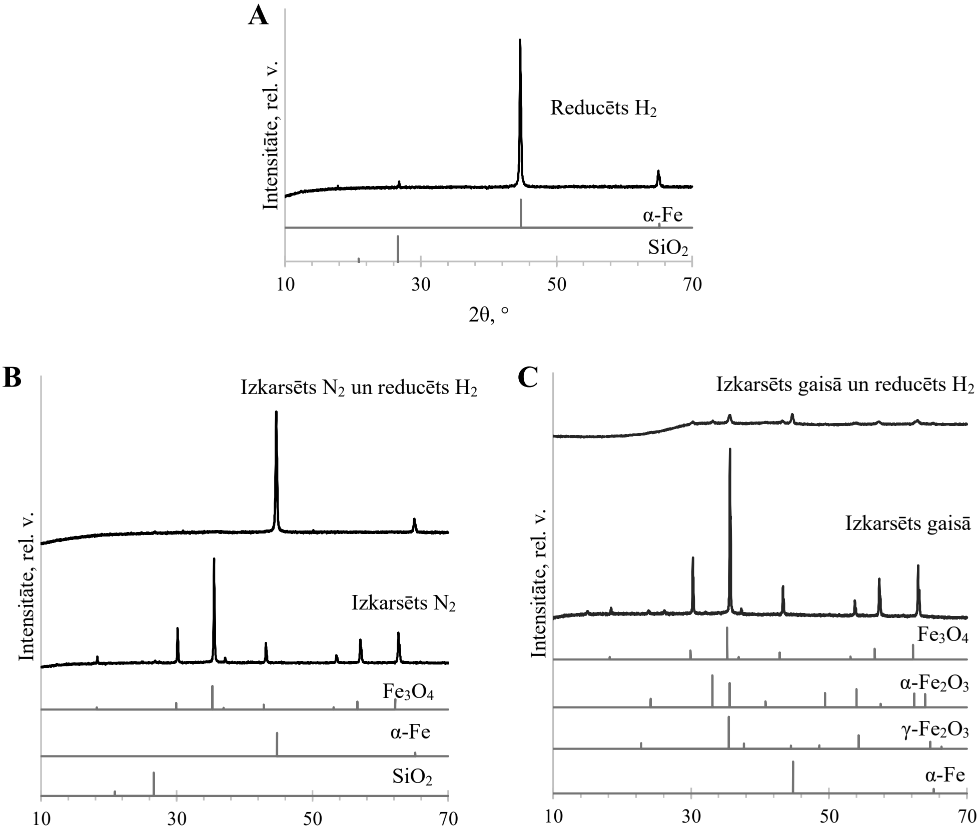

20. att. Co/Fe_3O_4 XRD pēc reducēšanas H_2 (A); Co/Fe_3O_4-N XRD pēc izkarsēšanas N_2 un pēc reducēšanas H_2 (B); Co/Fe_3O_4-A XRD pēc izkarsēšanas gaisā un pēc reducēšanas H_2 (C).

Kā redzams 21. attēlā, *XPS* analīze uzrādīja Fe^{2+} un Fe^{3+} virsmas formu līdzāspastāvēšanu visos paraugos. Co/Fe_3O_4 un Co/Fe_3O_4-N paraugiem pēc reducēšanas ar H_2 tika konstatēta papildu komponente ar zemu saites enerģiju, kas atbilst metāliskam Fe. Iegūtie dati liecina, ka paraugu virsma ir oksidēta. Joslu pārklāšanās dēļ kobalta signāla izvērtēšana nebija iespējama.

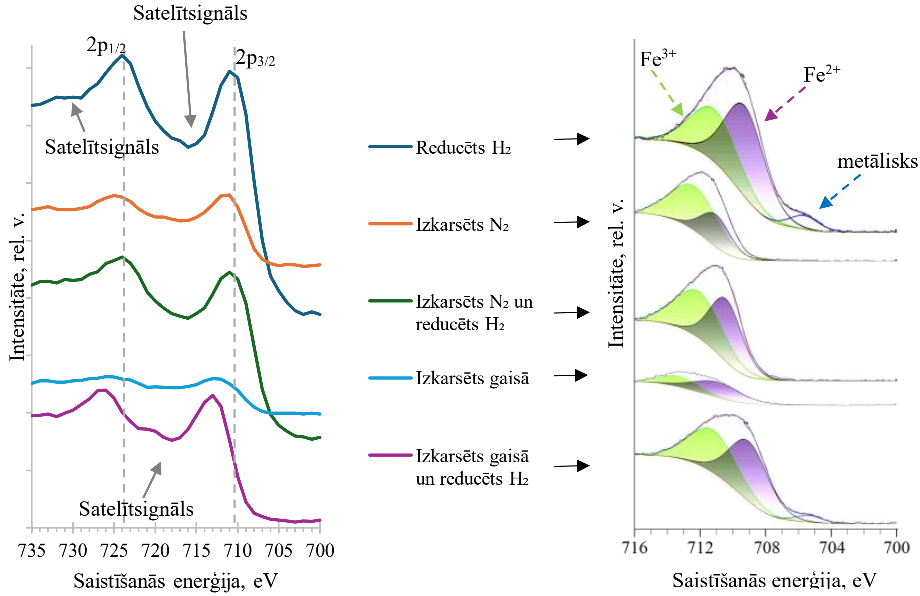

21. att. Fe 2p *XPS* spektri.

Katalizatoru pirmsapstrādes ietekme uz CO_2-FTS veiktspēju un produktu selektivitāti redzama 22. attēlā. Tā kā augstākā C_{5+} produktu selektivitāte tika novērota 280 °C temperatūrā, šajā temperatūrā tika analizēta katalizatora priekšapstrādes ietekme uz CO_2-FTS efektivitāti.

Nepromotēts Fe_3O_4 uzrādīja zemāko C_{5+} ogļūdeņražu selektivitāti (4 %). Pretstatā tam ar kobaltu promotēto katalizatoru C_{5+} selektivitāte atkarībā no priekšapstrādes procedūras bija robežās no 19,2 % līdz 36,8 %. Tas norāda, ka kobalta pievienošana, līdzīgi kā kālija gadījumā (1.2. nodaļa), var pastiprināt CO adsorbciju un vienlaikus samazināt H_2 adsorbciju uz katalizatora virsmas, tādējādi veicinot ogļūdeņražu virknes augšanu.

Būtiskākā atšķirība starp iepriekš neizkarsētu katalizatoru (Co/Fe_3O_4) un katalizatoriem, kas tika izkarsēti pirms reducēšanas (Co/Fe_3O_4-N un Co/Fe_3O_4-A), bija novērojama ogļūdeņražu selektivitātē, īpaši attiecībā uz C_{5+} produktiem. Šis novērojums liecina, ka kobalta fāzes stāvoklis ietekmē ogļūdeņražu virknes augšanu. Līdz ar to secināms, ka ogļūdeņražu selektivitāte ir būtiski atkarīga no katalizatora priekšapstrādes.

Visu ar kobaltu promotēto Fe_3O_4 katalizatoru pagatavošanā kā prekursors tika izmantots $Co(NO_3)_2$. Uz Fe_3O_4 uznestu $Co(NO_3)_2$ reducējot ar H_2 400 °C temperatūrā, paredzams, ka dominējošā izveidojusies kobalta fāze būs metālisks Co [66]. Tā kā Fe_3O_4 pilda nesēja funkciju, teorētiski iespējama arī Co-Fe sakausējuma veidošanās; tomēr, lai Co-Fe sakausējums veidotos ievērojamā daudzumā, parasti nepieciešama augstāka temperatūra [67]. Saskaņā ar literatūras datiem, Co/Fe_3O_4 katalizatorā dominējošā kobalta fāze ir metālisks Co, bet Co-Fe sakausējuma saturs ir minimāls. Literatūras dati liecina, ka metālisks Co veicina H_2 disociāciju un CO adsorbciju, tādējādi sekmējot C-C virknes augšanu un nodrošinot augstu C_{2+} produktu selektivitāti. Līdz ar to būtu paredzams, ka Co/Fe_3O_4 katalizators uzrādīs paaugstinātu katalītisko aktivitāti ogļūdeņražu veidošanās procesā. Tomēr, salīdzinot ar Co/Fe_3O_4-N un Co/Fe_3O_4-A, šis katalizators uzradīja zemāko C_{5+} produktu selektivitāti (19,2 %). Zemā katalītiskā aktivitāte, visticamāk, saistīta ar metāliskā Co tendenci oksidēties, īpaši ūdens tvaika klātbūtnē, tādējādi samazinot kobalta aktivitāti [68].

Co/Fe_3O_4-N gadījumā priekšapstrāde N_2 atmosfērā ar tai sekojošu reducēšanu H_2 vidē var veicināt kobalta ferīta špineļa ($CoFe_2O_4$) veidošanos uz virsmas, īpaši, ja metāliska Co veidošanās ir ierobežota [69]. Ņemot vērā ar Fe^{3+} bagāto Co/Fe_3O_4-A virsmu, kas iegūta pēc priekšapstrādes (izkarsēšanas) gaisā un tai sekojošas reducēšanas, arī šajā gadījumā paaugstināta temperatūrā iespējama $CoFe_2O_4$ veidošanās [70]. Tādējādi katalizatori, kas pirms reducēšanas ir izkarsēti, visticamāk, papildus metāliskam Co satur virsmas $CoFe_2O_4$, kas varētu izskaidrot to augsto C_{5+} ogļūdeņražu selektivitāti. Balstoties CO_2 konversijas un produktu selektivitātes rezultātos, par efektīvāko priekšapstrādes metodi ar kobaltu promotētam Fe_3O_4 katalizatoram atzīstama izkarsēšana N_2 ar tai sekojošu reducēšanu H_2 atmosfērā, jo tā nodrošināja labāko veiktspēju CO_2 hidrogenēšanas procesā.

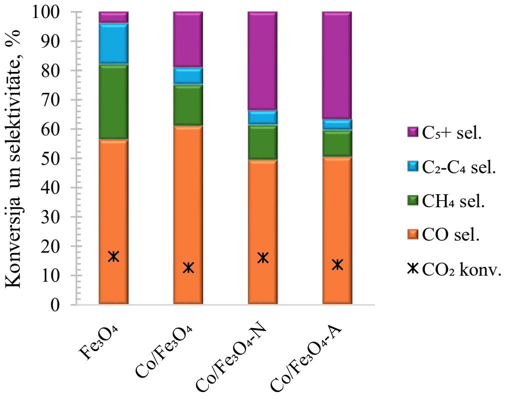

22. att. Priekšapstrādes procedūras ietekme uz ar kobaltu promotēta Fe_3O_4 katalītisko veiktspēju 280 °C temperatūrā.

Reakcijas temperatūras ietekme uz nepromotēta un ar kobaltu promotētu Fe_3O_4 katalizatoru CO_2-FTS veiktspēju un produktu selektivitāti redzama 23. attēlā. Paaugstinot reakcijas temperatūru no 280 °C līdz 320 °C, visiem katalizatoriem tika novērots konversijas pieaugums. Tomēr tajā pat laikā nepromotētajam un ar kobaltu promotētajiem Fe_3O_4 katalizatoriem reakcijas temperatūra atšķirīgi ietekmēja *RWGS* un FTS ātrumus (un tādējādi arī produktu selektivitāti).

Nepromotētajam Fe_3O_4 CO selektivitāte samazinājās, bet ogļūdeņražu selektivitāte ievērojami pieauga (23. A att.). CO selektivitātes samazināšanos paaugstinātā temperatūrā iespējams skaidrot ar sākotnēji izveidotā CO sekundāru pārveidi (palielināta FTS aktivitāte, pieaugot temperatūrai). Lai gan kopējā ogļūdeņražu selektivitāte, tajā skaitā – arī C_{2+} ogļūdeņražu selektivitāte, paaugstinot temperatūru, pieauga, augstākā C_{5+} ogļūdeņražu selektivitāte tika novērota 300 °C temperatūrā. Atšķirībā no tradicionālās FTS CO_2 hidrogenēšanai parasti nepieciešama augstāka H_2 koncentrācija, bet CO koncentrācija ir zemāka. Tas rada salīdzinoši augstu H/C attiecību uz katalizatora virsmas, kas savukārt veicina metāna veidošanos un kavē ogļūdeņražu virknes augšanu [71]. Pieaugot CO_2 konversijai (palielinoties RWGS aktivitātei), virsmas H/C attiecība samazinās, tādējādi palielinot virknes augšanas varbūtību.

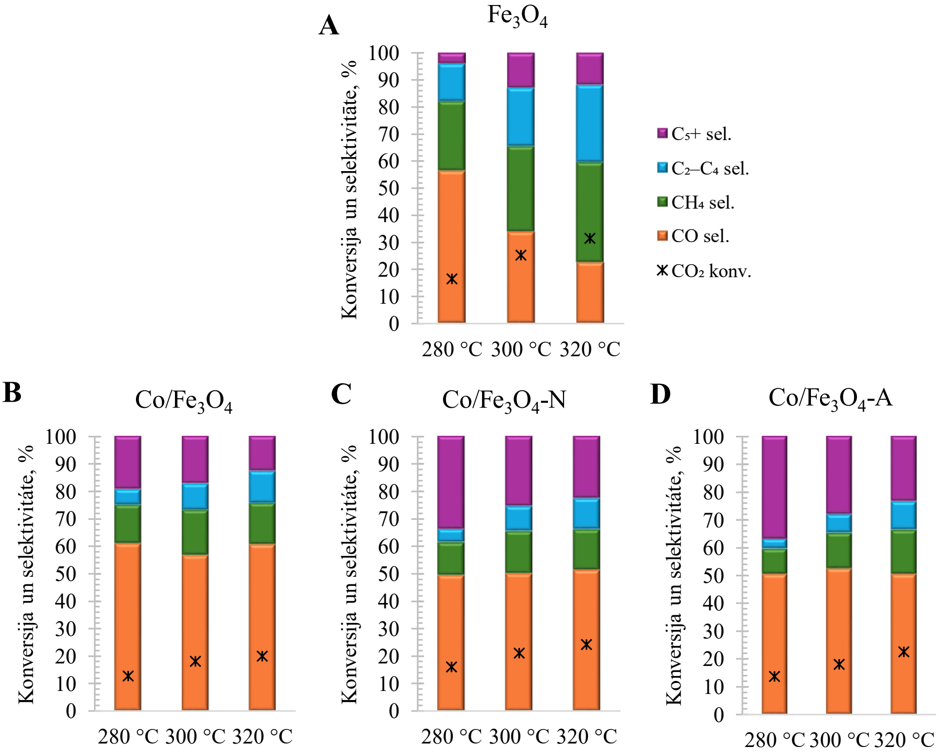

23. att. Reakcijas temperatūras ietekme uz nepromotēta un ar kobaltu promotētu Fe_3O_4 katalizatoru veiktspēju.

Ar kobaltu promotētajiem katalizatoriem CO selektivitāte saglabājās augsta (> 49 %) visā temperatūru diapazonā, kas liecina par *RWGS* dominanci. Būtiskākās temperatūras izraisītās izmaiņas šiem katalizatoriem bija saistītas ar C_2–C_4 un C_{5+} ogļūdeņražu veidošanos (23. B, C, D att.). Līdz ar temperatūras pieaugumu C_2–C_4 ogļūdeņražu proporcija strauji palielinājās, savukārt C_{5+} ogļūdeņražu proporcija samazinājās. Novērotā tendence atbilst tradicionālajai FTS, kur ogļūdeņražu sadalījumu raksturo Andersona-Šulca-Florija modelis. Tajā virknes augšanas varbūtība nosaka produktu virkņu garumus. Palielinoties reakcijas temperatūrai, virknes augšanas varbūtība samazinās, tādējādi mazinot garu virkņu veidošanās varbūtību un novirzot selektivitāti īsākas virknes ogļūdeņražu virzienā [72].

CO_2 hidrogenēšanas procesā par ogļūdeņražiem rodas ievērojams ūdens daudzums. Ūdens veidojas gan *RWGS*, gan FTS reakcijās, tādēļ, salīdzinot ar tradicionālo FTS procesu, ūdens fāze ir atšķaidītāka. Visiem katalizatoriem galvenais skābekli saturošais savienojums bija metanols; citi novērotie produkti bija *n*-spirti līdz *n*-butanolam un acetons. Palielinoties reakcijas temperatūrai, metanola koncentrācija strauji samazinājās, savukārt C_{2+} spirtu koncentrācija palielinājās. Visos gadījos skābekli saturošo savienojumu īpatsvars ūdens fāzē nepārsniedz 3 tilpuma %. Līdz ar to šo savienojumu izgūšana nav ekonomiski pamatota, un ūdens fāze jāuztver kā notekūdeņi, kam nepieciešama attīrīšana.

Rezultāti liecina, ka pētītajā temperatūras diapazonā temperatūrai ir lielāka ietekme uz CO_2 konversiju un selektivitāti nekā katalizatora priekšapstrādei, visticamāk, ietekmējot konkurējošo reakciju relatīvos ātrumus.

SECINĀJUMI

1. 280 °C ir optimāla FTS rekcijas temperatūras mezoporainiem uz silīcija dioksīda uznestiem dzelzs katalizatoriem, kas nodrošina vislabāko līdzsvaru starp augstu CO konversiju, uzlabotu C_{5+} selektivitāti un ierobežotu nevēlamo īsas virknes ogļūdeņražu veidošanos.

2. K/Fe attiecības palielināšana samazina metāna veidošanos FTS, vienlaikus palielinot C_{5+} ogļūdeņražu proporciju, kā arī veicinot olefīnu un skābekli saturošu savienojumu veidošanos, tomēr pārmērīgs kālija daudzums ierobežo tiešu lietojamību e-degvielu sintēzē augstā benzīna frakcijas olefīnu satura dēļ.

3. Uz SBA-15 uznests dzelzs katalizators uzrāda uzlabotu CO konversiju tā lielā virsmas laukuma un sakārtotās mezoporozitātes dēļ; tomēr nesēja mazās poras veicina sekundāras reakcijas un gāzu veidošanos, ierobežojot C_{5+} selektivitāti un padarot to piemērotāku īsas virknes ogļūdeņražu, nevis šķidro degvielu iegūšanai.

4. Ar kāliju promotēts uz SBA-15 uznests dzelzs katalizators uzrāda ierobežotu aktivitāti CO_2 hidrogenēšanā par metanolu; virsmas skābuma dēļ tas veicina DME veidošanos.

5. Sintēzes metode būtiski ietekmē katalizatora fāžu sastāvu, teksturālās īpašības un katalītisko veiktspēju; reducētāja asistēta izgulsnēšana nodrošina fāzes tīra $NiFe_2O_4$ ar minimālu kristalītu izmēru, maksimālu virsmas laukumu un augstu hidrogenēšanas aktivitāti veidošanos.

6. Ar kobaltu promotēta dzelzs katalizatora priekšapstrādes metode būtiski ietekmē katalizatora veiktspēju, ietekmējot sākotnējo fāžu sastāvu un līdz ar to arī aktīvās fāzes veidošanos un sastāvu; katalizatori, kas pirms CO_2-FTS tika izkarsēti N_2 atmosfērā vai gaisā, uzrāda augstāku C_{5+} selektivitāti.

PATEICĪBAS

- Gaļinai Dobelei (LVKĶI) par N_2 adsorbcijas-desorbcijas mērījumiem katalizatoriem;
- Tomam-Valdemāram Eidukam (RTU) un Agrim Bērziņam (LU) par *XRD* analīzēm;
- *Markus Kõiv* (Tartu Universitāte) par SEM;
- kolēģiem, īpaši Zanei Ābelniecei, Laumai Laipniecei, Anastasijai Gailei un Mārai Plotniecei par atbalstu un ieguldījumu šī darba izstrādē;
- Kristīnei Lazdovičai un Svetlanai Čornajai par vadīšanu un milzīgo atbalstu gadu gaitā!

Šis darbs tapa ar profesora Valda Kampara nozīmīgu atbalstu. Izsaku dziļu cieņu viņa piemiņai!

Promocijas darbs izstrādāts ar Eiropas Sociālā fonda atbalstu darbības programmas “Izaugsme un nodarbinātība” 8.2.2. specifiskā atbalsta mērķa “Stiprināt augstākās izglītības institūciju akadēmisko personālu stratēģiskās specializācijas jomās” projektā Nr. 8.2.2.0/20/I/008 “Rīgas Tehniskās universitātes un Banku augstskolas doktorantu un akadēmiskā personāla stiprināšana stratēģiskās specializācijas jomās”.

Pētījums tapis ar Rīgas Tehniskās universitātes Doktorantūras grantu programmas atbalstu.

Šis darbs izstrādāts ar Eiropas Savienības Atveseļošanas un noturības mehānisma atbalstu projektā Nr. 5.2.1.1.i.0/2/24/I/CFLA/003 “Konsolidācijas un pārvaldības izmaiņu ieviešana Rīgas Tehniskajā universitātē, Liepājas Universitātē, Rēzeknes Tehnoloģiju akadēmijā un Latvijas Jūras akadēmijā un Liepājas Jūrniecības koledžā virzībai uz izcilību augstākajā izglītībā, zinātnē un inovācijās” ar akadēmiskās karjeras doktorantūras granta atbalstu (granta ID: 1092).

Šis darbs izstrādāts ar Eiropas Savienības Atveseļošanas un noturības mehānisma atbalstu pētniecības un attīstības grantā Nr. RTU-PA-2024/1-0052 projektā Nr. 5.2.1.1.i.0/2/24/I/CFLA/003 “Konsolidācijas un pārvaldības izmaiņu ieviešana Rīgas Tehniskajā universitātē, Liepājas Universitātē, Rēzeknes Tehnoloģiju akadēmijā un Latvijas Jūras akadēmijā un Liepājas Jūrniecības koledžā virzībai uz izcilību augstākajā izglītībā, zinātnē un inovācijās”.

1862
RĪGAS TEHNISKĀ UNIVERSITĀTE

NACIONĀLAIS ATTĪSTĪBAS PLĀNS 2020

EIROPAS SAVIENĪBA
Eiropas Sociālais fonds

IEGULDĪJUMS TAVĀ NĀKOTNĒ

Finansē Eiropas Savienība
NextGenerationEU

2027
Nacionālais attīstības plāns

DOCTORAL THESIS PROPOSED TO RIGA TECHNICAL UNIVERSITY FOR PROMOTION TO THE SCIENTIFIC DEGREE OF DOCTOR OF SCIENCE

To be granted the scientific degree of Doctor of Science (PhD), the present Doctoral Thesis has been submitted for defence at the open meeting of RTU Promotion Council on 9 June 2026 at the Faculty of Natural Sciences and Technology of Riga Technical University, P. Valdena iela 3, Room 272.

OFFICIAL REVIEWERS

Associate Professor Dr. chem. Artis Kinēns
University of Latvia, Latvia

Associate Professor Dr. chem. Reinis Drunka
Riga Technical University, Latvia

Associate Professor, PhD Hamid Reza Godini
Aalto University, Finland

DECLARATION OF ACADEMIC INTEGRITY

I hereby declare that the Doctoral Thesis submitted for review to Riga Technical University for promotion to the scientific degree of Doctor of Science (PhD) is my own. I confirm that this Doctoral Thesis has not been submitted to any other university for promotion to a scientific degree.

Agija Stanke ……………………………. (signature)
Date: ………………………

The Doctoral Thesis has been prepared as a collection of thematically related scientific publications complemented by summaries in Latvian and English. The Doctoral Thesis unites five scientific publications and one manuscript. The scientific publications have been written in English.

TABLE OF CONTENTS

Appendix 1	Stanke, A., Lazdovica, K., Laipniece, L. Evaluation of the Fischer-Tropsch synthesis product selectivity over iron-based silica-supported catalyst under mild temperatures. *Environmental Progress and Sustainable Energy*, **2024**, 43(3), e14335.
Appendix 2	Stanke, A., Lazdovica, K., Gaile, A., Laipniece, L. Fischer-Tropsch synthesis product selectivity over silica-supported iron-based catalyst: Effect of K/Fe ratio. *Fuel*, **2025**, 387, 134399.

Appendix 3	Stanke, A., Kampars, V. Agglomeration of Fe/SBA-15 with clays for Fischer-Tropsch synthesis. *Energy Reports*, **2022**, 8, 461-466.
Appendix 4	Abelniece, Z., Cutrufello, M. G., Rombi, E., Stanke, A., Piirsoo, H., Mändar, H., Tamm, A. The structure-activity interactions of Cu/Zn, In/Pd and Fe/K catalysts supported on mesoporous SBA-15 for carbon dioxide hydrogenation at low pressure. *Chemical Papers*, **2024**, 78, 5103-5112.
Appendix 5	Stanke, A., Lazdovica, K. The promotional effect of potassium on iron-based silica supported catalyst for CO_2 hydrogenation. No: *International Multidisciplinary Scientific GeoConference Surveying Geology and Mining Ecology Management, SGEM 2022: Conference Proceeding*, 22(4.1), pp. 161–166.
Appendix 6	Stanke, A., Abelniece, Z., Sutka, A., Berzins, A., Kõiv, M., Lazdovica, K. $NiFe_2O_4$ catalysts for CO_2 hydrogenation: Performance analysis and comparative life cycle assessment of catalyst synthesis routes. *Unpublished results.*
Appendix 7	Stanke, A., Berzins, A., Velasco, J. A., Sarsuns, K., Puurunen, R. L., Lazdovica, K. Cobalt-promoted Fe_3O_4 catalysts for CO_2 hydrogenation to C_{2+} hydrocarbons: Effect of pretreatment method and reaction temperature. *Fuel Processing Technology,* **2026,** 288, 108467.

ABBREVIATIONS

BET	Brunauer–Emmett–Teller method for surface area analysis
BJH	Barrett–Joyner–Halenda method for analysing pore size distribution
CO_2-FTS	CO_2-based Fischer–Tropsch synthesis
DME	dimethyl ether
FTIR	Fourier-transform infrared
FTS	Fischer–Tropsch synthesis
GC-TCD/FID	gas chromatograph equipped with Thermal Conductivity and Flame Ionisation detectors
GC-MS	gas chromatograph coupled with a mass spectrometer
HVO	hydrotreated vegetable oil
NMR	nuclear magnetic resonance
RWGS	reverse water-gas shift
SBA-15	*Santa Barbara Amorphous* mesoporous silica-based material
SEM-EDS	scanning electron microscopy with energy dispersive X-ray spectroscopy
WGS	water-gas shift
XPS	X-ray photoelectron spectroscopy
XRD	X-ray diffraction
XRF	X-ray fluorescence

GENERAL OVERVIEW OF THE THESIS

Introduction

Energy has a significant role in humanity's progress, with fossil fuels driving unprecedented industrial and societal development. However, their extensive use has led to large anthropogenic CO_2 emissions, disrupting the natural carbon cycle [1] and causing biodiversity loss, environmental pollution, and climate change [2]. Since 2000, global energy consumption has increased by about one-third and is expected to continue rising, with fossil fuels still supplying nearly 80 % of demand [3], [4]. This heavy dependence on non-renewable resources poses long-term risks to both climate stability and energy security [5].

Transportation, the fastest-growing energy-consuming sector, accounts for roughly one quarter of global energy use. Since existing fuel production, distribution, and storage infrastructure is optimised for hydrocarbon fuels, a rapid transition to entirely new fuel systems would be costly and slow. Consequently, sustainable, drop-in fuels that are compatible with current infrastructure and vehicles offer a practical pathway for transport decarbonization [6]. In this context, electrofuels are emerging as a promising solution to rising energy demand and environmental constraints.

Electrofuels, or e-fuels, are a class of synthetic fuels whose production process involves the hydrogenation of carbon monoxide or carbon dioxide using hydrogen derived from water electrolysis [7]. Both CO and CO_2 hydrogenation involve complex reaction networks, resulting in a wide spectrum of products that strongly depend on the reaction conditions and the catalyst employed. CO and CO_2 can be hydrogenated to alcohols and hydrocarbons using transition-metal catalysts.

Catalytic CO hydrogenation into hydrocarbons is known as the Fischer–Tropsch synthesis (FTS). FTS products can be used for the synthesis of high-quality diesel fuel, gasoline, and aviation fuel. The reaction is typically carried out at elevated temperatures (200–350 °C) and pressures (10–20 bar). FTS is a reaction in which products formed *in situ* from hydrogen and carbon monoxide polymerise on the surface of the catalyst [8]. In general, FTS can be described by the following equation:

$$2nH_2 + nCO \rightarrow \text{-}(CH_2)_n\text{-} + nH_2O, \qquad \Delta H_{298K} = -152 \text{ kJ/mol}. \qquad (1.1)$$

The composition of products is determined by the balance between the chain growth probability on a catalyst's surface and the probability of chain termination, hydrogenation, and desorption of obtained compounds. Simultaneously with the main FTS reaction, various secondary reactions occur. Typically, the main FTS products are *n*-paraffins and 1-olefins. Minor products can include isomerised hydrocarbons, cyclic hydrocarbons, internal olefins, as well as aldehydes, ketones, acids, and alcohols, which are undesirable products for fuels [9], [10].

Two main mechanistic pathways are commonly proposed: the carbide mechanism and the CO insertion mechanism. In the carbide mechanism, CO dissociates (direct or H-assisted dissociation) and forms surface carbon species that are hydrogenated and coupled to form C-C bonds (Fig. 1).

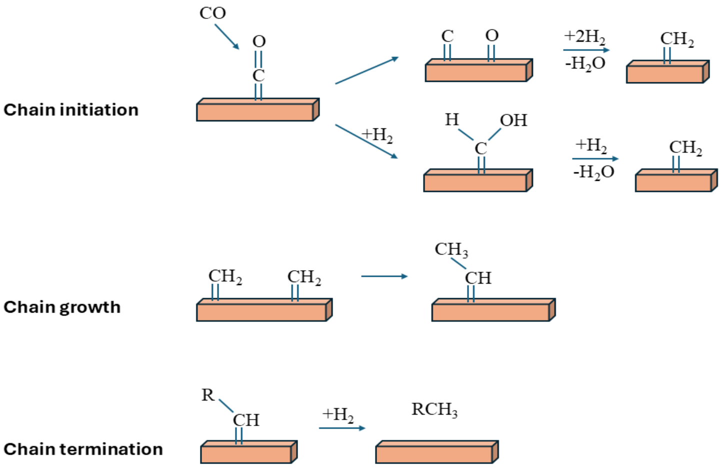

Fig. 1. Simplified representation of the carbide mechanism. Adapted from [11], [12].

In the CO insertion mechanism, it is assumed that C-C chain propagation proceeds *via* the insertion of CO monomers into surface-hydrogen (the first initiation) and the surface-carbon bond of surface hydrocarbon intermediates (Fig. 2).

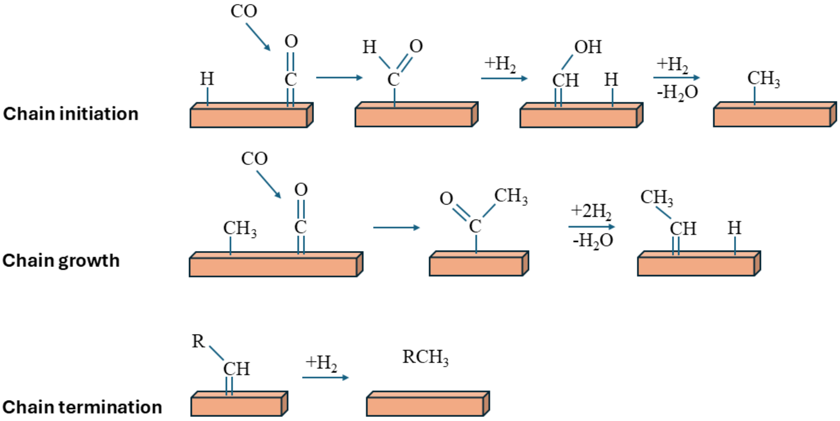

Fig. 2. Simplified representation of the CO insertion mechanism. Adapted from [11], [12].

During the FTS, a large amount of water is formed, which can accelerate catalyst deactivation and lead to a decrease in catalytic activity. Under reaction conditions, water can participate in the water-gas shift (WGS) reaction, forming hydrogen and carbon dioxide:

$$CO + H_2O \rightleftarrows CO_2 + H_2, \qquad \Delta H_{298K} = -41.2 \text{ kJ/mol.} \qquad (1.2)$$

The WGS reaction affects the concentrations (partial pressures) of CO, H_2, CO_2 and H_2O within the reaction system, thereby influencing the kinetics of primary and secondary FTS reactions as well as the final product distribution. This reaction is particularly significant when using synthesis gas (a mixture of CO and H_2) with a non-stoichiometric amount of hydrogen (typical of biomass-derived syngas).

While the hydrogenation of CO *via* FTS is a mature technology, the hydrogenation of CO_2 presents distinct and formidable physicochemical challenges. Compared to CO, CO_2 is a thermodynamically more stable molecule because carbon is in its highest oxidation state. Despite this, significant progress has been achieved in both academic research and industrial practice regarding CO_2 conversion into single-carbon (C_1) products such as carbon monoxide, methane, methanol and formic acid [13]. The synthesis of products with multiple carbon atoms (C_{2+}) is more complex due to the inertness of CO_2, the high energy barrier for C-C band formation, competing with CO_2 methanation and numerous side reactions.

One of the most promising approaches for CO_2 valorisation is the CO_2-based Fischer–Tropsch synthesis (CO_2-FTS). In the CO_2-FTS process, firstly, CO_2 is reduced to CO *via* the endothermic reverse water gas shift (RWGS) reaction (Equation 1.3.), then CO is hydrogenated to hydrocarbons *via* the exothermic FTS (Equation (1.1)) [14].

$$CO_2 + H_2 \rightleftarrows CO + H_2O, \qquad \Delta H_{298K} = 41.2\ \text{kJ/mol}. \tag{1.3}$$

Since CO_2 is a thermodynamically stable molecule, higher synthesis temperatures are required to improve conversion. CO_2-FTS is typically carried out at temperatures of 280–300 °C and pressures of 15–25 bar. Reaction temperature plays a dual role in the hydrogenation of CO_2 (and CO), creating a distinct conflict between reactant activation and product control. On one hand, elevated temperatures are thermodynamically required to activate the inert CO_2 molecule and drive the endothermic RWGS reaction; besides, higher temperatures exponentially increase the reaction rate. On the other hand, FTS is an exothermic process where lower temperatures favour hydrocarbon chain propagation. Consequently, overly high temperatures inevitably shift selectivity toward methane and other light hydrocarbons, necessitating a careful temperature optimisation essential for maximising the yield of desired products (C_{2+} hydrocarbons).

This Thesis summarises research on the hydrogenation of carbon oxides using iron-based catalysts to produce e-fuels and their precursors. Catalysts play a central role in CO and CO_2 hydrogenation by enabling the activation of these thermodynamically stable molecules and directing product selectivity toward desired hydrocarbons or oxygenates. Among the commonly used active metals, iron-based catalysts are particularly attractive due to their low cost, abundance, and multifunctional nature. Iron-based catalysts are capable of simultaneously catalysing WGS/RWGS reaction and FTS, which makes them especially suitable for CO_2 hydrogenation to hydrocarbons. Moreover, their flexible redox and carburization behaviour allows tuning of activity and selectivity through catalyst composition, structure and pretreatment.

Iron-based catalyst synthesis typically yields oxidic phases such as hematite (Fe_2O_3), which are inactive for FTS and require *in situ* activation *via* reduction with hydrogen, carbon monoxide or synthesis gas. Iron-based catalysts, often described as “living catalysts”, function as dynamic systems that evolve from an inactive oxidic precursor into a complex active phase composition. Upon exposure to reducing agents (H_2, CO), the catalyst progresses through a transformation sequence from oxides to metallic iron, eventually carburising to form iron carbides. The performance of the catalyst relies on the synergistic relationship between these evolving phases: magnetite (Fe_3O_4) is associated with the WGS/RWGS reaction, metallic iron is active for CO_2 dissociation, whereas iron carbides, particularly the Hägg carbide (Fe_5C_2), are the distinct active sites driving FTS.

The Doctoral Thesis comprises two chapters. Chapter 1 provides a systematic analysis of FTS products, with particular attention to hydrocarbon fractions and the aqueous phase. The influence of temperature as a reaction parameter and the role of SiO_2 supports and potassium as a promoter on product distribution are examined in detail to provide a comprehensive understanding of CO hydrogenation over iron-based catalysts. Chapter 2 provides a systematic analysis of CO_2-FTS performance, with particular attention to the influence of temperature as a reaction parameter and the role of catalyst synthesis and pretreatment methods on product distribution.

Aims and objectives

The aim of the Thesis is the synthesis of e-fuels and their precursors *via* CO and CO_2 hydrogenation reactions over iron-based catalysts, as well as the investigation of the relationships between catalyst characteristics, catalytic performance and obtained products.

The following tasks were set:

1) to synthesise and characterise various iron-based catalysts for CO and CO_2 hydrogenation;
2) to perform CO and CO_2 hydrogenation over iron-based catalysts and evaluate their catalytic performance and product selectivity;
3) to investigate the effects of the reaction temperature on CO and CO_2 conversion and hydrogenation product selectivity;
4) to determine the influence of promoters on the catalytic performance of iron-based catalysts in CO and CO_2 hydrogenation;
5) to evaluate the influence of $NiFe_2O_4$ synthesis methods on catalyst characteristics (phase purity, crystallite size) and catalytic performance in CO_2 hydrogenation;
6) to assess the effect of the catalyst precursor ($Co(NO_3)_2/Fe_3O_4$) pretreatment on catalytic performance in CO_2 hydrogenation;
7) to evaluate the influence of employed catalysts on the water phase formed during CO and CO_2 hydrogenation processes.

Scientific novelty and main results

This Thesis offers a comprehensive investigation into the thermochemical conversion of carbon oxides *via* the FTS and CO_2-FTS processes. During the course of the Thesis, systematic studies were conducted to deepen the fundamental understanding of FTS and CO_2-FTS, specifically evaluating how catalyst characteristics influence catalytic performance in the thermochemical conversion of carbon oxides. Overall, the Thesis contributes to understanding the complex interrelationships between catalyst structure/composition, reaction conditions and the resulting hydrogenation product composition and distribution.

Structure of the Thesis

The Doctoral Thesis has been prepared as a collection of thematically related scientific publications devoted to the investigation of the hydrogenation of carbon oxides into e-fuels and their precursors over iron-based catalysts. The Thesis consists of five original research articles, published in SCI journals, and unpublished results.

Publications and approbation of the Thesis

The results of the Thesis have been reported in five scientific publications and one manuscript. Additionally, the results have been disseminated at three scientific conferences.

Scientific publications

1. **Stanke, A.**, Berzins, A., Velasco, J. A., Sarsuns, K., Puurunen, R. L., Lazdovica, K. Cobalt-promoted Fe_3O_4 catalysts for CO_2 hydrogenation to C_{2+} hydrocarbons: Effect of pretreatment method and reaction temperature. *Fuel Processing Technology,* **2026**, 288, 108467. https://doi.org/10.1016/j.fuproc.2026.108467.
2. **Stanke, A.,** Abelniece, Z., Sutka, A., Berzins, A., Kõiv, M., Lazdovica, K. $NiFe_2O_4$ catalysts for CO_2 hydrogenation: Performance analysis and comparative life cycle assessment of catalyst synthesis routes. *The manuscript is submitted to the International Journal of Hydrogen Energy. Current status: Under review.*
3. **Stanke, A.**, Lazdovica, K., Gaile, A., Laipniece, L. Fischer–Tropsch synthesis product selectivity over silica-supported iron-based catalyst: Effect of K/Fe ratio. *Fuel*, **2025**, 387, 134399. https://doi.org/10.1016/j.fuel.2025.134399
4. Abelniece, Z., Cutrufello, M. G., Rombi, E., **Stanke, A.**, Piirsoo, H., Mändar, H., Tamm, A. The structure-activity interactions of Cu/Zn, In/Pd and Fe/K catalysts supported on mesoporous SBA-15 for carbon dioxide hydrogenation at low pressure. *Chemical Papers*, **2024**, 78, 5103–5112. https://doi.org/10.1007/s11696-024-03456-9
5. **Stanke, A.**, Lazdovica, K., Laipniece, L. Evaluation of the Fischer–Tropsch synthesis product selectivity over iron-based silica-supported catalyst under mild temperatures. *Environmental Progress and Sustainable Energy*, **2024**, 43(3), e14335. https://doi.org/10.1002/ep.14335
6. **Stanke, A.**, Kampars, V. Agglomeration of Fe/SBA-15 with clays for Fischer–Tropsch synthesis. *Energy Reports*, **2022**, 8, 461–466. https://doi.org/10.1016/j.egyr.2022.10.251

Results presented at the scientific conferences

1. **Stanke, A.**, Lazdovica, K. The promotional effect of potassium on iron-based silica supported catalyst for CO_2 hydrogenation. In: *International Multidisciplinary Scientific GeoConference Surveying Geology and Mining Ecology Management, SGEM 2022:*

Conference Proceeding, 22(4.1), pp. 161–166. https://doi.org/10.5593/sgem2022/4.1/s17.21 Bulgaria, Albena, 4 – 10 July 2022.

2. **Stanke, A.** The effect of kaolin and hectorite clay on the Fischer–Tropsch synthesis condensed hydrocarbon products. In: *9th IUPAC International Conference on Green Chemistry: ICGC Book of Abstracts,* Greece, Athens, 5–9 September 2022.
3. **Stanke, A.**, Lazdovica, K. The promotional effect of potassium on iron-based silica-supported catalyst for the hydrogenation of carbon oxides. In: *RTU 63. International Conference "Materials Science & Applied Chemistry": Program and Abstracts*, Latvia, Riga, October 21, 2022.

MAIN RESULTS OF THE THESIS

In recent years, the number of studies on FTS and CO_2-FTS has increased rapidly, driven by the escalating demand for energy and the urgent need to mitigate greenhouse gas emissions. However, despite extensive research, significant knowledge gaps remain, because FTS yields a complex, multi-phase product mixture, and its activity, selectivity, and by-product formation are highly sensitive to catalyst composition, promoter content, support effects and reaction conditions. Additionally, even though the formation of a significant amount of water is unavoidable in both FTS and CO_2-FTS, the role of the aqueous phase is often neglected in research.

Variations in experimental conditions and catalyst systems across studies have led to inconsistent conclusions, highlighting the need for in-depth, standardised investigations that link catalyst structure, preparation strategy and operating conditions to overall process performance.

In this Thesis, fundamental research was conducted to clarify the influence of catalyst support, promoter content and reaction temperature on CO conversion, hydrocarbon selectivity and oxygenate formation in FTS. The effects of reaction temperature and catalyst synthesis and pretreatment method on CO_2-FTS performance were investigated and discussed.

In this Thesis, the FTS and CO_2-FTS performance of iron-based catalysts was evaluated using a continuous flow fixed-bed reactor (Fig. 3). For all the experiments, separate mass flow controllers were used to regulate the flow of the reactant gases. N_2 was used as an internal standard for the calculations. The reaction temperature was measured using a K-type thermocouple embedded in the centre of the catalyst bed. The reaction effluent passed through a wax trap and a gas/liquid/liquid separator. All the condensed products were analysed off-line using a gas chromatograph coupled with a mass spectrometer (GC-MS), nuclear magnetic resonance spectroscopy (NMR) and a Fourier-transform infrared spectrometer (FTIR), whereas the gas phase was analysed on-line using a gas chromatograph equipped with Thermal Conductivity and Flame Ionisation detectors (GC-TCD/FID).

Several methods were employed for catalyst preparation. Obtained heterogenous catalysts were characterised by the following methods: X-ray diffraction (XRD) for studying the crystal phase and particle size; X-ray photoelectron spectroscopy (XPS) for studying the electronic states; X-ray dispersive fluorescence (XRF) for determination of iron concentration; scanning electron microscopy (SEM) for imaging the surface morphology; N_2 adsorption-desorption for determination of surface area and pore size distribution. Before FTS or CO_2-FTS, the catalysts were reduced *in situ* with CO or H_2 to generate the active metallic phase, which is essential for catalytic activity, since the reduction process removes surface oxides, increases the number of available active sites and enables efficient adsorption and activation of reactant molecules.

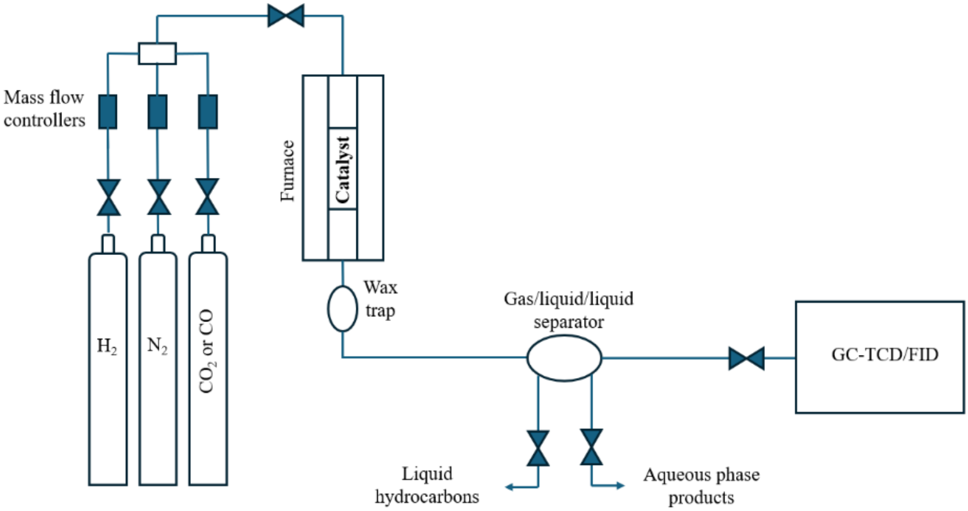

Fig. 3. Scheme of experimental setup.

1. CO hydrogenation

1.1. Effect of reaction temperature on the FTS performance of supported iron-based catalysts

Previous studies investigating the influence of process conditions, catalyst composition and structure on product selectivity have primarily focused on bulk iron catalysts. The effect of reaction temperature on FTS performance differs significantly between bulk and supported iron catalysts due to variations in metal dispersion, heat transfer and phase stability. Bulk catalysts tend to undergo pronounced structural and phase transformations at elevated temperatures, which strongly affect catalytic activity and product selectivity. In contrast, supported iron-based catalysts generally exhibit higher thermal stability and improved heat management, resulting in a more controlled response to temperature variations [15]. Consequently, supported iron-based catalysts are more promising than bulk catalysts for selective FTS.

In this Thesis, The influence of FTS reaction temperature in the range of 240–300 °C was investigated using a mesoporous SiO_2-supported iron-based catalyst. The catalyst was prepared by impregnating commercial silica granules with an aqueous 0.8 M $Fe(NO_3)_3$ solution at 50 °C for 5 hours. The material was subsequently filtered, dried at 110 °C for 2 hours and calcined in air at 550 °C for 5 hours. This preparation procedure ensured uniform precursor distribution within the support pores while preserving the structural integrity and mechanical stability of the granules.

Catalyst characterisation indicated that the catalyst's iron content, determined by XRF, was 11.4 wt.%. The XRD pattern exhibited diffraction peaks corresponding to hematite (α-Fe_2O_3). The broad peak observed at $2\theta = 24°$ was due to amorphous SiO_2. The average size of Fe_2O_3 crystallites for the catalyst, calculated using the Scherer equation, was 13 nm (Fig. 4 A). The N_2 adsorption-desorption isotherm of the catalyst support and impregnated catalyst exhibited the IUPAC type IV isotherm with H1 hysteresis loop, which is characteristic of mesoporous materials. The SEM-EDS mapping analysis confirmed an even and uniform distribution of iron oxide on the catalyst surface. The specific surface area of the impregnated catalyst (207 m^2/g) remained almost unchanged compared to that of the pure catalyst support (213 m^2/g). In contrast, following impregnation, the pore volume and pore size decreased compared to the pure catalyst support, from 0.88 cm^3/g to 0.79 cm^3/g and from 16.5 nm to 15.3 nm, respectively. The obtained characteristics suggest that the iron species were localised within the pores of the support without blocking them. The obtained catalyst characteristics are expected to be advantageous in FTS, as they may promote higher CO conversion and C_{5+} hydrocarbon selectivity compared to unsupported or poorly dispersed iron catalysts described in the literature [16].

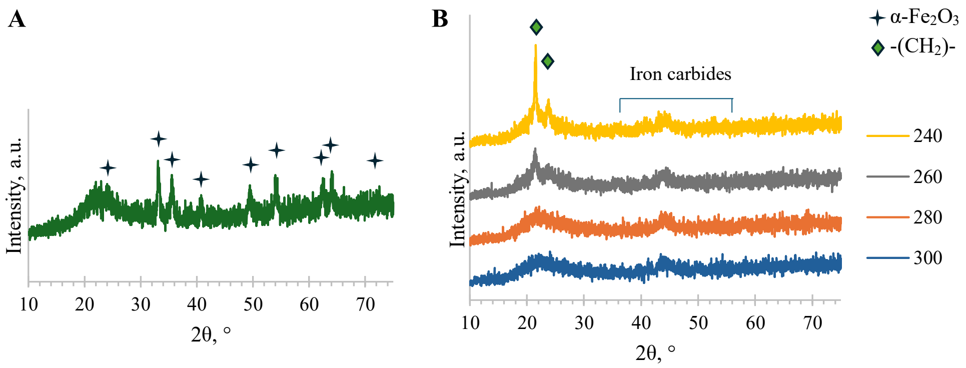

Fig. 4. XRD patterns of calcinated catalyst (A) and spent catalysts (B).

Figure 4 B shows that all the catalysts after FTS reactions exhibited peaks in the 2θ range of 35–52°, which can be identified as iron carbides, the active sites driving FTS. XRD patterns of the catalysts following reactions at 240 °C and 260 °C showed peaks at $2\theta = 21.4°$ and 23.9°, corresponding to waxes. Wax accumulation on the catalyst surface is identified as the primary factor contributing to the observed decline in catalyst performance at these temperatures.

As shown in Fig. 5, increasing the reaction temperature from 240 °C to 280 °C resulted in a substantial increase in CO conversion from 13.6 % to 34.2 %, indicating enhanced catalytic activity. Increasing the temperature to 300 °C had only a marginal effect, suggesting that the FTS reaction was approaching its intrinsic kinetic limitations. The gaseous phase remained dominant at all temperatures, reaching its maximum at 300 °C, while the liquid hydrocarbon fraction peaked at 280 °C and declined sharply at higher temperatures. The aqueous phase increased up to 280 °C and then decreased at higher temperatures. Waxes remained a minor product at all temperatures, showing a slight increase at 260 °C, followed by a decline at 280 °C. These results indicate that 280 °C represents an optimal operating temperature for the investigated catalyst, providing a favourable balance between CO conversion and C_{5+} hydrocarbon selectivity. At higher temperatures, secondary reactions and enhanced WGS activity promoted the formation of short-chain hydrocarbons. In contrast, lower temperatures resulted in reduced CO conversion and increased wax accumulation, which may contribute to catalyst deactivation.

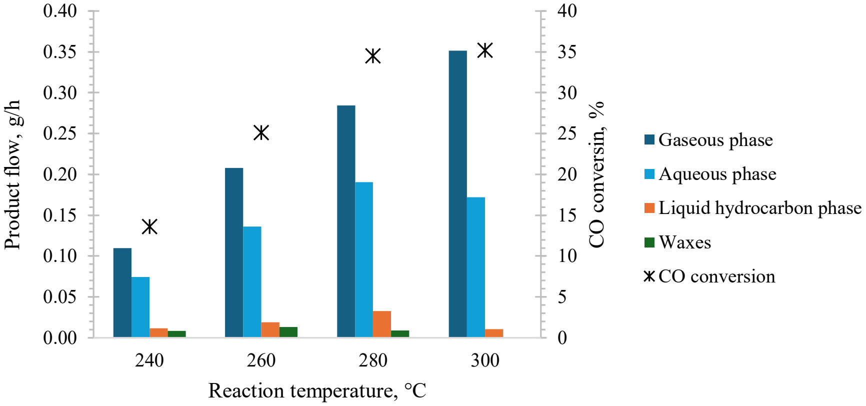

Fig. 5. Effect of the reaction temperature on the CO conversion and flow rates of gaseous, liquid hydrocarbon, solid (waxes) and aqueous phase products.

The liquid hydrocarbon fraction was analysed to assess its potential for e-fuel production. The resulting products exhibited chain lengths ranging from C_5 to C_{36}. Liquid hydrocarbons in the gasoline (C_5–C_{11}), kerosene (C_{10}–C_{14}), and diesel (C_{12}–C_{20}) ranges are considered particularly valuable. The majority of the liquid hydrocarbon products had chain lengths corresponding to the gasoline range (Fig. 6). An increase in reaction temperature resulted in enhanced selectivity toward gasoline-range hydrocarbons, rising from 54 % to 73 %. In contrast, selectivity for the kerosene range decreased from 51 % to 38 %, and for the diesel range from 44 % to 26 %.

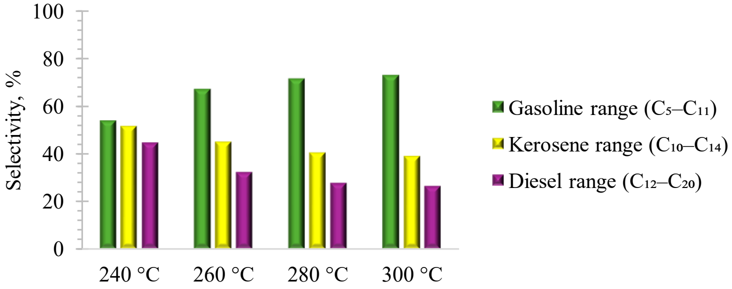

Fig. 6. Selectivity of gasoline range, kerosene range and diesel range hydrocarbons in the liquid hydrocarbon phase.

The gasoline fraction consisted primarily of *n*-paraffins, various olefins, branched hydrocarbons and medium-chain alcohols (Fig. 7). An increase in reaction temperature resulted in decreased selectivity for 1-olefins and increased formation of *n*-paraffins, internal olefins and branched hydrocarbons. This trend is consistent with the participation of 1-olefins in secondary reactions, including hydrogenation, isomerisation and readsorption. The requirements for marketed and delivered gasoline in the European Union are strictly regulated by the European Standard for Gasoline (EN 228). Maximum olefin content is limited to 18 % (v/v), whereas maximum aromatics content is limited to 35 % (v/v). A comparison between the produced gasoline fraction and the EN 228 requirements for gasoline indicates a higher olefin content in the sample. However, the catalyst used does not promote the formation of aromatic compounds.

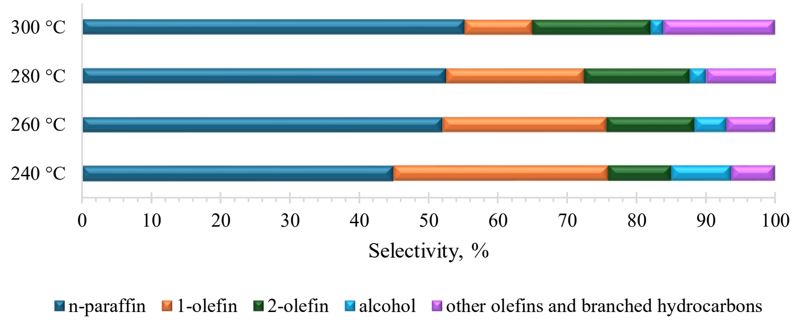

Fig. 7. Effect of the reaction temperature on the composition of gasoline range hydrocarbons.

During FTS, hydrocarbon chain growth proceeds simultaneously with water formation. For every methylene group (-CH_2-) added to the growing hydrocarbon chain, one molecule of water is formed (Equation (1.1)). The produced aqueous phase contains various oxygenated compounds, such as alcohols, acids, aldehydes and ketones. Oxygenates distribute between the aqueous and hydrocarbon phases based on their carbon chain length and molecular polarity. However, oxygenated compounds negatively affect product selectivity and pose environmental and economic challenges.

In the presence of this catalyst, oxygenates in the aqueous phase constituted a relatively low proportion of all FTS products (2.4 % at 240 °C, 3.1 % at 260 °C, 3.6 % at 280 °C and 3.5 % at 300 °C) compared to commercial catalysts reported in the literature, where water-soluble oxygenates represent approximately 6 % of total selectivity [17].

In the scientific literature, FTS research is primarily focused on target hydrocarbon products, while the chemical composition of the aqueous phase is often treated as secondary. The results showed that increasing the reaction temperature led to a higher oxygenate content in the aqueous phase and a marked shift in product selectivity (Fig. 8). Methanol and ethanol were the primary oxygenates detected in the aqueous phase. As the temperature increased from 240 °C to 300 °C, the proportion of methanol rose from 3.8 % to 10.4 % (v/v), while ethanol increased from 3.5 % to 5.2 % (v/v). Additional products identified included acetone and C_3–C_7 *n*-alcohols. Although elevated temperatures hindered the formation of longer-chain alcohols, they promoted the generation of carbonyl compounds. This behaviour was likely associated with enhanced secondary reactions of 1-olefins, leading to ketone formation. Although this catalyst is primarily designed for hydrocarbon synthesis, elevated reaction temperatures facilitate the formation of an aqueous phase enriched with specific oxygen-containing compounds, especially methanol and ethanol, which are both precursors to future fuels and "green" additives to today's gasoline.

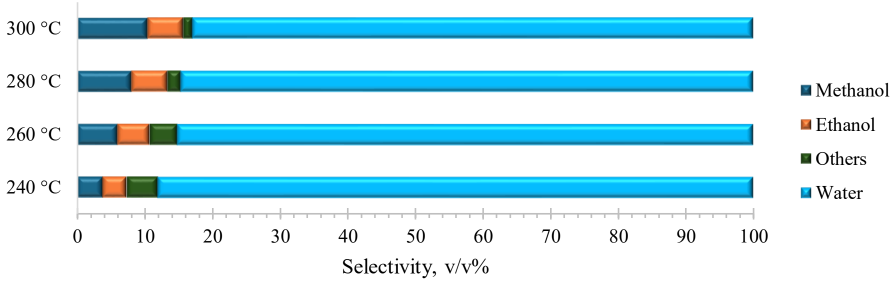

Fig. 8. Effect of the reaction temperature on the composition of the aqueous phase.

The experimental results demonstrate that a reaction temperature of 280 ºC represents the optimal operating conditions for mesoporous SiO_2-supported iron-based catalyst, as it ensures a favourable balance between high CO conversion, increased C_{5+} selectivity and suppressed wax formation. Deviation from this temperature resulted in either reduced activity at lower temperatures or enhanced formation of short-chain hydrocarbons at higher temperatures.

For a more detailed description of the research in this chapter, see the original publication in Appendix 1.

1.2. Effect of promoter (potassium) ratio in supported iron-based catalyst on the FTS performance

Among various promoters, potassium is one of the most widely used for iron-based FTS catalysts, and its influence on catalytic performance has been extensively investigated. However, reported effects on catalytic activity and oxygenate selectivity remain inconsistent. These discrepancies are mainly attributed to variations in catalyst composition, promoter loading and operating conditions. Furthermore, most previous investigations have focused on bulk catalysts, while systematic studies on supported systems remain limited.

In FTS catalysts, potassium is not present in the metallic state. Instead, it is present as a compound such as K_2O [18], KFe_xO_y [19], K_2CO_3, HCOOK [20], or as a surface-adsorbed cation (K^+) stabilised by oxygen-containing anions [18], [21].

The promoting effect of potassium is related to potassium altering the electronic density of the active sites, thereby influencing the bonding strength of adsorbed molecules [22]. It is observed that iron has a higher electron density when potassium is present [19], [22], [23]. This strengthens CO adsorption and weakens H_2 adsorption. The resulting lower H/C ratio on the catalyst’s surface suppresses hydrogenation reactions, thereby limiting CH_4 formation, while promoting hydrocarbon chain growth and the WGS reaction.

In this Thesis, the effects of the K/Fe ratio on product selectivity in a mesoporous SiO_2-supported iron-based catalyst were systematically investigated under industrially relevant operating conditions (P = 20 bar, T = 280 °C).

Mesoporous SiO_2-supported iron-based catalyst (K-0) was prepared according to the method described in Section 1.1. Catalysts with K/Fe molar ratios ranging from 0.02 to 0.06 were subsequently synthesised by impregnating K-0 with KNO_3 aqueous solutions. The concentrations of the impregnation solutions were adjusted to achieve K/Fe molar ratios of 0.02, 0.04, and 0.06 in the final catalysts. Following impregnation, the samples were dried at 110 °C for 2 hours and calcined in air at 550 °C for 5 hours.

The XRD patterns exhibited diffraction peaks characteristic of α-Fe_2O_3 as the predominant phase. The addition of potassium did not modify the hematite crystalline structure (Fig. 9 A). Potassium species were not detected by XRD, likely due to their high dispersion and low concentration. As shown in Fig. 9 B, XRD patterns of catalysts after FTS in the presence of potassium displayed peaks at $2\theta = 21.4°$ and 23.9°, which correspond to waxes. Waxes present on the catalyst surface decrease catalyst activity and mass transfer efficiency during FTS.

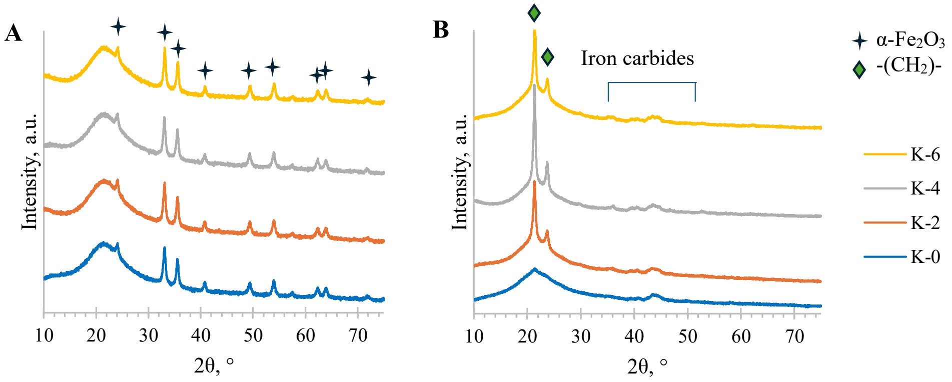

Fig. 9. XRD patterns of (A) as-prepared catalysts and (B) spent catalysts.

Analysis of the textural properties of the catalysts presented in Table 1 suggests that iron and potassium species are localised within the pores of the support. Furthermore, the data indicated that smaller pores might be blocked during the impregnation step.

Table 1

Textural properties of the catalyst support and potassium-promoted catalysts

Sample	BET surface area, m^2/g	Total pore volume, cm^3/g	Average pore diameter, nm
Support (SiO_2)	213	0.88	16.5
K-0	207	0.79	15.3
K-2	200	0.78	15.4
K-4	197	0.76	15.5
K-6	194	0.76	15.7

Figure 10 shows that the FTS experiments produced gaseous phase hydrocarbons, liquid phase hydrocarbons, waxes and an aqueous phase. The addition of potassium significantly affected all product phases except liquid hydrocarbons. Wax production displayed a volcano-type dependence on potassium content, reaching a maximum at a K/Fe ratio of 0.02. In contrast, gaseous phase products exhibited a parabolic trend, with a minimum at K/Fe = 0.02. This pattern was attributed to a rapid decrease in CH_4 selectivity from 21.5 % to 8.5 % and a concurrent rapid increase in CO_2 selectivity from 12.3 % to 18.7 % as the K/Fe ratio increased. Additionally, the yield of aqueous phase products steadily declined with increasing K/Fe ratio. The reduction in water formation, together with increased CO_2 selectivity, suggests enhanced WGS activity for potassium-promoted catalysts. The reduction in wax production at higher potassium levels may be explained by slower diffusion of long-chain hydrocarbons within the catalyst pores, which leads to prolonged occupation of active sites. CO conversion also followed a parabolic trend, likely due to a balance between physical diffusion limitations caused by wax accumulation in the pores and improved CO adsorption and dissociation resulting from higher potassium loading. The minimum at K/Fe = 0.02 marks the point at which wax accumulation severely hindered the reaction, before enhanced surface kinetics provided by higher potassium concentrations (K/Fe ≥ 0.04) compensated for the diffusion limitations.

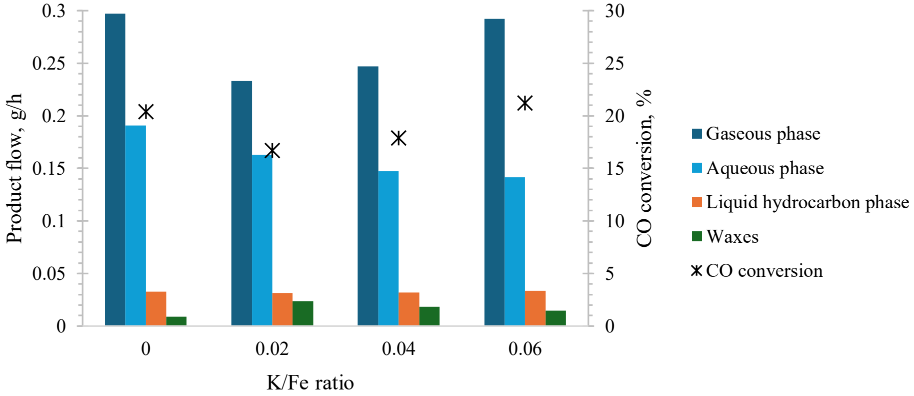

Fig. 10. Effect of the K/Fe ratio on the CO conversion and flow rates of gaseous, liquid hydrocarbon, solid (waxes) and aqueous phase products.

Given that the objective of this Thesis is the synthesis of e-fuels and their precursors, particular attention was directed to the influence of the K/Fe ratio on the liquid hydrocarbon phase products. Products were observed within the C_5–C_{36} range; however, most of the liquid hydrocarbon phase products fell within the gasoline range. In contrast to the effects of reaction temperature, increasing the K/Fe ratio resulted in selectivity towards the gasoline, kerosene, or diesel ranges remaining largely unchanged (Fig. 11).

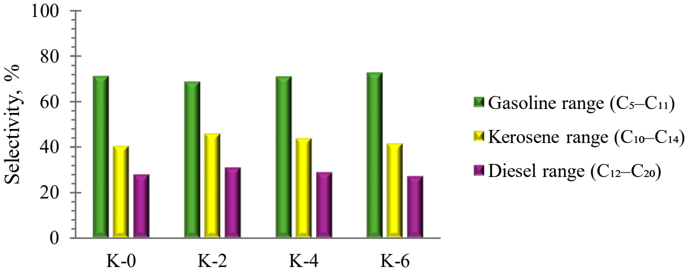

Fig. 11. Effect of the K/Fe ratio on the selectivity of gasoline range, kerosene range and diesel range hydrocarbons in the liquid hydrocarbon phase.

We evaluated the effect of the K/Fe ratio on the composition of gasoline range hydrocarbons. Increasing the K/Fe ratio from 0 to 0.04 resulted in significant changes in hydrocarbon composition, while a further increase to 0.06 produced minimal additional effects (Fig. 12). Potassium promotion reduced the catalyst's hydrogenation activity, which led to a decrease of more than half in *n*-paraffin content and more than a twofold increase in 1-olefin content for K-4 and K-6 catalysts compared to K-0. It was also observed that potassium inhibited the isomerisation of 1-olefins to internal olefins. As a result, catalysts with higher potassium content exhibited a higher 1-olefins to internal olefins ratio. Potassium also promoted hydrocarbon chain growth, leading to the formation of longer-chain alcohols. Due to their low water solubility, these longer-chain alcohols accumulated in the liquid hydrocarbon phase.

A comparison between the produced gasoline fraction and the EN 228 requirements for gasoline reveals a higher olefin content in the sample. This finding suggests that the potassium promoter is unsuitable for direct e-fuel production.

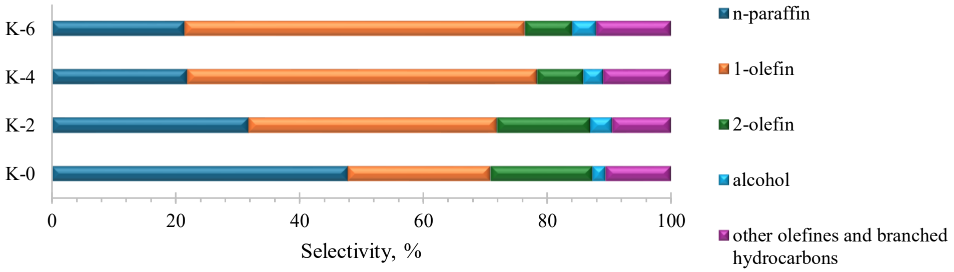

Fig. 12. Effect of the K/Fe ratio on the composition of gasoline range hydrocarbons.

Potassium did not increase the overall selectivity for aqueous phase oxygenates relative to total FTS products. Instead, the selectivity towards oxygenates soluble in water was reduced to approximately 2.1 % at a K/Fe ratio of 0.06. However, it significantly altered the chemical composition of the aqueous phase by changing the distribution and concentration of individual oxygenates.

Potassium addition promoted chain growth, thereby altering the aqueous phase oxygenate profile: methanol was the main product for the unpromoted catalyst, whereas ethanol became the predominant product for potassium-promoted catalysts. Other detected aqueous phase products included C_3–C_7 *n*-alcohols and acetone. Selectivity towards these products, except *n*-propanol, increased with higher K/Fe ratios. The overall oxygenate selectivity followed a parabolic trend, with the lowest oxygenate content observed for the K-4 catalyst (Fig. 13). This trend results from two factors: (1) potassium suppresses the catalyst's hydrogenation activity, leading to the formation of longer chain, less polar products, and (2) potassium enhances CO adsorption, thereby promoting oxygenate formation *via* a CO insertion mechanism.

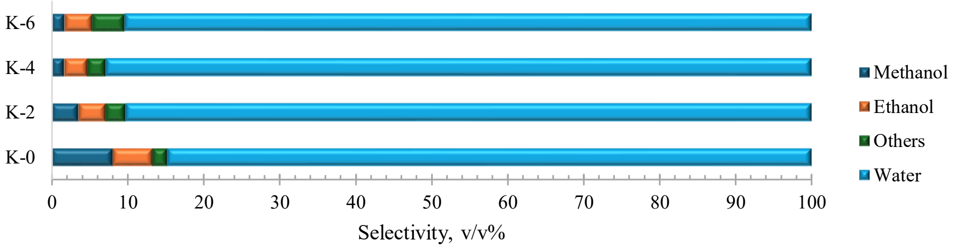

Fig. 13. Effect of the K/Fe ratio on the composition of the aqueous phase.

The experimental findings indicate that increasing the K/Fe ratio significantly influences catalysts' selectivity by suppressing methane formation and promoting the production of olefins, longer-chain hydrocarbons, and oxygenates. However, elevated K/Fe ratios lead to a higher olefin content in the gasoline fraction, limiting the direct use of these catalysts in e-fuel synthesis.

For a more detailed description of the research in this chapter, see the original publication in Appendix 2.

1.3. FTS performance of SBA-15-supported iron-based catalyst

Both promoters and supports influence CO conversion and product selectivity in the FTS process. Selection of an inert support with a narrow pore size distribution and high thermal stability is advisable. Furthermore, the support should possess sufficiently large pore diameters to accommodate iron oxide crystals, thereby preventing their migration to the outer surface during activation [24]. SBA-15 has gained attention as a support, offering a distinct advantage over traditional amorphous silica due to its highly ordered hexagonal periodic structure of two-dimensional pore channels and thick silica walls. These characteristics provide the high hydrothermal stability necessary to withstand the high partial pressures of water typical of FTS. Compared to previously viewed support, SBA-15 has smaller mesopores (5–9 nm) and a larger surface area (typically 500–1000 m^2/g) that facilitates the high dispersion of the active iron phase [25].

In this Thesis, FTS product selectivity was also examined using an SBA-15-supported iron-based catalyst. Although the support matrix discussed in previous chapters provides benefits such as cost-effectiveness, commercial availability, and a practical granular form, it is fundamentally limited by a low maximum iron loading capacity (< 12 wt.%). Therefore, SBA-15 was explored as a high surface area alternative.

The Fe/SBA-15 powder was prepared using a direct synthesis method adapted from the general SBA-15 synthesis procedure reported by Zhao et al. [26]. This approach resulted in more than a twofold increase in iron loading (28 wt.%) without compromising the ordered mesoporous framework or causing pore blockage. The resulting catalyst exhibited a high specific surface area of 57 m^2/g and an average pore diameter of approximately 7 nm. Small-angle XRD patterns confirmed the two-dimensional hexagonal mesoporous structure characteristic of SBA-15, exhibiting diffraction peaks relative to (100), (110), and (200) planes, while wide-angle XRD analysis indicated that iron was present predominantly as α-Fe_2O_3 (Fig. 14).

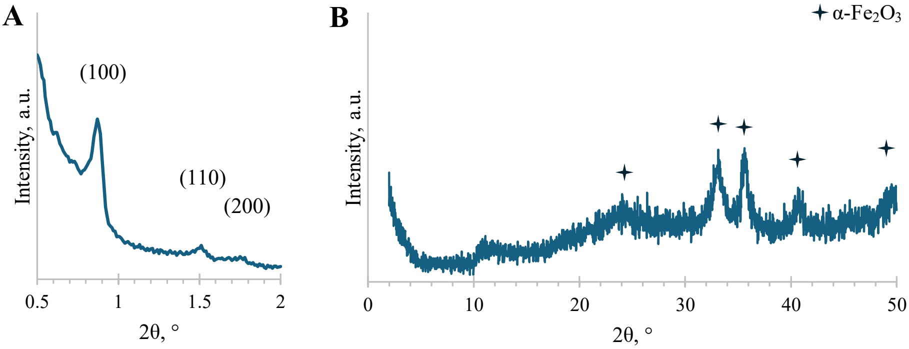

Fig. 14. Small-angle (A) and wide-angle (B) XRD patterns of Fe/SBA-15 catalyst.

While increased Fe content in the catalyst typically results in more active sites, this does not always correlate with improved FTS performance. The literature indicates that iron content most significantly influences CO conversion and CO_2 selectivity, whereas its effect on hydrocarbon selectivity is comparatively minor. Instead, hydrocarbon selectivity is strongly influenced by the catalyst support chosen [24], [27].

Table 2 indicates that the high CO conversion and CO_2 selectivity observed with Fe/SBA-15 can be attributed to the increased iron content in the catalyst. The initial catalytic tests demonstrated that porosity plays a significant role in silica-supported catalysts during the FTS reaction. However, this effect did not extend to the target product's selectivity. The C_{5+} selectivity was approximately half of that observed with the SiO_2-supported catalyst. Fe/SBA-15 demonstrates enhanced catalytic activity and increased selectivity for gaseous hydrocarbons, indicating its suitability for the efficient production of short-chain hydrocarbons.

Table 2

Comparison of the catalytic performance of Fe/SiO_2 and Fe/SBA-15 catalysts under 280 ºC and 20 bar

Catalyst	CO conversion, %	Selectivity, %			
		CO_2	CH_4	C_2–C_4	C_{5+}
Fe/SiO_2	34	8	11	12	69
Fe/SBA-15	54	19	17	30	34

The liquid hydrocarbon phase contained products with chain lengths from C_5 to C_{36}, with over 80 % within the gasoline range (Table 3). The small SBA-15 mesopores function as physical filters for hydrocarbon chain growth, restricting the outward diffusion of long-chain hydrocarbons. This increased residence time within the pores may promote hydrocracking as a secondary reaction, thereby favouring the formation of shorter-chain products [28].

Table 3

Comparison of the selectivity of the liquid hydrocarbon phase of Fe/SiO_2 and Fe/SBA-15 catalysts

	Fe/SiO_2	Fe/SBA-15
Gasoline range (C_5–C_{11}) selectivity, %	72	82
Kerosene range (C_{10}–C_{14}) selectivity, %	40	30
Diesel range (C_{12}–C_{20}) selectivity, %	28	17
Composition of gasoline range hydrocarbons		
n-paraffin selectivity, %	52	48
1-olefin selectivity, %	20	8
2-olefin selectivity, %	15	18
n- alcohol selectivity, %	2	1
Other olefins and branched hydrocarbons selectivity, %	11	25

The quantity of *n*-paraffins was comparable to that obtained with mesoporous SiO_2-supported iron-based catalysts described previously. In contrast, the proportion of 1-olefins decreased, while the proportions of internal olefins and branched hydrocarbons increased significantly. Under reaction conditions, 1-olefins exhibit high reactivity. Their readsorption at chain-growth sites can generate additional primary products, whereas adsorption at alternative sites and subsequent secondary reactions can yield branched hydrocarbons *via* an alkylidene mechanism [29], [30] or result in isomerisation to internal olefins through double-bond shift reactions [31]. These findings indicate that Fe/SBA-15, likely due to its small pore size, facilitates secondary reactions.

The use of Fe/SBA-15 led to lower oxygen content in the aqueous phase than with Fe/SiO_2. The primary oxygenates identified were methanol (3.8 % (v/v)) and ethanol (4.4 % (v/v)). In addition to the C_3–C_7 *n*-alcohols and acetone, acetic acid was detected. The formation of acetic acid can be attributed to multiple mechanisms. Improved surface properties may alter the distribution of reaction pathways among hydrogenation, CO insertion, and hydrocarbon formation. Furthermore, the surface of SBA-15 contains numerous silanol groups (≡Si-OH), which may influence the dynamics of these pathways and enhance the selectivity for oxygenates, including acetic acid.

Summarising the obtained results, it can be concluded that the SBA-15 support enhanced CO conversion due to its high surface area and ordered mesoporous structure. However, its small pores promoted secondary reactions and limited long-chain hydrocarbon growth, resulting in higher gaseous product formation and lower C_{5+} selectivity compared to SiO_2-supported catalysts, making it more suitable for short-chain hydrocarbon synthesis than for liquid fuel production.

The scientific publication of the research described in this chapter can be found in Appendix 3.

2. CO_2 hydrogenation

2.1. Potassium-promoted silica-supported iron-based catalysts for alcohol synthesis

Alcohol synthesis remains a prominent research focus within the field of CO_2 hydrogenation. Short-chain alcohols, including methanol and ethanol, are integral to sustainable energy systems as both efficient fuels and key chemical intermediates. When blended with gasoline, these alcohols enhance combustion performance and reduce emissions due to their high octane numbers. Beyond their direct application, short-chain alcohols are essential to alcohol-to-X pathways, in which dehydration and oligomerisation reactions transform them into energy-dense hydrocarbons suitable for aviation and diesel fuels. This process effectively connects light oxygenates to heavier fuel-range products [32].

Industrially, methanol is mainly manufactured from fossil-derived synthesis gas over $Cu/ZnO/Al_2O_3$ catalysts, operating at elevated pressures (50–100 bar) and temperatures (200–300 °C) [33]. Various metal and metal oxide-based catalysts have been evaluated for CO_2 conversion to methanol. Among them, copper-based systems, followed by indium oxide-based and palladium-based catalysts, have been most widely studied [34]. In contrast, the catalytic conversion of CO_2 to higher alcohols remains significantly less developed. Recently, iron-based catalysts have emerged as a promising approach for the synthesis of methanol and higher alcohols from CO_2 [35]–[37]. It is reported that the synergistic effects of the alkali promoter in the iron-based catalysts are responsible for the advanced synthesis of alcohols [37], [38].

This Thesis examined CO_2 hydrogenation to alcohols using potassium-promoted silica-supported iron-based catalysts. Catalysts were prepared by impregnating commercial silica-based supports (SiO_2 granules and SBA-15 powder) with aqueous solutions of $Fe(NO_3)_3$ and KNO_3. The obtained catalysts were dried and calcined in air. Iron loadings were 10 % for SiO_2 granules and 20 % for SBA-15. K/Fe ratios in catalysts were 0/100, 2/100, and 5/100 for SiO_2-supported catalysts and 5/100 for SBA-15-supported catalyst. The catalysts were correspondingly denoted as Fe/SiO_2, $2K/Fe/SiO_2$, $5K/Fe/SiO_2$, and 5K/Fe/SBA-15.

For all catalysts, iron was predominantly present as α-Fe_2O_3, and the addition of potassium did not alter the hematite crystalline phase. XRD did not detect potassium species due to their low concentration and high dispersion. The textural properties of catalysts are summarised in Table 4. As the potassium content increased, the surface area and pore volume of SiO_2-supported catalysts decreased, whereas the average pore diameter showed a slight increase.

These findings suggest that potassium may obstruct smaller pores. The SBA-15-supported catalyst exhibited the largest surface area and the smallest average pore diameter.

Table 4

Textural properties of the catalysts

Catalyst	BET surface area, m^2/g	Total pore volume, cm^3/g	Average pore diameter, nm
Fe/SiO_2	207	0.79	15.3
$2K/Fe/SiO_2$	201	0.78	15.5
$5K/Fe/SiO_2$	195	0.76	15.6
5K/Fe/SBA-15	318	0.77	7.9

The average CO_2 conversion achieved with SiO_2-supported catalysts was approximately 10 %, while the SBA-15-supported catalyst exhibited an average conversion of only 1 %. Previous studies have reported that, in calcined silica-supported iron-based catalysts, iron dispersion and particle size are influenced by the support's pore size. Supports with smaller pore sizes, such as SBA-15, may promote the formation of poorly reducible iron silicates [39]. Since smaller iron particles are generally more difficult to reduce and carburise, this phenomenon may account for the low catalytic performance observed for 5K/Fe/SBA-15.

Figure 15 presents the product distribution in the gaseous phase, excluding CO selectivity. For all catalysts, CH_4 was the predominant organic compound detected in the gaseous phase. Methanol was the only alcohol identified, while DME was observed exclusively for the 5K/Fe/SBA-15 catalyst. DME is produced by the dehydration of methanol, a reaction that typically requires a catalyst with acidic sites [40]. Purely siliceous SBA-15 materials possess only silanol groups, which exhibit low acid strength and are catalytically inactive [41]. However, surface acidity can be enhanced by doping SBA-15 with various metals, including iron. The incorporation of iron has been reported to increase the surface acidity of SBA-15 by generating Lewis acidic sites [42]. The combination of a relatively large surface area and iron loading in the 5K/Fe-SBA-15 catalyst likely provided sufficient acidity to catalyse DME formation.

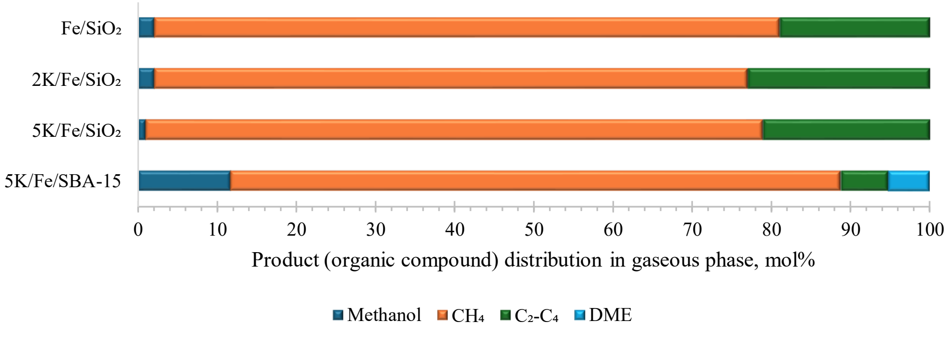

Fig. 15. The composition of the organic compounds in the gaseous phase.

Among the tested catalysts, 5K/Fe-SBA-15 exhibited the highest selectivity towards methanol. The calculated yield of methanol for this catalyst was 3 mg/h·g_{cat}. At the same time, the methanol yield obtained over SiO_2-supported catalysts increased from 1.3 mg/h·g_{cat} over Fe/SiO_2 to 2.7 mg/h·g_{cat} over 2K/Fe/SiO_2, after which it decreased rapidly to 0.3 mg/h·g_{cat} over 5K/Fe/SiO_2.

The obtained methanol yields are more than 50 times lower than those reported for copper or indium oxide-based catalysts in the literature [43]–[45]. These results indicate that, under the investigated conditions, potassium-promoted silica-supported iron-based catalysts exhibit limited activity in CO_2 hydrogenation.

More information about these studies can be found in Appendices 4 and 5.

2.2. Influence of synthesis method on the structure and performance of $NiFe_2O_4$ for e-CH_4 production

E-methane, synthesised from CO_2 using power-to-gas technologies, is a promising future fuel, particularly from a climate and energy perspective. Unlike biomethane, whose production is constrained by the availability of agricultural or biological waste, e-methane does not depend on land use nor compete with food production.

High CH_4 selectivity and CO_2 conversion in the Sabatier reaction with a nickel-containing catalyst are typically achieved at temperatures between 350 °C and 500 °C. At temperatures above 400 °C, the prevalence of undesirable side reactions increases, and both carbon deposition on the catalyst surface and nickel particle sintering are observed. In contrast, operating at lower temperatures presents challenges due to the need for highly active catalysts [46].

Bimetallic catalysts can offer significant advantages over traditional catalysts, primarily due to the unique synergistic interactions between the components. As a result, multicomponent catalysts often display enhanced catalytic activity due to improved dispersion and more effective utilisation of active sites. Recent studies in CO_2-FTS have highlighted the advantages of these synergies, demonstrating that they can significantly lower activation barriers and improve overall efficiency [47], [48].

Nickel ferrite ($NiFe_2O_4$) is a spinel oxide material that has garnered attention for its potential applications in catalysis due to its unique structural features, the possibility of tuning its composition, and its inherent thermal stability. The presence of both nickel and iron ions within the spinel lattice structure endows $NiFe_2O_4$ with interesting redox properties, making it a promising material for catalysing a variety of chemical reactions, including those involved in CO_2 conversion. Unlike simple mixtures of metal oxides, spinel-like structures typically provide narrower particle size distributions, improved stoichiometric control, and consequently a larger active surface area available for catalytic reactions [49].

The performance of bimetallic oxide catalysts is influenced by multiple factors, including the synthesis process, which determines the structure, morphology and overall properties of spinel oxides [50], [51]. The synthesis of phase-pure spinel $NiFe_2O_4$ with controlled particle size and homogeneity remains a considerable challenge. Variations in synthesis conditions often lead to secondary phases or impurities, which alter the crystal structure and, in turn, affect catalytic pathways and overall performance. Despite the investigation of various synthesis routes, a universal and reproducible method for producing highly pure, monodisperse spinel ferrite particles has not yet been established [52].

In this Thesis, the effect of the $NiFe_2O_4$ synthesis method on catalyst characteristics and CO_2-FTS performance was investigated. $NiFe_2O_4$ nanoparticles were synthesised using three distinct methods: sono-chemical, sol-gel auto-combustion and reducing agent-assisted co-precipitation (Fig. 16).

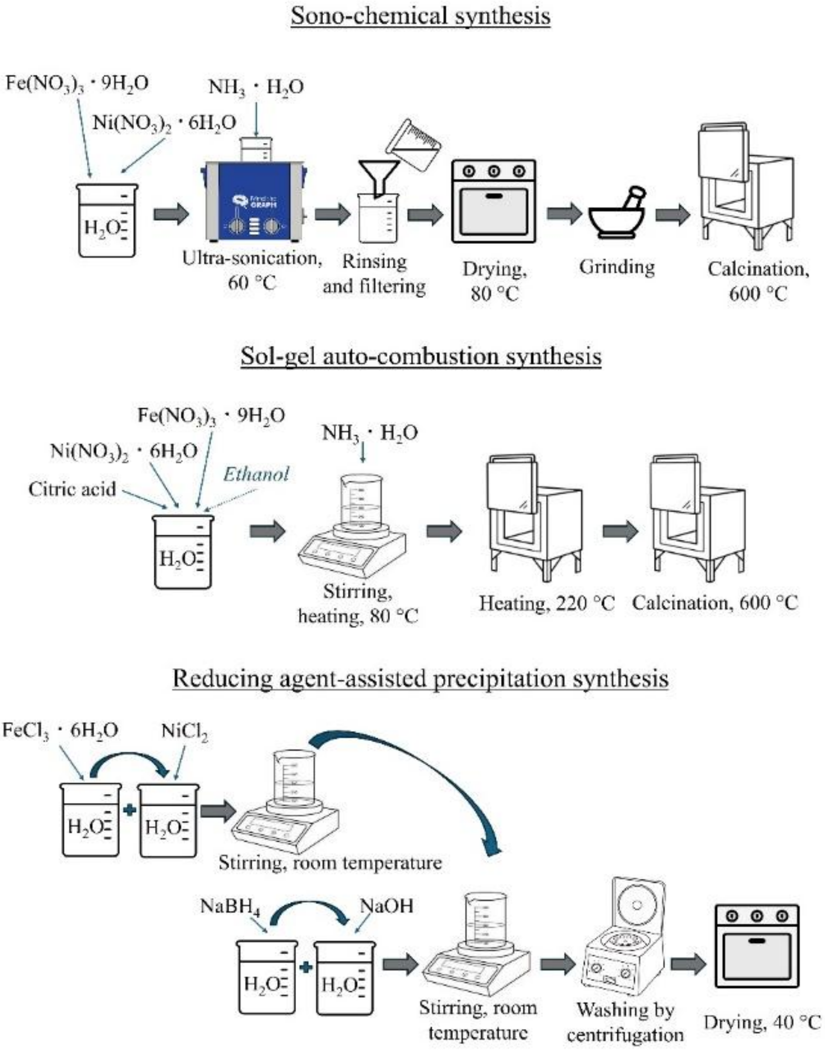

Fig. 16. Schematic representation of sono-chemical, sol-gel auto-combustion and reducing agent-assisted co-precipitation synthesis method.

Four samples were prepared *via* sono-chemical synthesis. Obtained nanoparticles were marked $NiFe_2O_4$-sono-X, where X represents the reaction pH (X = 8, X = 9, X = 10, X = 11). Two samples were prepared by sol-gel auto-combustion synthesis, using citric acid as fuel ($NiFe_2O_4$-Citric) or citric acid and ethanol as fuels ($NiFe_2O_4$-C-E). Sample $NiFe_2O_4$-Prec was prepared *via* reducing agent-assisted precipitation synthesis.

The phase composition and crystallite sizes of the synthesised $NiFe_2O_4$ nanoparticles are presented in Table 5. Elevated pH levels resulted in reduced efficiency of $NiFe_2O_4$ phase formation and an increased presence of Fe_2O_3 impurities in the samples. Additionally, with increasing pH, $NiFe_2O_4$ crystallite size decreased, suggesting accelerated nucleation. The results demonstrate that a pH of 8 is optimal, producing a high $NiFe_2O_4$ content (98 wt.%) and a small catalyst particle size (~ 26 nm). The sol-gel auto-combustion method produced samples characterised by reduced $NiFe_2O_4$ content and increased levels of secondary-phase impurities (Fe_2O_3 and NiO). Utilising citric acid as the sole fuel produced a sample with higher phase purity of $NiFe_2O_4$ (76 wt.%) compared to the method employing both citric acid and ethanol as fuels. The $NiFe_2O_4$-Citric sample exhibited the largest $NiFe_2O_4$ crystallite size (~ 73 nm) among the samples evaluated. Reducing agent-assisted precipitate synthesis enabled the production of phase-pure $NiFe_2O_4$ with small particles.

Table 5

Phase composition and crystallite size of the samples

Sample	Crystalline phase, wt%	Crystallite size of $NiFe_2O_4$, nm	Crystallite size of Fe_2O_3, nm	Crystallite size of NiO, nm
$NiFe_2O_4$-sono-8	$NiFe_2O_4$:Fe_2O_3, 98:2	25.6 ± 0.4	76 ± 21	-
$NiFe_2O_4$-sono-9	$NiFe_2O_4$:Fe_2O_3, 94:6	20.5 ± 0.3	70 ± 6	-
$NiFe_2O_4$-sono-10	$NiFe_2O_4$:Fe_2O_3, 60:40	15.6 ± 0.3	80 ± 1	-
$NiFe_2O_4$-sono-11	$NiFe_2O_4$:Fe_2O_3, 37:63	13.9 ± 0.5	44.7 ± 0.6	-
$NiFe_2O_4$-C-E	$NiFe_2O_4$:Fe_2O_3:NiO, 33:48:19	42.4 ± 1.6	85.9 ± 5.2	42.4 ± 3.9
$NiFe_2O_4$-Citric	$NiFe_2O_4$:Fe_2O_3:NiO, 76:18:6	73.3 ± 1.1	143 ± 16	50.9 ± 5.6
$NiFe_2O_4$-Prec	$NiFe_2O_4$, 100	12.0 ± 0.3	-	-

The highest-purity $NiFe_2O_4$ sample obtained from each respective synthesis method ($NiFe_2O_4$-sono-8, $NiFe_2O_4$-Citric, $NiFe_2O_4$-Prec) was further analysed by N_2 adsorption-desorption and SEM. The analysed samples exhibited IUPAC type IV isotherms with a hysteresis loop, typical of mesoporous materials (Fig. 17).

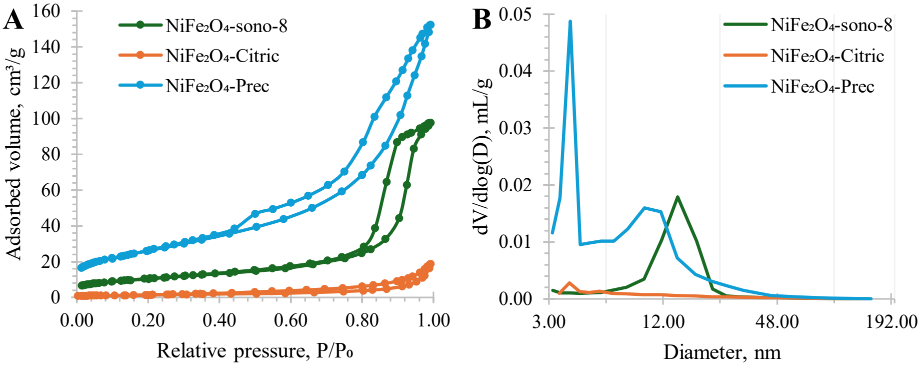

Fig. 17. N_2 adsorption-desorption isotherms (A) and BJH pore size distribution curves (B) of highest purity $NiFe_2O_4$ samples.

The $NiFe_2O_4$-Prec sample exhibited the highest BET surface area among the samples tested. The $NiFe_2O_4$-sono-8 sample possessed the narrowest pore size distribution, as evidenced by the minimal difference between average and mean pore diameters. Conversely, the $NiFe_2O_4$-Citric sample had the lowest surface area and the broadest pore size distribution, indicating substantial textural heterogeneity (Table 6).

Table 6

Textural properties of the samples

Catalyst	BET surface area, m^2/g	Total pore volume, cm^3/g	Average pore diameter, nm	Mean pore diameter [a], nm
$NiFe_2O_4$-sono-8	36.82	0.151	16.39	14.34
$NiFe_2O_4$-Citric	5.20	0.029	22.15	3.85
$NiFe_2O_4$-Prec	93.77	0.236	10.06	3.88

[a] Evaluated by the BJH desorption method.

SEM images indicated aggregate structures composed of spherical particles for both $NiFe_2O_4$-sono-8 and $NiFe_2O_4$-Prec, whereas $NiFe_2O_4$-Citric displayed particles adhered together as a result of agglomerate sintering (Fig. 18).

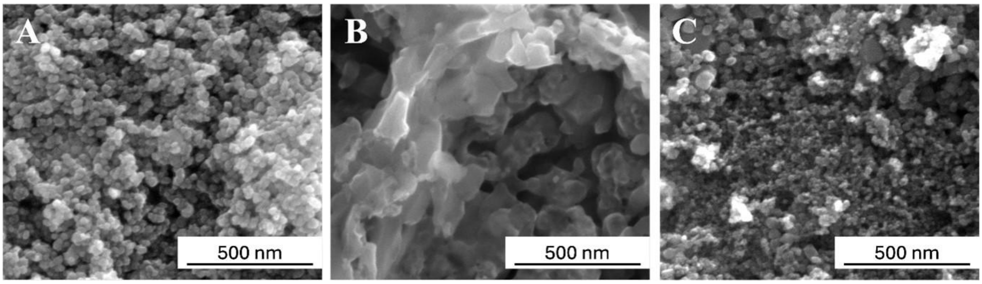

Fig. 18. SEM image of $NiFe_2O_4$-sono-8 (A), $NiFe_2O_4$-Citric (B) and $NiFe_2O_4$-Prec (C).

CO_2-FTS tests were performed using $NiFe_2O_4$-sono-8, $NiFe_2O_4$-Citric, and $NiFe_2O_4$-Prec. The CO_2-FTS performance of these samples at 280 °C, 20 bar is summarised in Fig. 19. Despite $NiFe_2O_4$-Citric acid having poor textural properties, it showed a slightly higher conversion (23.7 %) than other catalysts, most likely due to its large crystallite size, which makes it easier to both reduce and carburise.

Due to the high hydrogenation activity of the catalysts, CH_4 was the main hydrocarbon product for all catalysts. The liquid hydrocarbon phase was not formed in sufficient quantity to be recovered; in addition, part of the C_{5+} products remained in the gaseous state and were carried along with the stream. $NiFe_2O_4$-Prec exhibited the highest hydrogenation activity among the tested samples and yielded the least amount of C_{5+} hydrocarbons. $NiFe_2O_4$-sono-8, in turn, produced higher CO yields than other catalysts. Since $NiFe_2O_4$-sono-8 and $NiFe_2O_4$-Prec catalysts are nearly identical in terms of phase purity (Table 5), differences in the catalytic performance of these two catalysts can be attributed to the effect of particle size. It can be seen that smaller particle size promotes CH_4 formation, whereas larger particles exhibit higher selectivity for CO and C_{5+}. This is because catalysts with larger particle size can be carburised to a greater degree, while smaller particles are less prone to carburization into χ-Fe_5C_2, maintaining a larger proportion of phases that favour hydrogenation over chain growth [39], [53].

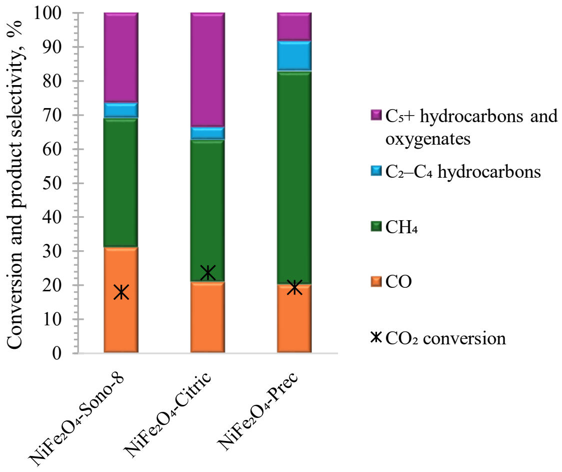

Fig. 19. Catalytic performance of $NiFe_2O_4$-based catalysts in CO_2 hydrogenation.

For all analysed catalysts, the amount of oxygenates in the aqueous phase was less than 1 % (v/v). As a result, the recovery of oxygenates is not reasonable, and the aqueous phase must be treated as wastewater. The aqueous phase for $NiFe_2O_4$-Prec was the purest; the catalyst exhibited the lowest alcohol selectivity among the other catalysts. This catalyst was thus more selective toward hydrocarbon formation. On the other hand, the aqueous phase for $NiFe_2O_4$-sono-8 contained the highest amount of alcohols but the least amount of acids.

The observed increase in methane selectivity, combined with the low yield of C_{5+} products and reduced oxygenate formation, suggests that $NiFe_2O_4$-Prec exhibits the highest hydrogenation activity among the catalysts evaluated. These characteristics indicate its potential as a catalyst for e-CH_4 applications.

For a more detailed description of the research in this chapter, see the manuscript in Appendix 6.

2.3. Effects of the pretreatment method and reaction temperature on cobalt-promoted Fe_3O_4 for CO_2-FTS

E-fuel, synthesised from CO_2 using power-to-liquid technologies, is widely recognised as a promising path towards a fossil-free society. E-fuels and hydrotreated vegetable oil (HVO) fuels are viable alternatives, as both can be utilised within existing fuel infrastructure and internal combustion engines without substantial technical modifications. E-fuels, which are synthesised by converting captured CO_2 and renewable electricity into liquid fuels, present greater long-term decarbonisation potential because, in contrast to HVO, they are not constrained by biomass availability or land-use limitations. Furthermore, e-fuels facilitate the direct utilisation and storage of surplus renewable energy, thereby supporting a more adaptable and climate-neutral energy system [54].

To improve the catalytic performance and enhance C_{2+} hydrocarbon selectivity, promoters are usually added to iron-based CO_2-FTS catalysts. Several studies have demonstrated that small amounts of cobalt can significantly improve C_{5+} selectivity while reducing CO formation [55], [56]. The incorporation of cobalt has been shown to increase the CO_2 conversion. It was also observed that the presence of cobalt promotes the reduction of iron species [57].

While the effects of promoters on iron-based CO_2 hydrogenation catalysts have been widely investigated [58], there is a lack of systematic studies on how synthesis routes and pretreatment strategies influence the performance of catalysts. Catalyst synthesis, pretreatment and activation procedures play an important role in defining the active phase composition, particle size and crystal structure of the catalyst. Before CO_2-FTS, iron-based catalysts are commonly activated using H_2, CO, or synthesis gas [59], [60], while cobalt-based catalysts are generally activated in a H_2 atmosphere [61]. The phase composition of the catalyst before reduction strongly influences the nature of the active phases formed afterwards, as the different precursor phases exhibit distinct reducibility, transformation pathways and thermodynamic stabilities.

Calcination atmosphere is a critical parameter that influences metal dispersion, catalyst oxidation state and reducibility. These factors ultimately affect the distribution of active species and reaction pathways [62]. Despite its importance, the role of calcination atmosphere has received limited attention in the context of iron-based CO_2 hydrogenation catalysts.

The catalytic performance of iron-based catalysts is strongly influenced not only by the presence of promoters and supports, but also by the catalyst's dynamic phase transformations under reaction conditions. In CO_2-FTS, hydrocarbon formation proceeds *via* an initial reduction of CO_2 to CO through the endothermic RWGS, followed by hydrocarbon chain growth through exothermic FTS. Iron-based catalysts are active for both reactions, with Fe_3O_4 as the active phase for RWGS and iron carbides for FTS. Reaction temperature governs the extent of iron oxide reduction and carburization, with higher temperatures favouring the formation of metallic iron and iron carbides, while lower temperatures stabilise oxide phases [63]. On the other hand, temperature affects the rate of RWGS and FTS and, therefore, also partial pressures of CO_2, H_2, CO and H_2O. High CO partial pressure promotes carburization to iron carbides, whereas elevated CO_2 and H_2O partial pressures suppress reduction and favour reoxidation. Higher H_2 partial pressure accelerates oxide reduction and carbide formation [64].

In this Thesis, the influence of the cobalt-promoted Fe_3O_4 catalyst pretreatment procedure was investigated and the effect of reaction temperature over the range of 280–320 °C was evaluated using unpromoted and cobalt-promoted Fe_3O_4 nanopowder catalysts.

Studies on the effect of Fe_3O_4 morphology on FTS activity have revealed that Fe_3O_4 nanospheres exhibited improved iron dispersion and facilitated the reduction and carburization of iron species, resulting in a higher density of active sites and improved C_{5+} hydrocarbons selectivity [65].

The cobalt-promoted Fe_3O_4-based catalyst precursor was prepared by impregnating Fe_3O_4 with an aqueous solution of $Co(NO_3)_2$. The concentration of the impregnation solution was calculated to ensure a Co to Fe molar ratio of 5:100. The catalyst precursor was divided into 3 parts and labelled as Co/Fe_3O_4, Co/Fe_3O_4-N and Co/Fe_3O_4-A. Then different pretreatment procedures were applied for each part. Co/Fe_3O_4 was reduced in H_2, Co/Fe_3O_4-N was calcined in N_2 and reduced in H_2, whereas Co/Fe_3O_4-A was calcined in air and reduced in H_2. An unpromoted Fe_3O_4 catalyst, used as a benchmark, before CO_2-FTS was reduced in H_2. The catalyst composition was evaluated by XRD and XPS, both after calcination and after reduction.

Catalyst characterisation indicated that α-Fe was the primary crystallite phase in Co/Fe_3O_4 following reduction in H_2. Iron in Co/Fe_3O_4-N after calcination in N_2 was predominantly present as Fe_3O_4, from which α-Fe was formed after the reduction in H_2. In contrast, Co/Fe_3O_4-A after calcination in air comprised of maghemite (γ-Fe_2O_3), whereas after the reduction in H_2, γ-Fe_2O_3, α-Fe_2O_3 and α-Fe were observed. Cobalt species were not detected by XRD due to their low concentration (Fig. 20).

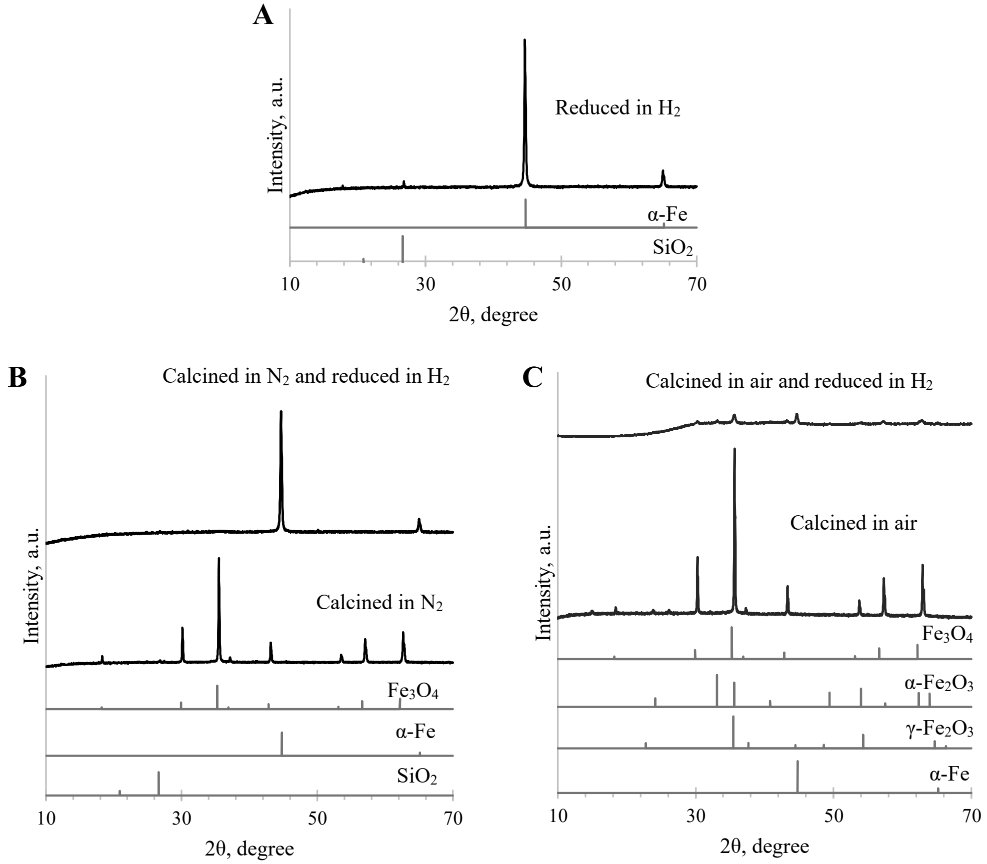

Fig. 20. XRD pattern of catalyst: Co/Fe_3O_4 after reduction in H_2 (A); XRD patterns of Co/Fe_3O_4-N after calcination in N_2 and after reduction in H_2 (B); XRD pattern of Co/Fe_3O_4-A after calcination in air and after reduction in H_2 (C).

As shown in Fig. 21, XPS revealed the coexistence of Fe^{2+} and Fe^{3+} surface species for all samples. For Co/Fe_3O_4 and Co/Fe_3O_4-N after reduction in H_2, an additional low-binding-energy component corresponding to metallic Fe was detected. The results indicate that the surface of the samples is oxidised. Due to band overlap, evaluation of the cobalt signal was not possible.

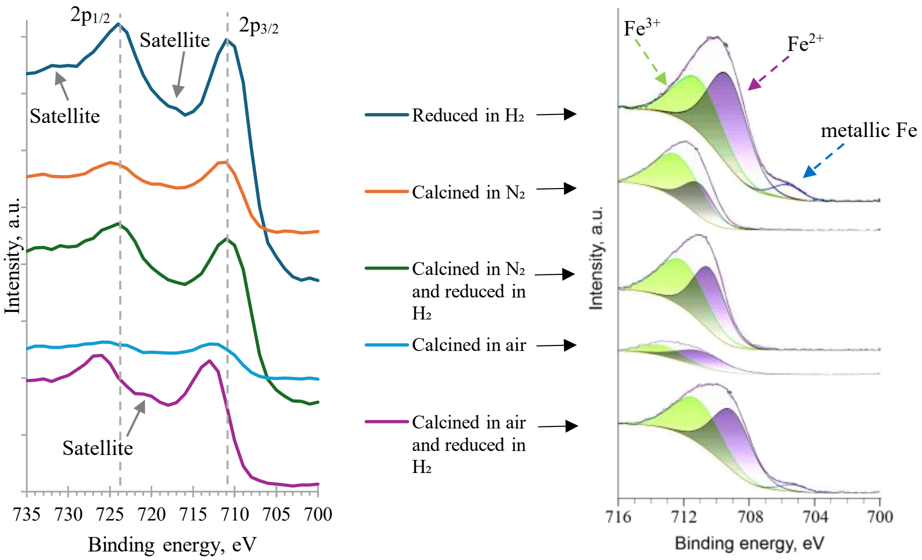

Fig. 21. Fe 2p XPS spectra.

Figure 22 shows the influence of catalyst pretreatment on CO_2-FTS performance and product selectivity. As the highest C_{2+} product selectivity was observed at 280 °C, the author evaluated the influence of catalyst pretreatment on CO_2-FTS performance at this temperature.

Unpromoted Fe_3O_4 showed the lowest C_{5+} hydrocarbon selectivity (4 %). On the other hand, C_{5+} hydrocarbon selectivity for cobalt-promoted catalysts, depending on the pretreatment procedure, ranged from 19.2 % to 36.8 %. This indicates that cobalt, similarly to potassium (Section 1.2), might strengthen the catalyst's CO adsorption and weaken H_2 adsorption, thus promoting hydrocarbon chain growth.

The main difference between the uncalcined (Co/Fe_3O_4) and calcined (Co/Fe_3O_4-N and Co/Fe_3O_4-A) catalysts was their hydrocarbon selectivity, particularly for C_{5+}. This observation indicates that the cobalt phase state influences chain growth and that hydrocarbon selectivity is highly dependent on catalyst pretreatment.

For the preparation of all cobalt-promoted Fe_3O_4 catalysts, $Co(NO_3)_2$ was employed as the precursor. When $Co(NO_3)_2$ on Fe_3O_4 is subjected to a H_2 atmosphere at 400 °C, metallic Co is expected to be the predominant phase formed [66]. Given that Fe_3O_4 serves as the support, the formation of a Co-Fe alloy is also theoretically possible; however, a significant extent of Co-Fe alloying generally requires higher temperatures [67]. According to literature data, the dominant cobalt phase in the Co/Fe_3O_4 catalyst is metallic Co, while the Co-Fe alloy content is minimal. The literature indicates that metallic Co facilitates H_2 dissociation and CO adsorption, thereby promoting C-C chain growth and leading to high C_{2+} selectivity. Therefore, Co/Fe_3O_4 is anticipated to demonstrate enhanced catalytic activity during hydrocarbon formation. However, this catalyst exhibits the lowest C_{5+} selectivity (19.2 %) in comparison to Co/Fe_3O_4-N and

Co/Fe_3O_4-A. The low catalytic activity is likely attributable to metallic cobalt's susceptibility to oxidation, especially when exposed to H_2O, which reduces its activity [68].

For Co/Fe_3O_4-N, pretreatment in a N_2 atmosphere at 450 °C followed by a reducing H_2 atmosphere may result in the formation of cobalt ferrite spinel ($CoFe_2O_4$) on the surface, especially when the formation of metallic Co is restricted [69]. Given the Fe^{3+} rich Co/Fe_3O_4-A surface produced by air pretreatment followed by reduction, the potential formation of $CoFe_2O_4$ at elevated temperatures remains plausible [70]. Thus, the calcined catalysts are likely to contain surface $CoFe_2O_4$ in addition to metallic Co, which may account for their increased selectivity toward C_{5+} hydrocarbons. Based on CO_2 conversion and product selectivity, N_2 calcination followed by H_2 reduction was identified as the most effective pretreatment for cobalt-promoted Fe_3O_4 catalysts, providing good performance in CO_2 hydrogenation.

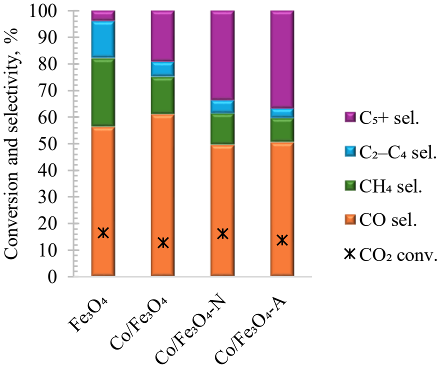

Fig. 22. The influence of pretreatment procedure on the catalytic performance of cobalt-promoted Fe_3O_4 at 280 °C.

Figure 23 shows the influence of reaction temperature on CO_2-FTS performance and product selectivity over unpromoted and cobalt-promoted Fe_3O_4 catalysts. For all catalysts, an increase in CO_2 conversion was observed with the elevation of the reaction temperature from 280 °C to 320 °C. At the same time, the reaction temperature affected the RWGS and FTS rates (and thus product selectivity) differently for unpromoted and cobalt-promoted catalysts.

For unpromoted Fe_3O_4, CO selectivity decreased, while hydrocarbon selectivity increased significantly (Fig. 23 A). The observed decrease in CO selectivity at elevated temperatures could be explained by secondary conversion of initially formed CO with increasing temperature (increased FTS activity). While the overall hydrocarbon selectivity, as well as C_{2+} hydrocarbon selectivity, increased with the elevation of reaction temperature, the highest selectivity towards C_{5+} hydrocarbons was observed at 300 °C. In contrast to conventional FTS, CO_2 hydrogenation usually requires a higher H_2 concentration, while the concentration of CO intermediates is lower. This creates a relatively high H/C ratio on the catalyst surface, which in turn promotes methane formation and suppresses hydrocarbon chain growth [71]. With increasing CO_2 conversion (increased RWGS activity), the surface H/C ratio decreases, thus leading to increased chain growth probability.

For cobalt-promoted catalysts, CO selectivity remained high (> 49 %) across all temperatures, indicating that the RWGS pathway was dominant. The most significant temperature-induced changes observed for cobalt-promoted catalysts were associated with the formation of C_2–C_4 and C_{5+} hydrocarbons (Fig. 23 B, C, D). As the temperature rose, C_2–C_4 hydrocarbon formation increased rapidly, while C_{5+} hydrocarbon selectivity decreased. This observed trend matches with conventional FTS, where hydrocarbon distribution is described by the Anderson–Schulz–Flory model, where the chain-growth probability determines the product chain lengths. Increasing the reaction temperature decreases the chain-growth probability, thereby shifting selectivity toward shorter hydrocarbons. These shorter hydrocarbons are thermodynamically favoured at higher temperatures [72].

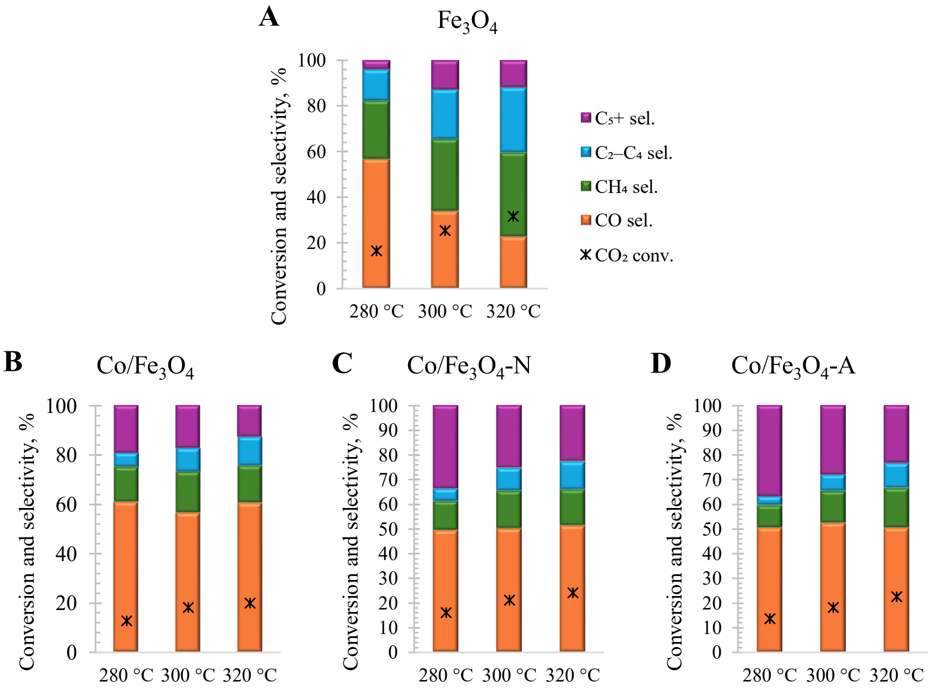

Fig. 23. The influence of reaction temperature on the catalytic performance of unpromoted and cobalt-promoted Fe_3O_4.

The process of CO_2 hydrogenation to hydrocarbons produces substantial wastewater. Water is produced *via* both the RWGS and the FTS reactions; thus, the aqueous phase is more dilute than in conventional FTS. For all catalysts, methanol was the main oxygenate; other observed products were *n*-alcohols up to *n*-butanol and acetone. With increasing reaction temperature, methanol concentration decreased rapidly, while the concentration of C_{2+} alcohols increased. At all temperatures, the amount of oxygenates in the aqueous phase was less than 3 % (v/v). As a result, the recovery of oxygenates is not reasonable, and the aqueous phase must be treated as wastewater.

These findings suggest that, within the examined temperature range, temperature exerts a greater influence than catalyst composition on CO_2 conversion and selectivity, most likely by regulating the relative rates of competing reaction pathways.

CONCLUSIONS

1. A reaction temperature of 280 °C is optimal for mesoporous SiO_2-supported iron catalysts, providing the best balance between high CO conversion, enhanced C_{5+} selectivity and limited formation of undesired short-chain hydrocarbons.

2. Increasing the K/Fe ratio suppresses methane selectivity while enhancing selectivity toward C_{5+} hydrocarbons and promoting the formation of olefins and oxygenates, yet excessive potassium loading limits direct applicability in e-fuel synthesis due to the high gasoline range olefin content.

3. SBA-15-supported catalyst shows enhanced CO conversion due to its high surface area and ordered mesoporosity; however, its small pores favour secondary reactions and gas formation, limiting C_{5+} selectivity and making it more suitable for short-chain hydrocarbon production rather than for liquid fuels.

4. Potassium-promoted SBA-15-supported iron-based catalyst exhibits limited activity in CO_2 hydrogenation to methanol, and due to surface acidity, promotes the formation of DME.

5. The synthesis method strongly affects catalysts' phase purity, textural properties and catalytic performance, with the reducing agent-assisted precipitate synthesis method producing the phase-pure $NiFe_2O_4$ with minimal crystallite size, maximal surface area and superior hydrogenation activity.

6. Cobalt-promoted iron-based catalyst pretreatment method strongly affects the performance of the catalysts by influencing the initial phase composition and, subsequently, also active phase formation and composition, with catalysts calcined prior to CO_2-FTS exhibiting higher C_{5+} selectivity.

ACKNOWLEDGEMENTS

I would like to express my deep gratitude to everyone who contributed to the completion of this thesis.

- Gaļina Dobele (LSIWC) for the N_2 adsorption-desorption measurements of the catalysts.
- Toms-Valdemārs Eiduks (RTU) and Agris Bērziņš (LU) for the XRD analysis.
- Markus Kõiv (University of Tartu) for the SEM analysis.
- Colleagues, especially Zane Ābelniece, Lauma Laipniece, Anastasija Gaile and Māra Plotniece, for their support and contribution to the development of this Thesis.
- Kristīne Lazdoviča and Svetlana Čornaja for their supervision and tremendous support over the years.

This Thesis was accomplished with the significant support of Professor Valdis Kampars. I express my deepest respect for his memory.

This research was supported by the European Social Fund within the Project No. 8.2.2.0/20/I/008, "Strengthening of PhD students and academic personnel of Riga Technical University and BA School of Business and Finance in the strategic fields of specialization" of the Specific Objective 8.2.2, "To Strengthen Academic Staff of Higher Education Institutions in Strategic Specialization Areas", of the Operational Programme "Growth and Employment".

The research was supported by the Riga Technical University's Doctoral Grant Programme.

This research was supported by the EU Recovery and Resilience Facility within Project No 5.2.1.1.i.0/2/24/I/CFLA/003 "Implementation of consolidation and management changes at Riga Technical University, Liepaja University, Rezekne Academy of Technology, Latvian Maritime Academy and Liepaja Maritime College for the progress towards excellence in higher education, science and innovation" academic career doctoral grant (ID 1092).

This research was supported by a research and development grant No. RTU-PA-2024/1-0052 under the EU Recovery and Resilience Facility funded project No. 5.2.1.1.i.0/2/24/I/CFLA/003 "Implementation of consolidation and management changes at Riga Technical University, Liepaja University, Rezekne Academy of Technology, Latvian Maritime Academy and Liepaja Maritime College for the progress towards excellence in higher education, science, and innovation".

REFERENCES

[1] S. Roy, A. Cherevotan, S. C. Peter, Thermochemical CO2 Hydrogenation to Single Carbon Products: Scientific and Technological Challenges, ACS Energy Lett. 3 (2018) 1938–1966. https://doi.org/10.1021/acsenergylett.8b00740.

[2] R. A. Sheldon, Biocatalysis and biomass conversion: Enabling a circular economy, Philosophical Transactions of the Royal Society A: Mathematical, Physical and Engineering Sciences 378 (2020). https://doi.org/10.1098/rsta.2019.0274.

[3] C. Panzone, R. Philippe, A. Chappaz, P. Fongarland, A. Bengaouer, Power-to-Liquid catalytic CO2 valorization into fuels and chemicals: focus on the Fischer–Tropsch route, Journal of CO2 Utilization 38 (2020) 314–347. https://doi.org/10.1016/j.jcou.2020.02.009.

[4] P. Zhai, Y. Li, M. Wang, J. Liu, Z. Cao, J. Zhang, Y. Xu, X. Liu, Y.-W. Li, Q. Zhu, D. Xiao, X.-D. Wen, D. Ma, Development of direct conversion of syngas to unsaturated hydrocarbons based on Fischer–Tropsch route, Chem 7 (2021) 3027–3051. https://doi.org/10.1016/j.chempr.2021.08.019.

[5] Y. Lv, Transitioning to sustainable energy: opportunities, challenges, and the potential of blockchain technology, Front. Energy Res. 11 (2023). https://doi.org/10.3389/fenrg.2023.1258044.

[6] B. Gajdzik, R. Wolniak, R. Nagaj, W.W. Grebski, T. Romanyshyn, Barriers to Renewable Energy Source (RES) Installations as Determinants of Energy Consumption in EU Countries, Energies (Basel). 16 (2023). https://doi.org/10.3390/en16217364.

[7] H. Ababneh, B. H. Hameed, Electrofuels as emerging new green alternative fuel: A review of recent literature, Energy Convers. Manag. 254 (2022). https://doi.org/10.1016/j.enconman.2022.115213.

[8] H. Mahmoudi, M. Mahmoudi, O. Doustdar, H. Jahangiri, A review of Fischer Tropsch synthesis process, mechanism, surface chemistry and catalyst formulation, (2017) 11–31. https://doi.org/10.1515/bfuel-2017-0002.

[9] W. Shafer, M. Gnanamani, U. Graham, J. Yang, C. Masuku, G. Jacobs, B. Davis, Fischer–Tropsch: Product Selectivity – The Fingerprint of Synthetic Fuels, Catalysts 9 (2019) 259. https://doi.org/10.3390/catal9030259.

[10] G. P. Van Der Laan, A. A. C. M. Beenackers, Kinetics and Selectivity of the Fischer–Tropsch Synthesis: A Literature Review, Catal. Rev. Sci. Eng. 41 (1999) 255–318. https://doi.org/10.1081/CR-100101170.

[11] J. A. Schaidle, L. T. Thompson, Fischer–Tropsch synthesis over early transition metal carbides and nitrides: CO activation and chain growth, J. Catal. 329 (2015) 325–334. https://doi.org/10.1016/j.jcat.2015.05.020.

[12] I. C. ten Have, B. M. Weckhuysen, The active phase in cobalt-based Fischer–Tropsch synthesis, Chem. Catalysis 1 (2021) 339–363. https://doi.org/10.1016/j.checat.2021.05.011.

[13] R. P. Ye, J. Ding, W. Gong, M. D. Argyle, Q. Zhong, Y. Wang, C. K. Russell, Z. Xu, A. G. Russell, Q. Li, M. Fan, Y. G. Yao, CO2 hydrogenation to high-value products via

heterogeneous catalysis, Nat. Commun. 10 (2019). https://doi.org/10.1038/s41467-019-13638-9.

[14] T. Xie, J. Wang, F. Ding, A. Zhang, W. Li, X. Guo, CO2 hydrogenation to hydrocarbons over alumina-supported iron catalyst : Effect of support pore size, Journal of CO2 Utilization 19 (2017) 202–208. https://doi.org/10.1016/j.jcou.2017.03.022.

[15] Q. Zhang, J. Kang, Y. Wang, Development of novel catalysts for Fischer–Tropsch synthesis: Tuning the product selectivity, ChemCatChem 2 (2010) 1030–1058. https://doi.org/10.1002/cctc.201000071.

[16] L. U. Okonye, Y. Yao, D. Hildebrandt, R. Meijboom, Contributing to energy sustainability: A review of mesoporous material supported catalysts for Fischer-Tropsch synthesis, Sustain. Energy Fuels 5 (2021) 79–107. https://doi.org/10.1039/d0se01442g.

[17] A. P. Steynberg, R. L. Espinoza, B. Jager, A. C. Vosloo, High temperature Fischer–Tropsch synthesis in commercial practice, Appl. Catal. A Gen. 186 (1999) 41–54. https://doi.org/10.1016/S0926-860X(99)00163-5.

[18] S. Zhao, X. W. Liu, C. F. Huo, Y. W. Li, J. Wang, H. Jiao, The role of potassium promoter in surface carbon hydrogenation on Hägg carbide surfaces, Appl. Catal. A Gen. 493 (2015) 68–76. https://doi.org/10.1016/j.apcata.2015.01.006.

[19] T. Yang, X.-D. Wen, Y.-W. Li, J. Wang, H. Jiao, Interaction of alkali metals with the Fe3O4(111) Surface, Surf. Sci. 603 (2009) 78–83. https://doi.org/10.1016/j.susc.2008.10.020.

[20] G. Jacobs, V. R. R. Pendyala, M. Martinelli, W. D. Shafer, M. K. Gnanamani, S. Khalid, A. MacLennan, Y. Hu, B. H. Davis, Fischer–Tropsch Synthesis: XANES Spectra of Potassium in Promoted Precipitated Iron Catalysts as a Function of Time On-stream, Catal. Letters 147 (2017) 1861–1870. https://doi.org/10.1007/s10562-017-2090-9.

[21] M. A. Petersen, M. J. Cariem, M. Claeys, E. Van Steen, A DFT perspective of potassium promotion of χ-Fe5C2(1 0 0), Appl. Catal. A Gen. 496 (2015) 64–72. https://doi.org/10.1016/j.apcata.2015.02.008.

[22] M. DRY, Heats of chemisorption on promoted iron surfaces and the role of alkali in Fischer–Tropsch synthesis, J. Catal. 15 (1969) 190–199. https://doi.org/10.1016/0021-9517(69)90023-2.

[23] M. C. Ribeiro, G. Jacobs, B. H. Davis, D. C. Cronauer, A. J. Kropf, C. L. Marshall, Fischer−Tropsch Synthesis: An In-Situ TPR-EXAFS/XANES Investigation of the Influence of Group I Alkali Promoters on the Local Atomic and Electronic Structure of Carburized Iron/Silica Catalysts, The Journal of Physical Chemistry C 114 (2010) 7895–7903. https://doi.org/10.1021/jp911856q.

[24] L. A. Cano, A. A. Garcia Blanco, G. Lener, S. G. Marchetti, K. Sapag, Effect of the support and promoters in Fischer–Tropsch synthesis using supported Fe catalysts, Catal. Today 282 (2017) 204–213. https://doi.org/10.1016/j.cattod.2016.06.054.

[25] M. Muñoz, D. Flores, G. Morillo, R. Narváez, A. Marcilla, M. Rosero, Comprehensive Review of SBA-15 Mesoporous Silica: Functionalization Strategies, Diffusion Mechanisms, and Emerging Applications, Sustainable Chemistry 6 (2025). https://doi.org/10.3390/suschem6040042.

[26] D. Zhao, J. Feng, Q. Huo, N. Melosh, G. H. Fredirickson, B. F. Chmelka, GalenD. Stucky, Triblock Copolymer Syntheses of Mesoporous Silica with Periodic 50 to 300 Angstrom Pores, Science (1979). 279 (1998) 548–552. https://doi.org/https://doi.org/10.1126/science.279.5350.548.

[27] Y. Liu, C. Pan, Y. Zou, F. Wu, Z. You, J. Li, Nano-Fe/SiO2 catalysts prepared by facile colloidal deposition: Enhanced durability in Fischer–Tropsch synthesis, Fuel 333 (2023). https://doi.org/10.1016/j.fuel.2022.126514.

[28] M. Lualdi, S. Lögdberg, G. Di Carlo, S. Järås, M. Boutonnet, A. M. Venezia, E. A. Blekkan, A. Holmen, Evidence for diffusion-controlled hydrocarbon selectivities in the fischer-tropsch synthesis over cobalt supported on ordered mesoporous silica, in: Top. Catal., 2011: pp. 1175–1184. https://doi.org/10.1007/s11244-011-9739-1.

[29] E. W. Kuipers, I. H. Vinkenburg, H. Oosterbeek, Chain length dependence of α-olefin readsorption in Fischer-Tropsch synthesis, J. Catal. 152 (1995) 137–146. https://doi.org/10.1006/jcat.1995.1068.

[30] B. Shi, L. Wu, Y. Liao, C. Jin, A. Montavon, Explanations of the formation of branched hydrocarbons during fischer-tropsch synthesis by alkylidene mechanism, Top. Catal. 57 (2014) 451–459. https://doi.org/10.1007/s11244-013-0201-4.

[31] G. P. Van Der Laan, A. A. C. M. Beenackers, Kinetics and selectivity of the Fischer–Tropsch synthesis: A literature review, Catal. Rev. Sci. Eng. 41 (1999) 255–318. https://doi.org/10.1081/CR-100101170.

[32] T. Biswal, K. P. Shadangi, P. K. Sarangi, R. K. Srivastava, Conversion of carbon dioxide to methanol: A comprehensive review, Chemosphere 298 (2022). https://doi.org/10.1016/j.chemosphere.2022.134299.

[33] K. Stangeland, H. Li, Z. Yu, CO2 hydrogenation to methanol: the structure–activity relationships of different catalyst systems, Energy Ecol. Environ. 5 (2020) 272–285. https://doi.org/10.1007/s40974-020-00156-4.

[34] S. Saeidi, S. Najari, V. Hessel, K. Wilson, F. J. Keil, P. Concepción, S. L. Suib, A. E. Rodrigues, Recent advances in CO2 hydrogenation to value-added products – Current challenges and future directions, Prog. Energy Combust. Sci. 85 (2021) 100905. https://doi.org/https://doi.org/10.1016/j.pecs.2021.100905.

[35] O. Tursunov, L. Kustov, A. Kustov, A Brief Review of Carbon Dioxide Hydrogenation to Methanol Over Copper and Iron Based Catalysts, Oil & Gas Sciences and Technology – Revue d'IFP Energies Nouvelles 72 (2017) 30. https://doi.org/10.2516/ogst/2017027.

[36] J.-L. Dubois, K. Sayama, H. Arakawa, CO2 Hydrogenation over Carbide Catalysts, Chem. Lett. 21 (1992) 5–8. https://doi.org/10.1246/cl.1992.5.

[37] R. Yao, J. Wei, Q. Ge, J. Xu, Y. Han, Q. Ma, H. Xu, J. Sun, Monometallic iron catalysts with synergistic Na and S for higher alcohols synthesis via CO2 hydrogenation, Appl. Catal. B 298 (2021). https://doi.org/10.1016/j.apcatb.2021.120556.

[38] D. Xu, M. Ding, X. Hong, G. Liu, Mechanistic aspects of the role of K promotion on Cu−Fe-based catalysts for higher alcohol synthesis from CO2 hydrogenation, ACS Catal. 10 (2020) 14516–14526. https://doi.org/10.1021/acscatal.0c03575.

[39] K. Cheng, M. Virginie, V. V Ordomsky, C. Cordier, P. A. Chernavskii, M. I. Ivantsov, S. Paul, Y. Wang, A. Y. Khodakov, Pore size effects in high-temperature Fischer-Tropsch synthesis over supported iron catalysts, J. Catal. 328 (2015) 139–150. https://doi.org/10.1016/j.jcat.2014.12.007.

[40] V. Dieterich, A. Buttler, A. Hanel, H. Spliethoff, S. Fendt, Power-to-liquid via synthesis of methanol, DME or Fischer–Tropsch-fuels: A review, Energy Environ. Sci. 13 (2020) 3207–3252. https://doi.org/10.1039/d0ee01187h.

[41] B. Dragoi, E. Dumitriu, C. Guimon, A. Auroux, B. Dragoi, E. Dumitriu, C. Guimon, A. Auroux, Acidic and adsorptive properties of SBA-15 modified by aluminum incorporation, Microporous and Mesoporous Materials 121 (2009) 7–17. https://doi.org/10.1016/j.micromeso.2008.12.023ï.

[42] B. Huang, Y. Chang, H. Wang, Z. Qu, Synergistic effects of acid-metal dual-site of Ag-Fe/SBA-15 catalyst boosting the elimination of formaldehyde, Chemical Engineering Journal 484 (2024). https://doi.org/10.1016/j.cej.2024.149658.

[43] N. Rui, Z. Wang, K. Sun, J. Ye, Q. Ge, C. jun Liu, CO2 hydrogenation to methanol over Pd/In2O3: Effects of Pd and oxygen vacancy, Appl. Catal. B 218 (2017) 488–497. https://doi.org/10.1016/j.apcatb.2017.06.069.

[44] M. Mureddu, F. Ferrara, A. Pettinau, Highly efficient CuO/ZnO/ZrO2@SBA-15 nanocatalysts for methanol synthesis from the catalytic hydrogenation of CO2, Appl. Catal. B 258 (2019). https://doi.org/10.1016/j.apcatb.2019.117941.

[45] Z. Li, Y. Men, S. Liu, J. Wang, K. Qin, D. Tian, T. Shi, L. Zhang, W. An, Boosting CO2 hydrogenation efficiency for methanol synthesis over Pd/In2O3/ZrO2 catalysts by crystalline phase effect, Appl. Surf. Sci. 603 (2022). https://doi.org/10.1016/j.apsusc.2022.154420.

[46] M. C. Bacariza, D. Spataru, L. Karam, J. M. Lopes, C. Henriques, Promising catalytic systems for CO2 hydrogenation into CH4: A review of recent studies, Processes 8 (2020) 1–45. https://doi.org/10.3390/pr8121646.

[47] C. Wei, H. Ding, Z. Zhang, F. Lin, Y. Xu, W. Pan, Research progress of bimetallic catalysts for CO2 hydrogenation to methane, Int. J. Hydrogen Energy 58 (2024) 872–891. https://doi.org/10.1016/j.ijhydene.2024.01.204.

[48] J. F. Wu, L. Y. Liang, Z. Che, Y. T. Miao, L. Chou, Bimetallic oxide catalysts for CO2 hydrogenation to methanol: Recent advances and challenges, Chinese Journal of Catalysis 73 (2025) 62–78. https://doi.org/10.1016/S1872-2067(25)64689-4.

[49] J. C. Navarro, C. Hurtado, M. Gonzalez-Castaño, L. F. Bobadilla, S. Ivanova, F. L. Cumbrera, M. A. Centeno, J.A. Odriozola, Spinel ferrite catalysts for CO2 reduction via reverse water gas shift reaction, Journal of CO2 Utilization 68 (2023). https://doi.org/10.1016/j.jcou.2022.102356.

[50] M. A. Almessiere, Y. Slimani, S. Guner, M. Sertkol, A. Demir Korkmaz, S. E. Shirsath, A. Baykal, Sonochemical synthesis and physical properties of Co0.3Ni0.5Mn0.2EuxFe2−xO4 nano-spinel ferrites, Ultrason. Sonochem. 58 (2019). https://doi.org/10.1016/j.ultsonch.2019.104654.

[51] S. I. El-Dek, M. A. Ali, S. M. El-Zanaty, S.E. Ahmed, Comparative investigations on ferrite nanocomposites for magnetic hyperthermia applications, J. Magn. Magn. Mater. 458 (2018) 147–155. https://doi.org/10.1016/j.jmmm.2018.02.052.

[52] S. J. Salih, W.M. Mahmood, Review on magnetic spinel ferrite (MFe2O4) nanoparticles: From synthesis to application, Heliyon 9 (2023). https://doi.org/10.1016/j.heliyon.2023.e16601.

[53] S. Guo, K. Lu, K. Zheng, X. Yu, P. Ren, Y. Yang, Y. W. Li, H. Chen, X. D. Wen, Atomic-level insight into the carburization process of iron-based catalysts: A ReaxFF molecular dynamics study, J. Catal. 438 (2024). https://doi.org/10.1016/j.jcat.2024.115719.

[54] L. Colelli, S. Dell'Aversano, C. Bassano, G. Vanga, K. Gallucci, G. Vilardi, Liquid e-fuels for a sustainable future: A comprehensive review of production, regulation, and technological innovation, Energy Convers. Manag. 347 (2026). https://doi.org/10.1016/j.enconman.2025.120529.

[55] R. Satthawong, N. Koizumi, C. Song, P. Prasassarakich, Light olefin synthesis from CO2 hydrogenation over K-promoted Fe-Co bimetallic catalysts, Catal. Today 251 (2015) 34–40. https://doi.org/10.1016/j.cattod.2015.01.011.

[56] R. Satthawong, N. Koizumi, C. Song, P. Prasassarakich, Bimetallic Fe-Co catalysts for CO2 hydrogenation to higher hydrocarbons, Journal of CO2 Utilization 3–4 (2013) 102–106. https://doi.org/10.1016/j.jcou.2013.10.002.

[57] C. Panzone, R. Philippe, A. Chappaz, P. Fongarland, A. Bengaouer, Power-to-Liquid catalytic CO2 valorization into fuels and chemicals: Focus on the Fischer–Tropsch route, Journal of CO2 Utilization 38 (2020) 314–347. https://doi.org/10.1016/j.jcou.2020.02.009.

[58] Q. Wang, K. Hu, R. Gao, L. Zhang, L. Wang, C. Zhang, Hydrogenation of Carbon Dioxide to Value-Added Liquid Fuels and Aromatics over Fe-Based Catalysts Based on the Fischer–Tropsch Synthesis Route, Atmosphere (Basel). 13 (2022). https://doi.org/10.3390/atmos13081238.

[59] D. B. Bukur, X. Lang, Y. Ding, Pretreatment effect studies with a precipitated iron Fischer–Tropsch catalyst in a slurry reactor, Appl. Catal. A Gen. 186 (1999) 255–275. https://doi.org/10.1016/S0926-860X(99)00148-9.

[60] T. Riedel, H. Schulz, G. Schaub, K.-W. Jun, J.-S. Hwang, K.-W. Lee, Fischer–Tropsch on Iron with H2/CO and H2/CO2 as Synthesis Gases: The Episodes of Formation of the Fischer–Tropsch Regime and Construction of the Catalyst, Top. Catal. 26 (2003) 41–54. https://doi.org/10.1023/B:TOCA.0000012986.46680.28.

[61] E. Patanou, N. E. Tsakoumis, R. Myrstad, E. A. Blekkan, The impact of sequential H2-CO-H2 activation treatment on the structure and performance of cobalt based catalysts for the Fischer–Tropsch synthesis, Appl. Catal. A Gen. 549 (2018) 280–288. https://doi.org/10.1016/j.apcata.2017.10.007.

[62] Y. Gao, W. Yi, J. Yang, K. Jiang, T. Yang, Z. Li, M. Zhang, Z. Liu, B. Wu, Effect of Calcination Atmosphere on the Performance of Cu/Al2O3 Catalyst for the Selective

Hydrogenation of Furfural to Furfuryl Alcohol, Molecules 29 (2024). https://doi.org/10.3390/molecules29122753.

[63] X. Yang, H. Zhang, Y. Liu, W. Ning, W. Han, H. Liu, C. Huo, Preparation of Iron Carbides Formed by Iron Oxalate Carburization for Fischer–Tropsch Synthesis, Catalysts 9 (2019) 347. https://doi.org/10.3390/catal9040347.

[64] W. Liu, S. Cheng, H. S. Malhi, X. Gao, Z. Zhang, W. Tu, Hydrogenation of CO2 to Olefins over Iron-Based Catalysts: A Review, Catalysts 12 (2022). https://doi.org/10.3390/catal12111432.

[65] J. Tu, M. Ding, Y. Zhang, Y. Li, T. Wang, L. Ma, C. Wang, X. Li, Synthesis of Fe3O4-nanocatalysts with different morphologies and its promotion on shifting C5+ hydrocarbons for Fischer–Tropsch synthesis, Catal. Commun. 59 (2015) 211–215. https://doi.org/10.1016/j.catcom.2014.10.019.

[66] C. Ehrhardt, M. Gjikaj, W. Brockner, Thermal decomposition of cobalt nitrato compounds: Preparation of anhydrous cobalt(II)nitrate and its characterisation by Infrared and Raman spectra, Thermochim. Acta 432 (2005) 36–40. https://doi.org/10.1016/j.tca.2005.04.010.

[67] S. Waseem Ullah, D. F. khan, S. Burki, M. U. Khan, H. Yin, Modeling, Simulations, Predictions, Calculations and Thermodynamic Assessments of Cobalt-Ferric Binary Alloys System Using Calphad Method and Pbine Database, Journal of Heterocyclics (2020) 3–6. https://doi.org/10.33805/2639-6734-109.

[68] W. Chen, I. A. W. Filot, R. Pestman, E. J. M. Hensen, Mechanism of Cobalt-Catalyzed CO Hydrogenation: 2. Fischer–Tropsch Synthesis, ACS Catal. 7 (2017) 8061–8071. https://doi.org/10.1021/acscatal.7b02758.

[69] Y. Zhang, J. Zhang, D. Sun, J.-M. Basset, J. Qian, L. Zhou, Effect of CoFe2O4 content in iron-cobalt bimetallic catalysts on the activity of methane decomposition for hydrogen production, Int. J. Hydrogen Energy 102 (2025) 1497–1506. https://doi.org/10.1016/j.ijhydene.2025.01.065.

[70] V. Berbenni, C. Milanese, G. Bruni, A. Girella, A. Marini, Mechanothermal Solid-state Synthesis of Cobalt(II) Ferrite and Determination of its Heat Capacity by MTDSC, Zeitschrift Für Naturforschung B 65 (2010) 1434–1438. https://doi.org/10.1515/znb-2010-1204.

[71] P. Gao, L. Zhang, S. Li, Z. Zhou, Y. Sun, Novel heterogeneous catalysts for CO2 hydrogenation to liquid fuels, ACS Cent. Sci. 6 (2020) 1657–1670. https://doi.org/10.1021/acscentsci.0c00976.

[72] J. Chen, C. Yang, Thermodynamic Equilibrium Analysis of Product Distribution in the Fischer–Tropsch Process under Different Operating Conditions, ACS Omega 4 (2019) 22237–22244. https://doi.org/10.1021/acsomega.9b03707.

PIELIKUMI/APPENDICES

1. pielikums

Appendix 1

Stanke A., Lazdovica K., Laipniece L.

Evaluation of the Fischer-Tropsch synthesis product selectivity over iron-based silica-supported catalyst under mild temperatures.

Environmental Progress and Sustainable Energy, **2024**, 43(3), e14335.

https://doi.org/10.1002/ep.14335

Received: 1 April 2023 | Revised: 10 October 2023 | Accepted: 10 December 2023

DOI: 10.1002/ep.14335

ENVIRONMENTAL PROGRESS
& SUSTAINABLE ENERGY

ORIGINAL RESEARCH

Sustainability

Evaluation of the Fischer-Tropsch synthesis product selectivity over iron-based silica-supported catalyst under mild temperatures

Agija Stanke | **Kristine Lazdovica** | **Lauma Laipniece**

Faculty of Materials Science and Applied Chemistry, Institute of Applied Chemistry, Riga Technical University, Riga, Latvia

Correspondence
Agija Stanke, Faculty of Materials Science and Applied Chemistry, Institute of Applied Chemistry, Riga Technical University, Paula Valdena 3, Riga, Latvia.
Email: agija.stanke@rtu.lv

Funding information
Ministry of Economics of the Republic of Latvia, Grant/Award Numbers: VPP-EM-AER-2018/3-0004, VPP-2018-ENERGY

Abstract

The circular economy is considered a keystone of sustainable development, and its implementation requires analyzing both product and by-products, as well as process waste. In this study Fischer-Tropsch synthesis product selectivity over Fe/SiO_2 catalyst was investigated in the reaction temperature range of 240 to 300°C. The composition of the gas, liquid hydrocarbon, and wax products is discussed alongside the aqueous phase, which is rarely addressed. It was found that 280°C is the optimal temperature for condensable hydrocarbon production over Fe/SiO_2 catalyst. The increase in reaction temperature led to a decrease in the selectivity of 1-olefins and alcohols in the liquid hydrocarbon phase and waxes, but at the same time contributed to an increase in the content of alcohols in the aqueous phase products.

KEYWORDS
iron catalyst, reaction temperature, sustainability

1 | INTRODUCTION

The excessive burning of fossil resources has caused such global problems as the decimation of the earth's biodiversity, depletion of natural resources, massive environmental pollution, and climate change.[1] In order to avoid further environmental issues, renewable energy sources and more efficient and integrated processes are needed.[2] The fastest growing industrial sector is transportation sector, which accounts for about a fourth of total world energy consumption. In addition, 89% of transport energy use is crude oil, the supply and price of which is strongly influenced by geopolitical issues.[3] Vehicle emissions are one of the main sources of environmental pollution.[4,5] Thus, transition toward sustainable renewable fuels by development of "drop-in" biofuels has become a focus of research.

"Drop-in" biofuels are biomass-based liquid fuels, that are functionally identical to conventional fuels and fully compatible with existing infrastructure. One of the approaches for production of "drop-in" biofuels is gasification coupled with Fischer-Tropsch synthesis (FTS).[6,7] FTS is a set of catalytic processes for the conversion of synthesis gas (H_2/CO) into broad spectrum of hydrocarbons – so called synthetic crude oil.

In general, FTS reaction can be presented as:

$$2nH_2 + nCO \rightarrow -(CH_2)_n- + nH_2O \tag{1}$$

The FTS product spectrum consists of a wide range (C_1–C_{70+}) complex multicomponent mixture of hydrocarbons and oxygenated products.[8,9] One of the FTS research directions is the selectivity control for obtaining expected ranged product.[10,11] However, in most cases, researchers focus on obtaining a specific target product or product phase (light olefins,[12] gasoline,[13,14] diesel,[15] jet fuel,[16,17] paraffin waxes[18,19]) without studying the minor products and/or by-products produced during the process. In fuel production, the target product phases of FTS are liquid hydrocarbons or waxes. FTS tail gas mainly consists of unreacted synthesis gas, N_2, CO_2, and short-chain hydrocarbons (C_1–C_5). Since most of the effluent gases are greenhouse gases, they require environmentally friendly post-treatment.

Environ Prog Sustainable Energy. 2024;43:e14335.
https://doi.org/10.1002/ep.14335

FTS tail gas can be partly recycled back to the CO hydrogenation reactor to increase the productivity of the process, or it can be combusted with air to supply the energy requirements for the process and to produce steam.[20,21] The aqueous phase, often referred as wastewater, contains considerable amounts of water-soluble compounds and requests purification, which requires additional resources.[22]

Nowadays, sustainable development based on circular economy concept is being promoted as a solution to reduce fossil fuel consumption.[23] It endorses the preservation of natural resources and the reduction or, preferably, elimination of waste.[1] In contrast to the linear flow of materials, the principle of the circular economy envisages the development of products in such a way that their recycling and reuse are inherently facilitated. This approach also promotes the valuation, reincorporation, and reuse of by-products, residue streams, and waste.[24,25] For the construction of circular economy models and indicators, it is pertinent to characterize the source, type of waste and/or by-product, generation rate and current disposal, as developed by authors in international research.[25] In order to apply the circular economy principle to FTS, it is necessary to look at the entire synthesis process as a whole and analyze all product phases including by-products.

Typically, main FTS products are *n*-paraffins, and 1-olefins. Minor products can include isomerized hydrocarbons, cyclic hydrocarbons, internal olefins, as well as aldehydes, ketones, acids, and alcohols which are undesirable products for fuels.[8,9] It is known that FTS activity and selectivity is a function of catalyst and reaction conditions.[18,26,27] Although iron, cobalt, nickel, and ruthenium show a sufficiently high hydrogenation activity in the FTS process, only Fe and Co catalysts are used for commercial applications.[28,29] Compared to cobalt, the advantages of iron catalysts are low cost, high availability, better resistance to poisons, higher water-gas shift (WGS) activity, ability to adapt to a wide range of H_2/CO ratios ($H_2/CO = 0.5–2.5$), and reaction temperatures ($T = 230–350°C$). Besides, the selectivity of iron catalysts can be altered by various manipulations, such as adding a promoter or changing process parameters (pressure, temperature, H_2/CO ratio).[9,30,31]

Both bulk, and supported iron catalysts can be used for FTS. The advantages of supported catalysts are increased surface area, improved dispersion, and stability of active phase, enhanced heat, and mass transfer and better mechanical stability of the catalyst.[10] However, in most cases, the effect of catalyst composition, structure and process conditions has been studied using bulk catalysts.[26,32–35] Since the studies are performed under different conditions or using different catalytic systems, there are still some inconsistencies. Considering the advantages of supported iron catalysts, in this study an iron catalyst supported on commercial mesoporous SiO_2 was used for FTS at moderate temperatures. Mesoporous SiO_2 catalyst support allows to obtain mechanically and thermally stable catalyst with a highly dispersed active phase,[36] moreover, a large amount of SiO_2 improves the reduction or carburization of iron oxides not directly bonding with silica.[37]

The aim of this study was to analyze all FTS products, and by-products as well as their selectivity changes as a function of the reaction temperature, thus bringing FTS closer to the circular economy principles. It is known that reaction rate and chain growth probability is linked to the reaction temperature. Lower temperatures favor formation of longer chain products while higher temperatures lead to the formation of shorter chain products. On the other hand, lower temperatures are limited by the reaction and conversion rate.[26,38] The moderate reaction temperature (240–300°C) would provide a compromise between CO conversion rate and yield of condensable products.

2 | MATERIALS AND METHODS

2.1 | Catalyst preparation

The supported iron catalyst used in this study was prepared by impregnation of catalyst support with $Fe(NO_3)_3{\cdot}9H_2O$ (Sigma-Aldrich). Commercial catalyst support, catalogue number 44740, consisting of 90 wt % SiO_2 and 10 wt % Al_2O_3 was purchased from Thermo Fisher Scientific.

First 27 g of the $Fe(NO_3)_3{\cdot}9H_2O$ was dissolved in 80 mL distilled water, then 30 g of catalyst support was added and the solution was stirred at 50°C for 5 h. Impregnated granules were filtered and dried at 110°C for 2 h. Finally, calcination was conducted at 550°C for 5 h in air. Obtained catalyst was denoted as Fe/SiO_2. Obtained catalyst was crushed and sieved to retain 1.0–2.0 mm particles.

2.2 | Catalyst characterization

Iron concentration was determined by using a Rigaku Supermini wavelength x-ray dispersive fluorescence spectrometer with a Rh x-ray tube (XRF). Previously, a calibration was performed using samples with known chemical composition.

The surface area and the pore size distribution were determined by N_2 adsorption–desorption isotherms obtained at −196°C on Quantachrome Instruments Nova 1200 E-Series surface and porosity analyzer. The samples were outgassed at 180°C for 8 h before measurement. The total pore volume was estimated from the amount adsorbed at a relative pressure (P/P_0) of 0.99. Brunauer–Emmett–Teller (BET) method was applied to calculate the specific surface area. The mesopore size distribution was obtained from desorption branches of the isotherms using the Barrett-Joyner-Halenda (BJH) method.

X-ray diffraction (XRD) patterns were recorded on a Bruker AXS D8 ADVANCE powder diffraction system using 40 kV, 40 mA Cu Kα radiation of 0.15406 nm wavelength in the 2θ angle ranging from 10 to 75° with the step size of 0.02°.

The surface of the Fe/SiO_2 catalyst was studied with a scanning electron microscopy (SEM) – energy dispersive spectroscopy (EDS) on Mira3/LMU (Tescan).

2.3 | Test of catalytic behavior

The catalytic performance tests were carried out in a fixed-bed micro-activity reactor (Microactivity-Effi, PID Eng&Tech S.L.). For each experiment about 0.93 g of catalyst with a particle size range 1.0–2.0 mm was placed in a stainless-steel tube reactor with an internal diameter of 9.1 mm. The inlet flow rates of the gases (CO, H_2, and N_2) were controlled separately by Bronkhorst El-Flow thermal mass flow controllers. The reaction temperature was measured by a K-type thermocouple placed in the center of the catalyst bed.

Prior to the catalytic tests, the catalyst was reduced in situ using CO with gas hourly space velocity (GHSV) = 1290 NmL g^{-1} h^{-1} under atmospheric pressure for 24 h.

The reduction temperature was programmed to increase from room temperature to 350°C at heating rate of 3°C min^{-1} and maintained at 350°C for 22 h. After the activation, the catalyst was cooled down to 160°C; subsequently a flow of H_2, CO, and N_2 mixture with GHSV = 4515 NmL g^{-1} h^{-1} was fed through the reactor. The molar ratio of H_2:CO:N_2 was 4:2:1. The pressure was increased from atmospheric to 20 bar (gauge). After the desired pressure was reached, the temperature was raised from 160°C to reaction temperature ($T = 240$, 260, 280, and 300°C) at a rate of 2°C min^{-1} and was maintained for 72 h.

After leaving the reactor, the exit gas passed through a series of traps to condense products. High molecular weight hydrocarbons (waxes) were collected in a hot trap ($P = 20$ bar, $T = 120$°C), and liquid products (oil and aqueous) were collected in a cold trap ($P = 20$ bar, $T = 5$°C). All condensed product phases were quantified and analyzed off-line.

2.4 | Product analysis

The exit gases were analyzed on-line by a gas chromatograph (GC) (Shimadzu Nexis GC-2030) equipped with flame ionization detector (FID) and thermal conductivity detector (TCD) with helium as carrier gas. The transfer line connecting reactor with the chromatograph was heated to 200°C to avoid product condensation.

Nitrogen in the syngas was assumed as inert during the reaction.

Following formulas were used to calculate conversion and selectivities:

$$\text{CO conversion (mol\%)}\, X_{CO} = \frac{CO_{in} - CO_{out}}{CO_{in}} \times 100\% \quad (2)$$

$$CO_2\text{ selectivity (mol\%)}\, S_{CO_2} = \frac{CO_{2\,out}}{CO_{in} - CO_{out}} \times 100\% \quad (3)$$

$$C_n\text{ selectivity (mol\%)}\, S_{C_n} = \frac{C_{n\,out}}{CO_{in} - CO_{out}} \times 100\% \quad (4)$$

$$C_{5+}\text{ selectivity (mol\%)}\, S_{C_{5+}} = 100\% - S_{CO_2} - \sum_{n=1}^{4} S_{C_n} \quad (5)$$

where CO_{in} represents molar flowrate of CO at inlet; CO_{out}, CO_{2out} and C_{nout} represent molar flowrate of CO, CO_2, and hydrocarbons with n carbon atoms at outlet.

Separated fractions of the liquid reaction products (aqueous phase products and hydrocarbon phase products), collected during the reaction, were analyzed off-line by a gas chromatograph (Shimadzu Nexis GC-2030) equipped with mass spectrometer (MS) (Shimadzu GCMS-QP2020 NX) and flame ionization detector, helium was used as carrier gas. No sample preparation was necessary before the injection of the sample onto the GC column. Acetone and alcohols in water phase were quantitated using external calibration.

Fractions of hydrocarbons with n carbon atoms (product distribution) were calculated from FID chromatograms as:

$$y_n = \frac{\sum X_n}{\sum X_{HC}} \times 100\% \quad (6)$$

where ΣX_n is the sum of peak areas of hydrocarbons with n carbon number and ΣX_{HC} is the sum of all hydrocarbon peak areas present at studied product phase.

Average liquid phase hydrocarbon chain length C_a was calculated as:

$$C_a = \frac{\sum n \cdot X_n}{\sum X_{HC}} \quad (7)$$

^{1}H and ^{13}C nuclear magnetic resonance (NMR) spectroscopy was used to study liquid hydrocarbon phase products and Fischer-Tropsch waxes collected over the entire duration of a 72 h reaction. Deuterated chloroform ($CDCl_3$) was used as a solvent, the waxes showed good solubility in $CDCl_3$ and there was no evidence of insoluble residues. All spectra were recorded on a Bruker AVANCE 300 spectrometer operating at 300 MHz for ^{1}H and 75 MHz for ^{13}C. All chemical shift values are referenced to $CDCl_3$ via the residual solvent signal ($\delta_H = 7.26$; $\delta_C = 76.90$).

The average molecular length was calculated from ^{1}H NMR spectra using Cookson approach[39]:

$$N = \frac{3I_{CH_2} + 2I_{CH_3}}{I_{CH_3}} \quad (8)$$

where I_{CH2} is the total intensity of the methylene protons and I_{CH3} is the intensity of the methyl protons. This assumes that sample consists only of n-alkanes.

Universal Attenuated Total Reflectance – Fourier Transform Infrared Spectroscopy (UATR-FTIR) was used for the analysis of liquid hydrocarbon phase, waxes, and aqueous phase products. Measurements were carried out on a PerkinElmer Spectrum 100 spectrometer connected with Universal ATR Sampling Accessory. The mid-infrared spectral range that is, 650–4000 cm^{-1} was selected. The characteristic absorptions of the functional groups used to study FTS products are included in Supplementary information.

3 | RESULTS AND DISCUSSION

3.1 | Catalyst characterization

The iron concentration of the calcined Fe/SiO_2 catalyst, determined by XRF, was 11.4 wt %.

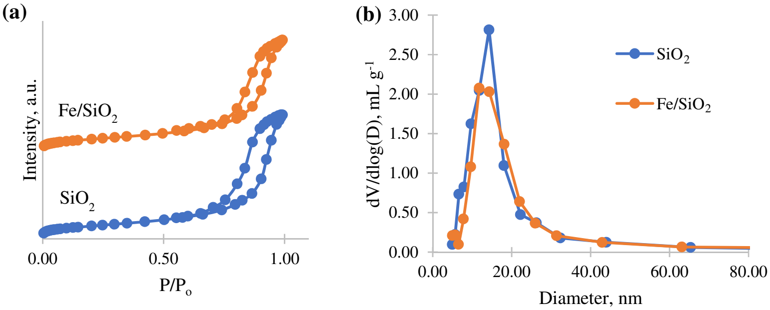

FIGURE 1 N_2 adsorption–desorption isotherms and BJH pore size distribution of catalysts.

TABLE 1 Textural properties of catalyst support and Fe/SiO_2 catalyst.

Sample	S_{BET}[a] (m^2 g^{-1})	V_{total}[b] (cm^3 g^{-1})	$D_{average}$[c] (nm)	D_{mean}[d] (nm)
SiO_2	213	0.88	16.5	14.3
Fe/SiO_2	207	0.79	15.3	11.8

[a] BET surface area.
[b] Total pore volume.
[c] Average pore diameter.
[d] Mean pore diameter evaluated by the BJH desorption method.

The N_2 adsorption–desorption isotherm of the catalyst support and impregnated catalyst exhibited the IUPAC type IV isotherm with H1 hysteresis loop due to the capillary condensation steps at relative pressure of $0.65 < P/P_0 < 0.95$ (Figure 1a), which are characteristic of mesoporous materials.[40] The BJH curves (Figure 1b) showed relatively narrow pore size distribution.

The detailed structure properties including BET surface area, pore volume and average pore diameter of catalyst was summarized in Table 1. Specific surface area for impregnated catalyst remained almost unchanged compared to pure catalyst support, whereas pore volume and pore size after impregnation with Fe decreased in respect to pure catalyst support. Obtained characteristics suggest that iron species are localized in the pores of the support without blocking them.

The SEM micrographs (Figure 2) show catalyst surface after calcination. The SEM–EDX results showed the presence of Si, Al, O, Fe. EDX mapping analysis confirmed even and uniform distribution of iron oxide on the catalyst surface.

XRD patterns of both calcinated and spent catalysts are presented in Figure 3. The pattern, recorded after calcination (Figure 3a), exhibited diffraction peaks corresponding to hematite (α-Fe_2O_3). The broad peak observed at $2\theta = 24°$ was due to amorphous SiO_2. The average size of Fe_2O_3 crystallites for the catalyst after calcination (before activation) calculated using Scherer equation was 13 nm.

The correlation between iron oxide particle size and supports pore diameter suggests that Fe_2O_3 crystallites are mostly localized in the sufficiently large pores of silica, which should protect the catalyst from the sintering and loss of active sites during reaction.

Figure 3b shows XRD patterns of the catalyst after FTS reactions. All catalysts exhibited peaks in the 2θ range of 35–52°, which can be identified as a combination of iron carbides. The XRD patterns of Fe/SiO_2 catalysts after reactions at 240 and 260°C exhibited peaks at $2\theta = 21.4$ and 23.9° due to presence of wax (paraffin).

To confirm the presence of hydrocarbons on catalysts after reactions, all samples were analyzed by UATR-FTIR. FTIR spectra of the Fe/SiO_2 catalysts after reactions at 240°C and 260°C showed absorption bands at 2916 and 2849 cm^{-1} corresponding to stretching vibrations of $-CH_2-$ and $-CH_3$ and absorption bands at 1427 and 1462 cm^{-1} corresponding to bending vibrations of $-CH_2-$ and $-CH_3$ (Figure 4a). Such absorption bands do not appear for catalysts after reactions at 280 and 300°C. Obtained results confirm the presence of wax on Fe/SiO_2 catalysts after reactions at 240 and 260°C and are in agreement with XRD results.

After recording the FTIR spectra, the catalysts were heated in nitrogen at 900°C and re-analyzed with UATR-FTIR. After thermal treatment, absorption bands characteristic of $-CH_2-$ and $-CH_3$ no longer appear in the FTIR spectra that is, waxes are removed from catalysts (Figure 4b).

3.2 | Effect of temperature on the catalytic activity and selectivity

The catalyst FTS activity and overall product selectivity after 72 h on stream at selected reaction temperature are summarized in Table 2. CO conversion and product selectivities are similar to those shown by silica-supported iron catalysts in a study by K. Cheng et al. on the effect of pore size under similar reaction conditions ($T = 300°C$, $H_2/CO = 2.1$, GHSV = 16,200 mL g^{-1} h^{-1}, 20 bar, time on stream 60 h).[36]

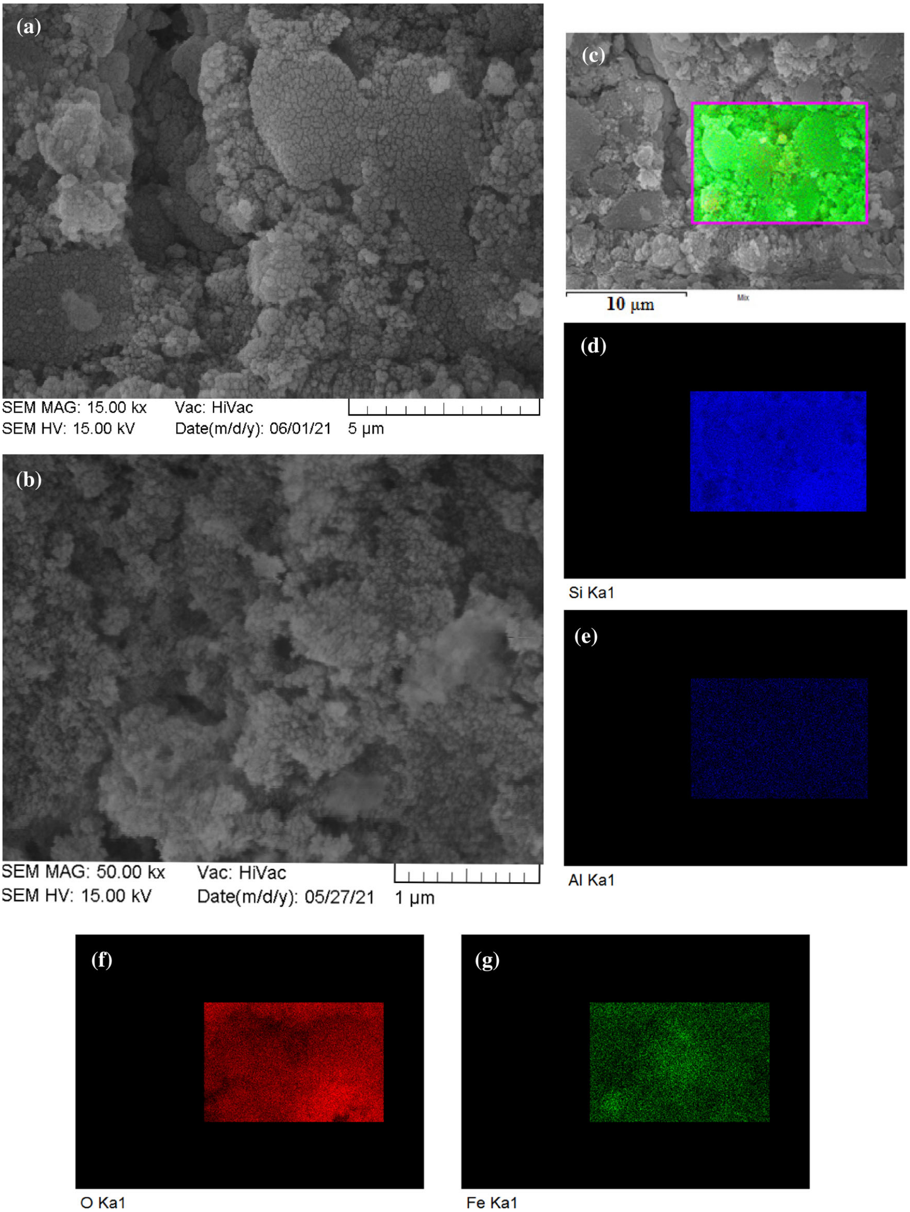

FIGURE 2 SEM images of calcinated Fe/SiO_2 catalyst with different magnifications (a, b). EDS layered overlap image (c); distribution of Si Kα1 (d); distribution of Al Kα1 (e); distribution of O Kα1 (f); distribution of Fe Kα1 (g) in Fe/SiO_2.

Obtained results show that CO conversion is increasing rapidly with temperature elevation from 240 to 280°C. Further increase in temperature to 300°C resulted in a negligible increase in conversion, while overall CO_2 and CH_4 selectivity continued to grow rapidly. It is known that for iron catalysts activity is limited by water. Water inhibits the Fischer–Tropsch reaction rate and since water is a major by-product of FTS, maximal sustainable conversion level is limited.[41,42]

During FTS, CO_2 can be produced through WGS (9) and Boudouard reactions (10):

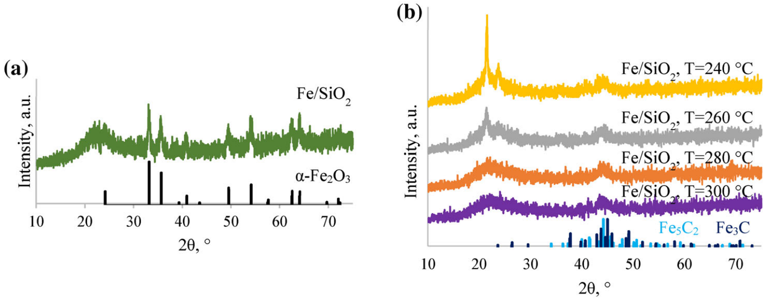

FIGURE 3 XRD patterns of calcinated catalyst (a) and spent catalysts (b).

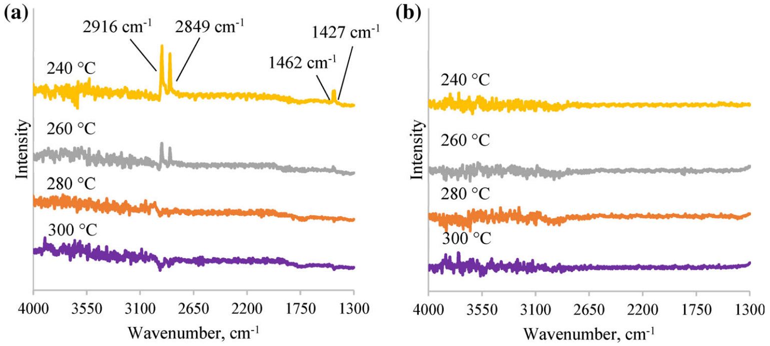

FIGURE 4 UATR-FTIR of spent catalysts (a) and N_2 treated catalysts (b).

TABLE 2 Effect of reaction temperature on the catalytic performance of Fe/SiO_2 (H_2/CO = 2, GHSV = 4515 NmL g^{-1} h^{-1}, 20 bar, time on stream 72 h).

Reaction temperature (°C)	CO conversion (%)	CO_2 selectivity (%)	CH_4 selectivity (%)	C_2–C_4 selectivity (%)	C_{5+} selectivity (%)
240	13.6	2.7	6.7	10.0	80.5
260	25.1	5.5	9.2	11.0	74.3
280	34.5	7.7	11.4	12.2	68.7
300	35.2	9.5	16.4	13.3	60.9

$$CO + H_2O \rightleftarrows CO_2 + H_2 \tag{9}$$

$$2CO \rightleftarrows CO_2 + C \tag{10}$$

It is known, that WGS activity increases with rising the temperature and proceed to equilibrium at high temperatures (≥300°C), based on kinetic effect.[42,43] The reaction rate of Boudouard reaction also increases with increasing temperature and becomes significant at about 300°C.[44] These reactions also contribute to the overall increase in CO conversion. In addition, WGS and Boudouard reactions affect concentrations (partial pressures) of CO, H_2, CO_2, and H_2O and thus have an impact on kinetics of primary and secondary reactions. As seen from Equations (9) and (10), the formation of CO_2 leads to the increase in H_2/CO ratio. High H_2/CO ratio in the reactor favors chain termination reactions.[42]

In order to assess the effect of reaction temperature on the overall FTS product distribution, the average flow rates of different phase products (solid, liquid, and gaseous) were plotted as function of the reaction temperature (Figure 5). It can be seen that raising the temperature to 280°C increases the yield of all products except waxes, while further raising the temperature increases only the amount of gaseous phase products. Obtained results suggests, that for Fe/SiO_2 catalyst 280°C is the final temperature after which side reactions begin to contribute more to the outcome of the FTS and the small increase in CO conversion observed at 300°C may be due to WGS and Boudouard reactions.

3.3 | Effect of temperature on the compositions of hydrocarbons in the gas phase

Gaseous phase products consisted mostly of CO_2 and C_1–C_8 hydrocarbons with approximately 1% of oxygenates (C_1–C_5 *n*-alcohols and acetone). Although all products passed through high pressure hot

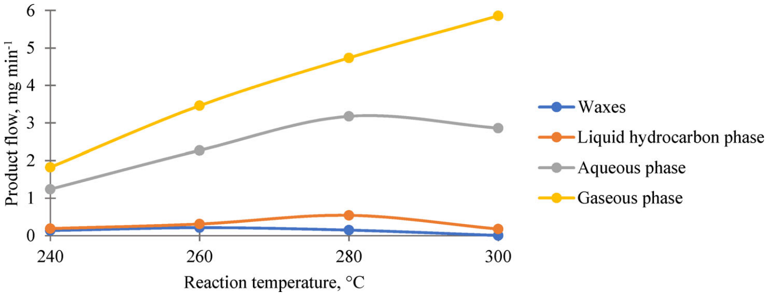

FIGURE 5 Solid (waxes), liquid hydrocarbon phase, water phase, and gaseous phase product flow rates as function of reaction temperature.

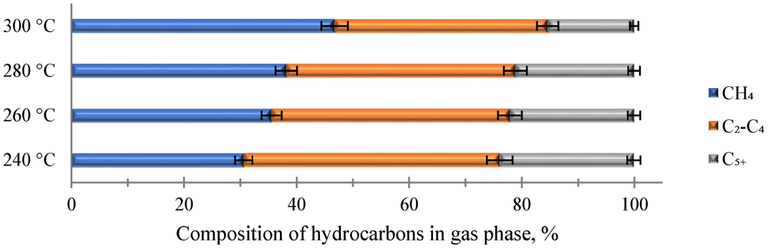

FIGURE 6 The influence of temperature on the composition of hydrocarbons in gas phase.

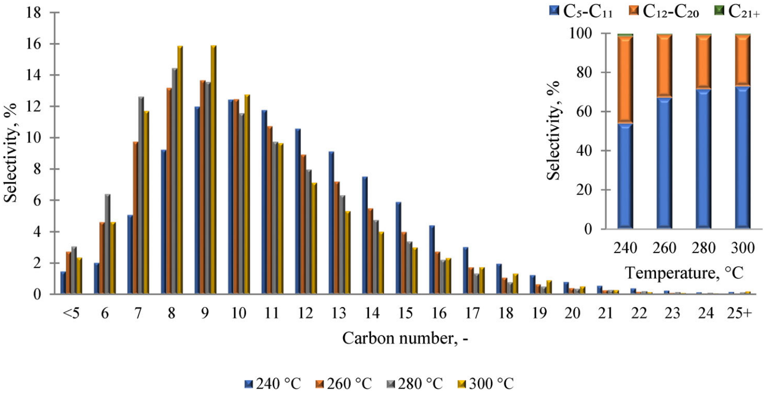

FIGURE 7 The influence of temperature on the liquid hydrocarbon phase product distribution (GC-FID/MS analysis).

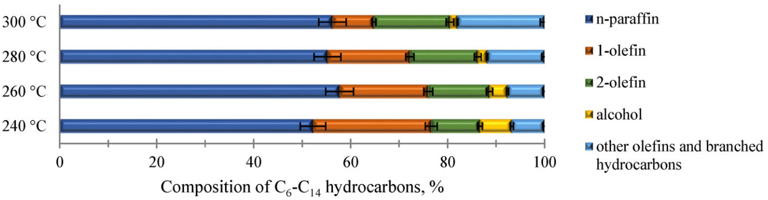

FIGURE 8 The influence of temperature on the composition of the C_6–C_{14} liquid hydrocarbon phase products (GC-FID/MS analysis).

(120°C) and cold (5°C) traps, small part of C_{5+} products were carried along with the gas stream. As the temperature increases, the selectivity of gaseous products increases (Table 2, Figure 5), besides the hydrocarbon composition ratio in gas phase also changes (Figure 6). The proportion of CH_4 in gaseous hydrocarbons increases, while the proportion of C_2–C_4 and C_{5+} fractions in gaseous hydrocarbons decreases from 45% and 24% at 240°C to 38% and 15% at 300°C, respectively. This can be explained by the fact that the selectivity of CH_4 changes faster than the selectivity of C_2–C_4 under the influence of temperature.

3.4 | Effect of the temperature on the compositions of the liquid hydrocarbon phase

The composition of FTS liquid hydrocarbon phase products was determined by using offline gas chromatography, NMR spectroscopy, and FTIR spectroscopy.

Liquid hydrocarbon phase products can be divided into 3 parts relatively corresponding to gasoline range (C_5–C_{11}), diesel range (C_{12}–C_{20}), and heavier (C_{21+}) hydrocarbons. The effect of reaction temperature on the liquid hydrocarbon product distribution is illustrated in Figure 7. The typical observed range of liquid hydrocarbons was C_5–C_{36}. Only very small amounts of the high end (C_{25+}) products were observed. The probability of chain growth decreases when reaction temperature is increased. Upon elevation of the temperature, the fraction of gasoline range hydrocarbons in the liquid hydrocarbon phase increased from 54% at 240°C to 74% at 300°C while diesel range hydrocarbons decreased from 44% at 240°C to 26% at 300°C.

Based on the GC-FID/MS chromatograms, detailed information on the composition of hydrocarbons could be obtained in the C_6–C_{14} range, where it was possible to differentiate the *n*-alcohol, 1-olefin, *n*-paraffin, *trans*-2-olefin, and *cis*-2-olefin peaks. Typical GC chromatogram of the liquid hydrocarbon phase products and order of elution is included in Supplementary information. Outside C_6–C_{14} range it was not possible to achieve acceptable resolution for quantification. Based on the peak area ratios the composition of liquid hydrocarbon phase products in C_6–C_{14} range was calculated (Figure 8).

The results show that the reaction temperature affects the distribution of liquid hydrocarbon phase products. At higher temperatures, the formation of longer chain alcohols is inhibited, consequently, the liquid hydrocarbon phase has a lower oxygenate content. Higher temperature promotes the formation of branched paraffins and internal olefins, at the same time proportion of 1-olefins decreases. Obtained results indicate that higher reaction temperature promotes secondary reactions of 1-olefins leading to the formation of internal olefins and branched hydrocarbons.

TABLE 3 Average chain length of liquid hydrocarbons obtained at different reaction temperatures calculated using GC and ^{1}H NMR.

Reaction temperature (°C)	Average chain length from ^{1}H NMR	Average chain length from GC
240	11.4	11.6
260	10.1	10.5
280	9.4	10.1
300	8.9	10.2

Information of the influence of the reaction temperature on the entire liquid hydrocarbon phase was obtained from NMR and FTIR spectroscopy. Obtained results coincide with GC–FID/MS and are included in Supplementary information.

Average liquid hydrocarbon chain lengths are calculated from GC and ^{1}H NMR (Table 3).

^{1}H NMR results show lower value compared to GC results, besides the higher reaction temperature, the greater the difference. When calculating the chain length from NMR spectra, it is assumed that sample consists only of *n*-alkanes (Equation 8) that is, that there is no branching in the sample and there are no other end groups as just —CH_3 (there are no alcohols, 1-olefins etc.). Thus, average liquid hydrocarbon chain length calculated from ^{1}H NMR may show elevated results for samples containing hydrocarbons with different end groups or may show reduced results for samples containing branched hydrocarbons. The difference between the GC and NMR results indicate that all samples contain branched hydrocarbons and the amount of branched hydrocarbons increases with increasing temperature. This is in agreement with the results obtained from gas chromatography.

3.5 | Effect of temperature on the compositions of the waxes

The composition of FTS waxes was determined using NMR spectroscopy and FTIR spectroscopy. FTIR analysis of the FTS waxes confirmed the presence of paraffins, olefins, and long-chain alcohols. As presented in Figure 9, the reaction temperature affects the composition of FTS waxes. Since the intensity of the absorption band at 720 cm^{-1} correspond to —CH_2— and thus is relatively representative of the hydrocarbon chain length, it was used to describe the chain growth. The chain growth probability is sensitive to the reaction temperature, higher reaction temperature inhibited the formation of long-chain alcohols and hydrocarbons. According to the obtained results, higher temperature (280 and 300°C) promotes the formation of waxes with similar carbon chain lengths but different composition.

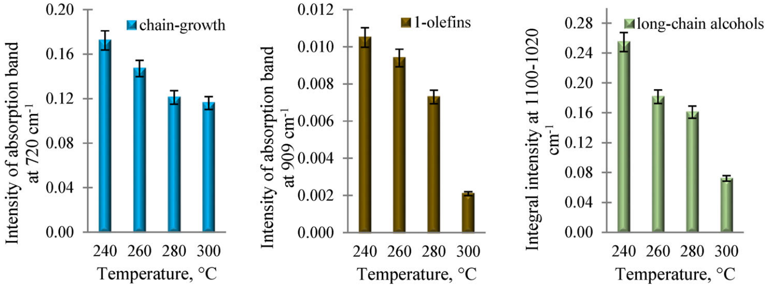

FIGURE 9 The influence of temperature on the composition of the FTS waxes, resulting from FTIR analysis.

At 300°C temperature, the waxes have the lowest content of oxygenates and unsaturated compounds.

^{1}H NMR spectra of waxes obtained at different reaction temperatures were similar to liquid hydrocarbon phase product ^{1}H NMR spectra, but all the signals were narrower and characteristic signals of olefins and oxygenates had very low intensities. Integral intensity ratio between signal of —CH_2— at 1.27 ppm and all the other signals was much greater witch indicates that waxes contain the same product groups as liquid hydrocarbon phase, but the chain length of components is larger.

^{13}C NMR spectra showed signals at 32.1, 29.9, 29.5, 22.9, and 14.3 ppm corresponding to γ, ε, δ, β, and α carbon groups in *n*-alkanes. Signals with smaller intensities corresponding to far from chain end methyl- branched alkanes were detected at 37.3, 30.2, and 27.3 ppm for —CH_2—; at 32.9 ppm for —CH—; and at 19.9 ppm for —CH_3 groups.[45] Signals for branched alkanes were clearly resolved, the same chemical shift interval in liquid hydrocarbons contains more and less distinct signals indicating complicated mixture of branched alkanes, alkenes, and alcohols. Other signals were not resolved from baseline in the same experimental conditions as for liquid hydrocarbon samples. Intensity of signals for branched alkane fragments relative to signals of unbranched fragments are increasing with increasing reaction temperature, showing the same trend as in liquid hydrocarbon phase for increase in branched alkane content with increasing temperature.

For waxes the average hydrocarbon chain length calculated from ^{1}H NMR decreases with increasing reaction temperature (Table 4).

TABLE 4 Influence of reaction temperature on the average chain length of waxes calculated from ^{1}H NMR.

Reaction temperature (°C)	Average chain length
240	20.4
260	18.7
280	17.9
300	17.3

3.6 | Effect of temperature on the aqueous phase products

The target products of the FTS are hydrocarbons, while aqueous phase is a by-product of the synthesis and is therefore often referred to as wastewater. However, as mentioned above, the aqueous phase makes up a large part of the condensable synthesis products and therefore, it is important to evaluate the effect of temperature also on the composition of this phase.

In this study, the FTIR and gas chromatography techniques have been used to investigate aqueous phase products. As presented in Figure 10, the reaction temperature affects the composition and distribution of aqueous phase products. The FTS aqueous phase was made

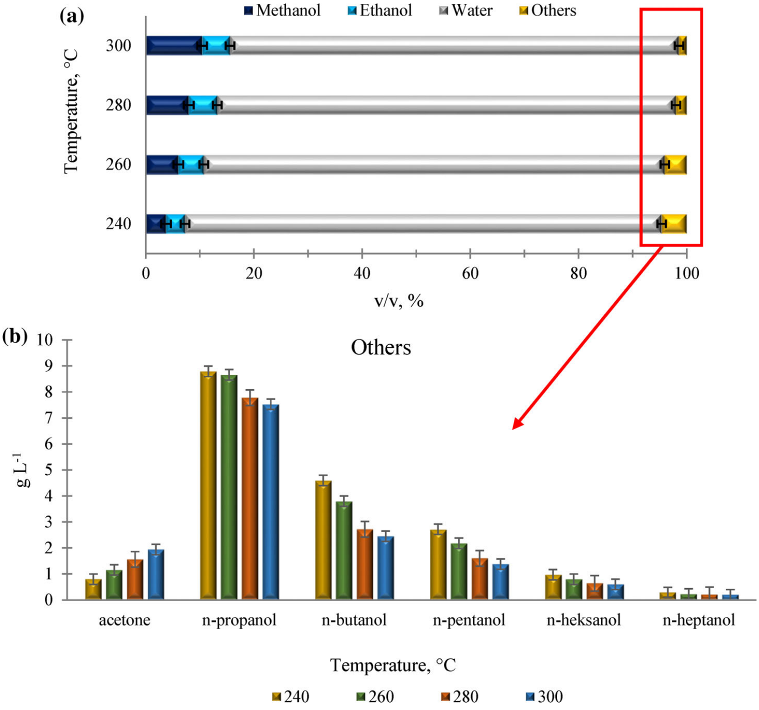

FIGURE 10 The influence of temperature on the composition of the FTS liquid aqueous phase products, resulting from FTIR (a) analysis and composition of other products besides methanol and ethanol, resulting from GC–MS (b) analysis.

of water, C_1–C_7 primary alcohols and a small amount of acetone. According to the obtained results, the content of oxygenates in the aqueous phase increased and selectivity of the products changed when the reaction temperature was raised from 240 to 300°C. It is known that the reaction temperature exerts influence on the chain growth probability,[26] the higher temperature inhibited the formation of C_3–C_7 *n*-alcohols and led to methanol and ethanol selectivity increase. The proportion of methanol and ethanol increased from 3.8% to 10.4% (v/v) and from 3.5% to 5.2% (v/v), respectively, with increasing temperature from 240 to 300°C.

Although higher temperatures reduce formation of longer-chain alcohols, it also contributes to the formation of carbonyl-containing compounds. According to the obtained results, the amount of acetone increased 2.4 times with the temperature rise from 240 to 300°C. Most likely, elevated temperatures promote secondary reactions of 1-olefins leading to the formation of ketones through Wacker-Tsuji oxidation.[8]

As one of the goals of the circular economy is waste reduction or zero-waste production, the water phase should not be seen as wastewater, but as a product or useful raw material. Given the high content of oxygenates in the aqueous phase, the profitability of alcohol extraction should probably be considered or the use of an aqueous phase to produce a windshield washer fluid should be considered.

4 | CONCLUSIONS

The CO conversion level and FTS product selectivity were strongly influenced by the reaction temperature. CO conversion level increased linearly from 13.6% to 34.5% with the temperature elevation from 240 to 280°C while further temperature elevation to 300°C resulted in negligible increase in CO conversion due to an increase in the reaction rate of WGS, and Boudouard reactions. As the reaction temperature affected both conversion and chain growth, the amount of waxes increased with increasing temperature from 240 to 260°C, the amount of liquid products increased with increasing temperature from 240 to 280°C. Further increasing the temperature, the yield of condensed products decreased, while the amount of gaseous products increased throughout the whole temperature range.

Examination of the spent catalysts indicated the presence of wax on the catalyst after FTS reactions at 240 and 260°C, which could contribute to catalyst deactivation.

A higher reaction temperature inhibits the formation of longer chain alcohols and favors the secondary reactions of 1-olefins, therefore the selectivity of alcohols and 1-olefins in liquid hydrocarbons and waxes decreased, while the selectivity of 2-olefins and branched hydrocarbons increased with increasing reaction temperature. The increase in reaction temperature contributed to the formation of shorter chain hydrocarbons. Since short chain alcohols are highly soluble in water, this, in turn, led to an increase in the alcohol content in aqueous phase products up to 23.8 v/v% at 300°C.

AUTHOR CONTRIBUTIONS

Agija Stanke: Conceptualization; investigation; writing – original draft; formal analysis; writing – review and editing; methodology; funding acquisition; visualization; data curation. **Kristine Lazdovica:** Conceptualization; investigation; supervision; formal analysis; methodology; validation; funding acquisition; project administration; resources; writing – review and editing. **Lauma Laipniece:** Investigation; formal analysis.

ACKNOWLEDGMENTS

This research is funded by the Ministry of Economics of the Republic of Latvia, project VPP-2018-ENERGY, project No. VPP-EM-AER-2018/3-0004.

DATA AVAILABILITY STATEMENT

The data that supports the findings of this study are available in the supplementary material of this article.

ORCID

Agija Stanke https://orcid.org/0000-0002-0470-9864

REFERENCES

1. Sheldon RA. Biocatalysis and biomass conversion: enabling a circular economy. *Philos Trans R Soc A Math Phys Eng Sci*. 2020;378(2176): 20190274. doi:10.1098/rsta.2019.0274
2. Puigjaner L, Pérez-Fortes M, Somoza-Tornos A, Espuña A. Editorial: perspectives of chemicals synthesis as a green alternative to fossil fuels. *Front Energy Res*. 2021;9:1-3. doi:10.3389/fenrg.2021.780533
3. DNV. Energy Transition Outlook 2022. https://www.dnv.com/energy-transition-outlook/index.html. Accessed January 4, 2023
4. Cai P, Zhang C, Jing Z, Peng Y, Jing J, Sun H. Effects of Fischer-Tropsch diesel blending in petrochemical diesel on combustion and emissions of a common-rail diesel engine. *Fuel*. 2021;305:121587. doi:10.1016/j.fuel.2021.121587
5. Díaz-Pérez MA, Serrano-Ruiz JC. Catalytic production of jet fuels from biomass. *Molecules*. 2020;25(4):802. doi:10.3390/molecules25040802
6. Kargbo H, Harris JS, Phan AN. “Drop-in” fuel production from biomass: critical review on techno-economic feasibility and sustainability. *Renew Sustain Energy Rev*. 2021;135:110168. doi:10.1016/j.rser.2020.110168
7. Karatzos S, van Dyk JS, McMillan JD, Saddler J. Drop-in biofuel production via conventional (lipid/fatty acid) and advanced (biomass) routes. Part I. *Biofuel Bioprod Biorefin*. 2017;11(2):344-362. doi:10.1002/bbb.1746
8. Shafer W, Gnanamani M, Graham U, et al. Fischer-Tropsch: product selectivity – the fingerprint of synthetic fuels. *Catalysts*. 2019;9(3): 259. doi:10.3390/catal9030259
9. Van Der Laan GP, Beenackers AACM. Kinetics and selectivity of the Fischer-Tropsch synthesis: a literature review. *Catal Rev Sci Eng*. 1999;41(3–4):255-318. doi:10.1081/CR-100101170
10. Zhang Q, Kang J, Wang Y. Development of novel catalysts for Fischer-Tropsch synthesis: tuning the product selectivity. *ChemCatChem*. 2010;2(19):1030-1058. doi:10.1002/cctc.201000071
11. Sun J, Yang G, Peng X, et al. Beyond cars: Fischer-Tropsch synthesis for non-automotive applications. *ChemCatChem*. 2019;11(5): 1412-1424. doi:10.1002/cctc.201802051
12. Liu Y, Chen JF, Zhang Y. The effect of pore size or iron particle size on the formation of light olefins in Fischer-Tropsch synthesis. *RSC Adv*. 2015;5(37):29002-29007. doi:10.1039/c5ra02319j
13. Zhu C, Bollas GM. Gasoline selective Fischer-Tropsch synthesis in structured bifunctional catalysts. *Appl Catal Environ*. 2018;235: 92-102. doi:10.1016/j.apcatb.2018.04.063

14. Li X, Chen Y, Liu S, et al. Enhanced gasoline selectivity through Fischer-Tropsch synthesis on a bifunctional catalyst: effects of active sites proximity and reaction temperature. *Chem Eng J*. 2021;416: 129180. doi:10.1016/j.cej.2021.129180
15. Zeng S, Su H, Ding N, Yu S, Liu K. Co/SBA-16: highly selective Fischer-Tropsch synthesis catalyst towards diesel fraction. *J Fuel Chem Technol*. 2014;42(4):449-454. doi:10.1016/S1872-5813(14)60021-9
16. Yang M, Zhu L, Zhuo Y, Liang J, Wang S. Selective Fischer-Tropsch synthesis for jet fuel production over Y3+modified Co/H-β catalysts. *Sustain Energy Fuels*. 2020;4(7):3528-3536. doi:10.1039/D0SE00468E
17. Martínez del Monte D, Vizcaíno AJ, Dufour J, Martos C. Effect of K, Co and Mo addition in Fe-based catalysts for aviation biofuels production by Fischer-Tropsch synthesis. *Fuel Process Technol*. 2019;194: 106102. doi:10.1016/j.fuproc.2019.05.025
18. Ail SS, Dasappa S. Investigations into enhanced wax production with combustion synthesized Fischer-Tropsch catalysts. *Energ Conver Manage*. 2016;116:80-90. doi:10.1016/j.enconman.2016.02.075
19. Yang J-I, Yang JH, Kim H-J, Jung H, Chun DH, Lee H-T. Highly effective cobalt catalyst for wax production in Fischer-Tropsch synthesis. *Fuel*. 2010;89(1):237-243. doi:10.1016/j.fuel.2009.07.008
20. Wei K, Yue S, Hou X, et al. Feasibility analysis of Fischer-Tropsch synthesis tail gas as a fuel for solid oxide fuel cells. *Int J Energy Res*. 2022; 46(8):10864-10874. doi:10.1002/er.7887
21. Hos T, Herskowitz M. Techno-economic analysis of biogas conversion to liquid hydrocarbon fuels through production of lean-hydrogen syngas. *ACS Eng Au*. 2022;2(5):450-460. doi:10.1021/acsengineeringau.2c00019
22. Zoppi G, Pipitone G, Gruber H, et al. Aqueous phase reforming of pilot-scale Fischer-Tropsch water effluent for sustainable hydrogen production. *Catal Today*. 2021;367:239-247. doi:10.1016/j.cattod.2020.04.024
23. Marchese M, Gandiglio M, Lanzini A. A circular approach for making Fischer-Tropsch e-fuels and e-chemicals from biogas plants in Europe. *Front Energy Res*. 2021;9:773717. doi:10.3389/fenrg.2021.773717
24. Cooney R, de Sousa DB, Fernández-Ríos A, et al. A circular economy framework for seafood waste valorisation to meet challenges and opportunities for intensive production and sustainability. *J Clean Prod*. 2023;392:136283. doi:10.1016/j.jclepro.2023.136283
25. Bejarano P-AC, Rodriguez-Miranda J-P, Maldonado-Astudillo RI, Maldonado-Astudillo YI, Salazar R. Circular economy indicators for the assessment of waste and by-products from the palm oil sector. *Processes*. 2022;10(5):903. doi:10.3390/pr10050903
26. Todic B, Nowicki L, Nikacevic N, Bukur DB. Fischer-Tropsch synthesis product selectivity over an industrial iron-based catalyst: effect of process conditions. *Catal Today*. 2016;261:28-39. doi:10.1016/j.cattod.2015.09.005
27. Barrios AJ, Gu B, Luo Y, et al. Identification of efficient promoters and selectivity trends in high temperature Fischer-Tropsch synthesis over supported iron catalysts. *Appl Catal B Environ*. 2020;273: 119028. doi:10.1016/j.apcatb.2020.119028
28. Ail SS, Dasappa S. Biomass to liquid transportation fuel via Fischer Tropsch synthesis – technology review and current scenario. *Renew Sustain Energy Rev*. 2016;58:267-286. doi:10.1016/j.rser.2015.12.143
29. Chun DH, Bae G, Min R, et al. Brief review of precipitated iron-based catalysts for low-temperature Fischer-Tropsch synthesis. *Top Catal*. 2020;63(2):793-809. doi:10.1007/s11244-020-01336-6
30. Chun DH, Park JC, Hong SY, et al. Highly selective iron-based Fischer-Tropsch catalysts activated by CO2-containing syngas. *J Catal*. 2014;317:135-143. doi:10.1016/j.jcat.2014.06.014
31. Wang D, Chen B, Duan X, Chen D, Zhou X. Iron-based Fischer-Tropsch synthesis of lower olefins: the nature of χ-Fe5C2 catalyst and why and how to introduce promoters. *J Energy Chem*. 2016;25(6): 911-916. doi:10.1016/j.jechem.2016.11.002
32. Riyahin M, Atashi H, Kalhori DM. Effect of process conditions on Fischer-Tropsch synthesis product selectivity over an industrial iron-based catalyst in slurry reactor. *Pet Sci Technol*. 2016;34(14): 1211-1218. doi:10.1080/10916466.2016.1193521
33. Gorimbo J, Muleja A, Liu X, Hildebrandt D. Fischer-Tropsch synthesis: product distribution, operating conditions, iron catalyst deactivation and catalyst speciation. *Int J Ind Chem*. 2018;9:317-333. doi:10.1007/s40090-018-0161-4
34. Liu Y, Teng BT, Guo XH, et al. Effect of reaction conditions on the catalytic performance of Fe-Mn catalyst for Fischer-Tropsch synthesis. *J Mol Catal A Chem*. 2007;272(1–2):182-190. doi:10.1016/j.molcata.2007.03.046
35. Feyzi M, Irandoust M, Mirzaei AA. Effects of promoters and calcination conditions on the catalytic performance of iron-manganese catalysts for Fischer-Tropsch synthesis. *Fuel Process Technol*. 2011;92(5): 1136-1143. doi:10.1016/j.fuproc.2011.01.010
36. Cheng K, Virginie M, Ordomsky VV, et al. Pore size effects in high-temperature Fischer-Tropsch synthesis over supported iron catalysts. *J Catal*. 2015;328:139-150. doi:10.1016/j.jcat.2014.12.007
37. Suo H, Wang S, Zhang C, et al. Chemical and structural effects of silica in iron-based Fischer-Tropsch synthesis catalysts. *J Catal*. 2012; 286:111-123. doi:10.1016/j.jcat.2011.10.024
38. Dieterich V, Buttler A, Hanel A, Spliethoff H, Fendt S. Power-to-liquid via synthesis of methanol, DME or Fischer-Tropsch-fuels: a review. *Energ Environ Sci*. 2020;13(10):3207-3252. doi:10.1039/d0ee01187h
39. Cookson DJ, Smith BE. Determination of structural characteristics of saturates from diesel and kerosene fuels by carbon-13 nuclear magnetic resonance spectrometry. *Anal Chem*. 1985;57(4):864-871. doi:10.1021/ac00281a020
40. Sing KSW, Everett DH, Haul RAW, et al. Reporting physisorption data for gas/solid systems with special reference to the determination of surface area and porosity. *Pure Appl Chem*. 1985;57(4):603-619.
41. Espinoza RL, Steynberg AP, Jager B, Vosloo AC. Low temperature Fischer-Tropsch synthesis from a Sasol perspective. *Appl Catal Gen*. 1999;186(1–2):13-26. doi:10.1016/S0926-860X(99)00161-1
42. Bukur DB, Todic B, Elbashir N. Role of water-gas-shift reaction in Fischer-Tropsch synthesis on iron catalysts: a review. *Catal Today*. 2016;275:66-75. doi:10.1016/j.cattod.2015.11.005
43. James OO, Chowdhury B, Mesubi MA, Maity S. Reflections on the chemistry of the Fischer-Tropsch synthesis. *RSC Adv*. 2012;2(19): 7347-7366. doi:10.1039/c2ra20519j
44. Paalanen PP, Weckhuysen BM. Carbon pathways, sodium-sulphur promotion and identification of iron carbides in iron-based Fischer-Tropsch synthesis. *ChemCatChem*. 2020;12(17):4202-4223. doi:10.1002/cctc.202000535
45. Nadkarni RAK. *Spectroscopic Analysis of Petroleum Products and Lubricants*. ASTM International; 2011. doi:10.1520/MONO9-EB

SUPPORTING INFORMATION

Additional supporting information can be found online in the Supporting Information section at the end of this article.

How to cite this article: Stanke A, Lazdovica K, Laipniece L. Evaluation of the Fischer-Tropsch synthesis product selectivity over iron-based silica-supported catalyst under mild temperatures. *Environ Prog Sustainable Energy*. 2024;43(3): e14335. doi:10.1002/ep.14335

2. pielikums

Appendix 2

Stanke A., Lazdovica K., Gaile A., Laipniece L.

Fischer-Tropsch synthesis product selectivity over silica-supported iron-based catalyst: Effect of K/Fe ratio.

Fuel, **2025**, 387, 134399.

https://doi.org/10.1016/j.fuel.2025.134399

Fuel 387 (2025) 134399

Contents lists available at ScienceDirect

Fuel

journal homepage: www.elsevier.com/locate/fuel

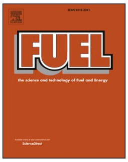

Full Length Article

Fischer-Tropsch synthesis product selectivity over silica-supported iron-based catalyst: Effect of K/Fe ratio

Agija Stanke *, Kristine Lazdovica, Anastasija Gaile, Lauma Laipniece

Riga Technical University, Faculty of Natural Sciences and Technology, Institute of Chemistry and Chemical Technology, Paula Valdena 3, Riga LV-1048, Latvia

ARTICLE INFO

Keywords:
CO hydrogenation
Fischer-Tropsch synthesis
Iron catalyst
Potassium

ABSTRACT

In this study, silica-supported iron-based catalysts with/without potassium promoter were tested for Fischer-Tropsch synthesis (FTS) at 280 °C and 20 bar. This paper discusses the effect of potassium to iron (K/Fe) ratio in the range from 0 to 0.06 on the selectivity and composition of the FTS gaseous phase, liquid hydrocarbon phase, solid phase (waxes), and aqueous phase products. The K/Fe ratio had minimal impact on the yield of liquid hydrocarbons, whereas the average flow rate of waxes peaked at K/Fe = 0.02. The amount of aqueous phase declined as the K/Fe ratio increased. Potassium contributed to the chain growth, which in turn lead to long-chain paraffin accumulation in the pores of the catalyst. Consequently, diffusion limitations lead to lower CO conversion levels for potassium-promoted catalysts reaching a minimum at K/Fe = 0.02. Results showed that an increase in the K/Fe ratio enhanced the formation of oxygenates and olefins. Potassium suppressed the rate of 1-olefins isomerization to internal olefins. The alcohol content in the aqueous phase followed a parabolic trend, reaching a minimum at K/Fe = 0.04. Methanol was the predominant alcohol for unpromoted catalyst, whereas ethanol became the primary alcohol with potassium-promoted catalysts.

1. Introduction

Since 2000, global energy consumption has increased by about a third, and it is predicted that it will continue to increase in the foreseeable future. Approximately 80 % of the consumed energy is based on fossil fuels – crude oil, coal and natural gas. As a result, among the most serious challenges of the 21st century are fighting against the increase in greenhouse gas concentrations and meeting the energy demand [1,2]. Replacement of conventional fossil fuels with sustainable alternatives is crucial to address these challenges.

Biomass-derived syngas is a sustainable precursor to synthetic fuels. Direct synthesis of hydrocarbon fuels through biomass gasification combined with Fischer-Tropsch synthesis (FTS) is a way to reduce dependence on oil and safeguard the environment [3]. FTS is a catalytic-polymerization process in which carbon monoxide and hydrogen molecules are converted into a broad spectrum of hydrocarbons according to the following equation [4]:

$$2nH_2 + nCO \rightarrow -(CH_2)_n- + nH_2O \qquad (1)$$

The main products are paraffins and olefins, while small amounts of oxygenates are also formed. The goal of FTS is the synthesis of so-called syncrude (mixture of liquid and solid-like C_{5+} hydrocarbons), while the gas phase and aqueous phase are mainly considered by-products [5]. FTS effluent (aqueous phase) containing oxygenates, and FTS exhaust (gas phase) consisting mainly of unreacted CO, H_2, CO_2, N_2 and short-chain hydrocarbons (C_1-C_4) may have a significant impact on the environment and require post-treatment [6,7].

The implementation of the circular economy principle in FTS effluent and exhaust management offers an efficient and sustainable long-term strategy to address the environmental challenges linked to this industrial process. The concept of circular economy aims to minimize waste generation and improve resource efficiency through the circularity of carbon material. The principle promotes the valuation of waste and by-products, as well as resource recovery, reuse, recycling and remanufacturing [6,8]. Depending on the composition there are different approaches to managing FTS exhaust: light hydrocarbons can be separated from the FTS exhaust, the FTS tail gas can be burnt as fuel in gas turbines and boilers or the FTS exhaust can be recycled back to the synthesis gas preparation section or back to the FTS reactor [9]. Similarly, there are different approaches regarding FTS water effluent

---

* Corresponding author.
E-mail addresses: agija.stanke@rtu.lv (A. Stanke), kristine.lazdovica@rtu.lv (K. Lazdovica), anastasija.gaile@rtu.lv (A. Gaile), lauma.laipniece@rtu.lv (L. Laipniece).

https://doi.org/10.1016/j.fuel.2025.134399
Received 21 October 2024; Received in revised form 14 December 2024; Accepted 13 January 2025

management. Depending on the concentration of the organic compounds in the FTS product water, recovery of the oxygenates can be performed. If the concentration of oxygen compounds is low and the recovery of these compounds cannot be justified, the water must be treated to reduce the environmental impact [10,11].

The yield of the synthesis and product distribution is highly dependent on the catalyst and the reaction conditions. Both cobalt- and iron-based catalysts are used in industrial-scale FTS, with iron catalysts being the most commonly used due to their easy availability and relatively low cost [12]. In addition, iron-based catalysts can be disposed of in landfills (if acceptable environmental standards are met) whereas spent cobalt-based catalysts must be reclaimed [13].

Due to their potential activity for a water–gas-shift (WGS) reaction, which helps to counterbalance the excess or lack of hydrogen in the feed, iron-based catalysts can adapt to a wide range of H_2/CO ratios. This makes them an attractive choice for utilizing CO-rich syngas from biomass [4]. Compared to cobalt-based catalysts, iron-based catalysts are much more flexible in terms of process parameters, they can be employed in low-temperature FTS (200–250 °C), as well as in medium-temperature FTS (250–300 °C) and high-temperature FTS (300–360 °C) [14,15]. Higher temperatures lead to increased reaction rates and higher conversion rates, however, at the same time C_{2+} product selectivity decreases [16]. Introduction of promoters is expected to enhance the yield of hydrocarbons effective for the production of transportation fuels (C_{5+} hydrocarbons and/or light olefins) [17].

Potassium is one of the most commonly used promoters for iron-based catalysts. The overall effects of potassium on the performance of iron-based FTS catalysts are widely studied over different catalyst systems. Most studies have focused on bulk catalysts often containing multiple promoters [18–24], although various supported catalysts have also been studied [25–28]. Supported catalysts offer improved mechanical strength, increased surface area and iron dispersion, as well as more effective utilization of the active phase and promoters [29].

Results regarding the effect of potassium on FTS activity are inconsistent. Some studies indicate that potassium has a negligible effect on FTS activity [18,24] or suppresses FTS activity [19], while others have reported a volcano-like dependence of FTS activity with increasing potassium loading [20,21,26,27]. Potassium has been shown to suppress the production of methane and increase the rate of WGS reaction [26]. In the WGS reaction, H_2O and CO are consumed whereas H_2 and CO_2 are produced. Thus, potassium enhances CO_2 selectivity. The addition of potassium has been reported to improve the adsorption of CO, while decreasing the adsorption of H_2, contributing to chain propagation reaction and enhancing olefin selectivity [16,22,24,30]. In addition, Dictor and Bell [19] observed that Fe_2O_3 promotion with potassium enhances the formation of branched hydrocarbons and aldehydes. However, the findings on the effect of potassium on oxygenate selectivity have been inconsistent across different studies. While Dictor and Bell [19] have reported that methanol is the dominant oxygenate and the addition of potassium reduces its formation, Ma et al. [28] have reported that ethanol is the dominant oxygenate, followed by propanol, methanol, butanol and pentanol in turn. The results indicated that potassium suppresses the formation of methanol and enhances the formation of higher-molecular-weight alcohols. Y. Yang et al. [20] investigated the effects of potassium content on the iron-manganese catalyst and observed a parabolic trend in oxygenate selectivity with increasing potassium loading. Variations in experimental conditions and/or different catalytic systems contribute to the inconsistent results observed in the research findings.

Even though potassium-promoted iron-based catalysts have been extensively studied, there are limited results on the effect of the K/Fe ratio on all FTS products, especially those considered as by-products. The present work focuses on a systematic understanding of the effects of the K/Fe ratio in silica-supported iron-based catalysts on the selectivity of all product phases under industrially relevant operation conditions (e.g. 280 °C, 20 bar). Given the importance of implementing circular economy principles in FTS, particular attention is turned to the effects of the K/Fe ratio on the FTS effluent (aqueous phase). Silica was chosen as catalyst support to facilitate the optimal use of iron and potassium by improving dispersion and enhancing accessibility for reactants and to obtain the maximum yield of C_{5+} hydrocarbons. Zhao et al. [17] studied the effect of the interaction between potassium and different structural promoters on FTS performance in iron-based catalysts. They observed that potassium-promoted catalysts containing SiO_2 were more effective from a hydrocarbon selectivity view and yielded the lowest CH_4 and the highest C_{5+} products. Similarly, the interaction between potassium and SiO_2 exists in silica-supported catalysts.

2. Materials and methods

2.1. Preparation of catalysts

A batch of SiO_2 commercial catalyst support granules (catalog number 44740) was purchased from *Thermo Fisher Scientific*. Manufacturer-given specifications for catalyst support are provided in Supplementary information (Table S1 and Table S2). 30 g of the SiO_2 granules were immersed in 80 mL 0.8 M $Fe(NO_3)_3$ aqueous solution. The solution with immersed granules was stirred at 50 °C for 5 h, filtered, and then granules were dried at 110 °C for 2 h, followed by calcination at 550 °C for 5 h. The obtained catalyst was named K-0 [31]. The iron concentration of the K-0 catalyst, determined by using a *Rigaku Supermini Wavelength* X-ray dispersive fluorescence spectrometer, was 11.4 wt %.

K-2, K-4 and K-6 catalysts were prepared by impregnation of K-0 with aqueous solutions of KNO_3. The concentrations of the impregnating solutions were calculated to obtain K/Fe = 0.02, K/Fe = 0.04 and K/Fe = 0.06 atomic ratios in the final catalysts. After impregnation, the samples were dried at 110 °C for 2 h and calcined at 550 °C for 5 h.

The catalyst granules were crushed and sieved to acquire particles in the range of 1.0 – 2.0 mm.

2.2. Catalyst characterization

The textural characteristics of catalysts were analyzed using N_2 physical adsorption–desorption isotherms obtained with a *Quantachrome Instruments Nova 1200 E-Series* surface and porosity analyzer at − 196 °C. Prior to analysis, the samples were degassed at 180 °C for 8 h. Specific surface area was estimated from the adsorption data recorded at p/p_0 ratios from 0.05 to 0.30 with differentiated step from 0.025 to 0.05 using the Brunauer-Emmett-Teller (BET) method. The pore volume and average pore diameter were determined from desorption branches of the isotherms using the Barrett-Joyner-Halenda (BJH) method. The equilibration time of adsorption and desorption was 60 s. The crystalline structure of catalysts before and after the FTS reaction was characterized using a *Bruker AXS D8 ADVANCE* powder X-ray diffractometer with Cu (Kα) radiation (λ = 1.5406 Å) operated at 40 kV and 40 mA. Samples were scanned at 1° min^{-1} from 10° to 75° with a step size 0.02°.

2.3. Catalyst testing and product analysis

FTS experiments were performed in a *PID-Micromeritics Microactivity-Effi* unit. Typically, 0.90 g of catalyst without dilution was loaded in the stainless steel fixed-bed reactor with an inner diameter of 9.1 mm. The catalyst was *in-situ* carbidized in pure CO at atmospheric pressure for 24 h at 350 °C with gas hourly space velocity (GHSV) = 1290 NmL $g^{-1}h^{-1}$. After the activation, the reaction was performed for 72 h at 280 °C and 20 bar in the H_2:CO:N_2 (molar ratio 4:2:1) with GHSV = 4515 NmL $g^{-1}h^{-1}$. Three separate mass flow controllers were used to regulate the flows of H_2, N_2 (*Bronkhorst El-Flow Select*) and CO (*Bronkhorst mini Coriflow*). K-type thermocouple positioned in the center of the catalyst bed was used to control the reaction temperature. Nitrogen was used as an internal standard for the calculation of conversion rate and product selectivity.

The reaction exit gas passed through a hot trap (120 °C) and a cold trap (5 °C) where reactor effluent was cooled down and heavy waxes, liquid hydrocarbons, water and gases were separated. The waxes were accumulated in the hot trap, liquid products were accumulated in the cold trap. Liquid products from the cold trap were collected once every 24 h, whereas waxes from the hot trap were collected after 72 h. Condensed products were quantified and analyzed off-line.

The gas phase was analyzed on-line using a *Shimadzu Nexis GC-2030* gas chromatograph. Transfer line between the reactor and the chromatograph was maintained at 200 °C to avoid product condensation. Analysis of H_2, N_2, CO, CH_4 and CO_2 was performed using two *Restek Porapak Q 80/100* columns (6 ft, 2 mmID), a *Restek Molesieve 5A 60/80* column (6 ft, 2 mmID) set up in a row and thermal conductivity detector (TCD). Helium was used as carrier gas. The column temperature was 55 °C. The flow pressure of the carrier gas was 200 kPa. A sample volume of 250 μL was injected using sample loop. Gaseous hydrocarbons were separated in a *Restek Rt–Q–Bond* (30 m, 0.53 mmID, 20 μm) column and analyzed by a flame ionization detector (FID). The column temperature was initially maintained at 55 °C for 12 min, then increased to 130 °C with a rate of 10c min^{-1}, then increased to 180 °C with a rate of 5 °C min^{-1}. The final temperature was maintained for 35 min. Helium carrier gas flow was 9.48 mL min^{-1}. A sample volume of 250 μL was injected using sample loop. The CO conversion rate was defined as the mole percentage of CO reacted (Eq. (2)). Product selectivity was defined as the mole percentage of carbon converted into the specific product during FTS (Eqs. (3)–(5)).

$$\text{CO conversion } X_{CO} = \frac{CO_{in} - CO_{out}}{CO_{in}} \bullet 100\% \tag{2}$$

$$CO_2\text{selectivity } S_{CO_2} = \frac{CO_{2out}}{CO_{in} - CO_{out}} \bullet 100\% \tag{3}$$

$$C_n\text{selectivity } S_{C_n} = \frac{C_{n\ out}}{CO_{in} - CO_{out}} \bullet 100\% \tag{4}$$

$$C_{5+}\text{ selectivity } S_{C_{5+}} = 100\% - (S_{CO_2} + S_{C_1} + S_{C_2} + S_{C_3} + S_{C_4}) \tag{5}$$

herein, CO_{in} and CO_{out}: the molar flow rate of CO at the inlet and outlet; $CO_{2\ out}$: the molar flow rate of CO_2 at the outlet; $C_{n\ out}$: the molar flow rate of hydrocarbons with n = 1–4 carbon atoms at the outlet.

Liquid FTS products were analyzed off-line by a *Shimadzu Nexis GC-2030* gas chromatograph equipped with *Restek Rtx®-5MS* column (30 m, 0.25 mmID, 0.1 μm), FID detector and *Shimadzu GCMS-QP2020 NX* mass spectrometer (MS). No sample preparation was needed prior to analysis. A sample volume of 1 μL was injected into split/splitless injector at 300 °C with a split ratio of 100:1 using *Shimadzu AOC-20i* auto injector. MS was operated in scan mode (10 – 500 Da). Helium carrier gas at a flow of 1.47 mL min^{-1} was used. For the analysis of the liquid hydrocarbon phase the column was operated with an initial temperature of 30 °C held for 5 min then increased to 300 °C with a rate of 10 °C min^{-1} and held for 5 min. For the analysis of the aqueous phase the column was operated with an initial temperature of 30 °C held for 5 min then increased to 300 °C with a rate of 20 °C min^{-1} and held for 3 min. Linear alcohols and acetone in the aqueous phase were quantified using external calibration.

Standard 1D ^1H and ^{13}C solution-state nuclear magnetic resonance (NMR) spectra were taken of the FTS liquid hydrocarbons and waxes using a *Bruker Avance 300 (300 MHz)* or *Bruker Avance 500 (500 MHz)* nuclear magnetic resonance spectrometer. Samples were diluted in deuterated chloroform ($CDCl_3$), the solubility in $CDCl_3$ was good and no insoluble residues were observed. Residual solvent signals were used as the chemical shift reference ($\delta_H = 7.26$; $\delta_C = 77.16 \pm 0.06$). ^1H NMR and ^{13}C NMR peak assignments in $CDCl_3$ solvent used to study FTS products are provided in Supplementary information (Table S3 and Table S4).

The average hydrocarbon chain length N_c was calculated from ^1H NMR spectra using a modified Cookson approach [32,33]:

$$[\textit{Total C within chain}] = [A] + [B] + [E]/2 + [G]/2 \tag{6}$$

$$[\textit{Total C at chain ends}] = [C]/2 + [D]/2 + [F]/3 + [H]/3 \tag{7}$$

$$N_c = 2 \bullet \left(\frac{[\text{Total C } \textit{within} \text{ chain}]}{[\text{Total C at chain } \textit{ends}]} \right) + 2 \tag{8}$$

where [A] is the intensity of the signal at ~ 5.82 ppm ($CH_2 = \mathbf{C\underline{H}}$–), [B] is the intensity of the signal at ~ 5.42 ppm (–$\mathbf{C\underline{H}}$ = $\mathbf{C\underline{H}}$–), [C] is the intensity of the signal at ~ 4.95 ppm ($\mathbf{C\underline{H_2}}$ = CH–), [D] is the intensity of the signal at ~ 3.65 ppm (–$\mathbf{C\underline{H_2}}$-OH), [E] is the intensity of the signal at ~ 2.01 ppm ((CH_2 = CH-$\mathbf{C\underline{H_2}}$–)), [F] is the intensity of the signal at 1.60–1.65 ppm (–CH = CH-$\mathbf{C\underline{H_3}}$), [G] is the intensity of the signal at ~ 1.27 ppm (–$\mathbf{C\underline{H_2}}$–); [H] is the intensity of the signal at ~ 0.89 ppm (–$\mathbf{C\underline{H_3}}$).

FTS liquid hydrocarbons, waxes and aqueous phase products were analyzed by Fourier Transform Infrared Spectroscopy (FTIR) using *PerkinElmer Spectrum 100* spectrometer connected with *Universal Attenuated Total Reflectance* (UATR) accessory. No sample preparation was needed prior to analysis. Spectra were recorded from 650 to 4000 cm^{-1} with a resolution of 4 cm^{-1}. The characteristic absorptions of the functional groups employed to examine FTS products are provided in Supplementary information (Table S5). Methanol, ethanol and water were quantified using external calibration with standards prepared volumetrically in distilled water.

The elemental analyses of waxes were performed by combustion analysis using a *Euro Vector EA 3000* CHN/O analyzer. The amount of oxygen was calculated by the difference:

$$O(wt.\%) = 100\% - (C\% + H\% + N\%) \tag{9}$$

where C%, H%, N% are the weight percents of carbon, hydrogen and nitrogen.

Acidity analysis of the liquid hydrocarbon phase and the aqueous phase was quantified by the KOH titration method. The method was based on EN 14104 standard method for the determination of acid value in light-coloured Fatty Acid Methyl Esters. For determination of acid value, samples were weighed in an Erlenmeyer flask and dissolved in isopropanol. After the addition of 1 % phenolphthalein solution in ethanol, samples were titrated with potassium hydroxide standard solution in ethanol (0.050 M) to persisting faint purple coloration. The acid value (AV) in mg KOH/g was calculated according to the formula:

$$AV = \frac{V_{KOH} \times c_{KOH} \times 56.1}{m_s} \tag{10}$$

where V_{KOH} – volume of potassium hydroxide standard solution (mL); c_{KOH} – concentration of potassium hydroxide standard solution (mol/L); m_s – mass of the sample (g).

3. Results and discussion

3.1. Catalyst characterization

The textural properties of the support and catalysts are summarized in Table 1. The N_2 physisorption isotherms and corresponding pore size

Table 1

N_2 -physisorption results of the catalyst support and catalysts.

Sample	BET surface area (m^2/g)	Total pore volume (cm^3/g)	Average pore diameter (nm)
SiO_2	213	0.88	16.5
K-0	207	0.79	15.3
K-2	200	0.78	15.4
K-4	197	0.76	15.5
K-6	194	0.76	15.7

distribution patterns of the catalyst support (SiO_2) and K-0, K-2, K-4, K-6 catalysts are shown in Fig. S1. Typical IUPAC type IV isotherms with H1 hysteresis loop which are characteristic of mesoporous silica with a narrow distribution of cylindrical or tubular pores [34] are observed for all samples. As shown in Table 1, after impregnation with iron and potassium, pore volume, average pore diameter and specific surface area decreased compared to pure catalyst support. These results indicate that iron and potassium species are localized in the pores of the support and that smaller pores might be blocked during the impregnation step.

The XRD patterns of catalysts before FTS reaction are shown in Fig. 1A. The broad peak observed at $2\theta = 20–25°$ corresponds to amorphous silica. All catalysts exhibit the presence of α-Fe_2O_3 (hematite) (PDF 01-071-5088). The impregnation of potassium did not affect the hematite crystalline phase detected by XRD. No peaks assigned to potassium species are observed which is likely due to their high dispersion and low contents.

To better understand the activity of the samples, the catalysts were analyzed by XRD after FTS.

The XRD patterns of the used catalysts are shown in Fig. 1B. The patterns exhibit several peaks at $2\theta = 35$-$52°$, which can be attributed to a mixture of iron carbides. Due to weak diffraction signals, it is not possible to distinguish the type of iron carbide. Besides these peaks, the XRD patterns of K-2, K-4 and K-6 after FTS exhibit peaks at $2\theta = 21.4°$ and $2\theta = 23.9°$, which can be identified as paraffin wax (–CH_2-) (PDF 40–1995). UATR-FTIR confirmed the presence of hydrocarbons on the catalysts K-2, K-4 and K-6. Absorption bands corresponding to stretching vibrations of –CH_2- (2916 cm^{-1}) and –CH_3 (2849 cm^{-1}), as well as absorption bands corresponding to bending vibrations of –CH_2- (1427 cm^{-1}) and –CH_3 (1462 cm^{-1}), are observed in the FTIR spectra of K-2, K-4 and K-6 whereas no such absorption bands are observed in the spectrum of K-0 (Fig. 2).

The obtained results indicate that the addition of potassium promotes the accumulation of waxes on the catalyst. According to the literature it is known that during low-temperature FTS long-chain paraffins accumulate in the pores of the catalyst and the characteristic of the reaction shifts from a two-phase gas–solid reaction to a three-phase gas–liquid-solid reaction. This increases the diffusion length – when macro pores are filled, synthesis gas can only be transported by diffusion *via* liquid phase [35,36]. The effectiveness factor of the reaction rate regarding to pore diffusion for catalysts with particle size in the millimeter range becomes less than one. This unwanted effect is usually unavoidable [36].

3.2. Effect of K/Fe ratio on the FTS performance

The effect of potassium on the FTS performance after 72 h on stream is shown in Table 2. The average flow rates of the FTS gaseous phase, liquid hydrocarbon phase, solid phase (waxes) and aqueous phase as a function of the K/Fe ratio in catalysts are shown in Fig. 3. Catalytic performance with time on stream and the calculation of carbon balances after FTS are included in the Supplementary information (Fig. S2 and Table S6). CO conversion showed a parabola-like trend reaching a minimum conversion value of 16.7 % with K-2 catalyst. The drop in CO conversion can be explained by the accumulation of waxes in the catalyst pores which creates internal mass transfer limitations and reduces the effective rate of CO consumption [37]. Potassium as a promoter is reported to improve the adsorption of CO in terms of both bonding strength and adsorption quality [26]. As a result, an increase in potassium content leads to faster CO adsorption and dissociation and subsequently CO conversion increases. The observed CO conversion in our study aligns with data reported by Cheng et al. [38] who investigated the effect of pore size on the performance of silica-supported iron-based catalysts, reporting CO conversion rates between 0 and 30 % ($T = 300$ °C, $P = 20$ bar, $H_2/CO = 2.1$). Similarly, our results are in line with those of Farias et al. [25] who investigated the influence of potassium addition ($K/Fe = 0.06, 0.12, 0.18$) on silica-supported, copper-promoted iron-based catalysts, where CO conversion ranged from 5 to 52 % at 270 °C, 20 atm, and an H_2/CO ratio of 1.0.

CH_4 selectivity decreased from 21.6 % for unpromoted catalyst to 8.5 % for K-6 catalyst. The results are consistent with many previous studies on the role of potassium on the adsorption of CO and H_2 (e.g. potassium strengthens CO adsorption and weakens H_2 adsorption thus promoting chain growth and decreasing CH_4 selectivity) [16,22,24,30].

The lowest flow rate of gaseous phase products was at $K/Fe = 0.02$ (Fig. 3). Increasing the amount of potassium contributed to the increase in average flow rate of gaseous phase products primary due to a significant increase in CO_2 selectivity. All reaction products passed through hot and cold traps, however small part of C_{5+} products remained in the gaseous state and were carried along the stream. GC analysis of gaseous phase showed reaction products with chain length up to C_7. Distribution

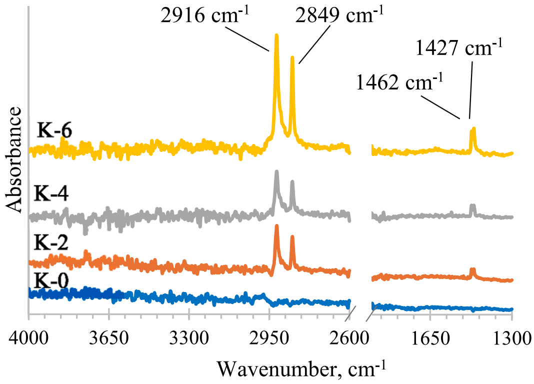

Fig. 2. UATR-FTIR spectra of spent catalysts.

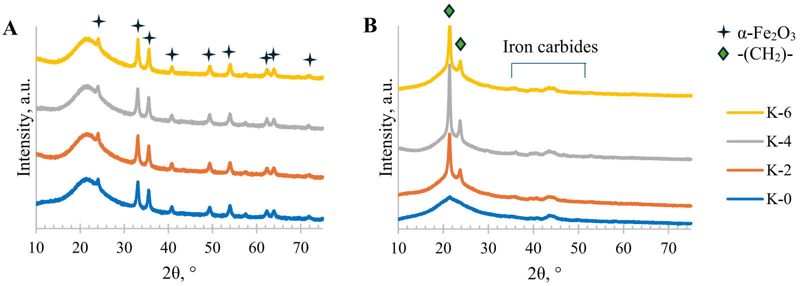

Fig. 1. XRD patterns of as-prepared catalysts (A) and spent catalysts (B).

Table 2
CO conversion and product selectivity of K-0, K-2, K-4 and K-6 catalysts after 72 h.

Catalyst	CO conversion (%)	CO_2 selectivity (%)	CH_4 selectivity (%)	C_2-C_4 selectivity (%)	C_{5+} selectivity (%)
K-0	20.4	12.3	21.6	21.3	44.8
K-2	16.7	16.1	12.6	19.4	51.9
K-4	17.9	17.8	9.3	17.6	55.3
K-6	21.2	18.7	8.5	17.8	55.0

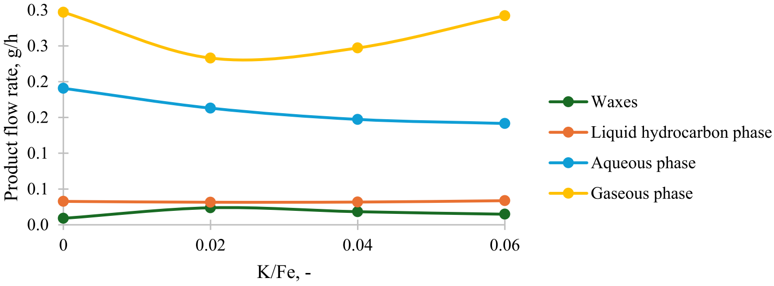

Fig. 3. Influence of potassium on the flow rates of solid (waxes), liquid hydrocarbon, aqueous and gaseous phase products.

of gaseous C_2-C_7 hydrocarbons is included in the Supplementary information (Fig. S3). An increase in K/Fe ratio contributed to the formation of unsaturated products. Given the low CO conversion level and low selectivity for C_1-C_4 products, the most effective options for exhaust management could be recycling the exit gas either back to the synthesis gas preparation section or back to the FTS reactor.

The addition of potassium had the greatest effect on the average flow rates of the aqueous phase and solid phase. The amount of the aqueous phase showed steady decline with the increase in K/Fe ratio in catalysts. The decreased flow rate of aqueous phase together with the increase in CO_2 selectivity indicates that potassium promoter enhances the water–gas shift reaction ($CO + H_2O \rightleftarrows CO_2 + H_2$) activity. The average flow rate of waxes showed volcano-like trend with the maximum at K/Fe = 0.02. In the presence of the K-2 catalyst, the amount of waxes increased

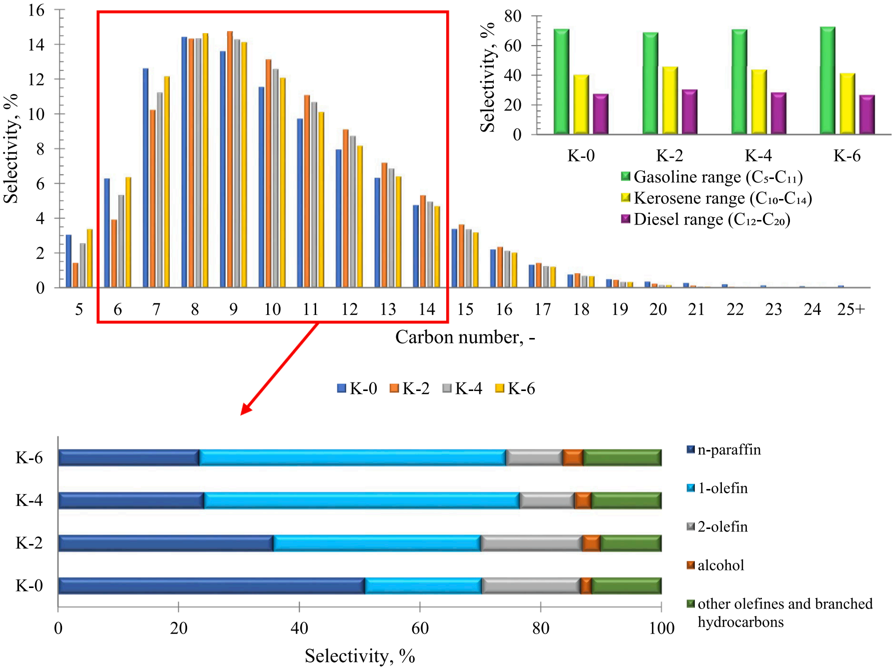

Fig. 4. Evaluation of liquid hydrocarbon phase product selectivity over K-0, K-2, K-4 and K-6.

2.7 times compared to the K-0 catalyst. However, a further increase in the K/Fe ratio started to reduce the formation of waxes. The amount of waxes adsorbed on the catalyst surface is negligible and does not affect the calculated average flow rate of the waxes. The decrease in the amount of wax could be explained by the stronger physisorption of heavier hydrocarbons on the catalyst surface and slower diffusion of long chain hydrocarbons through catalyst pores leading to longer occupation of the active sites.

The K/Fe ratio had practically no effect on the average flow rate of liquid hydrocarbon phase.

3.3. Effect of potassium on the composition of the liquid hydrocarbon phase products

FTS liquid hydrocarbon products with chain lengths corresponding to the gasoline range (C_5-C_{11}), kerosene range (C_{10}-C_{14}) and diesel range (C_{12}-C_{20}) are considered particularly valuable. Despite all FTS reaction products passing through the hot trap to condense waxes, a small part of C_{20+} products reached the cold trap. GC-FID/MS analysis of the FTS liquid hydrocarbon phase showed products with chain lengths from C_5 to C_{36}. Fig. 4 shows the effect of the K/Fe ratio on the liquid hydrocarbon phase. Most of the liquid hydrocarbon phase products (69–73 %) are of chain length corresponding to the gasoline range. Although the potassium promoter alters hydrocarbon chain length selectivity, the total proportion of hydrocarbons with chain lengths corresponding to the gasoline range, kerosene range and diesel range remains almost unchanged.

While potassium has little effect on liquid hydrocarbon yield, the composition of the liquid hydrocarbon phase was greatly altered by K/Fe ratio in catalysts. In the GC–MS/FID chromatogram, it was possible to differentiate *n*-paraffin, 1-olefin, 2-olefin, and *n*-alcohol peaks in the C_6-C_{14} range, thus it was possible to obtain detailed information on the composition of the area. However, it was not possible to obtain acceptable resolution for quantification outside the C_6–C_{14} range. The catalysts with higher potassium loading exhibited a lower hydrogenation activity, the content of *n*-paraffins decreased whereas the content of 1-olefins increased with the addition of potassium. Potassium contributes to chain growth and accordingly also enhances the formation of longer-chain alcohols. Since the solubility of longer-chain alcohols in water is very low, the content of oxygenates in liquid hydrocarbon phase increased with increased K/Fe ratio.

In order to evaluate the effect of potassium on the composition of the entire liquid hydrocarbon phase, the samples were analyzed using NMR and FTIR spectroscopy methods. The ^{13}C NMR spectra of liquid hydrocarbon phase (Fig. S4-S7) showed signals at ~ 14.1, 22.7, ~32.0, ~29.3 and 29.7 ppm corresponding to α-, β-, γ-, δ-, ε- carbons in *n*-alkanes. Low-intensity resonances observed between 20 and 40 ppm are due to branched alkanes. Methylene group adjacent to hydroxyl group of the *n*-alcohols ($R\text{-}\underline{\mathbf{C}}H_2\text{-}OH$) showed low intensity signal at ~ 63.1 ppm. Resonances attributed to 1-olefins are found at ~ 114.0 ($\underline{\mathbf{C}}H_2 = CH–$) and ~ 139.2 ppm ($CH_2 = \underline{\mathbf{C}}H–$). Resonances attributed to 2-olefins are found at ~ 123.6, ~124.5, ~139.0 and 131.7 ppm, confirming the existence of both *cis*- and *trans*-isomers of 2-olefins in the mixture.

The ^{1}H NMR spectra of liquid hydrocarbon phase (Fig. S8-S11) showed resonances for methyl protons at ~ 0.89 ppm and methylene protons at ~ 1.27 ppm. Resonances of low intensity detected at 3.64–3.65 ppm were attributed to oxygenated species. All spectra showed proton signals between 4.6 and 6.0 ppm corresponding to olefinic proton groups. Signals of 1-olefines were found at 4.93–5.00 ppm ($R\text{-}CH = C\underline{\mathbf{H}}_2$) and at 5.82 ppm ($R\text{-}C\underline{\mathbf{H}} = CH_2$), overlapping signals at 5.40–5.42 ppm were attributed to internal olefines ($R\text{-}C\underline{\mathbf{H}} = C\underline{\mathbf{H}}\text{-}R$). It was possible to calculate the ratio of 1-olefins/*n*-paraffins and internal olefins/total olefins in the mixture depending on the catalyst used. The 1-olefin/*n*-paraffin ratio and internal olefin/total olefin ratio were found to be in good agreement with the selectivity results from GC–MS/FID analysis of the liquid hydrocarbon phase products. The average chain length calculated from GC and ^{1}H NMR (Table S7) shows a volcano-like trend with the maximum at K/Fe = 0.02. The observed reduction in hydrocarbon chain length at higher potassium levels may be attributed to increased H_2/CO ratio in the reactor due to enhanced WGS activity.

n-Paraffins and 1-olefins are primary FTS products. Under reaction conditions (1)-olefins are reactive, and readsorption of olefins on growth sites may also lead to primary products whereas adsorption on other sites and secondary reactions of 1-olefins may lead to the formation of branched hydrocarbons *via* alkylidene mechanism [39,40] or isomerization to internal olefins *via* double-bond shift reactions [41]. With an increasing K/Fe ratio the content of olefins in liquid hydrocarbon phase increases whereas the proportion of internal olefins decreases, indicating that potassium suppresses the rate of 1-olefins isomerization.

Results obtained from FTIR spectroscopy coincide with GC–FID/MS and NMR and are included in Supplementary information (Fig. S12). Alcohols were the only detected oxygenates, no signals corresponding to carbonyl and carboxyl groups were found in the GC–MS, ^{1}H NMR, ^{13}C NMR and FTIR spectra.

However, the detection of carboxylic compounds at low levels is difficult due to sensitivity of analytical methods (amount of acids could be under detection limit of NMR and FTIR); the GC–MS method used was not specific to carboxylic acids. Therefore acidity of liquid hydrocarbon phase was quantified by KOH titration method. The determined concentrations of carboxylic acids are 0.008 mmol/g (K-0), 0.010 mmol/g (K-2), 0.016 mmol/g (K-4) and 0.022 mmol/g (K-6). Oxygenates are not primary FTS products. According to literature, alcohol, carboxylic acid and carbonyl group-containing compound formation may be due to parallel reactions that involve CO insertion in the methylene-metal or methyl-metal bond [42]. As potassium strengthens CO adsorption and hinders H_2 adsorption, an increase in the K/Fe ratio enhances the formation of oxygenates. According to the CO insertion mechanism, alcohols are formed *via* hydrogenation of intermediate [RCO-s] whereas acids are formed by the reaction between intermediate acyl [RCO-s] and hydroxyl [OH-s] species [43]. Potassium suppresses hydrogen adsorption, leading to lower hydrogenation activity and subsequently concentration of acids rose with increasing K/Fe ratio in catalysts.

3.4. Effect of K/Fe ratio on the composition of waxes

Heavier waxy products (C_{25+}) have limited value as final products; however, they can be transformed into more desirable products through various post-processing techniques. Hydrocracking can be used to produce liquid fractions (gasoline, kerosene, diesel oil), catalytic cracking can be used to produce light olefins, hydro-isomerization dewaxing technology can be used to produce high-quality lube base oil, etc. [44–46].

NMR analysis of the wax products (Fig. S13-S20) shows that long-chain *n*-paraffins are dominant compounds in the mixture. The average chain length was found to be from 16.99 to 18.91 with maximum at K/Fe = 0.02 (Table 3). It was possible to detect resonances attributed to olefins and oxygenated species from ^{1}H- and ^{13}C NMR spectra as well. The increase in the potassium content contributed to the formation of alcohols in FTS wax. In contrast to the liquid hydrocarbon phase, the majority of olefins in the waxes were internal olefines. This is due to heavier hydrocarbon higher residence time leading to re-

Table 3

Average chain length, 1-olefin/*n*-paraffin ratio and internal olefin/total olefin ratio of waxes, calculated form ^{1} H NMR.

Catalyst	Average chain length	1-Olefin/*n*-paraffin ratio	Internal olefin/ *n*-paraffin ratio	Internal olefin/ total olefin ratio
K-0	16.99	0.0008	0.0063	0.89
K-2	18.91	0.0018	0.0092	0.83
K-4	18.59	0.0068	0.0114	0.63
K-6	18.46	0.0055	0.0114	0.68

adsorption and secondary reactions of 1-olefins. The content of 1-olefins was insignificant at first (K-0), but with increase in K/Fe ratio the amount of 1-olefins as well as internal olefines increased. In addition, the amount of 1-olefins increased more rapidly, so the ratio of internal olefins/total olefins decreased. This again indicates that potassium enhances the formation of olefins and suppresses the extent of 1-olefin isomerization to internal olefins.

Results obtained from FTIR spectroscopy coincide with NMR. FTIR spectra of FTS waxes (Fig. S21) show absorption bands corresponding to O–H and C-O stretching vibrations at 3345 and 1056 cm^{-1} which indicates alcohols. The absorption bands between 2854––3075 cm^{-1} and 1378––1465 cm^{-1} correspond to the methyl- and methylene group stretching and bending vibrations which indicate paraffins and olefins. The presence of absorption band corresponding to $= CH_2$ bending vibrations (909 cm^{-1}) indicates 1-olefins, while the presence of absorption band at 965 cm^{-1} corresponds to $–CH = CH–$ (*trans*) bending vibrations indicating *trans*-olefins. The intensity of absorption band at 720 cm^{-1} ($–CH_2$-) serves as an indicator of hydrocarbon chain length and is used to describe the chain growth. As shown in Fig. 5, an increase in the K/Fe ratio increased the relative amount of olefins and long-chain alcohols in the waxes several times.

The elemental CHN/O analysis data of FTS waxes are reported in Table 4. An increase in the amount of oxygen (O) and a decrease in the amount of hydrogen (H) in the waxes as the K/Fe ratio in the catalyst increases indicate the formation of oxygen-containing and unsaturated and/or longer chain products. This is in good agreement with the results obtained from NMR and FTIR.

3.5. *Effect of potassium on the aqueous phase products*

During FTS, hydrocarbon chain growth occurs simultaneously with water formation. The amount of aqueous phase produced is equivalent to the amount of oil produced. Due to their polar nature, short-chain oxygenates produced in FTS tend to dissolve primarily in the aqueous phase. Vapor–liquid–liquid equilibrium and the type of FTS technology used determines the composition of aqueous phase [47,48].

The aqueous phase obtained using K-0, K-2, K-4 and K-6 catalysts contained oxygenates with chain lengths from C_1 to C_7. The K/Fe ratio in catalysts affected the composition of aqueous phase (Fig. 6). According to the obtained results, potassium promoter suppressed the formation of methanol. Methanol was the main product in aqueous phase for K-0, whereas ethanol was the main product in aqueous phase for the potassium-promoted catalysts. Overall oxygenate selectivity showed parabola-like trend with the lowest content of oxygenates for K-4 catalyst.

Potassium favours formation of longer-chain products, including longer-chain oxygenates. As the carbon chain length of alcohols increased, solubility in water decreased. This leads to lower oxygenate content in aqueous phase for potassium-promoted catalysts compared to K-0. Additionally, potassium enhances CO adsorption which in turn favours the formation of oxygen-containing compounds through a CO-insertion mechanism. As a result, oxygenate content in aqueous phase for K-6 catalyst increases compared to K-2 and K-4 catalysts.

Table 4
Elemental analysis of FTS waxes.

Catalyst	(C)%	(H)%	(N)%	(O)%
K-0	84.6	14.3	0	1.0
K-2	84.5	14.1	0	1.4
K-4	84.5	13.8	0	1.8
K-6	84.4	13.6	0	2.0

Acidity of aqueous phase was quantified by KOH titration method. The determined concentrations of carboxylic acids are 0.024 mmol/g (K-0), 0.029 mmol/g (K-2), 0.047 mmol/g (K-4) and 0.053 mmol/g (K-6). As mentioned in 3.3., both acids and alcohols are formed in reactions involving intermediate [RCO-s]. The activation energy for alcohol formation is lower than that for acids leading to alcohols as the predominant oxygenated products. The addition of potassium lowers the hydrogenation activity, so the formation of alcohols by successful hydrogenation of intermediate [RCO-s] is hindered, while the formation of acids in the reaction of intermediate [RCO-s] and [OH-s] remains more possible.

Since the aqueous phase contains significant amount of oxygenates, the recovery of the oxygenates could be justified and should be performed.

4. Conclusions

The effect of K/Fe ratio in potassium-promoted iron-based silica-supported catalysts on FTS products was investigated in the range of 0–0.06. The results obtained from N_2 adsorption–desorption analysis indicated that iron and potassium species were localized in the pores of SiO_2 and that the impregnation step may have blocked some smaller pores of the support.

Examination of spent catalysts indicated the presence of waxes on the potassium-promoted catalysts. Both K/Fe ratio and internal mass transfer limitations created by the accumulation of waxes in the catalyst pores influenced the CO conversion and product selectivity.

Due to internal mass transfer limitations, CO conversion level for potassium-promoted catalysts were lower compared to unpromoted catalyst, reaching a minimum at K/Fe = 0.02. However, with increasing K/Fe ratio CO conversion level increased due to potassium strengthening CO adsorption.

The K/Fe ratio influenced average flowrate of products. The addition of potassium suppressed the formation of CH_4 and enhanced the formation of longer chain hydrocarbons. K/Fe ratio had minimal influence on liquid hydrocarbon yield, while the lowest gas phase production and the highest wax formation occurred at K/Fe = 0.02. As the K/Fe ratio increased, CO_2 selectivity rose while the amount of aqueous phase decreased, indicating enhanced water–gas shift (WGS) activity.

With higher K/Fe ratios the content of olefins and carboxylic acids

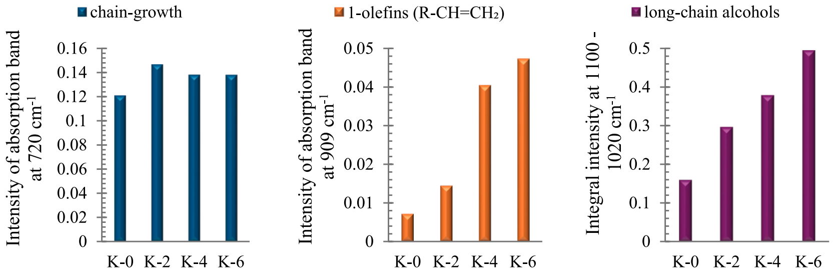

Fig. 5. Evaluation of the composition of FTS waxes.

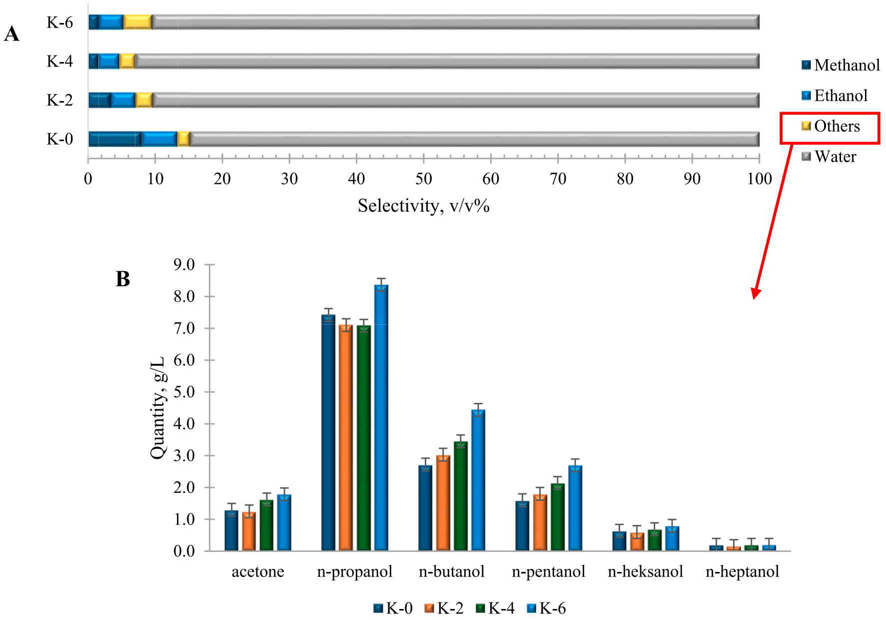

Fig. 6. Evaluation of aqueous phase product selectivity over K-0, K-2, K-4 and K-6 resulting from FTIR and GC–MS analysis.

increased indicating that potassium-promoted catalysts had lower hydrogenation activity. The majority of olefins in liquid hydrocarbon phase were 1-olefins, while in waxes majority were internal olefins due to readsorption and secondary reactions of 1-olefins driven by the longer residence time of heavier hydrocarbons. However, with increasing K/Fe ratio the proportion of internal olefins decreased indicating that potassium suppressed the rate of 1-olefins isomerization.

The increased chain growth probability for K-promoted catalysts resulted in an increase in oxygenate content in liquid hydrocarbon and wax products, while alcohol content in the aqueous phase showed a parabola-like trend with a minimum at K/Fe = 0.04. Methanol was the main alcohol for the K-0 catalyst, while ethanol was the main alcohol for potassium-promoted catalysts.

CRediT authorship contribution statement

Agija Stanke: Writing – review & editing, Writing – original draft, Methodology, Investigation, Funding acquisition, Formal analysis, Conceptualization. **Kristine Lazdovica:** Supervision, Methodology, Investigation, Formal analysis, Conceptualization. **Anastasija Gaile:** Investigation, Formal analysis. **Lauma Laipniece:** Investigation, Formal analysis.

Declaration of competing interest

The authors declare that they have no known competing financial interests or personal relationships that could have appeared to influence the work reported in this paper.

Acknowledgements

This research/publication was supported by Riga Technical University's Doctoral Grant programme.

Appendix A. Supplementary data

Supplementary data to this article can be found online at https://doi.org/10.1016/j.fuel.2025.134399.

Data availability

The authors confirm that the data supporting the findings of this study are available within the article (and/or its supplementary materials).

References

[1] Panzone C, Philippe R, Chappaz A, Fongarland P, Bengaouer A. Power-to-Liquid catalytic CO2 valorization into fuels and chemicals: focus on the Fischer-Tropsch route. J CO2 Util 2020;38:314–47. https://doi.org/10.1016/j.jcou.2020.02.009.

[2] Zhai P, Li Y, Wang M, Liu J, Cao Z, Zhang J, et al. Development of direct conversion of syngas to unsaturated hydrocarbons based on Fischer–Tropsch route. Chem 2021;7:3027–51. https://doi.org/10.1016/j.chempr.2021.08.019.

[3] dos Santos RG, Alencar AC. Biomass-derived syngas production via gasification process and its catalytic conversion into fuels by Fischer–Tropsch synthesis: A review. Int J Hydrogen Energy 2020;45:18114–32. https://doi.org/10.1016/j.ijhydene.2019.07.133.

[4] Gholami Z, Gholami F, Tišler Z, Hubáček J, Tomas M, Bačiak M, et al. Production of Light Olefins via Fischer-Tropsch Process Using Iron-Based Catalysts: A Review. Catalysts 2022;12:174. https://doi.org/10.3390/catal12020174.

[5] Teimouri Z, Abatzoglou N, Dalai AK. Kinetics and Selectivity Study of Fischer–Tropsch Synthesis to C5+ Hydrocarbons: A Review. Catalysts 2021;11:330. https://doi.org/10.3390/catal11030330.

[6] Moreroa M, Malematja TP, Ijoma GN. Integrating the circular economy model into the management and treatment of Fischer–Tropsch effluents—a conversion of waste to energy (biogas) opportunity. IET Renew Power Gener 2024. https://doi.org/10.1049/rpg2.12976.

[7] Wei K, Yue S, Hou X, Jiang Y, Jiang C, Yao Y, et al. Feasibility analysis of Fischer-Tropsch synthesis tail gas as a fuel for solid oxide fuel cells. Int J Energy Res 2022;46:10864–74. https://doi.org/10.1002/er.7887.

[8] Marchese M, Gandiglio M, Lanzini A. A Circular Approach for Making Fischer–Tropsch E-fuels and E-chemicals From Biogas Plants in Europe. Front Energy Res 2021;9. https://doi.org/10.3389/fenrg.2021.773717.

[9] Sun L, Smith R. The Simulation and Analysis of Coal to Liquids Processes 2012:1221–5. https://doi.org/10.1016/B978-0-444-59506-5.50075-4.

[10] Nel RJJ, de Klerk A. Fischer−Tropsch Aqueous Phase Refining by Catalytic Alcohol Dehydration. Ind Eng Chem Res 2007;46:3558–65. https://doi.org/10.1021/ie061555r.

[11] Zoppi G, Pipitone G, Gruber H, Weber G, Reichhold A, Pirone R, et al. Aqueous phase reforming of pilot-scale Fischer-Tropsch water effluent for sustainable hydrogen production. Catal Today 2021;367:239–47. https://doi.org/10.1016/j.cattod.2020.04.024.

[12] Ail SS, Dasappa S. Biomass to liquid transportation fuel via Fischer–Tropsch synthesis – Technology review and current scenario. Renew Sustain Energy Rev 2016;58:267–86. https://doi.org/10.1016/j.rser.2015.12.143.

[13] Martinelli M, Gnanamani MK, LeViness S, Jacobs G, Shafer WD. An overview of Fischer-Tropsch Synthesis: XtL processes, catalysts and reactors. Appl Catal A Gen 2020;608:117740. https://doi.org/10.1016/j.apcata.2020.117740.

[14] Fischer N, Claeys M. In situ characterization of Fischer–Tropsch catalysts: a review. J Phys D Appl Phys 2020;53:293001. https://doi.org/10.1088/1361-6463/ab761c.

[15] Keunecke A, Dossow M, Dieterich V, Spliethoff H, Fendt S. Insights into Fischer–Tropsch catalysis: current perspectives, mechanisms, and emerging trends in energy research. Front Energy Res 2024;12. https://doi.org/10.3389/fenrg.2024.1344179.

[16] Buthelezi AS, ChelseaL T, Heeres HJ, Shozi ML, van de Bovenkamp HH, Ntola P. Fischer-Tropsch synthesis using promoted, unsupported, supported, bimetallic and spray-dried iron catalysts: A review. Results Chem 2024;9:101623. https://doi.org/10.1016/j.rechem.2024.101623.

[17] Zhao G, Zhang C, Qin S, Xiang H, Li Y. Effect of interaction between potassium and structural promoters on Fischer–Tropsch performance in iron-based catalysts. J Mol Catal A Chem 2008;286:137–42. https://doi.org/10.1016/j.molcata.2008.02.019.

[18] Luo M, O`Brien RJ, Bao S, Davis BH. Fischer–Tropsch synthesis: induction and steady-state activity of high-alpha potassium promoted iron catalysts. Appl Catal A Gen 2003;239:111–20. https://doi.org/10.1016/S0926-860X(02)00379-4.

[19] Dictor R. Fischer–Tropsch synthesis over reduced and unreduced iron oxide catalysts. J Catal 1986;97:121–36. https://doi.org/10.1016/0021-9517(86)90043-6.

[20] Yang Y. Effect of potassium promoter on precipitated iron-manganese catalyst for Fischer–Tropsch synthesis. Appl Catal A Gen 2004;266:181–94. https://doi.org/10.1016/j.apcata.2004.02.018.

[21] Yang Y, Zhang H, Ma H, Qian W, Sun Q, Ying W. Effect of alkalis (Li, Na, and K) on precipitated iron-based catalysts for high-temperature Fischer–Tropsch synthesis. Fuel 2022;326:125090. https://doi.org/10.1016/j.fuel.2022.125090.

[22] Liu X, Ma C, Zhao W, Zhang J, Chen J. Effects of promoters on carburized fused iron catalysts in Fischer–Tropsch synthesis. J Fuel Chem Technol 2021;49:1504–12. https://doi.org/10.1016/S1872-5813(21)60159-7.

[23] Martínez del Monte D, Vizcaíno AJ, Dufour J, Martos C. Effect of K, Co and Mo addition in Fe-based catalysts for aviation biofuels production by Fischer–Tropsch synthesis. Fuel Process Technol 2019;194:106102. https://doi.org/10.1016/j.fuproc.2019.05.025.

[24] Wan H, Wu B, Zhang C, Xiang H, Li Y. Promotional effects of Cu and K on precipitated iron-based catalysts for Fischer–Tropsch synthesis. J Mol Catal A Chem 2008;283:33–42. https://doi.org/10.1016/j.molcata.2007.12.013.

[25] Farias FEM, Rabelo Neto RC, Baldanza MAS, Schmal M, Fernandes FAN. Effect of K promoter on the structure and catalytic behavior of supported iron-based catalysts in fischer-tropsch synthesis. Braz J Chem Eng 2011;28:495–504. https://doi.org/10.1590/S0104-66322011000300015.

[26] Tian Z, Wang C, Yue J, Zhang X, Ma L. Effect of a potassium promoter on the Fischer–Tropsch synthesis of light olefins over iron carbide catalysts encapsulated in graphene-like carbon. Catal Sci Technol 2019;9:2728–41. https://doi.org/10.1039/C9CY00403C.

[27] Miller DG, Moskovits M. A study of the effects of potassium addition to supported iron catalysts in the Fischer–Tropsch reaction. J Phys Chem 1988;92:6081–5. https://doi.org/10.1021/j100332a047.

[28] Ma W, Kugler EL, Dadyburjor DB. Potassium Effects on Activated-Carbon-Supported Iron Catalysts for Fischer−Tropsch Synthesis. Energy Fuel 2007;21:1832–42. https://doi.org/10.1021/ef060654e.

[29] Jahangiri H, Bennett J, Mahjoubi P, Wilson K, Gu S. A review of advanced catalyst development for Fischer–Tropsch synthesis of hydrocarbons from biomass derived syn-gas. Catal Sci Technol 2014;4:2210–29. https://doi.org/10.1039/C4CY00327F.

[30] Chun DH, Rhim GB, Youn MH, Deviana D, Lee JE, Park JC, et al. Brief Review of Precipitated Iron-Based Catalysts for Low-Temperature Fischer–Tropsch Synthesis. Top Catal 2020;63:793–809. https://doi.org/10.1007/s11244-020-01336-6.

[31] Stanke A, Lazdovica K, Laipniece L. Evaluation of the Fischer-Tropsch synthesis product selectivity over iron-based silica-supported catalyst under mild temperatures. Environ Prog Sustain. Energy 2024;43. https://doi.org/10.1002/ep.14335.

[32] Cookson DJ, Smith BE. Determination of structural characteristics of saturates from diesel and kerosene fuels by carbon-13 nuclear magnetic resonance spectrometry. Anal Chem 1985;57:864–71. https://doi.org/10.1021/ac00281a020.

[33] Partington R, Clarkson J, Paterson J, Sullivan K, Wilson J. Quantitative carbon distribution analysis of hydrocarbons, alcohols and carboxylic acids in a Fischer–Tropsch product from a Co/TiO2 catalyst during gas phase pilot plant operation. J Anal Sci Technol 2020;11:42. https://doi.org/10.1186/s40543-020-00235-5.

[34] Rouquerol J, Avnir D, Fairbridge CW, Everett DH, Haynes JM, Pernicone N, et al. Recommendations for the characterization of porous solids (Technical Report). Pure Appl Chem 1994;66:1739–58. https://doi.org/10.1351/pac199466081739.

[35] Unglaub C, Jess A. Enhancing Kerosene Selectivity of Fischer–Tropsch Synthesis by Periodical Pore Drainage Via Hydrogenolysis. Catalysis Research 2023;03:1–19. https://doi.org/10.21926/cr.2303022.

[36] Rößler S, Kern C, Jess A. Accumulation of liquid hydrocarbons during cobalt-catalyzed Fischer–Tropsch synthesis - influence of activity and chain growth probability. Catal Sci Technol 2019;9:4047–54. https://doi.org/10.1039/C9CY00671K.

[37] Pöhlmann F, Kern C, Rößler S, Jess A. Accumulation of liquid hydrocarbons in catalyst pores during cobalt-catalyzed Fischer–Tropsch synthesis. Catal Sci Technol 2016;6:6593–604. https://doi.org/10.1039/C6CY00941G.

[38] Cheng K, Virginie M, Ordomsky VV, Cordier C, Chernavskii PA, Ivantsov MI, et al. Pore size effects in high-temperature Fischer–Tropsch synthesis over supported iron catalysts. J Catal 2015;328:139–50. https://doi.org/10.1016/j.jcat.2014.12.007.

[39] Kuipers EW, Vinkenburg IH, Oosterbeek H. Chain length dependence of α-olefin readsorption in Fischer-Tropsch synthesis. J Catal 1995;152:137–46. https://doi.org/10.1006/jcat.1995.1068.

[40] Shi B, Wu L, Liao Y, Jin C, Montavon A. Explanations of the Formation of Branched Hydrocarbons During Fischer–Tropsch Synthesis by Alkylidene Mechanism. Top Catal 2014;57:451–9. https://doi.org/10.1007/s11244-013-0201-4.

[41] Van Der Laan GP, Beenackers AACM. Kinetics and Selectivity of the Fischer-Tropsch Synthesis: A Literature Review. Catal Rev Sci Eng 1999;41:255–318. https://doi.org/10.1081/CR-100101170.

[42] Saeidi S, Najari S, Fazlollahi F, Nikoo MK, Sefidkon F, Klemeš JJ, et al. Mechanisms and kinetics of CO2 hydrogenation to value-added products: A detailed review on current status and future trends. Renew Sustain Energy Rev 2017;80:1292–311. https://doi.org/10.1016/j.rser.2017.05.204.

[43] Teng B, Zhang C, Yang J, Cao D, Chang J, Xiang H, et al. Oxygenate kinetics in Fischer–Tropsch synthesis over an industrial Fe-Mn catalyst. Fuel 2005;84:791–800. https://doi.org/10.1016/j.fuel.2004.12.008.

[44] Farias FEM, Sales FG, Fernandes FAN. Effect of operating conditions and potassium content on Fischer-Tropsch liquid products produced by potassium-promoted iron catalysts. J Nat Gas Chem 2008;17:175–8. https://doi.org/10.1016/S1003-9953(08)60047-X.

[45] Pinna D. Wax composition transients during Fischer–Tropsch synthesis. J Catal 2003;214:251–60. https://doi.org/10.1016/S0021-9517(02)00151-3.

[46] Yang C, Liu L, Zhu G, Xie C, Zhang X, Zhang X. Catalytic Cracking of Fischer-Tropsch Wax on Different Zeolite Catalysts. Catalysts 2023;13:1223. https://doi.org/10.3390/catal13081223.

[47] Ahad N, de Klerk A. Fischer–Tropsch acid water processing by Kolbe electrolysis. Fuel 2018;211:415–9. https://doi.org/10.1016/j.fuel.2017.09.075.

[48] Zhang R, Huang Y, Zheng K, Xu C. Design and control of fraction cutting for the separation of mixed alcohols from the Fischer–Tropsch aqueous by-products. Chin J Chem Eng 2022;50:143–54. https://doi.org/10.1016/j.cjche.2022.08.005.

3. pielikums

Appendix 3

Stanke, A., Kampars, V.

Agglomeration of Fe/SBA-15 with clays for Fischer-Tropsch synthesis.

Energy Reports, **2022**, 8, 461-466

https://doi.org/10.1016/j.egyr.2022.10.251

Available online at www.sciencedirect.com
ScienceDirect
Energy Reports 8 (2022) 461–466
www.elsevier.com/locate/egyr

7th International Conference on Advances on Clean Energy Research, ICACER 2022 April 20–22, 2022, Barcelona, Spain

Agglomeration of Fe/SBA-15 with clays for Fischer–Tropsch synthesis

Agija Stanke*, Valdis Kampars[1]

Riga Technical University, Institute of Applied Chemistry, Paula Valdena 3, Riga, LV-1048, Latvia

Received 6 October 2022; accepted 9 October 2022
Available online 28 October 2022

Abstract

The huge contribution of the transportation sector to GHG emissions motivates the search for a sustainable and renewable alternative to fossil fuels. Fischer–Tropsch synthesis (FTS) is a catalytic process to convert synthesis gas into hydrocarbons for the production of fuels and chemicals. However, further development of FTS catalysts is still needed in order to make the process based on renewables economically viable. In this work mesoporous Fe/SBA-15 was synthesized. Two natural clays (hectorite and kaolin) were used as catalyst binders and promoters. The agglomeration with the clays did not disrupt the mesoporous structure of Fe/SBA-15. The effect of the clay and the effect of the catalyst form (i.e. powder or granules) on the FTS performance was investigated at 280 °C and 20 bar. Comparing catalysts agglomerated with kaolin and hectorite, better performance was observed for catalysts containing kaolin. Catalysts in the form of powder showed better performance in CO converted per gram of iron than the same catalysts in the form of granules. Granular catalysts promoted the formation of gaseous products.

Peer-review under responsibility of the scientific committee of the 7th International Conference on Advances on Clean Energy Research, ICACER, 2022.

Keywords: SBA-15; Iron catalyst; Fischer–Tropsch synthesis; CO

---

1. Introduction

The rapid growth of the world's population together with technological developments has led to a significant increase in consumption, production, and, consequently, environmental pollution. One of the main challenges is greenhouse gas (GHG) emissions, which contribute to climate change and global warming. Amongst different human activities, transportation makes the largest contribution to the GHG emissions [1]. Therefore, the transition to sustainable renewable fuels is crucial.

Fischer-Tropsch synthesis (FTS) is a catalytic process for the conversion of synthesis gas into broad spectrum of hydrocarbons suitable for the production of fuels and chemicals. Recently, interest in FTS as a sustainable process

---

* Corresponding author.
E-mail address: agija.stanke@gmail.com (A. Stanke).

[1] deceased

https://doi.org/10.1016/j.egyr.2022.10.251

Peer-review under responsibility of the scientific committee of the 7th International Conference on Advances on Clean Energy Research, ICACER, 2022.

Nomenclature

Pulv.	Powder
Gran.	Granules

has been growing, as the synthesis gas required for the process can be obtained from alternative and renewable feedstocks such as biomass, and waste [2]. Most Group VIII metals have Fischer–Tropsch activity, but only iron and cobalt catalysts are used on an industrial scale. The advantages of iron catalysts are availability, low cost, ability to adapt to a wide range of H_2/CO ratios, and reaction temperatures [3]. The main disadvantage of iron catalysts is the relatively short lifetime due to sintering, iron phase change, and carbon deposition [4]. In addition, during FTS catalysts can become mechanically instable, and fine catalyst particles can contaminate the reactor and further equipment [5].

Catalyst supports and structural promoters are used to stabilize catalyst particles, while chemical promoters are used to improve catalytic performance. The most commonly used FTS iron catalyst promoters are Zn, Mn, Al, Si, Cu, Ru, K, Na, Cs, and Rb compounds [6]. SBA-15 is an ordered mesoporous SiO_2 material with a large surface area and narrow pore size distribution. The high thermal and hydrothermal stability of SBA-15 makes it a suitable catalyst support for Fischer–Tropsch synthesis [7]. In catalyst manufacture binders such as natural clays, alumina, silica are often used to increase catalyst mechanical strength. Clays can also help in adsorption processes [8], besides, they contain components, which can act as promoters [9]. Although different promoters for Fischer–Tropsch iron catalysts have been widely investigated, clay minerals are not amongst them.

In this study two natural clays (hectorite and kaolin) were used as a catalyst promoters and binders to the Fe/SBA-15 catalyst granules. Hectorite clay is a magnesium-lithium silicate ($Na_{0.6}Mg_{2.7}Li_{0.3}Si_4O_{10}(OH)_2$) [10]. Kaolin clay is a hydrated aluminum silicate ($Al_2Si_2O_5(OH)_4$), containing impurities such as K, Na, Fe in large quantities [11]. Since diffusional restrictions of reactant gases and reaction products within large catalyst granules could affect the Fischer–Tropsch synthesis rate and product selectivity, the effect of the clay and the effect of the catalyst form (i.e. powder or granules) on the FTS performance was investigated.

2. Materials and methods

Iron nitrate nonahydrate ($Fe(NO_3)_3 \cdot 9H_2O$, 96%) was purchased from *Carl Roth* and used as iron source for the synthesis of iron containing mesostructured catalysts. Non-ionic surfactant Pluronic P123 ($EO_{20}PO_{70}EO_{20}$, $M_w = 5800$, 99%), tetraethyl orthosilicate (TEOS, 98%), nitric acid (HNO_3, 70%) and ethanol (C_2H_5OH, 99.8%) were purchased form *Merck*. Black clay (100% hectorite) and white clay (100% kaolin) were purchased from *DNC*.

2.1. Catalyst preparation

The powder Fe/SBA-15 has been prepared *via* direct synthesis method by adapting general SBA-15 synthesis method published by Zhao et al. [12]. 4 g of triblock copolymer P123 were dissolved in 150 mL of 1.45 M aqueous solution of HNO_3. The resultant mixture was stirred and heated up to 40 °C before adding the iron precursor. The mass of the $Fe(NO_3)_3 \cdot 9H_2O$ was calculated to obtain 30 wt% iron in the final catalysts. Then 9.15 mL of the silicon precursor (TEOS) was added dropwise. After that the resultant gel was hydrothermally aged at 40 °C for 24 h and 100 °C for 48 h under static conditions. The solid was recovered by filtration, and air-dried. Surfactant was removed by calcination in air at 550 °C for 5 h with a 1 °C min^{-1} temperature ramping. The solid was then recovered as an orange-brown powder. Iron concentration in Fe/SBA-15 determined by XRF was 28.1 wt%.

Macroscopically structured catalyst granules were made by agglomeration of powder Fe/SBA-15 with clays. Inorganic clay (hectorite or kaolin) was used as a binder. Deionized water was added to the mix of Fe/SBA-15 and clay (2:1 wt%). Obtained paste was kneaded in order to obtain homogeneous composition.

Catalyst rods (D = 1.6 mm) were made by extrusion. Extruded rods were cut in 3–5 mm length particles, dried in air at 50 °C for 5 h and finally calcined in air at 550 °C for 5 h with a 1 °C min^{-1} temperature ramping. Catalyst granules containing hectorite were denoted as Fe/SBA-15/H while catalyst granules containing kaolin were denoted as Fe/SBA-15/K.

2.2. Catalyst characterization

Powder X-ray diffraction (XRD) analysis was acquired by a *Bruker AXS D8 ADVANCE* diffractometer operated at 40 kV and 40 mA using Cu Kα radiation with a wavelength of 0.15406 nm. Small angle XRD patterns (SXRD) were recorded in the 2θ range of 0.5–2° with the step size of 0.01° and wide angle XRD patterns (WXRD) were recorded in the 2θ range of 2–50° with the step size of 0.02°.

The adsorption–desorption isotherms of N_2 at -196 °C were measured on *Quantachrome Instruments Nova 1200 E-Series* surface and porosity analyzer. Prior to the experiment, the samples were degassed at 180 °C for 4 h. The catalysts surface areas were calculated using the Brunauer–Emmett–Teller (BET) method. The total pore volumes were estimated from the amount adsorbed at a relative pressure (P/P_0) of 0.99. The pore size distributions were estimated from desorption isotherms using the Barrett–Joyner–Halenda (BJH) method.

2.3. Test of catalytic behavior

The catalytic properties of Fe/SBA-15 were tested in powder form, while Fe/SBA-15/H and Fe/SBA-15/K were tested both in granular and powder form. FTS experiments were carried out in a commercial customized micro-activity reactor (*Microactivity-Effi, PID Eng&Tech S.L.*) employing a tubular high-pressure fixed-bed stainless steel reactor (9.1 mm I.D. × 304.8 mm length). A porous plate made of Hastelloy C (20 µm in size) was used to support the catalytic bed inside the isothermal temperature zone of the reactor. Quartz wool was used as an additional support using a powdered catalyst. Typically, a reactor was loaded with 0.35 g of catalyst powder previously diluted with quartz sand to avoid hot spots during the reaction, or 0.70 g of catalyst granules without dilution. Prior to catalytic testing, all fresh catalysts were reduced *in-situ* in a stream of CO at 350 °C for 22 h with a 3 °C min^{-1} temperature ramping under atmospheric pressure. After the reduction, the temperature was lowered up to 160 °C and the feed gas was switched to the reactant gas (H_2, CO and N_2 mixture). The molar ratio of H_2:CO:N_2 was 4:2:1 and the flow rate was 70 mL min $^{-1}$. Then the operation parameters were gradually increased to the reaction conditions. FTS tests were carried out at 20 bar and 280 °C for 72 h.

The reactor effluent passed through a hot trap (120 °C) to collect heavy waxes and a cold trap (5 °C) to recover liquid hydrocarbon phase and water.

The gaseous product stream was analyzed on-line with a gas chromatograph (*Shimadzu Nexis GC-2030*) equipped with four columns, flame ionization detector (FID) and thermal conductivity detector (TCD). *Restek Rt-Q-Bond* (30 m, 0.53 mmID, 20 µm) column and FID detector was used for the analysis of gaseous hydrocarbons. Two *Restek Porapak Q 80/100* columns (6 ft, 2 mmID), a *Restek Molesieve 5A 60/80* column (6 ft, 2 mmID) set up in a row and TCD detector was used for the analysis of H_2, N_2, CO, CH_4, and CO_2 in the exit gas.

Nitrogen in the syngas was assumed as inert during the reaction.

Following formulas were used to calculate conversion and selectivities:

$$\text{CO conversion (mol\%)} \qquad X_{\text{CO}} = \frac{\text{CO}_{in} - \text{CO}_{out}}{\text{CO}_{in}} \cdot 100 \tag{1}$$

$$\text{CO}_2 \text{ selectivity (mol\%)} \qquad S_{\text{CO}_2} = \frac{\text{CO}_{2out}}{\text{CO}_{in} - \text{CO}_{out}} \cdot 100\% \tag{2}$$

$$C_{\text{n}} \text{ selectivity (mol\%)} \qquad S_{C_n} = \frac{C_{n\,out}}{\text{CO}_{in} - \text{CO}_{out}} \cdot 100\% \tag{3}$$

$$C_{5+} \text{ selectivity (mol\%)} \qquad S_{C_{5+}} = 100\% - S_{\text{CO}_2} - \sum_{n=1}^{4} S_{C_n} \tag{4}$$

where CO_{in} represents molar flowrate of CO at inlet; CO_{out}, $\text{CO}_{2\text{out}}$ and $C_{\text{n out}}$ represent molar flowrate of CO, CO_2, and hydrocarbons with n carbon atoms at outlet. Iron time yield (FTY) was used to represents moles of CO converted per gram of iron per second.

3. Results and discussion

The N_2 adsorption curves and pore size distribution of Fe/SBA-15, Fe/SBA-15/H, Fe/SBA-15/K as well as of both clays used as binders are shown in Fig. 1. Typical IUPAC type IV isotherm with H1 hysteresis loop characteristic of

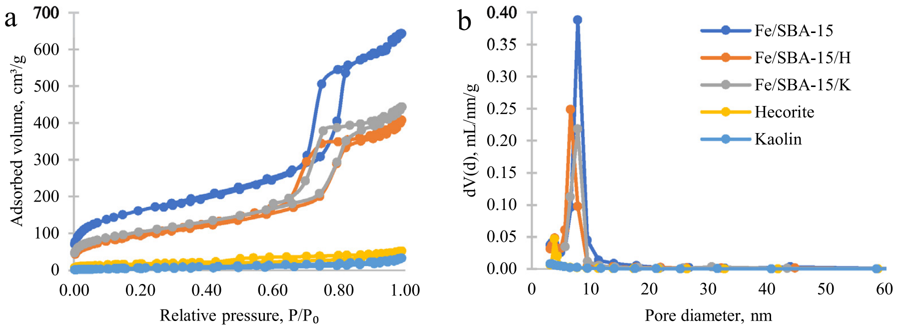

Fig. 1. (a) N_2 adsorption-desorption isotherms, and (b) pore size distribution of catalysts and clays.

mesoporous materials with narrow distribution of cylindrical or tubular pores [13] were observed for all 3 catalysts (Fig. 1a), indicating that agglomeration with clay does not disrupt the mesoporous structure of Fe/SBA-15.

Textural properties of catalysts and clays are presented in Table 1. As it can be seen from Fig. 1. and Table 1, both hectorite and kaolin have relatively small amount of mesopores and small surface area, therefore, after mixing Fe/SBA-15 with the clay, the surface area, and the pore volume of the Fe/SBA-15/H and Fe/SBA-15/K catalysts are reduced. However, the mean pore diameter changes only slightly, indicating that the clays do not clog the pores of Fe/SBA-15.

Table 1. Textural properties of catalysts and clays.

Sample	S_{BET}[a] (m^2/g)	V_{total}[b] (cm^3/g)	$D_{average}$[c] (nm)	D_{mean}[d] (nm)
Fe/SBA-15	572.4	0.99	6.95	7.82
Fe/SBA-15/H	334.0	0.63	7.55	6.62
Fe/SBA-15/K	368.2	0.69	7.45	7.84
Hectorite	52.0	0.08	6.24	3.85
Kaolin	15.2	0.05	13.32	3.13

[a] BET surface area.
[b] Total pore volume.
[c] Average pore diameter.
[d] Mean pore diameter evaluated by the BJH desorption method.

The SXRD patterns (Fig. 2a) of catalysts showed one intense reflection at $2\theta = 0.9^\circ$ and two reflections with smaller intensities at $2\theta = 1.6^\circ$ and $2\theta = 1.8^\circ$, which is characteristic of the 2D hexagonal mesoporous structure (p6 m) of SBA-15. The WXRD patterns of catalysts after calcination (before reaction) showed reflections corresponding to hematite (α-Fe_2O_3 PDF 01-071-5088). The WXRD patterns of Fe/SBA-15/K and Fe/SBA-15/H showed also additional reflections corresponding to quartz (SiO_2 PDF 01-070-7344), and muscovite ($K(Al_4Si_2O_9(OH)_3)$ PDF 01-070-3754). The WXRD patterns of catalysts after Fischer–Tropsch synthesis reaction showed intense reflections characteristic of quartz, microcline ($KAlSi_3O_4$ PDF 01-084-1455), dolomite ($CaMg(CO_3)_2$ PDF 00-001-0942), and calcite ($CaCO_3$ PDF 00-005-0586). Since both clays used as binders are natural clays, they may contain impurities. The description of the purchased clays indicates that these clays contain natural microelements as quartz, calcium, magnesium, iron, nitrogen, potassium, and strontium, which can explain the presence of dolomite and calcite after reactions. For Fe/SBA-15/K granules, Fe/SBA-15/H granules, and Fe/SBA-15 powder it was possible to differentiate reflections with smaller intensities at $2\theta = 35$–50° corresponding to different iron carbide phases. As it can be seen from Fig. 2c, each catalyst exhibited reflections corresponding to different combinations of iron carbides. The formation of these different carbide combinations could have been influenced by both the clay composition and the diffusion constraints of the reactant gases and reaction products.

Table 2 summarizes the activity and product selectivity of Fe/SBA-15, Fe/SBA-15/H and Fe/SBA-15/K in powder form and of Fe/SBA-15/H and Fe/SBA-15/K in granular form. The catalytic activity during FTS was evaluated at

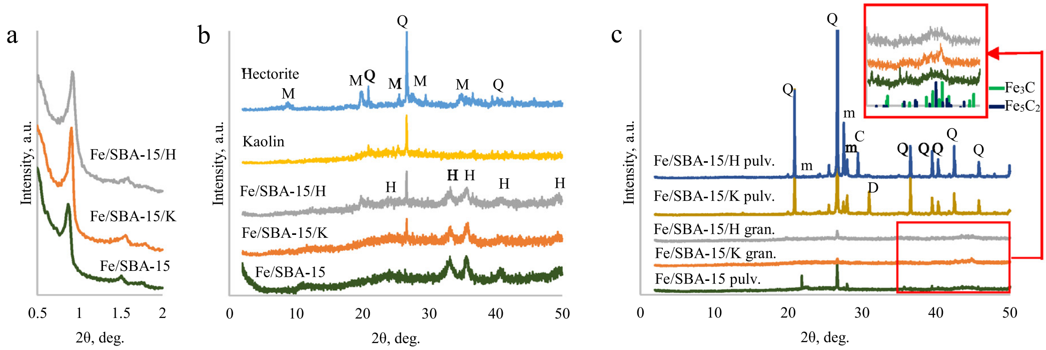

Fig. 2. (a) SXRD, and (b) WXRD patterns of catalysts after calcination; (c) WXRD patterns of catalysts after reaction. H – hematite, Q – quartz, M – muscovite, m – microcline, D – dolomite, C - calcite.

Table 2. Catalytic performance of Fe/SBA-15 catalysts.

Catalyst	CO conversion (%)	FTY (10^{-5} mol_{CO} gFe^{-1} s^{-1})	Selectivity (%)			
			CO_2	CH_4	$C_2 - C_4$	C_{5+}
Fe/SBA-15 pulv.	53.6	8.1	19.5	16.9	29.9	33.7
Fe/SBA-15/H pulv.	30.8	7.1	4.6	11.3	14.7	69.4
Fe/SBA-15/K pulv.	39.4	9.1	12.9	12.9	23.4	50.7
Fe/SBA-15/H gran.	43.3	5.0	25.7	25.4	35.2	13.7
Fe/SBA-15/K gran.	52.6	6.1	22.9	23.4	31.4	22.3

280 °C and 20 bar. As it can be seen from data presented in Table 2, catalytic performance was strongly affected by composition of catalysts and by catalyst form (i.e., powder or granules). This could be explained by different diffusion limitations depending on the shape of catalyst. Catalysts in the form of powder showed better performance in CO converted per gram of iron than the same catalysts in the form of granules. Granular catalysts promoted the formation of gaseous products. Comparing catalysts agglomerated with kaolin and hectorite, better performance can be observed for catalysts containing kaolin. Fe/SBA-15/K in the powdered form showed the best performance in CO converted per gram of iron.

4. Conclusions

Agglomeration with hectorite and kaolin clay does not disrupt the mesoporous structure of Fe/SBA-15. Clay used as binder also acts as promoter and affects the course of the FTS reaction. Diffusion limits due to the catalyst form (i.e. powder or granules) have grate impact on the catalytic performance. Powdered catalysts show better performance than granular catalysts in means of CO conversation and mols of CO converted per gram of iron. Granular catalysts contribute to the formation of CH_4 and CO_2. Catalysts containing kaolin clay show better performance than catalysts containing hectorite clay.

Declaration of competing interest

The authors declare that they have no known competing financial interests or personal relationships that could have appeared to influence the work reported in this paper.

Data availability

No data was used for the research described in the article.

Acknowledgments

This work has been supported by the European Social Fund within the Project No 8.2.2.0/20/I/008 «Strengthening of Ph.D. students and academic personnel of Riga Technical University and BA School of Business and Finance in the strategic fields of specialization» of the Specific Objective 8.2.2 «To Strengthen Academic Staff of Higher Education Institutions in Strategic Specialization Areas» of the Operational Programme «Growth and Employment». This research/publication was supported by Riga Technical University's Doctoral Grant programme, Latvia.

References

[1] Kazancoglu Ozbiltekin-Pala, Ozkan-Ozen Yesim Deniz. Prediction and evaluation of greenhouse gas emissions for sustainable road transport within Europe. Sustain Cities Soc 2021;70:102924.

[2] Barrios Gu, Luo Peron, Chernavskii Virginie, Wojcieszak Thybaut, Ordomsky, Khodakov Andrei Y. Identification of efficient promoters and selectivity trends in high temperature Fischer–Tropsch synthesis over supported iron catalysts. Appl Catalysis B: Environ 2020;273:119028.

[3] Nielsen Moss, Bjørnlund Liu, Knop-Gericke Klyushin, Grunwaldt Sheppard, Doronkin Zimina, Smitshuysen Damsgaard, Wagner, Hansen Thomas Willum. Reduction and carburization of iron oxides for Fischer – Tropsch synthesis. J Energy Chem 2020;51:48–61.

[4] Zhao Lv, Wang Li, Wang Zhang, Li Jinlin. Comparison of preparation methods of iron-based catalysts for enhancing Fischer–Tropsch synthesis performance. Mol Catalysis 2018;449:99–105.

[5] Cheng Virginie, Ordomsky Cordier, Chernavskii Ivantsov, Paul Wang, Khodakov Andrei Y. Pore size effects in high-temperature Fischer – Tropsch synthesis over supported iron catalysts. J Catalysis 2015;328:139–50.

[6] Feyzi Irandoust, Mirzaei Ali Akbar. Effects of promoters and calcination conditions on the catalytic performance of iron–manganese catalysts for Fischer–Tropsch synthesis. Fuel Process Technol 2011;92:1136–43.

[7] Xiong Zhang, Liew, Li Jinlin. Fischer–Tropsch synthesis: The role of pore size for Co/SBA-15 catalysts. J Mol Catalysis A: Chem 2008;295(1–2):68–76.

[8] Saini Pinto, Pires João. Natural clay binder based extrudates of mesoporous materials: Improved materials for selective adsorption of natural and biogas components. Green Chem 2011;13(5):1251–9.

[9] Nawaz Ahmad, Asif Klemeš, Mubashir Munir, Zafar Bokhari, Mukhtar Saqib, Khoo, Show Pau Loke. Phyllosilicate derived catalysts for efficient conversion of lignocellulosic derived biomass to biodiesel: A review. Bioresour Technol 2022;343:126068.

[10] Zhang Zhou, Petit, Zhang Hao. Hectorite: Synthesis, modification, assembly and applications. Appl Clay Sci 2019;177:114–38.

[11] Aimdate Srifa, Koo-amornpattana Sakdaronnarong, Klysubun Kiatphuengporn, Assabumrungrat Wongsakulphasatch, Kaveevivitchai Sudoh, Watanabe Fukuhara, Ratchahat Sakhon. Natural Kaolin-based Ni catalysts for CO_2 methanation: On the effect of Ce enhancement and microwave-assisted hydrothermal synthesis. ACS Omega 2021;6(21):13779–94.

[12] Zhao Feng, Huo Melosh, Fredirickson Chmelka, Stucky Galen D. Triblock copolymer syntheses of mesoporous silica with periodic 50 to 300 angstrom pores. Science 1998;279(80):548–52, 5350.

[13] Sing, Williams Ruth T. Physisorption hysteresis loops and the characterization of nanoporous materials. Adsorption Sci Technol 2004;22(10):773–82.

4. pielikums

Appendix 4

Abelniece, Z., Cutrufello, M.G., Rombi, E., Stanke, A., Piirsoo, H., Mändar, H., Tamm, A.

The structure-activity interactions of Cu/Zn, In/Pd and Fe/K catalysts supported on mesoporous SBA-15 for carbon dioxide hydrogenation at low pressure.

Chemical Papers, **2024**, 78, 5103-5112.

https://doi.org/10.1007/s11696-024-03456-9

Chemical Papers
https://doi.org/10.1007/s11696-024-03456-9

ORIGINAL PAPER

The structure–activity interactions of Cu/Zn, In/Pd and Fe/K catalysts supported on mesoporous SBA-15 for carbon dioxide hydrogenation at low pressure

Zane Abelniece[1] · **Maria Giorgia Cutrufello**[2] · **Elisabetta Rombi**[2] · **Agija Stanke**[1] · **Helle-Mai Piirsoo**[3] · **Hugo Mändar**[3] · **Aile Tamm**[3]

Received: 11 April 2023 / Accepted: 8 April 2024

Abstract

To minimize greenhouse gas emissions, efficient carbon dioxide capture and utilization need to be addressed. In this study, to determine the structure–activity interplay, three different promising catalytic systems for the CO_2 hydrogenation process were synthesized using mesoporous silica SBA-15 as a support material: copper-based catalyst with zinc, indium-based catalyst with palladium and iron-based catalyst with potassium. The role of metal–metal oxide interaction has been showed. The use of Cu/Zn catalytic system and SBA-15 allowed to obtain very small crystallite size of tenorite and zinc oxide, good dispersion of active phases with strong basic sites. In order to find the most effective catalyst providing the maximal methanol yield and selectivity, these catalytic systems were compared under the same reaction conditions (250 °C, 20 bar, H_2 to CO_2 molar ratio 4 to 1) using fixed-bed tubular micro-activity reactor. Results showed that the highest methanol yield can be obtained with Cu/Zn/SBA-15 catalyst as might be expected according to obtained characterization.

Keywords Carbon dioxide · Catalysts · Copper-zinc · Indium-palladium · Iron-potassium · Methanol

Introduction

The amount of greenhouse gases in the atmosphere increases leading to adverse effects on environment and climate. Currently, the amount of carbon dioxide (CO_2) emission exceeds the levels adopted in the Paris Agreement. To reduce the negative effects of greenhouse gases on the environment, more efficient utilization of fossil fuels as well as CO_2 capture and utilization need to be addressed. Carbon capture, utilization, and storage is an emissions reduction technology that has attracted a great attention in recent years due to its high efficiency (Atsbha et al. 2021). One of the carbon utilization methods is the catalytic hydrogenation of CO_2 which converts CO_2 into energy products, such as methanol. Methanol has a wide range of applications: it can be used to produce a variety of chemicals and it is also an alternative fuel. Today, methanol is mainly synthesized in an industrial process from fossil sources using $Cu/ZnO/Al_2O_3$ catalysts, that converts synthesis gas ($H_2/CO/CO_2$) into methanol under rather harsh conditions (at a pressure of 50–100 bar and a temperature of 200–300 °C). In recent years, the interest of direct hydrogenation to methanol has increased significantly. The catalytic hydrogenation of CO_2 is green and environmentally-friendly method, especially if the cost-effective and safe conditions are applied (Stangeland et al. 2020).

Effective catalyst is a key parameter to CO_2 hydrogenation performance. The most efficient catalysts for CO_2 hydrogenation to methanol are multi-component catalytic systems consisting of intermixed metal and metal oxides nanoparticles.

The most effective/promising catalytic systems for CO_2 hydrogenation to methanol reported in the literature are copper-zinc oxide based catalysts, indium oxide-palladium-based catalysts (Stangeland et al. 2020) and

---

✉ Zane Abelniece
zaneabelniece@gmail.com

[1] Institute of Applied Chemistry, Riga Technical University, Paula Valdena Str. 3, Riga 1048, Latvia

[2] Department of Chemical and Geological Sciences, University of Cagliari, Cittadella Universitaria Di Monserrato, S.S. 554 Bivio Per Sestu, 09042 Monserrato, CA, Italy

[3] Institute of Physics, University of Tartu, W. Ostwaldi Str. 1, 50411 Tartu, Estonia

iron-potassium-based catalysts (Xi et al. 2021). The complexity of the multi-component catalytic systems and challenges in elucidating the active sites are the main stumbling blocks in developing rational catalyst design strategies (Stangeland et al. 2020).

The main role of ZnO in Cu/Zn catalyst has been proposed to increase Cu dispersion, the exposure of more active Cu sites. ZnO prevents the agglomeration of Cu particles, thus leading to the large Cu surface area needed for methanol synthesis (Mureddu et al. 2019). A large Cu surface area is important to obtain high activity, but there are differences in intrinsic activity between Cu/ZnO-based catalysts with different preparation history. Additionally, the fact that the migration of Zn species to Cu surface generates active sites, oxygen vacancies or Cu–Zn surface alloy may facilitate CO_2 hydrogenation to methanol (Chen et al. 2022).

Recently, In_2O_3-based catalysts with oxygen vacancies have been reported to possess higher methanol selectivity than Cu/Zn-based catalysts (Jiang et al. 2020; Li et al. 2022; Rui et al. 2017). Over the last decade, indium-based catalysts have gained significant interest for CO_2 hydrogenation to methanol, based on low activity for the reverse water–gas shift reaction, which results in high methanol selectivity over a wide temperature range. Ye et al. predicted that methanol formation is favourable on the defective $In_2O_3(110)$ surface containing oxygen vacancies (Ye et al. 2013). In Jiang et al. work it was shown that the addition of Pd enhanced the number of oxygen vacancies on the surface of In_2O_3 and facilitated the CO_2 activation through interaction with In_2O_3 (Jiang et al. 2020).

The synergistic effects of K (and Na) in the iron catalyst are responsible for the excellent higher alcohol synthesis (Xu et al. 2020; Yao et al. 2021). As limited progress has been made in the hydrogenation of CO_2 to alcohols with iron catalysts, in this study Fe/K on SBA-15 was used to determine the activity in reactions. Xi et al. reported that well-dispersed Fe_2O_3 and In_2O_3 phases with oxygen vacancies can be observed on Ce-ZrO_2 support (Xi et al. 2021). Potassium can greatly affect CO_2 and H_2 activation, thus regulating CO_2 conversion and product selectivity (Xu et al. 2020).

The thermodynamics of CO_2 conversion also limits methanol synthesis due to the competing reverse water–gas shift reaction. Furthermore the by-product water can have negative effects on the activity and stability of the catalyst during CO_2 hydrogenation to methanol (Stangeland et al. 2020). The effective solution for the stabilization of the active phase/nanoparticles and improvement of catalytic and mechanical properties is the dispersion of the active phase onto a suitable, high-surface area support, such as SBA-15 (Santa Barbara Amorphous mesoporous silica). It is well known that supports can increase active metal surface area and stabilize the particles from sintering thus improving the catalytic and mechanical properties (Chen et al. 2022). SBA-15 ordered mesoporous structure allows the formation of active nanophases with narrow particle size distribution, the wall thickness ensures the thermal stability of the support, and the size of pores allows the easy diffusion of the gaseous molecules (Mureddu et al. 2019).

It was found in recent years that metal-support interaction and creation of interfacial sites promotes metal dispersion, and changes concentration of acid sites, basic sites, and oxygen vacancies on the catalyst surface (Chen et al. 2022). Mureddu et al. studied CO_2 hydrogenation to methanol using Cu/Zn/Zr/SBA-15 catalyst and showed that strong metal–support interaction could prevent the restructuring effects of copper particles like particle agglomeration during the reaction (Mureddu et al. 2019). The study revealed that better results can be achieved when a thin amorphous homogeneous layer of the active phase is formed, rather than larger particles located at the external surface, leading to improved activity and selectivity of the catalyst (Mureddu et al. 2019).

In this study SBA-15 was applied as carrier material providing large surface to disperse the active components and to ensure the thermal stability during the reaction. SBA-15 has abundant mesopores beneficial to mass transferwhich makes it a promising catalyst support for industrial applications (Mao et al. 2022). Besides, our previous study reveals that methanol yield obtained using Cu/ZnO/SBA-15 catalyst is comparable to the yield obtained with the commercial catalyst (Abelniece et al. 2022). Three different promising catalytic systems for the CO_2 hydrogenation process were studied and the influence of metal—support interaction on the structure of catalysts and the activity of CO_2 hydrogenation reaction was investigated using mesoporous SBA-15 as a support material. These catalytic systems are: copper-based catalyst (with Zn), indium-based catalyst (with Pd) and iron-based catalyst (with K). These catalytic systems were compared at the same reaction conditions to find the most effective one providing the maximal methanol yield and selectivity.

Direct comparison of these catalysts with identical metal content under selected identical reaction conditions (fixed-bed tubular micro-activity reactor, 20 bar and the temperature 250 °C) is performed for the development of more effective catalysts, which can promote commercialization of the CO_2 hydrogenation process. The optimal reaction temperature to obtain maximal yield of methanol was found 250 °C by H_2/CO_2 molar ratio 3/1 for Cu/Zn/S/Kaolin catalyst during previous studies (Abelniece et al. 2021). Also, other authors have found that 250 °C is the temperature most favourable for methanol production (Mureddu et al. 2019). Higher temperatures could increase the conversion of CO_2, but would decrease the yield of methanol simultaneously increasing that of CO. Usually, the studies of CO_2

conversion were carried out at a pressure of 30 bar or higher, but in this study was conducted under relatively low pressure (20 bar), providing that the process is more secure.

Materials and methods

Preparation of catalysts

SBA-15 (S) was purchased from ACS Material LLC and used as a carrier material for all three catalysts. Catalysts were prepared by co-impregnation method.

Cu/Zn/S: an aqueous solution (20 ml) with appropriate amount of $Cu(NO_3)_2•2.5H_2O$ and $Zn(NO_3)_2•6H_2O$ was made to obtain metal loadings: Cu 20 and Zn 7%. The solution was added dropwise to 1.05 g of S, then mixed and heated for 2 h, and finally treated in ultrasound bath for 2 h. Afterwards, the solid obtained was dried overnight at 90 °C and then calcined in a muffle furnace at 400 °C for 4 h. Cu/Zn molar ratio is 3.2.

In/Pd/S: 10 mL of aqueous solution of $In(NO_3)_3•3H_2O$ was mixed with 10 mL of aqueous solution of $Pd(NO_3)_2•2H_2O$ (metal loadings: In 20% and Pd 6%). This solution was added dropwise to 1.05 g of S, then mixed and heated for 2 h, and finally treated in ultrasound bath for 2 h. Afterwards solid obtained was dried overnight at 90 °C and then calcined at 400 °C for 4 h. In/Pd molar ratio is 3.2.

Fe/K/S: 10 mL of aqueous solution of $Fe(NO_3)_3•9H_2O$ was mixed with 10 mL of aqueous solution of KNO_3 (metal loadings: Fe 20 and K 1%). This solution was added dropwise to 1.05 g of S, then mixed and heated for 2 h, and finally treated in ultrasound bath for 2 h. Afterwards solid obtained was dried overnight at 90 °C and then calcined at 400 °C for 4 h. Fe/K molar ratio is 13.

Characterization of catalysts

X-ray diffraction analysis (XRD) of samples in both small angle scattering (SAXS) and wide angle scattering (WAXS) modes was performed on diffractometer SmartLab™ (Rigaku, Japan) using Cu rotating anode operated at 45 kV and 180 mA, and a coordinate sensitive 1D detector D/teX Ultra (WAXS range in reflection Bragg–Brentano optical scheme) or a scintillation detector (SAXS range implementing transmission SAXS optics). Diffraction patterns were measured between angles of 8° and 80° with step size of 0.02° (2θ) and scan speed of 5 deg min^{-1} (WAXS), or from 0.1° to 2.5° with step size of 0.01° (2θ) and scan speed of 0.26 deg min^{-1} (SAXS). Programme *PDXL* (Rigaku) and ICDD database PDF-2 (2020) were used for identification of phases. X-ray apparent crystallite size was calculated from Scherrer equation. Instrumental broadening of reflections was determined on standard reference material SRM-660 (LaB_6).

The surface area and the pore size were determined by N_2 adsorption–desorption isotherms obtained using a Quantachrome Instruments Nova 1200 E-Series surface and porosity analyzer at − 196 °C. The samples were outgassed at 150 °C for 24 h before measurement. Total surface area was estimated by using the Brunauer–Emmett–Teller (BET) method. Pore diameters were derived from desorption isotherms using the Barrett-Joyner-Halenda (BJH) method.

Morphology and composition were studied using scanning electron microscope (SEM) (Helios Nanolab 600 by FEI) equipped with energy-dispersive X-ray (EDX) analysis detector (INCA Energy 350 by Oxford Instruments). The structure of the catalysts was investigated with transmission electron microscope Titan Themis 200 (FEI) operating at 200 kV in scanning mode (STEM). The powdered sample was mixed with ethanol to make a suspension. Energy-dispersive X-ray (EDX) spectroscopy was done with SuperX (Bruker) system in the same microscope.

Inductively coupled plasma atomic emission spectroscopy (ICP-AES) analyses were performed with a 5110 ICP-OES spectrometer (Agilent Technologies) to determine the chemical composition. To determine K, Fe, In, and Si contents, the samples were prepared as follows: after calcination at 300 °C for 12 h, ca. 0.04 g of sample were mixed with lithium tetraborate (1:15 *w*/*w*), placed in a platinum crucible, and then fused at 1000 °C in a furnace for 30 min. After cooling of the melt, the resultant fusion bead was dissolved at 80 °C for about 30 min with 100 mL of a HNO_3 solution (0.80 M) and finally diluted to the desired volume with Milli-Q water. Pd amount was determined by treating ca. 0.05 g of sample with a mixture of HCl (37%) and HNO_3 (70%) (3:1 by volume) at 80 °C for 3 h; after filtration, the solution was diluted to the desired volume with Milli-Q water.

Temperature programmed reduction (TPR) was performed on a TPD/R/O 1100 apparatus (Thermoquest) equipped with a TCD detector, using ca. 0.05 g of sample. TPR runs were carried out with a H_2/Ar mixture (5 vol% of H_2, 30 mL/min) from 40 to 950 °C (hold 30 min), with a heating rate of 10 °C/min. Prior to analysis, the samples were pretreated under flowing Ar (20 mL/min) at 300 °C for 1 h. The amount of H_2 consumed was calculated after calibration of the TCD response using CuO as the standard.

Temperature programmed desorption of CO_2 (CO_2-TPD) was performed from 40 to 500 °C (heating rate 10 °C/min, hold 45 min) using He (20 mL/min) as the gas carrier. Prior to analysis, the samples (ca. 0.15 g) were saturated with pulses of pure CO_2 (pulse volume 0.347 mL) at 40 °C under flowing He (50 mL/min). Prior to analysis, the samples were pretreated under flowing Ar (20 mL/min) at 300 °C for 1 h. The TCD response was calibrated by performing a pulse calibration run (at 40 °C, CO_2 pulse volume 0.347 mL, He flow rate = 20 mL/min) in an empty reactor.

Catalyst testing

The CO_2 hydrogenation was performed in a fixed-bed stainless steel tubular micro-activity reactor (Microactivity-Effi, PID Eng&Tech S.L.*),* reactor dimensions are: internal diameter 9.1 mm, length 305 mm. For each experiment, 0.2 g of catalyst mixed with sand to 3 mL volume was loaded in a catalyst bed above the quartz wool. The catalysts were reduced at atmospheric pressure under a flow of H_2 at flow rate of 50 mL min^{-1} at 350 °C for Cu/Zn/S and Fe/K/S catalysts and at 200 °C for In/Pd/S catalyst for 4 h. The temperature was lowered to 160 °C; subsequently a flow of H_2 (99.995% purity), CO_2 (99.995%) and N_2 (99.9%) mixture (4:1:1) was fed through the reactor at a flow rate of 60 mL min^{-1}, similar like in our previous study (Abelniece et al. 2022). The pressure was increased from atmospheric to 20 bar and the temperature from 160 to 250 °C. The time on stream after achieving the reaction temperature was 50 h. After leaving the reactor, the exit gas passed through cold trap ($T = 5$ °C) to condense products. The reactor outlet gas composition was analyzed on-line by a gas chromatograph (Shimadzu Nexis *GC-2030*) and the condensed products with infra-red spectrometer, the same as in (Abelniece et al. 2022).

The CO_2 conversion (X) and product distribution (D_{prod}) were calculated as follows:

$$X_{CO_2} = \left(\frac{nCO_{2\ in} - nCO_{2\ out}}{nCO_{2\ in}} \right) \times 100 \quad (1)$$

$$D_{prod} = \left(\frac{A_i}{\sum A_i} \right) \times 100 \quad (2)$$

where nCO_{2in} and nCO_{2out} is the number of moles of CO_2 at the inlet and outlet, respectively. A_i and ΣA_i represent the moles of selected product '*i*' and total moles of all products, respectively.

The space time yield of methanol (*STY*) was calculated as follows:

$$STY_{CH_3OH} = m_{CH_3OH} / \left(m_{cat} \cdot t \right) \quad (3)$$

where m_{CH3OH} represents the total mass of methanol formed (g), t indicates the time of reaction (h), m is the mass of the catalyst (g).

Each experiment was carried out twice and the average value was calculated.

Results and discussion

Elemental composition of catalysts

The elemental composition of the catalysts, determined by ICP-AES analysis, is reported in Table 1. The metal contents loaded on SBA-15 are close to the nominal values, the largest difference being observed for In (4.7%) in the In/Pd/S sample. The results show that co-impregnation method allows to obtain the catalysts with certain metal content.

Structural and phase composition characterization of catalysts

The ordered mesoporous structure of SBA-15 was observed in all samples by three diffraction reflections on SAXS patterns (Fig. 1a). A broad reflection between diffraction angles of 15° and 30° on WAXS patterns correspond to amorphous silica of mesoporous SBA-15 (Fig. 1b). The labels at the positions of the first three reflections of SAXS patterns of ordered mesoporous SBA-15 (Fig. 1a) show the Miller indices of the corresponding lattice planes (Zhao et al. 1998).

The reflections on the diffraction pattern of Cu/Zn/S were identified belonging to tenorite (CuO, ICDD PDF-2 card number 89–2529). The crystallite size of tenorite, averaged over the two strongest reflections (−111) and (111), was 2.5(5) nm. The reflections corresponding to ZnO were not observed, most likely due to ZnO being well dispersed into an X-ray amorphous.

Qualitative phase analysis of sample In/Pd/S identified two crystalline phases. The main phase was cubic In_2O_3 (ICDD PDF-2 card number 71–2194), and the second was tetragonal palladinite (PdO, ICDD PDF-2 card number 41–1107). Crystallite size of In_2O_3, averaged over six different crystallographic directions that showed in diffraction pattern the strongest and not overlapping reflections, was 12(2) nm. A rough estimation of the crystallite size for PdO was possible to give only by comparing the broadening

Table 1 Chemical composition of catalysts

Sample	Cu (wt.%)	Zn	In	Pd	Fe	K	Si
Cu/Zn/S	18.8	6.1					30.6
In/Pd/S			15.2	5.3			35.0
Fe/K/S					17.4	1.07	36.5

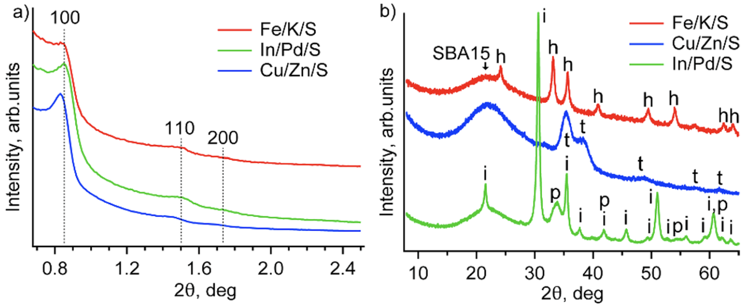

Fig. 1 **a** Transmission SAXS patterns of samples. **b**. WAXS patterns of samples. The reflections of SBA-15, tenorite, palladinite, hematite and In_2O_3 are marked with SBA-15, *t*, *p*, *h* and *i*, correspondingly. A vertical offset of patterns was applied to avoid overlapping

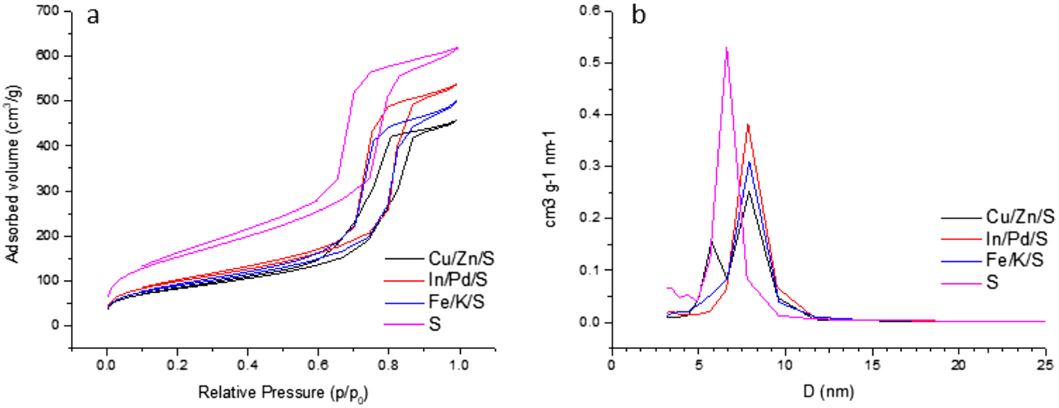

Fig. 2 **a** N_2 adsorption–desorption isotherms. **b** Pore size distribution of catalysts

values of reflections from In_2O_3 with a broad (101) reflection from PdO located at diffraction angle 33.8°. The latter was approximately four times broader, corresponding to the crystallite size approximately 3 nm.

The only crystalline phase observed in the sample Fe/K/S was hematite (Fe_2O_3, ICDD PDF-2 card number 76–8402). The crystallite size of hematite, averaged over six strongest and not overlapping reflections, was 13(1) nm.

Textural characterization

Figure 2a exhibits IUPAC type IV isotherms with a H1 hysteresis loop for all three catalysts, corresponding to the mesoporous materials consisting of ordered array of cylindrical pores (Alothman 2012), which indicates that the mesoporous structure of SBA-15 was not damaged after incorporation of the active phases. The hysteresis loop for Cu/Zn/S shows a little different shape. Furthermore, Fig. 2b demonstrates that In/Pd/S and Fe/K/S catalysts have a uniform pore size distribution (average diameter 7.8 nm), but the pore size distribution for Cu/Zn/S is uneven. It could be explained by partial pore filling. The surface area of catalysts is similar (see Table 2)—however the Cu/Zn/S has relatively the smallest comparing with others due to the larger metal content loaded, see ICP-AES results, Table 1.

Table 2 Specific surface area, pore diameter, and pore volume of the catalysts

Sample	BET surface area [m^2/g]	Dpore [nm][a]	Vtotal [cm^3/g][b]
S	554	6.8	0.96
Cu/Zn/S	304	7.9	0.71
In/Pd/S	353	7.8	0.83
Fe/K/S	318	7.9	0.77

[a] Pore diameters were derived from the desorption branches of the isotherms by using the BJH method

[b] Total pore volumes were estimated from the absorbed amount at a relative pressure of $p/p_0 = 0.99$

Morphology of the catalysts

Nanoparticles in the size range comparable with SBA-15 pores were visible with STEM for Cu/Zn/S catalyst (see Fig. 3a). Homogeneous distribution of nanoparticles, seemingly along the pores is apparent and regular dispersion of elements, including loaded metals, was obtained (see STEM-EDX elemental maps in Fig. 3b–e (oxygen not shown)). STEM confirms partial pore filling for Cu/Zn/S catalyst noticed by N_2 adsorption–desorption isotherms, the images showed that the active phase is distributed on the surface and in the pores.

Particles larger than the size of the pores were obtained with In/Pd/S and Fe/K/S catalysts (see Figs. 4 and 5). From these SEM images, it could be seen that the surface features that could be attributed to the metal oxides possessed dimensions in similar scale, however, some agglomeration occurs (see Fig. 4). The particles are larger than the average crystallite sizes determined for In_2O_3 and hematite from diffractograms. It could be, that a particle consists of multiple crystallites or on average particles are smaller than imaged in the figures.

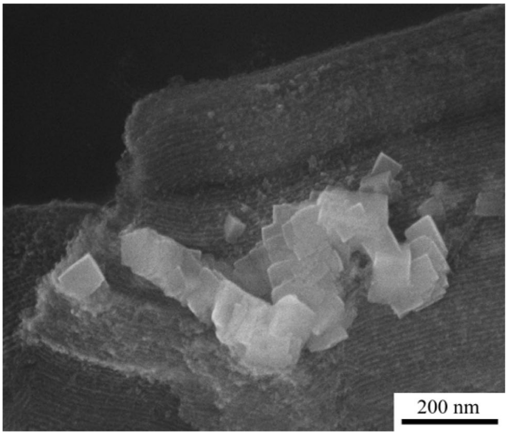

Fig. 4 SEM image of In/Pd/S catalyst

Reducibility of catalysts

TPR profile of the Cu/Zn/S catalyst shows a well-defined peak with a maximum corresponding to 320 °C (Fig. 6a), which is ascribable to the reduction of CuO to metallic copper. Upon closer inspection, a tailing of the peak towards low temperatures is observed, suggesting the overlapping of different contributions. For a CuO/ZnO catalyst, Shozi and co-authors (Shozi et al. 2017) reported a TPR profile showing two peaks at 292 and 340 °C, which were ascribed to the reduction of CuO through the following steps: $CuO \rightarrow Cu_2O \rightarrow Cu^0$. Accordingly, a two-steps reduction of copper oxide may also occur in the present case.

The reduction profile of the In/Pd/S sample (Fig. 6b) shows a negative peak at about 90 °C followed by two intense partially overlapping peaks at ca. 440 and 650 °C, which are made up of different contributions, as suggested by their asymmetrical and enlarged shape. A less intense feature is also observable at ca. 880 °C. According to the literature (Mendez et al. 2008; Batista et al. 2001; Zheng et al. 2008; Echeandia et al. 2014) the negative peak at

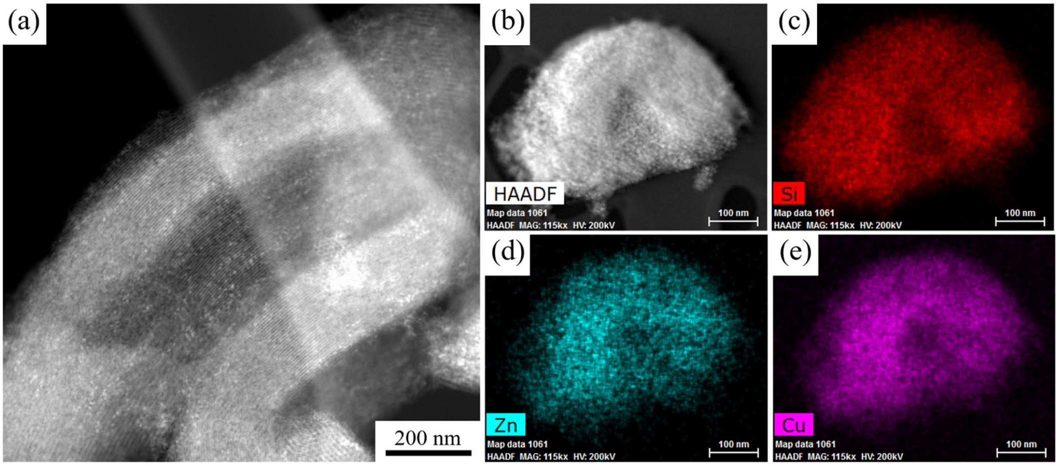

Fig. 3 **a** STEM image of Cu/Zn/S catalyst, **b**–**e** STEM-EDX elemental mapping of Cu/Zn/S catalyst

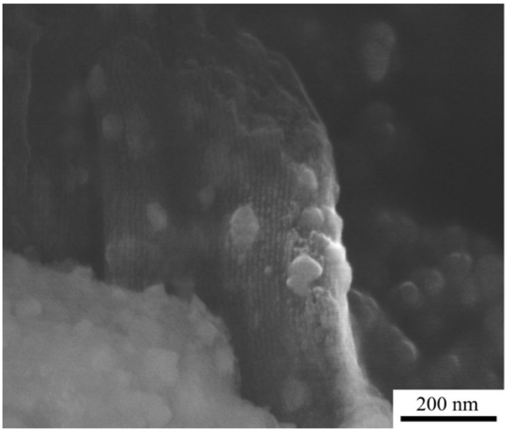

Fig. 5 SEM image of Fe/K/S catalyst

low temperature can be ascribed to the decomposition of Pd β-hydrides formed on Pd^0 deriving from the reduction of PdO_x clusters, which are reduced at low temperatures (Zheng et al. 2008; Echeandia et al. 2014), lower than the starting temperature adopted for these TPR analyses. The shoulder appearing in the temperature range 200–300 °C can be attributed to the reduction of surface In_2O_3 and the formation of oxygen vacancies (Jiang et al. 2020; Wang et al. 2020), whereas peaks at higher temperatures can be ascribed to the reduction of bulk In_2O_3 (Rui et al. 2017).

The Fe/K/S sample (Fig. 6c) shows a very complex TPR profile consisting of several unresolved peaks in the temperature range 400–950 °C. Similar reduction features were observed for SBA-15-suppored Fe-based catalysts by Cano and co-workers (Cano et al. 2017), who ascribed such a complex profile to the reduction of Fe^{3+} and Fe^{2+} species in oxides particles of different sizes and with different interactions with the silica support. Moreover, in the case of a *K*-promoted sample, they also observed a contribution at very high temperatures (> 720 °C), which was ascribed to the formation of K^+ ionic species on the SBA-15 surface. The appearance of the numerous reduction peaks in the TPR profile of the present Fe/K/S sample can be explained accordingly.

For the Cu/Zn/S, In/Pd/S, and Fe/K/S catalysts, the extent of reduction (%) was calculated from the amount of hydrogen consumed during TPR analyses by considering stoichiometric Me^{n+}:H_2 ratios equal to 1:1 ($Me = Cu^{2+}$) or 2:3 ($Me = In^{3+}$, Fe^{3+}). The obtained values were 100, 79, and 65%, indicating that the reducibility of the Me^{n+} species decreases in the order $Cu^{2+} > In^{3+} > Fe^{3+}$.

Basicity of catalysts

The surface basic properties of the prepared samples were investigated by CO_2-TPD, and the results are shown in Fig. 7. According to the literature (Wang et al. 2020), desorption peaks at lower temperatures (50–300 °C) are ascribable to CO_2 interacting with weak (α-type) and medium strength (β-type) basic sites, related to OH^- groups and to metal–oxygen pairs, respectively (Gao et al. 2013); strong basic sites (γ-type), responsible for desorption peaks at higher temperatures, are instead associated with low-coordination oxygen atoms (Gao et al. 2013). The TPD profile of Cu/Zn/S presents only one peak with a maximum corresponding to 480 °C (Fig. 7.), which is indicative of the presence of strong basic sites. On the contrary the other two samples show contributions in a wider interval of temperatures (80–500 °C), which point out the presence of sites in the whole range of basic strength. The amount of adsorbed CO_2, estimated from the peak area after calibration of the TCD response, was 20, 109, and 55 mmol/g for Cu/Zn/S, In/Pd/S, and Fe/K/S, respectively.

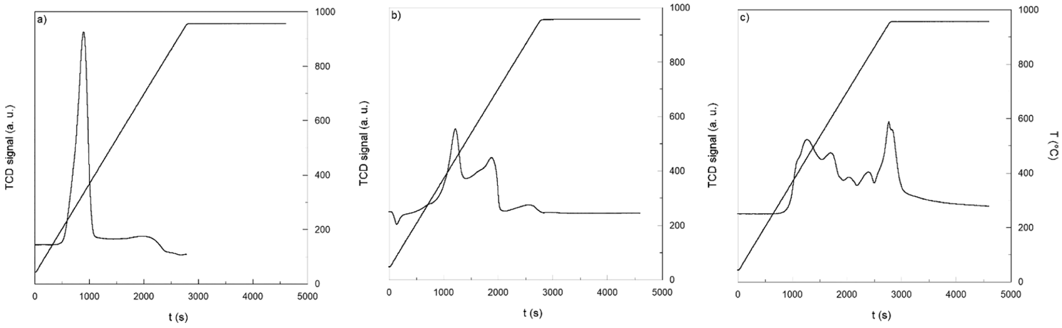

Fig. 6 TPR profiles of the as-prepared catalysts: **a** Cu/Zn/S, **b** In/Pd/S, **c** Fe/K/S

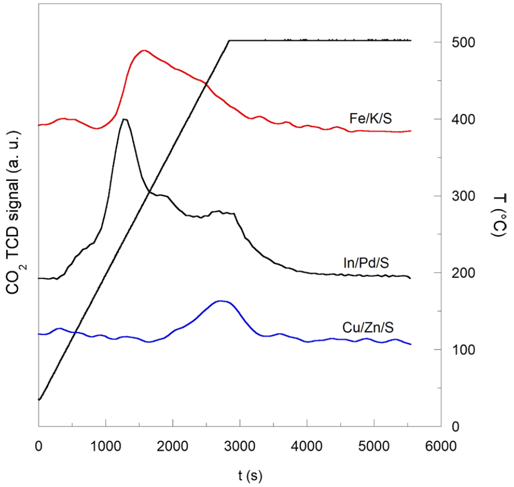

Fig. 7 CO$_2$-TPD profiles of the as-prepared catalysts

Catalytic activity

The catalysts were tested in the CO$_2$ hydrogenation reaction under the same reaction conditions, 250 °C, 20 bar, H$_2$ to CO$_2$ molar ratio 4 to 1. The results are reported in Figs. 8 and 9. The highest catalytic activity was shown by the Cu/Zn/S catalyst, for which CO2 conversion reached 21.3% and STY was 175 mgCH$_3$OH h^{-1} gcat^{-1}. The comparison with previous published results shows that kaolinite as admixture did not enhance the yield of methanol, see Table 3. The present STY value is comparable with that obtained by Mureddu et al. (158 mgCH$_3$OH h^{-1} gcat^{-1}), for a similar catalyst, tested in different reaction conditions (30 bar) (Mureddu et al. 2019). Considering the equilibrium CO$_2$ conversion by different reaction conditions: 523 K 30 bar 3:1—23.07 mol% and 523 K 20 bar 4:1—23.33 mol% (Shen et al. 2000), our obtained STY comparison, 158 and 175 mgCH$_3$OH h^{-1} gcat^{-1}, accordingly, has similar tendency. Cu/Zn/S catalyst showed high activity during the whole reaction time (50 h) (see Fig. 8). The obtained results could be explained by the presence of strong basic sites in Cu/Zn/S. It is known that surface basicity enhances CO$_2$ adsorption and promotes CO$_2$ conversion, as well as it can increase methanol selectivity (Li et al. 2019). This high activity can also be attributed to the good dispersion of the tenorite and zinc oxide phases and the small size of the nanoparticles.

In/Pd/S showed lower activity for methanol production than Cu/Zn/S—the CO$_2$ conversion was 3.1%, and the methanol yield (3 mg$_{CH3OH}$ h^{-1} g$_{cat}$$^{-1}$) obtained was extremely lower than that of Cu/Zn/S catalyst. In addition, the In/Pd/S catalyst showed lower methanol selectivity as it produced also 9% methane (see product distribution in dry gaseous phase, Fig. 9). This can be attributed to the lower reducibility of In^{3+} than Cu^{2+} and the metal-support interaction—for In/Pd/S catalyst the particles are larger and distributed mainly on the surface of the SBA-15.

Fe/K/S catalyst showed the lowest activity (CO$_2$ conversion 0.8%) in CO$_2$ hydrogenation reaction, the main product obtained was methane (see Fig. 9). The CO$_2$ hydrogenation reaction results of Fe/K supported on SBA-15 showed that the metal-support interaction affected the properties of this catalyst, resulting in methane as the main reaction product, similarly to Fischer–Tropsch synthesis at temperatures below 250 °C (Toncón-Leal et al. 2022).

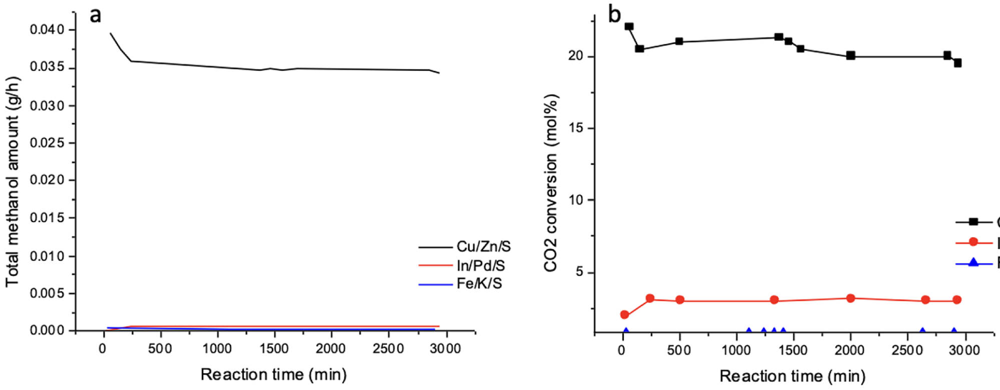

Fig. 8 Catalytic activity: **a** total methanol amount obtained, **b** CO$_2$ conversion efficiency against reaction time

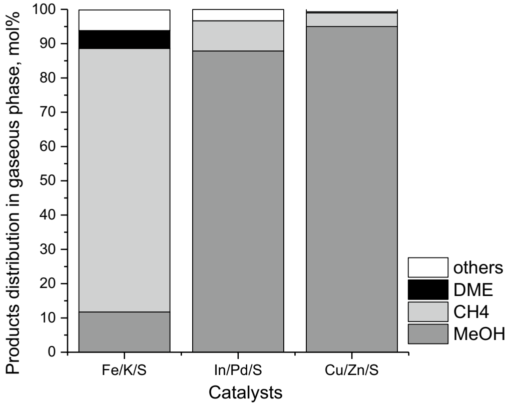

Fig. 9 Product distribution in gaseous phase

Conclusions

Three different catalytic systems were synthesized using mesoporous silica SBA-15 as a support material by co-impregnation method: copper-based catalyst with zinc, indium-based catalyst with palladium and iron-based catalyst with potassium. The characterization showed that main phases obtained were tenorite, palladinite, indium oxide and hematite, respectively. ICP-AES results showed that Cu/Zn catalytic system is the most appropriate for loading on SBA-15 support, as practically all metal amount calculated was loaded. Catalyst characterization showed that the smallest nanoparticles, the good dispersion of metal oxide phases and the highest reducibility can be obtained with Cu/Zn/S catalyst. CO_2-TPD data showed presence of strong basic sites for Cu/Zn/S. It resulted with the highest methanol yield in CO_2 hydrogenation reaction, 0.035 g/h at 250 °C, 20 bar, H_2 to CO_2 molar ratio 4 to 1 using fixed-bed tubular micro-activity reactor.

Acknowledgements This work has been supported by the European Regional Development Fund within the Activity 1.1.1.2 “Post-doctoral Research Aid” of the Specific Aid Objective 1.1.1 “To increase the research and innovative capacity of scientific institutions of Latvia and the ability to attract external financing, investing in human resources and infrastructure” of the Operational Programme “Growth and Employment” (No.1.1.1.2/VIAA/3/19/396). The study was partially supported by the Estonian Research Agency project PRG4 and the European Regional Development Fund project “Emerging orders in quantum and nanomaterials” (TK134).

Declarations

Conflict of interest The authors declare that they have no known competing financial interests or personal relationships that could have appeared to influence the work reported in this paper.

References

Abelniece Z, Kampars V, Piirsoo HM, Mändar H, Tamm A (2021) The effect of temperature on methanol synthesis via CO_2 hydrogenation at low pressure over ZnO/CuO/SBA-15/kaolin catalyst. Int Multidiscip Sci GeoConf SGEM 21(41):119–126

Abelniece Z, Kampars V, Piirsoo HM, Mändar H, Tamm A (2022) Effect of the Cu/ZnO/SBA-15/kaolinite preparation method on the catalyst structural properties and catalytic performance at CO_2 hydrogenation at low pressure. Environ Prog Sustain Energ. https://doi.org/10.1002/ep.13905

Alothman ZA (2012) A review: fundamental aspects of silicate mesoporous materials. Materials 5(12):2874–2902. https://doi.org/10.3390/ma5122874

Atsbha TA, Yoon T, Seongho P, Lee C-J (2021) A review on the catalytic conversion of CO_2 using H_2 for synthesis of CO, methanol, and hydrocarbons. J CO2 Utilization 44:101413. https://doi.org/10.1016/j.jcou.2020.101413

Batista J, Pintar A, Mandrino D, Jenko M, Martin V (2001) XPS and TPR examinations of γ-alumina-supported Pd-Cu catalysts. Appl Catal A 206(1):113–124. https://doi.org/10.1016/S0926-860X(00)00589-5

Cano LA, Garcia Blanco AA, Lener G, Marchetti SG, Sapag K (2017) Effect of the support and promoters in Fischer–Tropsch synthesis using supported Fe catalysts. Catal Today 282:204–213. https://doi.org/10.1016/j.cattod.2016.06.054

Chen H, Cui H, Lv Y, Liu P, Hao F, Xiong W, Luo H (2022) CO2 hydrogenation to methanol over Cu/ZnO/ZrO2 catalysts: effects of ZnO morphology and oxygen vacancy. Fuel 314:123035. https://doi.org/10.1016/j.fuel.2021.123035

Table 3 Comparison of catalysts studied in this work and previously

Catalyst	Catalyst composition	Preparation method	Reaction conditions	Methanol yield, mg CH_3OHh^{-1} $gcat^{-1}$	Reference
CZS_K_1	Cu, Zn, SBA-15, kaolinite. Metal loadings (experimental) of Cu and Zn are 19 and 3 wt.%, respectively	Co-impregnation method with glycine	250 ℃, 20 bar, H2: CO2 molar ratio 3:1	36	(Abelniece et al. 2022)
Cu/Zn/S	Cu, Zn, SBA-15. Metal loadings (experimental) of Cu and Zn are 20 and 7 wt.%, respectively	Co-impregnation method	250 ℃, 20 bar, H2: CO2 molar ratio 4:1	175	This work

Echeandia S, Pawelec B, Barrio VL, Arias PL, Cambra JF, Loricera CV, Fierro JLG (2014) Enhancement of phenol hydrodeoxygenation over Pd catalysts supported on mixed HY zeolite and Al2O3. An approach to *O*-removal from bio-oils. Fuel 117:1061–1073. https://doi.org/10.1016/j.fuel.2013.10.011

Gao P, Li F, Zhan H, Zhao N, Xiao F, Wei W, Zhong L, Wang H, Sun Y (2013) Influence of Zr on the performance of Cu/Zn/Al/Zr catalysts via hydrotalcite-like precursors for CO_2 hydrogenation to methanol. J Catal 298:51–60. https://doi.org/10.1016/j.jcat.2012.10.030

Jiang H, Lin J, Xiaohui W, Wang W, Chen Y, Zhang M (2020) Efficient hydrogenation of CO_2 to methanol over Pd/In2O3/SBA-15 catalysts. J CO2 Utilization 36:33–39. https://doi.org/10.1016/j.jcou.2019.10.013

Li Z, Men Y, Liu S, Wang J, Qin K, Tian D, Shi T, Zhang L, An W (2022) Boosting CO2 hydrogenation efficiency for methanol synthesis over Pd/In2O3/ZrO2 catalysts by crystalline phase effect. Appl Surf Sci 603(May):154420. https://doi.org/10.1016/j.apsusc.2022.154420

Mao D, Zhang J, Zhang H, Wu D (2022) A highly efficient Cu-ZnO/SBA-15 catalyst for CO_2 hydrogenation to CO under atmospheric pressure. Catal Today 402(March):60–66. https://doi.org/10.1016/j.cattod.2022.03.002

Mendez CM, Olivero H, Damiani DE, Volpe MA (2008) On the role of Pd β-hydride in the reduction of nitrate over Pd based catalyst. Appl Catal B 84(1–2):156–161. https://doi.org/10.1016/j.apcatb.2008.03.019

Mureddu M, Ferrara F, Pettinau A (2019) Highly efficient CuO/ZnO/ZrO2@SBA-15 nanocatalysts for methanol synthesis from the catalytic hydrogenation of CO_2. Appl Catal B Environ 258:117941. https://doi.org/10.1016/j.apcatb.2019.117941

Rui N, Wang Z, Sun K, Ye J, Ge Q, Liu C, jun. (2017) CO_2 hydrogenation to methanol over Pd/In2O3: effects of Pd and oxygen vacancy. Appl Catal B 218:488–497. https://doi.org/10.1016/j.apcatb.2017.06.069

Shaozhong Li Y, Wang BY, Guo L (2019) A highly active and selective mesostructured Cu/AlCeO catalyst for CO_2 hydrogenation to methanol. Appl Catal A Gen 571:51–60. https://doi.org/10.1016/j.apcata.2018.12.008

Shen W-J, Jun K-W, Choi H-S, Lee K-W (2000) Thermodynamic investigation of methanol and dimethyl ether synthesis from CO_2 Hydrogenation. Korean J Chem Eng 17(2000):210–216. https://doi.org/10.1007/BF02707145

Shozi ML, Dasireddy VDBC, Singh S, Mohlala P, Morgan DJ, Iqbal S, Friedrich HB (2017) An investigation of Cu-Re-ZnO catalysts for the hydrogenolysis of glycerol under continuous flow conditions. Sustain Energy Fuels 1(6):1437–1445. https://doi.org/10.1039/C7SE00199A

Stangeland K, Li H, Yu Z (2020) CO2 hydrogenation to methanol: the structure–activity relationships of different catalyst systems. Energy Ecol Environ 5(4):272–285. https://doi.org/10.1007/s40974-020-00156-4

Toncón-Leal CF, Múnera JF, Arroyo-Gómez JJ, Sapag K (2022) Fe, Co and Fe/Co catalysts supported on SBA-15 for Fischer–Tropsch synthesis. Catal Today 394–396:150–160. https://doi.org/10.1016/j.cattod.2021.07.023

Wang W, Qu Z, Song L, Fu Q (2020) CO2 hydrogenation to methanol over Cu/CeO2 and Cu/ZrO2 catalysts: tuning methanol selectivity via metal-support interaction. J Energy Chem 40:22–30. https://doi.org/10.1016/j.jechem.2019.03.001

Xi X, Zeng F, Zhang H, Wu X, Ren J, Bisswanger T, Stampfer C, Hofmann JP, Palkovits R, Heeres HJ (2021) CO_2 hydrogenation to higher alcohols over K-promoted bimetallic Fe−in catalysts on a Ce−ZrO2 support. ACS Sustain Chem Eng 9(18):6235–6249. https://doi.org/10.1021/acssuschemeng.0c08760

Xu D, Ding M, Hong X, Liu G (2020) Mechanistic aspects of the role of K promotion on Cu−Fe-based catalysts for higher alcohol synthesis from CO_2 hydrogenation. ACS Catal 10(24):14516–14526. https://doi.org/10.1021/acscatal.0c03575

Yao R, Wei J, Ge Q, Xu J, Han Y, Ma Q, Xu H, Sun J (2021) Monometallic iron catalysts with synergistic Na and S for higher alcohols synthesis via CO_2 hydrogenation. Appl Catal B 298(July):120556. https://doi.org/10.1016/j.apcatb.2021.120556

Ye J, Liu C, Mei D, Ge Q (2013) Active oxygen vacancy site for methanol synthesis from CO_2 hydrogenation on In2O3 (110): a DFT study. ACS Catal 3(6):1296–1306. https://doi.org/10.1021/cs400132a

Zhao D, Feng J, Huo Q, Melosh N, Fredrickson GH, Chmelka BF, Stucky GD (1998) Triblock copolymer syntheses of mesoporous silica with periodic 50 to angstrom pores. Science 279(5350):548–552. https://doi.org/10.1126/science.279.5350.548

Zheng J, Guo M, Song C (2008) Characterization of Pd catalysts supported on USY zeolites with different SiO_2/Al_2O_3 ratios for the hydrogenation of naphthalene in the presence of benzothiophene. Fuel Process Technol 89(4):467–474. https://doi.org/10.1016/j.fuproc.2007.11.025

Stanke, A., Lazdovica, K.

The promotional effect of potassium on iron-based silica supported catalyst for CO_2 hydrogenation.

*International Multidisciplinary Scientific GeoConference Surveying Geology and Mining Ecology Management, SGEM **2022**: Conference Proceeding,* 22(4.1), pp. 161–166.

https://doi.org/10.5593/sgem2022/4.1/s17.21

THE PROMOTIONAL EFFECT OF POTASSIUM ON IRON-BASED SILICA SUPPORTED CATALYST FOR CO2 HYDROGENATION

Agija Stanke[1]

Dr. Kristine Lazdovica[2]

[1] Riga Technical University, Institute of Applied Chemistry, **Latvia**
[2] Riga Technical University, Institute of Applied Chemistry, **Latvia**

ABSTRACT

Climate change is one of the biggest global challenges. As a result of human activity, large amounts of greenhouse gases are released into the atmosphere, contributing to global warming. Carbon dioxide (CO_2) is a major greenhouse gas, therefore, hydrogenation of CO_2 to value-added chemicals and liquid fuels is of great importance for a sustainable future. It is well known that iron-based catalysts can demonstrate good activity in the hydrogenation of CO_2. However, catalysts need to be improved to promote the formation of liquid hydrocarbons. In this study, a series of silica supported iron catalysts promoted with potassium were prepared by impregnation method. The samples were characterized by X-ray fluorescence spectroscopy, X-ray diffraction, and N_2 adsorption-desorption analysis. Catalytic performance of K-0, K-2, and K-5 was investigated for CO_2 hydrogenation in a fixed bed reactor operated at 300 degrees Celsius and 20 bar. The reaction products were analysed by gas chromatography and FT-IR spectroscopy. The results showed that promotion with potassium reduces the selectivity of methane and reduces the amount of gas phase hydrocarbons. At the same time promotion with potassium contributed to the formation of alcohols in the liquid phase products. The highest methanol yield was obtained using the K-2 catalyst, while the K-5 catalyst promoted the formation of both methanol and ethanol in the liquid phase.

Keywords: CO2 hydrogenation, iron catalyst, potassium

INTRODUCTION

Climate change, caused by rising greenhouse gas emissions, is one of today's biggest global challenges. Human activities release large amounts of greenhouse gases into the atmosphere, which contribute to global warming [1]. Carbon dioxide (CO_2) is a major greenhouse gas, therefore, hydrogenation of CO_2 to value-added chemicals and liquid fuels is of great importance for a sustainable future [2].

Direct CO_2 hydrogenation to hydrocarbons can be achieved via modified Fischer-Tropsch synthesis route [3]. This synthesis route is a combination of two reactions: the reverse water gas shift (RWGS; Eq. 1) and the Fischer-Tropsch synthesis (FTS; Eq. 2).

$$\text{RWGS} \qquad nCO_2 + nH_2 \leftrightarrow nCO + nH_2O \qquad (1)$$

$$\text{FTS} \qquad nCO + 2nH_2 \leftrightarrow (\text{-}CH_2\text{-})_n + nH_2O \qquad (2)$$

Iron-based catalysts are capable of catalysing both FTS and RWGS reactions and thus are preferred catalyst candidates for CO_2 hydrogenation via modified Fischer-Tropsch synthesis [4].

Compared to traditional FTS, hydrogenation of CO_2 requires more hydrogen. High H/C ratio in turns promotes the formation of methane [5]. The use of a potassium promoter can inhibit methane formation and promote the growth of the hydrocarbon chain [6]. Potassium is one of the most widely used promoters for FTS iron-based catalysts [7], however, there are still some inconsistencies due to the fact that studies are performed under different conditions or using different catalytic systems. Besides, it should be noted that the effect of the potassium promoter depends not only on the loading of potassium but also on the conversion of CO [8].

On the other hand, the effect of potassium on the CO_2 hydrogenation have not been extensively studied. In this study the effect of potassium on the catalytic performance of silica-supported iron-based catalyst is investigated for direct CO_2 hydrogenation.

MATERIALS & METHODS

Iron-based catalysts used in the study were prepared by wet impregnation method on SiO_2 support granules with a surface area of 261 m^2/g and pore volume 1.09 mL/g.

80 mL of 0.84 M aqueous solution of Fe nitrate was added to the SiO_2 support (30 g), and the mixture was left to stir for 5 h. Mixture was then filtered, and the granules were dried in an oven at 110 °C for 2 h and then calcined at 550 °C for 5 h. The catalyst was denoted as K-0. To obtain catalysts with K/Fe molar ratios 2/100 and 5/100, calculated amounts of KNO_3 were dissolved in ethanol and catalyst granules were immersed in these solutions, the solvent was evaporated, and the granules were calcined at 550 °C for 5 h. Catalysts were denoted as K-2, and K-5, respectively.

X-ray fluorescence (XRF) analysis was performed using *Rigaku Supermini Wavelength* X-ray dispersive fluorescence spectrometer (WDXRFS) with a Rh X-ray tube to determine iron concentration.

Nitrogen physisorption experiments were performed using surface area and pore size analyser *Nova 1200e (Quantachrome Instruments)* to characterize the porosity of the catalysts. The total pore volume was determined from the amount of nitrogen absorbed at a relative pressure of 0.99. The average pore diameter and pore size distribution were obtained by the Barrett-Joyner-Halenda (BJH) method.

The powder X-ray diffraction (XRD) patterns were obtained with a *Bruker AXS ADVANCE* diffractometer using Cu-K_α radiation to identify the phases of iron-based catalysts.

CO_2 hydrogenation tests were performed in a fixed-bed reactor. Before each experiment, 0.7 g of catalyst was loaded in the reactor. The catalyst was reduced by H_2 at 400 °C under atmospheric pressure for 4 h. Then the heating was stopped, and the temperature naturally decreased to 250 °C. Subsequently, the pressure of reactor was slowly increased up to 20 bar by feeding the reactant gases (H_2:CO_2:N_2 3:1:1). Lastly, the temperature of the reactor was elevated to 300 °C.

The reaction effluent gases passed hot trap (120 °C) and cold trap (5 °C). After these product collectors, the tail gas was analysed using a gas chromatograph (*Shimadzu Nexis GC-2030*).

H_2, CH_4, CO_2, N_2, and CO were separated using two *Restek Porapak Q* columns and a *Restek Molesieve 5A* column and detected with a thermal conductivity detector (TCD). C_1 – C_8 hydrocarbons in the gas phase were analysed on *Restek Rt-Q-Bond* column with a flame ionization detector (FID).

Condensed products were analysed using a gas chromatograph (*Shimadzu Nexis GC-2030*) with *Restek Rtx®-5MS* column and FID, and mass spectrometer (*Shimadzu GCMS-QP2020NX*).

Fourier Transform Infrared (FTIR) spectra of condensed products were taken in mid-infrared range of 650-4000 cm^{-1} using *PerkinElmer Spectrum 100* spectrometer fitted with a diamond prism *Universal Attenuated Total Reflectance Sampling* accessory.

RESULTS & DISCUSSION

The textural properties of catalysts are summarized in Table 1. With increasing potassium contents, the surface area and pore volume decreases while average pore diameter slightly increases. These results could indicate that potassium might be clogging the smaller pores.

Table 1. Texture properties of catalysts

Catalyst	Surface area, m^2/g	Average pore diameter, nm	Mean pore diameter, nm	Pore volume, cm^3/g
K-0	207	15.3	11.8	0.79
K-2	201	15.5	11.8	0.78
K-5	195	15.6	11.7	0.76

The crystallite structures of the samples before and after the CO_2 hydrogenation reaction were characterized by XRD as shown in Figure 1. The XRD patterns were compared with the ICDD files. For all catalysts before the CO_2 hydrogenation reaction peaks corresponding to hematite (α-Fe_2O_3; ICDD card no: 00-033-0664) can be observed. No other phases corresponding to Fe or K species were detected in the diffractograms.

After the CO_2 hydrogenation diffraction peaks corresponding to iron carbide (Fe_5C_2; ICDD card no: 01-080-4102) and moissanite (α-SiC; ICDD card no: 01-072-9272) can be observed. Fe_5C_2 is reported to catalyse both FTS and RWGS reactions, besides its activity towards FTS or RWGS is dependent on the CO_2 conversion level. At low CO_2 conversions Fe_5C_2 will catalyse RWGS while at high CO_2 conversions it will be more active towards FTS [9]. The role of α-SiC on CO_2 hydrogenation is not previously reported.

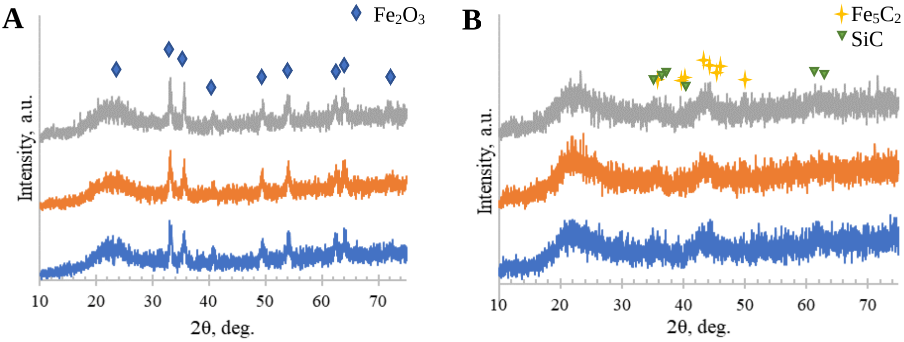

Figure 1. XRD patterns of catalysts before (A) and after (B) the CO_2 hydrogenation reaction

The effect of potassium promotion on the CO_2 hydrogenation was investigated at T=300 °C, P=20 bar. Since the effect of the potassium promoter may vary depending on the conversion level, data for the hydrocarbon selectivity were taken at a conversion of 10%.

Figure 2 shows the effect of potassium on the relative yields of gas phase hydrocarbons evaluated by GC-MS/FID. As it can be seen, the relative yields of hydrocarbons decreased with increasing loading of potassium. At the same time, the overall proportion of CH_4, C_2H_x, C_3H_x, and C_4H_x remained almost unchanged (Figure 3). Only in the presence of K-2 catalyst the proportion of CH_4 in gas phase hydrocarbons slightly decreased while the proportion of C_3H_x hydrocarbons slightly increased.

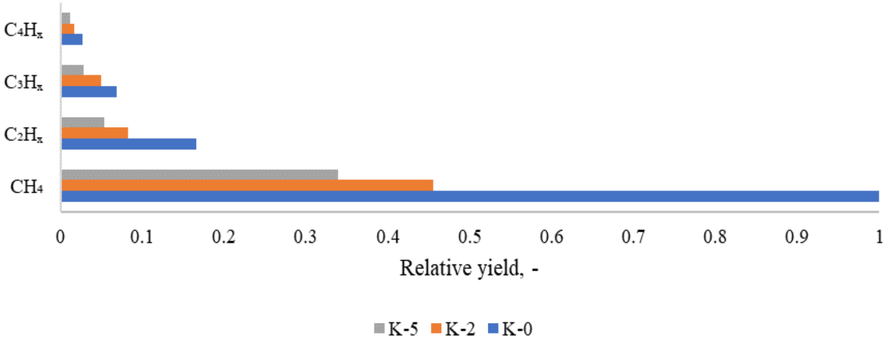

Figure 2. Effect of potassium on the relative yields of gas phase hydrocarbons

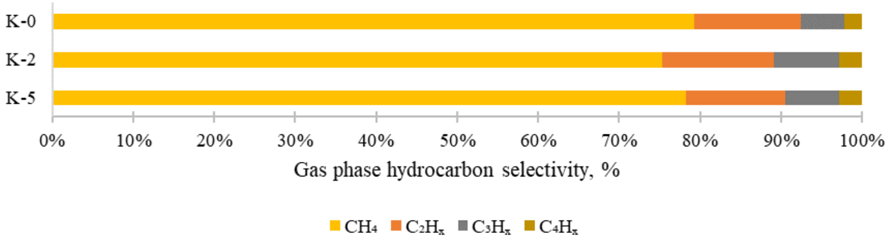

Figure 3. Effect of potassium on the gas phase hydrocarbons

Reaction condensed products consisted of water, methanol, ethanol, *n*-propanol, and acetone (Figure 4). With the loading of potassium increasing, the selectivity of n-propanol decreased, and the selectivity of acetone increased, whereas methanol and ethanol showed parabola like dependency of potassium loading. The highest yield of condensed products was observed for K-2 catalyst. The main product for K-0 and K-2 was methanol, whereas the main product for K-5 was acetone. Alcohols are primary Fischer-Tropsch synthesis products, whereas ketones are secondary products. Results indicate that potassium promotes the secondary reactions of 1-olefins leading to the formation of ketones (acetone) through Wacker-Tsuji oxidation [10].

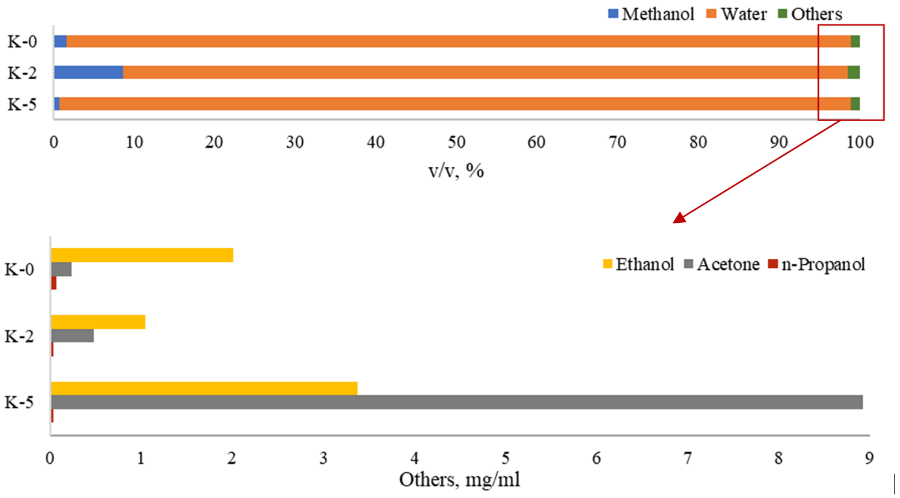

Figure 4. The influence of potassium on the composition of the aqueous phase products, resulting from FTIR and GC-MS/FID analysis

CONCLUSION

Iron-based silica supported catalysts promoted with potassium were synthesised and tested for CO_2 hydrogenation at 300 °C and 20 bar. The addition of the potassium promoter slightly reduced the surface area and pore volume of the catalyst, indicating that the potassium precursor is located in the pores of the catalyst. XRD results indicated the presence of α-Fe_2O_3 before the CO_2 hydrogenation and the presence of Fe_5C_2 and SiC after the CO_2 hydrogenation.

CO_2 hydrogenation reaction product yields and composition of products was strongly influenced by the potassium content. With increasing loading of potassium relative yields of gas phase products (i.e. C_1-C_4 hydrocarbons) decreased. Potassium contributed to the formation of oxygenates – methanol was the main aqueous phase product for K-0 and K-2 catalysts, while acetone was the main aqueous phase product for K-5. It can be concluded that potassium promotes the secondary reactions of 1-olefins.

The best CO_2 hydrogenation performance was observed over K-2 catalyst. Using this catalyst, it was possible to obtain the largest amount of condensed products with the methanol content of 8.1 v/v%.

ACKNOWLEDGEMENTS

This work has been supported by the European Social Fund within the Project No 8.2.2.0/20/I/008 «Strengthening of PhD students and academic personnel of Riga Technical University and BA School of Business and Finance in the strategic fields of specialization» of the Specific Objective 8.2.2 «To Strengthen Academic Staff of Higher Education Institutions in Strategic Specialization Areas» of the Operational Programme «Growth and Employment». This research/publication was supported by Riga Technical University's Doctoral Grant programme.

REFERENCES

[1] Li W., Wang H., Jiang X., Zhu J., Liu Z., Guo X., Song C., A short review of recent advances in CO2 hydrogenation to hydrocarbons over heterogeneous catalysts, RSC Adv., vol. 8, pp 7651–7669, 2018.

[2] Choi Y.H., Jang Y.J., Park H., Kim W.Y., Lee Y.H., Choi S.H., Lee J.S., Carbon dioxide Fischer-Tropsch synthesis: A new path to carbon-neutral fuels, Appl. Catal. B Environ., vol. 202, pp 605–610, 2017.

[3] Wei J., Ge Q., Yao R., Wen Z., Fang C., Guo L., Xu H., Sun J., Directly converting CO2 into a gasoline fuel, Nat. Commun., vol. 8, pp 1–8, 2017.

[4] Albrecht M., Rodemerck U., Schneider M., Bröring M., Baabe D., Kondratenko E. V., Unexpectedly efficient CO2 hydrogenation to higher hydrocarbons over non-doped Fe2O3, Appl. Catal. B Environ., vol. 204, pp 119–126, 2017.

[5] Gao P., Zhang L., Li S., Zhou Z., Sun Y., Novel heterogeneous catalysts for CO2 hydrogenation to liquid fuels, ACS Cent. Sci., vol. 6, pp 1657–1670, 2020.

[6] Rodemerck U., Holeňa M., Wagner E., Smejkal Q., Barkschat A., Baerns M., Catalyst development for CO2 hydrogenation to fuels, ChemCatChem., vol. 5, pp 1948–1955, 2013.

[7] Wan H., Wu B., Zhang C., Xiang H., Li Y., Promotional effects of Cu and K on precipitated iron-based catalysts for Fischer-Tropsch synthesis, J. Mol. Catal. A Chem., vol. 283, pp 33–42, 2008.

[8] Ma W., Shafer W.D., Jacobs G., Yang J., Sparks D.E., Hamdeh H.H., Davis B.H., Fischer-Tropsch synthesis: Effect of CO conversion on CH4 and oxygenate selectivities over precipitated Fe-K catalysts, Appl. Catal. A , Gen., vol. 560, pp 144–152, 2018.

[9] Liu J., Zhang G., Jiang X., Wang J., Song C., Guo X., Insight into the role of Fe5C2 in CO2 catalytic hydrogenation to hydrocarbons, Catal. Today., vol. 371, pp 162–170, 2021.

[10] Shafer W.D., Gnanamani M.K., Graham U.M., Yang J., Masuku C.M., Jacobs G., Davis B.H., Fischer-Tropsch: Product selectivity-the fingerprint of synthetic fuels, Catalysts., vol. 9, 2019.

6. pielikums

Appendix 6

Stanke, A., Abelniece, Z., Sutka, A., Berzins, A., Kõiv, M., Lazdovica, K.

$NiFe_2O_4$ catalysts for CO_2 hydrogenation: Performance analysis and comparative life cycle assessment of catalyst synthesis routes.

Nepublicētie rezultāti / Unpublished results

$NiFe_2O_4$ catalysts for CO_2 hydrogenation: Performance analysis and comparative life cycle assessment of catalyst synthesis routes

Agija Stanke[a*], Zane Abelniece[a], Andris Sutka[b], Agris Berzins[c], Markus Kõiv[d], Kristine Lazdovica[a]

[a]Riga Technical University, Faculty of Natural Sciences and Technology, Institute of Chemistry and Chemical Technology, Paula Valdena 3, Riga, LV-1048, Latvia

[b]Riga Technical University, Faculty of Natural Sciences and Technology, Institute of Physics and Material Science, Paula Valdena 7, Riga, LV-1048, Latvia

[c]University of Latvia, Faculty of Medicine and Life Sciences, Department of Chemistry, Riga, LV-1048, Latvia

[d]University of Tartu, Faculty of Science and Technology, Institute of Physics, W. Ostwaldi 1, 50411 Tartu, Estonia

Abstract. This study integrates an experimental evaluation of the CO_2 hydrogenation performance of $NiFe_2O_4$ spinel ferrite catalysts with a comparative life cycle assessment of their synthesis routes. Three synthesis methods were investigated: sono-chemical, sol-gel auto-combustion, and reducing agent-assisted precipitation. The employed synthesis method significantly influenced the phase purity, structural properties and catalytic performance of $NiFe_2O_4$. Sono-chemical synthesis demonstrated strong pH sensitivity; higher pH reduced crystallite size but increased phase impurities. Sol-gel auto-combustion yielded highly heterogeneous samples. The reducing agent-assisted precipitation produced phase-pure $NiFe_2O_4$ with a small crystallite size and high surface area, resulting in superior hydrogenation activity. Life cycle assessment identified electricity consumption as the dominant contributor to most of the impact categories. $NiFe_2O_4$-Prec (reducing agent-assisted precipitation) exhibited the lowest environmental burden across the majority of analysed categories. Given its high phase purity, superior hydrogenation activity and reduced ecological footprint, $NiFe_2O_4$-Prec is identified as a promising candidate for sustainable e-LNG production.

Keywords: *CO_2 hydrogenation, nickel ferrite catalysts, spinel, environmental impact*

1. Introduction

The global energy landscape is undergoing a paradigm shift driven by the urgent need to decarbonise hard-to-abate sectors, such as heavy industry, aviation and shipping. Maritime

---

[*] Corresponding author. Tel. +371 22434622 (A. Stanke)

E-mail addresses: Agija.Stanke@rtu.lv (A. Stanke), Zane.Abelniece@rtu.lv (Z. Abelniece), Andris.Sutka@rtu.lv (A. Sutka), Agris.Berzins@lu.lv (A. Berzins), markus.koiv@ut.ee (M. Kõiv), Kristine.Lazdovica@rtu.lv (K. Lazdovica)

transport accounts for approximately 3% of global greenhouse gas (GHG) emissions [1]. Without additional measures to curb ship emissions, GHG emissions from the shipping sector are projected to increase by up to 130% by 2050 [2]. The International Maritime Organisation's (IMO) updated Ship Energy Efficiency Plan, promoting energy efficiency and the uptake of low- and zero-carbon fuels, targets net-zero emissions by 2050, with interim reductions of 20-30% by 2030 and 70-80% by 2040 [3].

To meet the IMO's ambitious net-zero targets, the production of e-fuels via Power-to-X processes represents a critical strategic pathway. This approach integrates hydrogen derived from water electrolysis with CO_2 captured from industrial effluents or directly from the air [4,5]. Within this framework, CO_2-based Fischer-Tropsch synthesis (CO_2-FTS) emerges as a key technology, coupling the reverse water-gas shift (RWGS) reaction (Eq. 1) with subsequent Fischer-Tropsch synthesis (FTS) (Eq. 2) to yield synthetic hydrocarbons [6].

$$CO_2 + H_2 \leftrightarrow H_2O + CO \qquad \Delta H^0_{298} = 41.2\ \text{kJ/mol} \qquad (1)$$

$$CO + 2H_2 \rightarrow (\text{-}CH_2\text{-}) + H_2O \qquad \Delta H^0_{298} = -152\ \text{kJ/mol} \qquad (2)$$

However, large-scale CO_2-FTS commercialisation remains limited due to challenges in conversion efficiency and product selectivity caused by kinetic and thermodynamic constraints [7–9]. The key factors in advancing this technology are optimised reactor systems and highly efficient, selective catalysts, capable of producing desired products at high yields with minimal energy input [7].

Iron-based catalysts are widely used for their dual functionality in promoting both the RWGS and FTS reactions. The integration of secondary metals with high activity for CO hydrogenation into a spinel oxide lattice has emerged as a superior strategy for improving CO_2-FTS performance. Unlike simple mixtures of metal oxides, spinel-like structures typically provide narrower particle size distributions, improved stoichiometric control, and consequently a larger active surface area available for catalytic reactions [10]. The spinel structure of $NiFe_2O_4$ offers a unique synergistic effect where nickel promotes high hydrogenation activity while iron species facilitate the necessary RWGS and carbon-carbon coupling essential for FTS.

Catalyst's textural properties, morphology, phase purity, and particle size can influence the catalytic performance. However, establishing definitive structure-activity relationships remains challenging due to the complex reaction pathways, the many parallel and sequential processes and structural evolution of catalysts [11,12]. Literature reports on particle size effects are often contradictory: while some studies associate smaller nanoparticles with high CH_4 selectivity [5,13,14], others observe a shift toward CO or increased methanation as particle size increases [9,15]. These contrasting results may be attributed to the variations in CO_2 hydrogenation conditions employed, the different catalytic systems used, and the diverse catalyst synthesis approaches adopted.

Despite the availability of numerous synthesis techniques, ranging from high-temperature solid-state reactions to various wet-chemical routes like co-precipitation, sol-gel and sono-chemical synthesis, no universal approach exists. Each method presents inherent trade-offs between crystallinity, particle size control and scalability [16,17]. While co-precipitation and sol-gel synthesis are widely utilised for their accessibility, sono-chemical synthesis offers a distant advantage in producing highly monodispersed nanoparticles with precise size distribution [14,18]. Consequently, the choice of synthesis method remains critical, as it directly affects the catalyst's phase purity, textural characteristics and overall performance in practical catalytic and functional applications.

The primary objective of this study is to elucidate the synthesis-structure-performance relationship of $NiFe_2O_4$ catalysts in CO_2 hydrogenation. A reaction temperature of 320 °C was chosen because it represents a “compromise point” in CO_2 hydrogenation over Fe-Ni catalysts, striking a balance between activity, selectivity, and catalyst stability. While previous research has often focused on optimising a single preparation route, this work provides a systematic comparison of three distinct wet-chemical approaches: sono-chemical synthesis, sol-gel auto-combustion and reducing agent-assisted precipitation. Furthermore, acknowledging the shift toward holistic catalyst design, this study integrates a prospective Life Cycle Assessment (LCA). This allows for a preliminary evaluation of the environmental trade-offs and health impacts associated with each synthesis at the laboratory scale. By bridging the gap between fundamental materials science, structural characterisation and environmental sustainability, this research offers critical insights into the responsible development of spinel-based catalysts for the green energy transition.

2. Experimental/Materials and methods

Iron(III) nitrate nonahydrate ($Fe(NO_3)_3{\cdot}9H_2O$), ammonium hydroxide ($NH_3{\cdot}H_2O$) and citric acid monohydrate ($C_6H_8O_7{\cdot}H_2O$) were purchased from Thermo Fisher Scientific. Nickel(II) nitrate hexahydrate ($Ni(NO_3)_2{\cdot}6H_2O$) was purchased from Alfa Aesar. Iron(III) chloride hexahydrate ($FeCl_3{\cdot}6H_2O$), nickel chloride ($NiCl_2$) and sodium borohydride ($NaBH_4$) were purchased from Sigma-Aldrich. Ethanol and sodium hydroxide (NaOH) were purchased from Lach-Ner. All chemicals were of reagent grade and used as received, without further purification.

2.1. Preparation of nickel ferrite ($NiFe_2O_4$) nanoparticles

Nickel ferrite nanoparticles were synthesised via three different methods: sono-chemical, sol-gel auto-combustion, and reducing agent-assisted precipitation. Schematic diagrams of the synthesis processes are shown in Fig. 1.

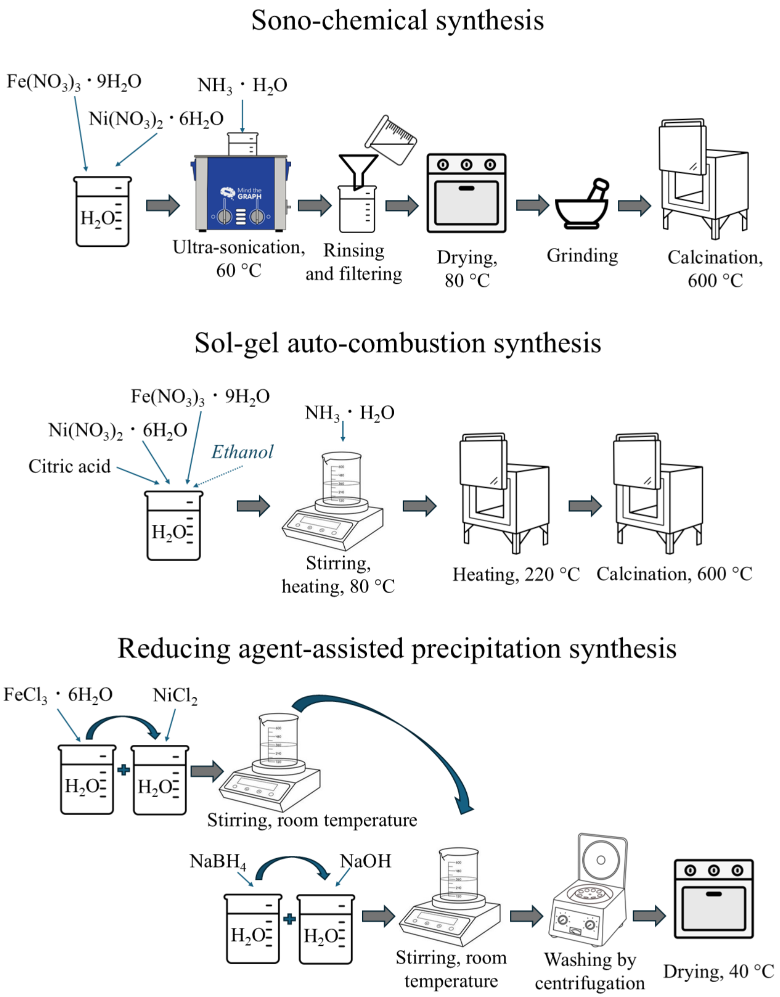
Sono-chemical synthesis

Sol-gel auto-combustion synthesis

Reducing agent-assisted precipitation synthesis

Fig. 1. Schematic diagram of the $NiFe_2O_4$ synthesis processes.

2.1.1. Sono-chemical synthesis

$Fe(NO_3)_3 \cdot 9H_2O$ (0.016 mol) and $Ni(NO_3)_2 \cdot 6H_2O$ (0.008 mol) were dissolved in 80 mL of distilled water and ultrasonicated in an *Elmasonic S30H* ultrasonic bath at 60 °C for 20 min. During ultra-sonication, $NH_3 \cdot H_2O$ (30%) was added dropwise to adjust the pH value, and the obtained suspension was further ultra-sonicated for 30 min. The precipitate was then rinsed with distilled water until pH 7, filtered and dried at 80 °C for 8 h. The product was then ground in a mortar to obtain a fine powder. The powder was calcined at 600 °C for 30 min in an air atmosphere with a heating ramp of 5 °C min^{-1}. Obtained nanoparticles were marked $NiFe_2O_4$-sono-X, where X represents the reaction pH (X=8, X=9, X=10, X=11).

2.1.2. Sol-gel auto-combustion synthesis

Citric acid (0.024 mol), $Fe(NO_3)_3{\cdot}9H_2O$ (0.016 mol) and $Ni(NO_3)_2{\cdot}6H_2O$ (0.008 mol) were dissolved in 80 mL of distilled water. Then, ethanol (0.048 mol) was added. The mixture was continuously stirred at 80 °C for 30 min. Then the pH was adjusted to around 7 by dropwise adding $NH_3{\cdot}H_2O$ (30%). The mixture was continuously stirred and kept at 80 °C until viscous brown gel formation. The gel was heated at 220 °C for 30 min in an air atmosphere with a heating ramp of 5 °C min^{-1}. The obtained powder was then calcined at 600 °C for 30 min in an air atmosphere with a heating ramp of 5 °C min^{-1}. The obtained nanoparticles were denoted as $NiFe_2O_4$-C-E.

Nanoparticles $NiFe_2O_4$-Citric were synthesised following the same procedure, except that ethanol was not used.

2.1.3. Reducing agent-assisted precipitation synthesis

Four separate aqueous solutions were prepared by dissolving $FeCl_3{\cdot}6H_2O$ (0.04 mol), $NiCl_2$ (0.02 mol), $NaBH_4$ (0.02 mol) and NaOH (0.05 mol), each in 25 mL of deionised water. Then, $FeCl_3$ solution was added to $NiCl_2$ solution, while $NaBH_4$ solution was added to NaOH solution. After mild stirring at room temperature for 10 minutes, the metal salt solution was added to the solution of NaOH and $NaBH_4$. The precipitation reaction occurred vigorously. After 10 minutes of stirring, the precipitated particles were washed with deionised water by centrifugation (6137 rpm, 10 min) several times while the pH was neutral. After washing, the sample was dried at 40 °C in ambient air till no weight loss could be observed. The obtained nanoparticles were denoted as $NiFe_2O_4$-Prec.

2.2. Characterisation

X-ray powder diffraction (XRPD) patterns were measured at ambient temperature on a AXS D8 Advance (Bruker) diffractometer using Cu Kα radiation (λ=0.1541 nm). The tube voltage and current were set to 40 kV and 40 mA. The diffraction patterns were recorded using a scanning speed of 5.0s/0.02° from 20° to 70° on the 2θ scale. For phase identification, the

ICDD (The International Centre for Diffraction Data) database PDF-2/Release 2021 was used. The phase composition of samples and crystallite sizes of the identified phases were determined by Rietveld refinement using Profex software. For all the phases, crystal structure data were obtained from COD (Crystallography Open Database): COD ID 9008693 for bunsenite (NiO), 9000139 for hematite (α-Fe_2O_3) and 1006116 for trevorite ($NiFe_2O_4$).

Textural properties of the catalysts were determined by N_2 adsorption-desorption analysis using Quantachrome Instruments Nova 1200 E-Series sorption analyser at -196 °C. Before the measurements, the samples were degassed at 150 °C for 24 h. The specific surface area was calculated by the Brunauer-Emmet-Teller (BET) method. Pore size distribution was determined by the Barrett-Joyner-Halenda (BJH) method based on the adsorbed amount at $P/P_0=0.99$.

Scanning electron microscopy (SEM) images were obtained using a Helios™ NanoLab 600 dual-beam microscope (FEI) operated at an accelerating voltage of 15 kV. The images were acquired using the secondary electron (SE) signal collected by an Everhart-Thornley detector (ETD).

2.3. CO_2 hydrogenation over nickel ferrite nanoparticles

CO_2 hydrogenation tests were performed in a stainless steel fixed-bed reactor. Tests were performed using the highest-purity $NiFe_2O_4$ sample obtained from each respective synthesis method. A 0.1 g catalyst was diluted with quartz sand to a 2 mL volume and filled into the reactor above a layer of quartz wool. The catalyst was reduced at 400 °C for 22 h in H_2 with a flow rate of 50 mL/min at atmospheric pressure. Then the reactor was cooled to 280 °C, and CO_2 (10 mL/min), H_2 (30 mL/min) and N_2 (10 mL/min) were continuously fed into the reactor using separate mass flow controllers. N_2 was used as an internal standard. The pressure was then gradually increased to 20 bar, and the temperature was gradually increased to 320 °C. The condensable products were collected in a cold trap (5 °C, 20 bar). The reaction exit gases were analysed on-line by a gas chromatograph (Shimadzu Nexis GC-2030). The conversion of CO_2 and the selectivity of products were calculated according to the equations:

CO_2 conversion $$X_{CO_2} = \frac{CO_{2\ in} - CO_{2\ out}}{CO_{2\ in}} \cdot 100\% \quad (1)$$

CO selectivity $$S_{CO} = \frac{CO_{out}}{CO_{2\ in} - CO_{2\ out}} \cdot 100\% \quad (2)$$

C_n selectivity $$S_{C_n} = \frac{C_{n\ out}}{CO_{2\ in} - CO_{2\ out}} \cdot 100\% \quad (3)$$

C_{5+} selectivity $$S_{C_{5+}} = 100\% - S_{CO} - S_{C_1} - S_{C_2} - S_{C_3} - S_{C_4} \quad (4)$$

were $CO_{2\ in}$ and $CO_{2\ out}$ represent the molar flow rate of CO_2 at the reactor inlet and outlet; CO_{out} represents the molar flow rate of CO at the reactor outlet; $C_{n\ out}$ represents the molar flow rate of hydrocarbons with n=1-4 carbon atoms at the reactor outlet.

Condensed reaction products were analysed off-line by gas chromatography using Shimadzu Nexis GC-2030 and Fourier Transform Infrared Spectroscopy (FTIR) using PerkinElmer Spectrum 100. The acidity of condensed products was determined by the KOH titration method.

The details of these procedures are reported in our previous study [19].

2.4. Life cycle assessment

2.4.1. Goal and scope definition

The objective of this assessment was to conduct a comparative LCA of three laboratory-scale synthesis routes for $NiFe_2O_4$ catalysts to identify and quantify their respective environmental burdens. A cradle-to-gate boundary was defined (Fig. 2), encompassing all stages from raw material extraction to the final synthesis of the catalyst. The catalyst use phase, end-of-life management, and transportation of precursors were excluded from the system boundaries.

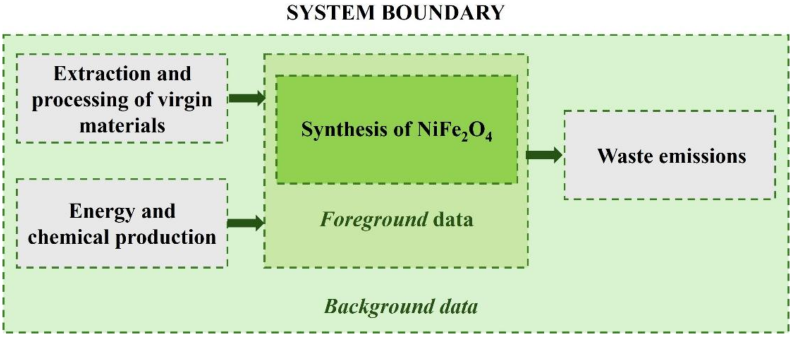

Fig. 2. System boundary for the LCA of the $NiFe_2O_4$ synthesis.

The functional unit was defined as the production of 1 kg of $NiFe_2O_4$ catalyst. Process modelling was performed using openLCA v2.4.1 software integrated with the Ecoinvent 3.11 (cut-off) database. Impact assessment was carried out using the Environmental Footprint 3.1 (EF v.3.1) method. For chemical precursors not present in the Ecoinvent database (iron nitrate, nickel nitrate and nickel chloride), proxy processes were developed based on stoichiometric requirements and weight distribution data to ensure a comprehensive inventory.

From the EF v.3.1 method, the following midpoint impact categories were selected for detailed analysis: acidification, climate change, ecotoxicity (freshwater), energy resources (non-renewable), eutrophication (freshwater), eutrophication (marine), eutrophication (terrestrial), human toxicity (carcinogenic), human toxicity (non-carcinogenic), ionising radiation (human health), material resources (metals/minerals), particulate matter formation, photochemical oxidant formation (human health), water use. Impact categories contributing less than 0.02 points to normalisation results were considered negligible and excluded.

2.4.2. Life Cycle Inventory

The foreground data for the sono-chemical, sol-gel auto-combustion, and reducing agent-assisted precipitation synthesis methods were primary data obtained directly from laboratory-scale experiments. To establish a robust inventory, specific assumptions were made regarding waste streams: liquid effluents were modelled as discharged to the municipal sewage system, gaseous emissions as released to the atmosphere, and solid residues as disposed of in landfill. The energy consumption of the equipment used for the laboratory-scale syntheses is provided in the Supplementary Information (Table S1). The corresponding inventories for each modelled process are also included in the Supplementary Information (Tables S2–S8).

3. Results and discussion

3.1. Catalyst characterisation

Table 1 shows the phase composition and crystallite sizes of the synthesised $NiFe_2O_4$ determined by the Rietveld refinement method. The XRPD diffractograms of synthesised samples are included in the Supplementary information (Fig. S1). For the sonochemically synthesised samples, the results indicated that crystallisation was sensitive to pH. As the pH increased, the average crystallite size of $NiFe_2O_4$ decreased; however, this was accompanied by a rise in phase impurities. At higher pH, nucleation is enhanced. Since growth and nucleation compete, the simultaneous formation of numerous nuclei limits their individual growth, resulting in smaller crystallite sizes [20]. At elevated pH, the accelerated precipitation of metal hydroxides can disrupt the stoichiometric balance between cations due to their differing precipitation kinetics, which often results in the formation of secondary impurity phases alongside the spinel ferrite [21].

$NiFe_2O_4$ samples synthesised *via* the sol-gel auto-combustion method had relatively larger crystallite sizes compared to samples obtained *via* other methods. In the sol-gel auto-combustion method, nanoparticle morphology, crystallite size, surface area, and phase formation are dependent on the type of fuel used and the fuel-to-oxidant ratio [22]. The synthesis method, employing both citric acid and ethanol as fuels, yielded a sample with smaller crystallite sizes, although with lower phase purity, compared to the synthesis using citric acid as the sole fuel.

The phase pure $NiFe_2O_4$ was obtained by reducing agent-assisted precipitation synthesis.

Table 1. Phase composition and crystallite size of the samples

Sample	**Crystalline phase (wt%)**	**Crystallite size of $NiFe_2O_4$ (nm)**	**Crystallite size of Fe_2O_3 (nm)**	**Crystallite size of NiO (nm)**
$NiFe_2O_4$-sono-8	$NiFe_2O_4$:Fe_2O_3, 98:2	25.6±0.4	76±21	-
$NiFe_2O_4$-sono-9	$NiFe_2O_4$:Fe_2O_3, 94:6	20.5±0.3	70±6	-
$NiFe_2O_4$-sono-10	$NiFe_2O_4$:Fe_2O_3, 60:40	15.6±0.3	80±1	-
$NiFe_2O_4$-sono-11	$NiFe_2O_4$:Fe_2O_3, 37:63	13.9±0.5	44.7±0.6	-
$NiFe_2O_4$-C-E	$NiFe_2O_4$:Fe_2O_3:NiO, 33:48:19	42.4±1.6	85.9±5.2	42.4±3.9
$NiFe_2O_4$-Citric	$NiFe_2O_4$:Fe_2O_3:NiO, 76:18:6	73.3±1.1	143±16	50.9±5.6
$NiFe_2O_4$-Prec	$NiFe_2O_4$, 100	12.0±0.3	-	-

N_2 adsorption-desorption analysis was used to analyse the highest-purity $NiFe_2O_4$ sample obtained from each respective synthesis method ($NiFe_2O_4$-sono-8, $NiFe_2O_4$-Citric, $NiFe_2O_4$-Prec). The analysed samples exhibited IUPAC type IV isotherms with a hysteresis loop (Fig. 3A), typical of mesoporous materials. $NiFe_2O_4$-sono-8 exhibited the isotherm with an H1 hysteresis loop, while $NiFe_2O_4$-Citric and $NiFe_2O_4$-Prec exhibited the isotherm with an H3 hysteresis loop. The H1 hysteresis loop is characteristic of materials with a narrow range of uniform mesopores, whereas the type H3 hysteresis loop is observed in materials with non-rigid aggregated particle structures that display varying geometries [23,24].

Fig. 3B compares the BJH pore size distribution curves of the analysed $NiFe_2O_4$ samples. BJH pore size distribution of $NiFe_2O_4$-sono-8 and $NiFe_2O_4$-Citric each exhibited a single peak, while BJH pore size distribution of $NiFe_2O_4$-Prec exhibited two peaks: one narrow peak centred at approx. 3.9 nm and one broad peak in the range of 4.4 nm to 59 nm. The first peak can be associated with the internal voids within particles, while the broad peak could be attributed to pores located between the particles.

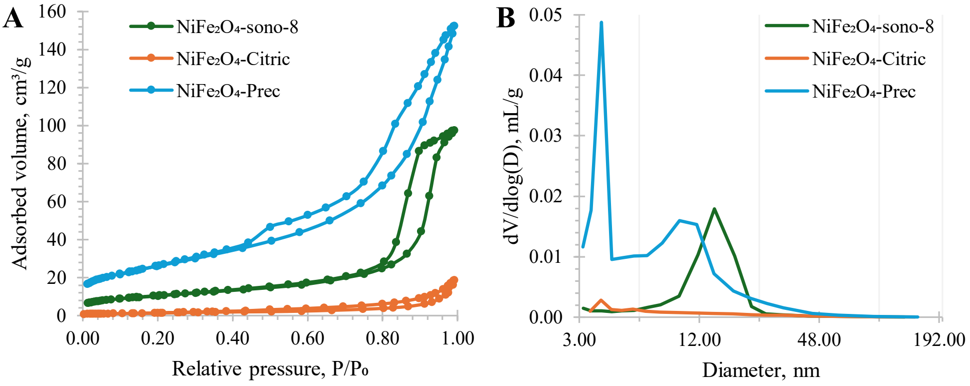

Fig. 3. N_2 adsorption-desorption isotherms and BJH pore size distribution curves of synthesised $NiFe_2O_4$.

The textural properties derived from N_2 adsorption-desorption analysis are listed in Table 2. The $NiFe_2O_4$-Prec sample showed the highest BET surface area among the tested materials. The $NiFe_2O_4$-sono-8 sample demonstrated the narrowest pore size distribution, as indicated by the minimal difference between the average and mean pore diameters. In contrast, the $NiFe_2O_4$-Citric sample displayed the lowest surface area and the broadest pore size distribution, suggesting a high degree of textural heterogeneity.

Table 2. Textural properties of the samples

Catalyst	**S_{BET}[a] (m^2/g)**	**V_{total}[b] (cm^3/g)**	**$D_{average}$[c] (nm)**	**D_{mean}[d] (nm)**
$NiFe_2O_4$-sono-8	36.82	0.151	16.39	14.34
$NiFe_2O_4$-Citric	5.20	0.029	22.15	3.85
$NiFe_2O_4$-Prec	93.77	0.236	10.06	3.88

[a] BET surface area.

[a] Total pore volume.

[a] Average pore diameter.

[a] Mean pore diameter evaluated by the BJH desorption method.

Fig. 4 shows the SEM images of the highest-purity $NiFe_2O_4$ sample obtained from each synthesis method. Both $NiFe_2O_4$-sono-8, prepared by sono-chemical synthesis, and $NiFe_2O_4$-Prec, prepared by reducing agent-assisted precipitation synthesis, consist of aggregate structures of spherical particles, while $NiFe_2O_4$-Citric, prepared by the sol-gel auto-combustion method, consists of particles adhered together due to agglomerate sintering.

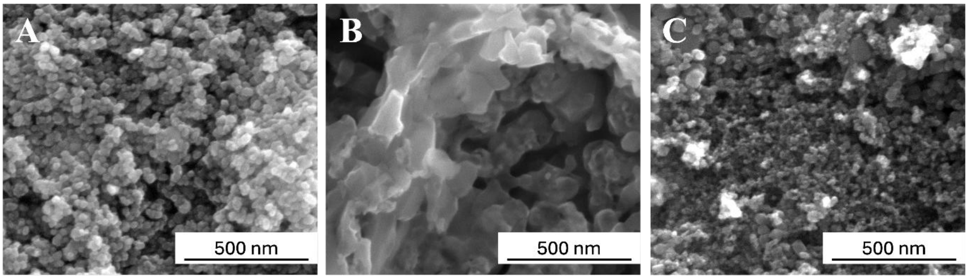

Fig. 4. SEM image of $NiFe_2O_4$-sono-8 (A), $NiFe_2O_4$-Citric (B) and $NiFe_2O_4$-Prec (C).

3.2. Catalytic performance

The CO_2-FTS performance of the synthesised $NiFe_2O_4$ catalysts was evaluated at 320 °C, 20 bar, $H_2/CO_2 = 3$. The reaction temperature of 320 °C was selected as an optimised "compromise point" to balance CO_2 activation, hydrocarbon selectivity, and catalyst stability. According to the literature, at this temperature, the carburization of iron into active Hägg carbide (χ-Fe_5C_2) phase, crucial for hydrocarbon growth in FTS, is kinetically favoured [25]. At the same time, the deactivation of χ-Fe_5C_2 by oxidation due to high H_2O concentration is limited [26] and Ni sintering and carbon deposition are minimised [27].

The CO_2 conversion and product selectivity after 48 h are shown in Table 3. The CO_2 conversion over the synthesised $NiFe_2O_4$ catalysts ranged from 18.0% to 23.7%. $NiFe_2O_4$-Citric exhibited the highest conversion despite its inferior textural properties (lowest surface area and high heterogeneity). According to the literature, CO_2 conversion to CO is weakly influenced by catalyst particle size [29,30]. This suggests that the specific phase composition and the resulting structural evolution during activation outweigh the impact of the initial surface area. $NiFe_2O_4$-Citric, in addition to the $NiFe_2O_4$ phase, contained Fe_2O_3 and NiO phases (Table 1). During H_2 activation, Fe_2O_3 is readily reduced to magnetite (Fe_3O_4, the active phase for RWGS) and metallic iron (α-Fe). Under CO_2 hydrogenation conditions, Hägg carbide (χ-Fe_5C_2, the active phase for FTS) forms from Fe/Fe_3O_4 [5,31,32]. In contrast, spinel $NiFe_2O_4$ undergoes only partial reduction to a mixed system of metals, metal oxides, and NiFe alloy/alloy carbides, which, together with the $NiFe_2O_4$ spinel phase, form the active catalytic phases responsible for CO and hydrocarbon formation [33–35].

It is known that product selectivity is strongly affected by the catalyst's hydrogenation activity. Additionally, product selectivity was found to be a function of the catalyst's particle size and phase composition. In the present study, CH_4 was the dominant hydrocarbon product for all catalysts, reflecting the high inherent hydrogenation activity of Ni-containing catalysts. Since $NiFe_2O_4$-sono-8 and $NiFe_2O_4$-Prec catalysts are nearly identical in phase purity (Table 1), differences in their catalytic performance can be attributed to particle size. $NiFe_2O_4$-Prec, the catalyst with the smallest particle size, exhibited the highest CH_4 selectivity, whereas $NiFe_2O_4$-sono-8, with a particle size double that of the precipitated sample, showed higher CO and C_{5+} selectivity. The observed differences in product selectivity might be because catalysts with larger particle size can be carburised to a greater degree, while smaller particles are less prone to carburization into χ-Fe_5C_2, maintaining a larger proportion of phases that favour hydrogenation over chain growth [28,29].

Although $NiFe_2O_4$-Citric exhibited the largest particle size, its selectivity profile diverged from that of $NiFe_2O_4$-sono-8. The observed deviation can be attributed to differences in phase composition, as $NiFe_2O_4$-Citric contained secondary phases Fe_3O_4 (18%) and NiO (6%). The lower CO selectivity observed for the $NiFe_2O_4$-Citric is likely due to the presence of Fe_2O_3 as a precursor to FTS active iron carbide phases. The enhanced FTS activity is evidenced by a higher CO_2 conversion rate coupled with reduced CO selectivity. Conversely, the presence of NiO introduces alternative reaction pathways: NiO-based catalysts are known to promote CO_2 methanation at approximately 280 °C [30] and can cause hydrocracking or cleavage of -C-C-bonds even at temperatures up to 340 °C [31] thus contributing to the formation of shorter-chain products.

Table 3. Catalytic performance of $NiFe_2O_4$-based catalysts in CO_2 hydrogenation.

Catalyst	**CO_2 conversion (%)**	**Selectivity, %**			
		CO	**CH_4**	**C_2-C_4**	**C_{5+}**
$NiFe_2O_4$-sono-8	18.0	31.1	38.0	4.5	26.5
$NiFe_2O_4$-Citric	23.7	20.9	41.9	3.8	33.4
$NiFe_2O_4$-Prec	19.4	20.2	62.6	8.8	8.5

In CO_2 hydrogenation to hydrocarbons, both the RWGS and FTS reactions produce water; as a result, the amount of aqueous phase exceeds the amount of hydrocarbons produced. Due to the oxygenated compounds dissolved in the aqueous phase, the obtained CO_2-FTS wastewater is smelly, toxic and needs to be treated to minimise the environmental impact [5,32,33]. Alcohols are usually the dominant oxygenated products, while minor quantities of acids, aldehydes, ketones and esters can also be produced [34]. The quantification of acids is crucial in industrial processes because their corrosive nature can lead to equipment degradation [34]. Aqueous phase product selectivity over $NiFe_2O_4$-sono-8, $NiFe_2O_4$-Citric and $NiFe_2O_4$-Prec catalysts is provided in Table 4. For all catalysts, methanol was the main oxygenate product. The aqueous phase for $NiFe_2O_4$-Prec was the purest; the catalyst exhibited the lowest alcohol selectivity compared to other catalysts. This catalyst was thus more selective toward hydrocarbon formation. On the other hand, the aqueous phase for $NiFe_2O_4$-sono-8 contained the highest amount of alcohols but the least amount of acids. Furthermore, the relatively high ethanol yield and the presence of propanol suggest that $NiFe_2O_4$-sono-8 possesses a strong capability for carbon chain growth, which is consistent with the conclusions from the gas phase product analysis.

The increased methane selectivity, low yield of C_{5+} products and suppressed oxygenate formation indicate that $NiFe_2O_4$-Prec have the highest hydrogenation activity among the tested catalysts. These properties make it a potential e-LNG catalyst.

Table 4. Aqueous phase product selectivity

Catalyst	**Carboxylic acids (mmol/g)**	**Methanol (mg/mL)**	**Ethanol (mg/mL)**	**n-Propanol (mg/mL)**	**Acetone (mg/mL)**
$NiFe_2O_4$-sono-8	0.08	4.72	0.76	0.1	0.1
$NiFe_2O_4$-Citric	0.19	3.45	0.49	-	-
$NiFe_2O_4$-Prec	0.13	2.41	0.40	-	0.1

3.2. Life cycle impact assessment

The environmental profiles of the $NiFe_2O_4$-sono-8, $NiFe_2O_4$-Citric and $NiFe_2O_4$-Prec synthesis routes, characterised using the EF v.3.1 midpoint indicators, are presented in Figs. 5-7. It is important to note that laboratory-scale data typically exhibit higher impacts compared to commercial materials produced through optimised industrial-scale processes due to lower material throughput and unoptimized energy efficiency.

$NiFe_2O_4$-sono-8 (Fig. 5) and $NiFe_2O_4$-Citric (Fig. 6) exhibited similar environmental impacts, with electricity consumption being the predominant contributor across most considered impact categories. The exceptions were terrestrial eutrophication and depletion of material resources, where the production of $Fe(NO_3)_3$ was the dominant contributor. In the $NiFe_2O_4$-sono-8 synthesis, waste emissions accounted for more than 10% of the impacts on freshwater ecotoxicity and marine eutrophication, primarily due to wastewater containing nitrates and ammonium.

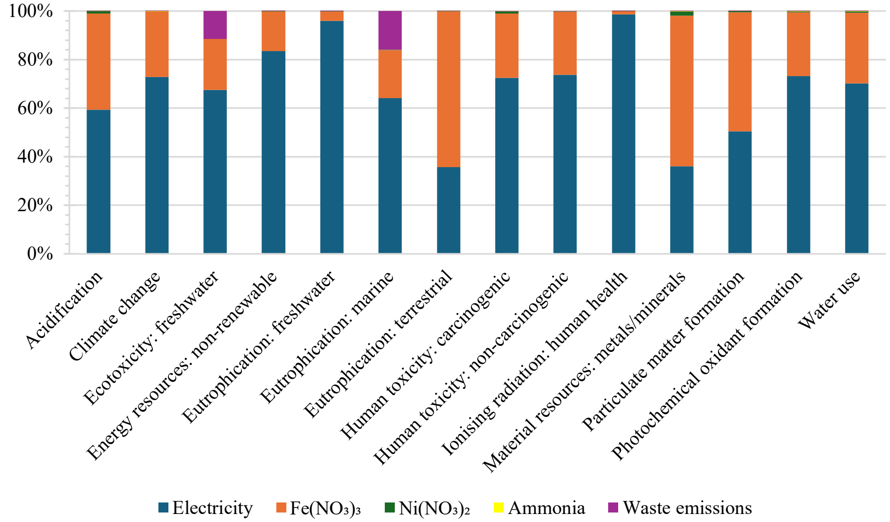

Fig. 5. $NiFe_2O_4$-sono-8 characterisation results.

In contrast, for the $NiFe_2O_4$-Citric synthesis, waste emissions contributed over 10% to marine eutrophication, terrestrial eutrophication, and photochemical oxidant formation, and more than 5% to acidification and particulate matter formation. These effects are mainly attributed to the release of carbon dioxide and nitrogen oxides during the thermal decomposition of nitrates and citric acid.

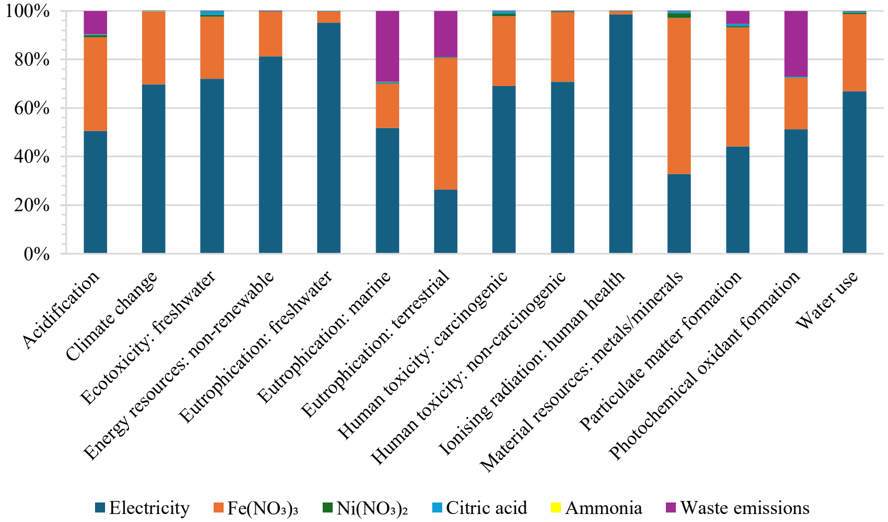

Fig. 6. $NiFe_2O_4$-Citric characterisation results.

For the $NiFe_2O_4$-Prec synthesis process, electricity consumption was again the dominant factor, contributing over 90% to almost all assessed impact categories (Fig. 7). In contrast to $NiFe_2O_4$-sono-8 and $NiFe_2O_4$-Citric, precursors used in the $NiFe_2O_4$-Prec synthesis process ($FeCl_3$, $NiCl_2$) showed a significantly lower ecological footprint compared to the nitrates used in the other two synthesis routes. However, the $NiFe_2O_4$-Prec synthesis process showed a disproportionate impact on freshwater ecotoxicity and carcinogenic human toxicity due to wastewater containing sodium, borate, chloride, iron, and residual nickel ions. While inorganic borates generally display low acute toxicity [35], the toxicity of sodium and chloride ions has been proven in many studies [36–39].

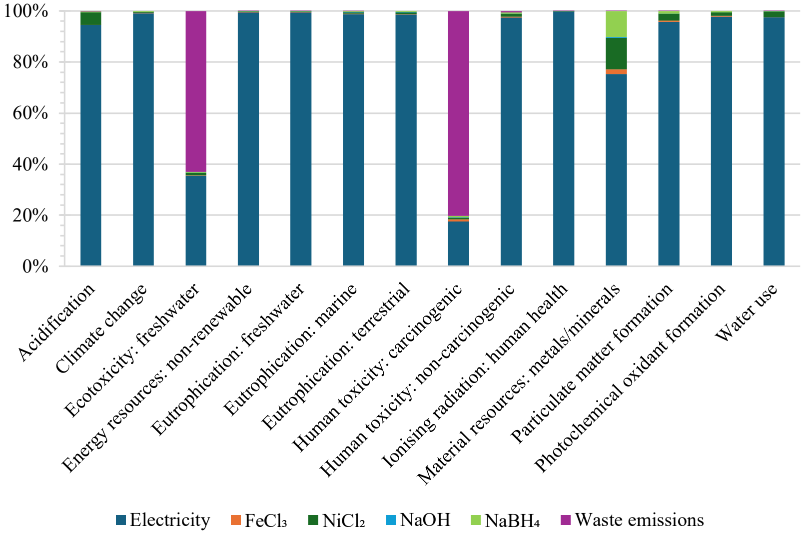

Fig. 7. $NiFe_2O_4$-Prec characterisation results.

To determine the relative significance of the impacts, the EF v.3.1 results were normalised against the global reference (2010), representing the annual per capita environmental burden (Fig. 8). The normalised results showed that all three synthesis routes have broadly comparable overall environmental impacts. Non-renewable energy resources and freshwater eutrophication were identified as the most critical environmental hotspots across all synthesis methods. Among the processes evaluated, reducing agent-assisted precipitation generally demonstrated the lowest impact across most categories. The exceptions were freshwater ecotoxicity, human toxicity (carcinogenic), and ionising radiation, where $NiFe_2O_4$-Prec exhibited the highest values among the analysed synthesis methods. The results indicate that with optimised energy recovery and targeted wastewater treatment, the precipitation synthesis method offers the highest potential for sustainable scaling.

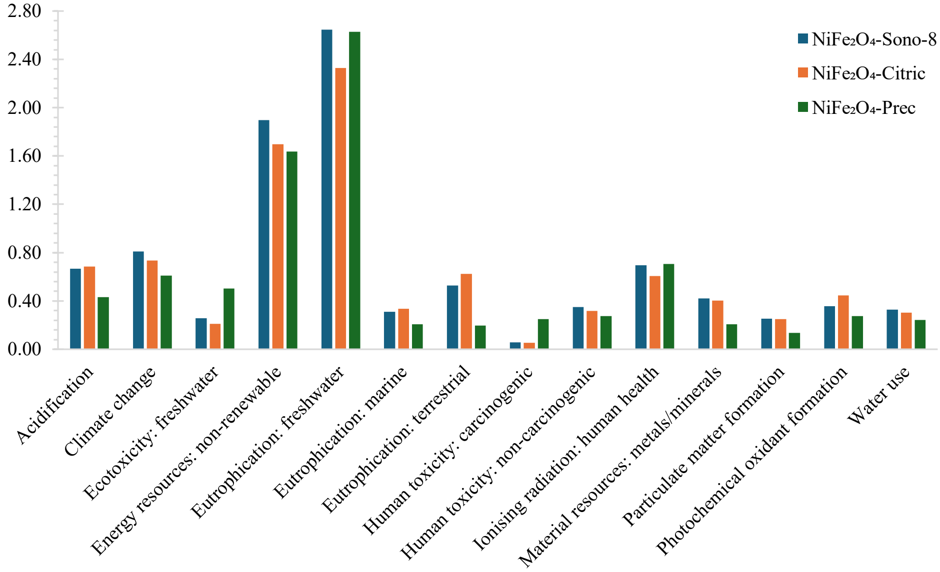

Fig. 8. Comparison of normalisation results for $NiFe_2O_4$-sono-8, $NiFe_2O_4$-Citric and $NiFe_2O_4$-Prec synthesis processes.

4. Conclusions

In this study, $NiFe_2O_4$-based catalysts for CO_2 hydrogenation to hydrocarbons were synthesised *via* sono-chemical, sol-gel auto-combustion, and reducing agent-assisted precipitation methods. The highest-purity $NiFe_2O_4$ samples obtained from each respective synthesis method were characterised and tested for CO_2-FTS. The choice of synthesis route was found to be a critical determinant of both the structural characteristics and resulting catalytic performance. Reducing agent-assisted precipitation ($NiFe_2O_4$-Prec) proved to be the most effective route for obtaining phase-pure $NiFe_2O_4$ with the highest BET surface area. Sono-chemical synthesis demonstrated strong pH sensitivity, where higher pH reduced crystallite size but increased phase impurities. Conversely, the sol-gel auto-combustion synthesis yielded samples with a high degree of heterogeneity in terms of phase composition. In the present study, CO_2 conversion at 320 °C ranged from 18.0 to 23.7%. $NiFe_2O_4$-Citric, despite its poor textural characteristics, showed slightly enhanced conversion and FTS activity, likely due to the synergistic presence of secondary NiO and Fe_2O_3 phases. CH_4 was the primary gaseous phase hydrocarbon product across all catalysts, whereas aqueous phase analysis identified methanol as the dominant oxygenate. The results indicated that a smaller particle size promotes CH_4 formation. $NiFe_2O_4$-Prec demonstrated the highest overall hydrogenation activity, resulting in superior CH_4 yields and the highest aqueous phase purity (lowest oxygenate content).

LCA identified electricity consumption as the primary driver of environmental impact across most categories. $NiFe_2O_4$-Prec presented the lowest environmental burden in the majority of categories. The superior structural properties, high hydrogenation activity, and relatively low environmental footprint of $NiFe_2O_4$-Prec highlight its potential as an effective catalyst for e-LNG production through CO_2 valorisation.

Funding: This work has been supported by research and development grant NoRTU-PA-2024/1-0052 under the EU Recovery and Resilience Facility funded project No. 5.2.1.1.i.0/2/24/I/CFLA/003 "Implementation of consolidation and management changes at Riga Technical University, Liepaja University, Rezekne Academy of Technology, Latvian Maritime Academy and Liepaja Maritime College for the progress towards excellence in higher education, science, and innovation". This work has been supported by Estonian Research Council (grant TEM-TA31).

References

[1] Tomos BAD, Stamford L, Welfle A, Larkin A. Decarbonising international shipping – A life cycle perspective on alternative fuel options. Energy Convers Manag 2024;299. https://doi.org/10.1016/j.enconman.2023.117848.

[2] Watanabe MDB, Cherubini F, Cavalett O. Climate change mitigation of drop-in biofuels for deep-sea shipping under a prospective life-cycle assessment. J Clean Prod 2022;364. https://doi.org/10.1016/j.jclepro.2022.132662.

[3] Galimova T, Lagouvardou S, Kian H, Breyer C. Comparing sustainable fuel adoption in the energy transition for maritime and aviation transport. Renewable and Sustainable Energy Reviews 2025;224. https://doi.org/10.1016/j.rser.2025.116124.

[4] Skov IR, Schneider N. Incentive structures for power-to-X and e-fuel pathways for transport in EU and member states. Energy Policy 2022;168. https://doi.org/10.1016/j.enpol.2022.113121.

[5] Panzone C, Philippe R, Chappaz A, Fongarland P, Bengaouer A. Power-to-Liquid catalytic CO2 valorization into fuels and chemicals: Focus on the Fischer-Tropsch route. Journal of CO2 Utilization 2020;38:314–47. https://doi.org/10.1016/j.jcou.2020.02.009.

[6] Xie T, Wang J, Ding F, Zhang A, Li W, Guo X. CO2 hydrogenation to hydrocarbons over alumina-supported iron catalyst : Effect of support pore size. Journal of CO2 Utilization 2017;19:202–8. https://doi.org/10.1016/j.jcou.2017.03.022.

[7] Roy S, Cherevotan A, Peter SC. Thermochemical CO2 Hydrogenation to Single Carbon Products: Scientific and Technological Challenges. ACS Energy Lett 2018;3:1938–66. https://doi.org/10.1021/acsenergylett.8b00740.

[8] Lu Q, Rosen J, Zhou Y, Hutchings GS, Kimmel YC, Chen JG, et al. A selective and efficient electrocatalyst for carbon dioxide reduction. Nat Commun 2014;5. https://doi.org/10.1038/ncomms4242.

[9] Li W, Wang H, Jiang X, Zhu J, Liu Z, Guo X, et al. A short review of recent advances in CO2 hydrogenation to hydrocarbons over heterogeneous catalysts. RSC Adv 2018;8:7651–69. https://doi.org/10.1039/c7ra13546g.

[10] Navarro JC, Hurtado C, Gonzalez-Castaño M, Bobadilla LF, Ivanova S, Cumbrera FL, et al. Spinel ferrite catalysts for CO2reduction via reverse water gas shift reaction. Journal of CO2 Utilization 2023;68. https://doi.org/10.1016/j.jcou.2022.102356.

[11] Zhu J, Zhang G, Li W, Zhang X, Ding F, Song C, et al. Deconvolution of the Particle Size Effect on CO2Hydrogenation over Iron-Based Catalysts. ACS Catal 2020;10:7424–33. https://doi.org/10.1021/acscatal.0c01526.

[12] Zhu J, Shaikhutdinov S, Cuenya BR. Structure-reactivity relationships in CO2 hydrogenation to C2+ chemicals on Fe-based catalysts. Chem Sci 2024. https://doi.org/10.1039/d4sc06376g.

[13] Wang CX, Liu HX, Gu H, Li JY, Lai XM, Fu XP, et al. Hydroxylated TiO2-induced high-density Ni clusters for breaking the activity-selectivity trade-off of CO2 hydrogenation. Nature Communications 2024;15. https://doi.org/10.1038/s41467-024-52547-4.

[14] Wei C, Ding H, Zhang Z, Lin F, Xu Y, Pan W. Research progress of bimetallic catalysts for CO2 hydrogenation to methane. Int J Hydrogen Energy 2024;58:872–91. https://doi.org/10.1016/j.ijhydene.2024.01.204.

[15] Wu HC, Chang YC, Wu JH, Lin JH, Lin IK, Chen CS. Methanation of CO2 and reverse water gas shift reactions on Ni/SiO2 catalysts: the influence of particle size on selectivity and reaction pathway. Catal Sci Technol 2015;5:4154–63. https://doi.org/10.1039/c5cy00667h.

[16] Soufi A, Hajjaoui H, Elmoubarki R, Abdennouri M, Qourzal S, Barka N. Spinel ferrites nanoparticles: Synthesis methods and application in heterogeneous Fenton oxidation of organic pollutants – A review. Applied Surface Science Advances 2021;6. https://doi.org/10.1016/j.apsadv.2021.100145.

[17] Orege JI, Wei J, Ge Q, Sun J. Spinel-structured nanocatalysts: New opportunities for CO2 hydrogenation to value-added chemicals. Nano Today 2023;51. https://doi.org/10.1016/j.nantod.2023.101914.

[18] Singh Yadav R, Kuřitka I, Vilcakova J, Jamatia T, Machovsky M, Skoda D, et al. Impact of sonochemical synthesis condition on the structural and physical properties of MnFe2O4 spinel ferrite nanoparticles. Ultrason Sonochem 2020;61. https://doi.org/10.1016/j.ultsonch.2019.104839.

[19] Fedorov A, Linke D. Data analysis of CO2hydrogenation catalysts for hydrocarbon production. Journal of CO2 Utilization 2022;61. https://doi.org/10.1016/j.jcou.2022.102034.

[20] Stanke A, Lazdovica K, Gaile A, Laipniece L. Fischer-Tropsch synthesis product selectivity over silica-supported iron-based catalyst: Effect of K/Fe ratio. Fuel 2025;387. https://doi.org/10.1016/j.fuel.2025.134399.

[21] Li H, Wu H zhong, Xiao G xian. Effects of synthetic conditions on particle size and magnetic properties of NiFe2O4. Powder Technol 2010;198:157–66. https://doi.org/10.1016/j.powtec.2009.11.005.

[22] Gao J ming, Zhang M, Cheng F, Guo M. Process development for selective precipitation of valuable metals and simultaneous synthesis of single-phase spinel ferrites from saprolite-limonite laterite leach liquors. Hydrometallurgy 2017;173:98–105. https://doi.org/10.1016/j.hydromet.2017.08.004.

[23] Dippong T, Levei EA, Cadar O. Recent advances in synthesis and applications of MFe2O4 (M = Co, Cu, Mn, Ni, Zn) nanoparticles. Nanomaterials 2021;11. https://doi.org/10.3390/nano11061560.

[24] Silva DPS, Solano JRS, Sousa L V., Silva BJB, Quintela PHL, Silva AOS. Modification of MCM-41 type structures by carbon deposition and acid washing for CO2 adsorption. J Solgel Sci Technol 2021;97:382–92. https://doi.org/10.1007/s10971-020-05432-7.

[25] Sing KSW, Williams RT. Physisorption Hysteresis Loops and the Characterization of Nanoporous Materials. Adsorption Science & Technology 2004;22:773–82. https://doi.org/10.1260/0263617053499032.

[26] De Smit E, Cinquini F, Beale AM, Safonova O V., Van Beek W, Sautet P, et al. Stability and reactivity of ε-Χ-θ iron carbide catalyst phases in fischer-tropsch synthesis: Controlling μc. J Am Chem Soc 2010;132:14928–41. https://doi.org/10.1021/ja105853q.

[27] Mai F, Jess A. CO2 Conversion to Higher Hydrocarbons on Iron-Based Catalysts: Promoter Impact and Kinetic Studies. Chem Eng Technol 2025;48. https://doi.org/10.1002/ceat.12010.

[28] Li L, Zeng W, Song M, Wu X, Li G, Hu C. Research Progress and Reaction Mechanism of CO2 Methanation over Ni-Based Catalysts at Low Temperature: A Review. Catalysts 2022;12. https://doi.org/10.3390/catal12020244.

[29] Cheng K, Virginie M, Ordomsky V V, Cordier C, Chernavskii PA, Ivantsov MI, et al. Pore size effects in high-temperature Fischer-Tropsch synthesis over supported iron catalysts. J Catal 2015;328:139–50. https://doi.org/10.1016/j.jcat.2014.12.007.

[30] Guo S, Lu K, Zheng K, Yu X, Ren P, Yang Y, et al. Atomic-level insight into the carburization process of iron-based catalysts: A ReaxFF molecular dynamics study. J Catal 2024;438. https://doi.org/10.1016/j.jcat.2024.115719.

[31] Xiang M, Gao Z, Ji X, Li D, Deng Y, Ding Y, et al. Boosting CO2 hydrogenation to methane over Ni-based ETS-10 zeolite catalyst. Front Chem 2022;10. https://doi.org/10.3389/fchem.2022.1041843.

[32] Malins K, Malina I. The effects of supported Pd, Pt, Re, Rh, Ru, Ir, Au, and Ni catalysts on renewable hydrocarbon production from alternative feedstock. Biomass Bioenergy 2023;171. https://doi.org/10.1016/j.biombioe.2023.106732.

[33] Liao X, Wang F, Wang Y, Cai Y, Liu H, Wang X, et al. Constructing Fe-based bi-MOFs for photo-catalytic ozonation of organic pollutants in Fischer-Tropsch waste water. Appl Surf Sci 2020;509. https://doi.org/10.1016/j.apsusc.2020.145378.

[34] Zoppi G, Pipitone G, Gruber H, Weber G, Reichhold A, Pirone R, et al. Aqueous phase reforming of pilot-scale Fischer-Tropsch water effluent for sustainable hydrogen production. Catal Today 2021;367:239–47. https://doi.org/10.1016/j.cattod.2020.04.024.

[35] Teng BT, Zhang CH, Yang J, Cao DB, Chang J, Xiang HW, et al. Oxygenate kinetics in Fischer-Tropsch synthesis over an industrial Fe-Mn catalyst. Fuel 2005;84:791–800. https://doi.org/10.1016/j.fuel.2004.12.008.

[36] Hubbard SA. Comparative toxicology of borates. Biol Trace Elem Res 1998;66:343–57. https://doi.org/10.1007/BF02783147.

[37] Meteyer CU, Dubielzig RR, Dein FJ, Baeten LA, Moore MI, Jehl JR, et al. Sodium toxicity and pathology associated with exposure of waterfowl to hypersaline playa lakes of southeast New Mexico. vol. 9. 1997.

[38] Belamy T, Legeay A, Etcheverria B, Cordier M-A, Gourves P-Y, Baudrimont M. Acute Toxicity of Sodium Chloride, Nitrates, Ortho-Phosphates, Cadmium, Arsenic and Aluminum for Juveniles of the Freshwater Pearl Mussel: Margaritifera Margaritifera (L.1758). Environments 2020;7:48. https://doi.org/10.3390/environments7060048.

[39] Doungous O, Al-Khayri JM, Kouassi MK. Sodium Toxicity: Should NaOH Be Substituted by KOH in Plant Tissue Culture? Front Plant Sci 2022;13. https://doi.org/10.3389/fpls.2022.829768.

[40] Elphick JRF, Bergh KD, Bailey HC. Chronic toxicity of chloride to freshwater species: Effects of hardness and implications for water quality guidelines. Environ Toxicol Chem 2011;30:239–46. https://doi.org/10.1002/etc.365.

7. pielikums

Appendix 7

Stanke A., Berzins, A., Velasco, J.A., Sarsuns K., Puurunen, R. L., Lazdovica K.

Cobalt-promoted Fe_3O_4 catalysts for CO_2 hydrogenation to C_{2+} hydrocarbons: Effect of pretreatment method and reaction temperature

Fuel Processing Technology, **2026**, 288, 108467

https://doi.org/10.1016/j.fuproc.2026.108467

Fuel Processing Technology 288 (2026) 108467

Contents lists available at ScienceDirect

Fuel Processing Technology

journal homepage: www.elsevier.com/locate/fuproc

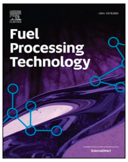

Cobalt-promoted Fe_3O_4 catalysts for CO_2 hydrogenation to C_{2+} hydrocarbons: Effect of pretreatment method and reaction temperature

Agija Stanke [a,*], Agris Berzins [b], Jorge A. Velasco [c], Kristaps Sarsuns [b], Riikka L. Puurunen [c], Kristine Lazdovica [a]

[a] *Riga Technical University, Faculty of Natural Sciences and Technology, Institute of Chemistry and Chemical Technology, Riga LV-1048, Latvia*
[b] *University of Latvia, Faculty of Medicine and Life Sciences, Department of Chemistry, Riga LV-1048, Latvia*
[c] *Aalto University, School of Chemical Engineering, Department of Chemical and Metallurgical Engineering, 02150 Espoo, Finland*

ARTICLE INFO

Keywords:
CO_2-FTS
Hydrocarbons
Sustainability
CO_2 hydrogenation

ABSTRACT

This study investigates the influence of cobalt promotion, reaction temperature (280–320 °C) and catalyst pretreatment strategies on the CO_2 hydrogenation performance of Fe-based catalysts. The cobalt-promoted catalyst precursors were subjected to three pretreatment routes: calcination in N_2 followed by H_2 activation, calcination in air followed by H_2 activation, and direct reduction in H_2. Temperature studies revealed a trade-off between activity and product quality: increasing temperature to 320 °C enhanced CO_2 conversion but shifted product distribution toward thermodynamically favoured light hydrocarbons. For the unpromoted catalyst, elevated temperatures increased overall hydrocarbon yield by altering the surface H/C ratio. Conversely, for the stable cobalt-promoted catalysts, the reverse water-gas shift (RWGS) pathway remained dominant and stable (>49% CO selectivity) across all temperatures. Crucially, the pre-treatment environment dictated the final catalyst properties by controlling phase reduction and surface basicity. The uncalcined and N-calcined catalysts reduced to a metallic α-Fe, generating moderate surface basicity, while air calcination resulted in an incompletely reduced catalyst with strong basic sites. While air calcination maximised long-chain hydrocarbon selectivity and suppressed oxygenate formation in the aqueous phase, N_2 calcination provided the best balance of high CO_2 conversion, low CO selectivity, and stable phase composition.

1. Introduction

The continuous increase in anthropogenic greenhouse gas (GHG) emissions has led to significant environmental and climatic impacts, including global warming, ocean acidification, and biodiversity loss. Carbon dioxide (CO_2) is the dominant contributor, accounting for approximately three-quarters of total global GHG emissions [1]. Consequently, mitigating CO_2 emissions represents one of the major scientific and technological challenges of the 21st century.

Carbon Capture and Utilisation (CCU) has emerged as a key technology for reducing CO_2 emissions while simultaneously offering an efficient use of resources and promoting economic growth [2]. CCU consists of the chemical conversion of the recovered CO_2 into valuable chemicals and fuels [3]. There are already industrial processes for the direct conversion of CO_2 into single-carbon (C_1) products. In addition, direct CO_2 hydrogenation to longer-chain (C_{2+}) hydrocarbons via CO_2-based Fischer–Tropsch synthesis (CO_2-FTS) is currently being actively researched [4,5].

CO_2-FTS consists of two reactions in series – initially, CO_2 is reduced to carbon monoxide (CO) through the reverse water gas shift reaction (RWGS) (Eq. 1), then hydrocarbons are generated from CO through FTS (Eq. 2).

$$CO_2 + H_2 \leftrightarrow H_2O + CO, \Delta H^0{}_{298} = 41.2\ kJ/mol \tag{1}$$

$$CO + 2H_2 \rightarrow (-CH_2-) + H_2O, \Delta H^0{}_{298} = -152\ kJ/mol \tag{2}$$

Iron-based catalysts are active for both reactions, with magnetite (Fe_3O_4) serving as the active phase for the RWGS reaction and Hägg carbide (χ-Fe_5C_2) as the active phase for FTS [6]. Unmodified iron-based catalysts typically exhibit low activity and high selectivity toward undesired by-products such as CO and methane (CH_4). The incorporation

---

* Corresponding author.
E-mail addresses: Agija.Stanke@rtu.lv (A. Stanke), Agris.Berzins@lu.lv (A. Berzins), jorge.velasco@aalto.fi (J.A. Velasco), Kristaps.Sarsuns@lu.lv (K. Sarsuns), Riikka.puurunen@aalto.fi (R.L. Puurunen), Kristine.Lazdovica@rtu.lv (K. Lazdovica).

https://doi.org/10.1016/j.fuproc.2026.108467
Received 18 January 2026; Received in revised form 9 April 2026; Accepted 24 April 2026

of cobalt has been shown to enhance hydrogenation activity and promote CO consumption, thereby shifting the RWGS equilibrium toward higher CO_2 conversion [7,8]. Several studies have demonstrated that small amounts of cobalt can significantly improve C_{5+} selectivity while reducing CO formation [9,10]. Excessive cobalt loading, however, can increase methane formation and suppress long-chain hydrocarbon (C_{5+}) selectivity [11].

Catalyst performance in CO_2-FTS is strongly influenced by the nature of the active phase, particle size, crystal structure, and metal–support interactions, all of which are determined by synthesis and pretreatment conditions such as calcination and activation [12,13]. While the effects of promoters and supports on iron-based CO_2 hydrogenation catalysts have been widely investigated [14], there is a lack of systematic studies on how synthesis routes and pretreatment strategies influence the performance of cobalt-promoted Fe_3O_4 catalysts.

Iron-based catalysts are commonly activated using H_2, CO, or synthesis gases [15,16], while cobalt-based catalysts are generally activated in a H_2 atmosphere [17]. Extensive research has examined the activation of iron-based catalysts by syngas, which leads to the formation of active iron carbide species that promote FTS reactions [18]. In contrast, cobalt-based catalysts utilise metallic cobalt as the active phase instead of carbide phases; consequently, H_2 reduction is employed as the standard activation procedure [19]. The presence of a cobalt promoter enhances H_2 adsorption and dissociation, thereby modifying the reduction behaviour of Fe_3O_4 [20]. These interactions suggest that H_2 pretreatment may be a rational and effective activation strategy for cobalt-promoted Fe_3O_4 catalysts prior to CO_2-FTS.

Calcination conditions are another critical parameter that influences metal dispersion, oxidation state, and reducibility. These factors ultimately affect the distribution of active species and reaction pathways [21]. The literature on Fe catalysts for FTS and CO_2 -FTS has largely focused on calcination temperature, while the effect of calcination atmosphere (air, N_2, or Ar) remains comparatively underexplored. The calcination conditions of catalysts determine the resulting oxide phases, regulate the size and dispersion of metal particles, and consequently influence reducibility, carburization, and FTS activity [22,23]. Few studies have directly examined Fe-based catalysts calcined under different atmospheres. Most existing research emphasises calcination temperature, promoters, or reduction pretreatments rather than systematic comparisons of calcination atmospheres, highlighting a gap in this area of catalyst preparation research. Few authors have studied the influence of calcination atmosphere on CO hydrogenation. Akbari et al. investigated the effects of air-calcination and argon-calcination on the physicochemical properties and catalytic performance of Fe-Co/MgO catalysts for FTS. They showed that calcination atmosphere affected catalyst particle size and reducibility, leading to different FTS performance, with air calcined catalyst demonstrating higher activity and CH_4 selectivity [24]. Roknabadi et al. investigated the FTS performance of Fe-Mn-Ce/γ-Al_2O_3 catalysts calcined under air or under nitrogen. Although CO conversion was similar for both catalysts (24.04% vs 25.69%), product selectivity differed due to different phases formed during catalyst pretreatment. The air calcined catalyst demonstrated lower CO_2 selectivity and higher C_{2+} hydrocarbon selectivity [25]. Feyzi et al. reported that iron-manganese catalyst calcined in air exhibited higher CO conversion and C_2-C_4 selectivity than those calcined in nitrogen [26]. Despite its importance, the role of calcination atmosphere has received limited attention in the context of iron-based CO_2 hydrogenation catalysts. Specifically, how different thermal pretreatments dictate the activation behaviour, phase evolution, and overall CO_2 hydrogenation performance of cobalt-promoted Fe-based systems remains a critical knowledge gap.

To address this, the present study systematically evaluates the effect of pretreatment on the performance of low-loading cobalt-promoted Fe_3O_4 catalysts (Co:Fe = 5:100). The catalyst precursor ($Co(NO_3)_2/Fe_3O_4$) was subjected to different pretreatment protocols: calcination in N_2 followed by H_2 activation, calcination in air followed by H_2 activation, and direct reduction in H_2. In heterogeneous catalysis, it is standard practice to perform calcination at temperatures exceeding both the subsequent reduction and reaction conditions to lock thermal stability. Following this principle, an inert N_2 calcination at 450 °C was chosen to decompose the cobalt precursor while retaining the original Fe_3O_4 support structure. Conversely, an air calcination at 550 °C was applied to explicitly drive the reconstructive phase transition from Fe_3O_4 to α-Fe_2O_3. All samples were reduced under H_2 at 400 °C to effectively reduce the oxidic precursors without inducing thermal sintering. The catalytic performance was subsequently evaluated across a critical temperature range (280–320 °C) to identify the optimal thermodynamic balance between CO_2 conversion and product selectivity, including a detailed analysis of the often-overlooked aqueous phase composition.

The novelty of this work lies in directly correlating these tailored pretreatment procedures with the resulting characteristic evolution of the catalyst, which in turn governs the catalytic performance and product selectivity. Furthermore, the insights established in this study will significantly impact future research by shifting the focus of catalyst optimisation from complex, expensive chemical modifications toward accessible thermal engineering. This work proves that the structural stability and product selectivity of iron-based catalysts can be finely tuned through simple alterations in thermal pretreatment.

2. Experimental/materials and methods

Iron(II, III) oxide (Fe_3O_4) nanopowder (catalogue number 637106) and analytical grade cobalt(II) nitrate hexahydrate ($Co(NO_3)_2$•$6H_2O$) were purchased from Merck.

2.1. Catalyst synthesis and pretreatment

In order to evaluate the influence of the catalyst pretreatment procedure on CO_2 hydrogenation, a cobalt-promoted catalyst precursor was prepared, divided into three parts (labelled as Co/Fe_3O_4, Co/Fe_3O_4-N and Co/Fe_3O_4-A) and subjected to different pretreatments. Fe_3O_4 was impregnated using an aqueous solution of $Co(NO_3)_2$, with the concentration of the impregnating solution calculated to ensure a Co to Fe molar ratio of 5 to 100. After impregnation, the catalyst precursor was dried in an oven at 80 °C for 5 h.

For each experiment, 0.5 g of catalyst precursor was used. Co/Fe_3O_4 was diluted with quartz sand to 2 mL and reduced in a H_2 flow of 50 mL/min at 400 °C for 22 h with a heating rate of 3 °C/min. Co/Fe_3O_4-N was diluted with quartz sand to 2 mL and calcined in a N_2 flow of 50 mL/min at 450 °C for 30 min with a heating rate of 3 °C/min, then the temperature was decreased to 400 °C, and the catalyst was reduced in a H_2 flow of 50 mL/min at 400 °C for 22 h. Co/Fe_3O_4-A was diluted with quartz sand to 2 mL and calcined in air in a muffle furnace at 550 °C for 30 min with a heating rate of 5 °C/min. After calcination, the powder was transferred to the reactor, where it was reduced in a H_2 flow of 50 mL/min at 400 °C for 22 h.

To better assess the effect of cobalt promotion, an unpromoted Fe_3O_4 was reduced in a H_2 flow of 50 mL/min at 400 °C for 22 h and used as a benchmark catalyst.

2.2. CO_2 hydrogenation

Following the reduction step, the reactor was cooled to 260 °C, and a gas mixture comprising H_2 (30 mL/min), CO_2 (10 mL/min), and N_2 (10 mL/min) was introduced using individual mass flow controllers. N_2 was used as an internal standard. The system pressure was then gradually increased to 20 bar, and the temperature was raised to 280 °C. This temperature was held for 24 h, after which it was increased to 300 °C for an additional 24 h. Finally, the temperature was elevated to 320 °C and maintained for a further 24 h. Gaseous products were analysed on-line using a Shimadzu Nexis GC-2030 gas chromatograph, while condensable products were collected every 24 h from a cold trap held at 5 °C and 20 bar and analysed off-line. The CO_2 conversion (X_{CO2}) and product selectivity (S) are calculated as:

$$X_{CO_2} = \frac{CO_{2in} - CO_{2out}}{CO_{2in}} \bullet 100\% \tag{3}$$

$$S_{CO} = \frac{CO_{out}}{CO_{2in} - CO_{2out}} \bullet 100\% \tag{4}$$

$$S_{C_n} = \frac{C_{nout}}{CO_{2in} - CO_{2out}} \bullet 100\% \tag{5}$$

$$S_{C_{5+}} = 100\% - S_{CO} - S_{C_1} - S_{C_2} - S_{C_3} - S_{C_4} \tag{6}$$

where $CO_{2\ in}$ and $CO_{2\ out}$ are the molar flow rate of CO_2 at the reactor inlet and outlet; CO_{out} and $C_{n\ out}$ are the molar flow rate of CO and hydrocarbons with n carbon atoms at the reactor outlet, respectively.

Condensed products were analysed using gas chromatography (Shimadzu Nexis GC-2030). The acidity of the condensed phase was evaluated by the KOH titration method. Comprehensive methodological details are provided in our previous publication [27].

2.3. *Catalyst characterisation*

Thermal degradation studies were conducted using a thermogravimetric analyser (PerkinElmer STA 6000). Fe_3O_4, $Co(NO_3)_2{\bullet}6H_2O$ and cobalt-promoted catalyst precursor ($Co(NO_3)_2$ on Fe_3O_4) were heated from 30 to 600 °C at 10 °C/min under a pure nitrogen flow of 20 mL/min, monitored by a mass-flow controller.

In order to understand the effect of the pre-treatment procedure, catalysts after calcination in N_2 and air, as well as after reduction in H_2, were analysed by XRD and XPS. Before the analysis, quartz sand was separated from the samples using a magnet.

X-ray powder diffraction (XRPD) patterns of catalysts were measured at ambient temperature on a *Bruker D8 Discover* diffractometer using copper radiation (Cu Kα) at the wavelength of 1.54180 Å, equipped with a LynxEye position-sensitive detector. The tube voltage and current were set to 40 kV and 40 mA. The divergence slit was set at 0.6 mm, and the antiscatter slit was set at 8.0 mm. The diffraction patterns were recorded using a scanning speed of 3.0 s/0.02° from 10° to 70° on the 2θ scale. For phase identification, the ICDD (*The International Centre for Diffraction Data*) database PDF-2/Release 2021 was used. Crystallite sizes were estimated using two complementary approaches. For the Scherrer equation method, $K\alpha_2$ stripping by was applied prior to analysis, and FWHM values were measured for 2–3 characteristic, well-resolved diffraction peaks per phase, selected to avoid overlap with reflections from other phases, using DIFFRAC.EVA software. Crystallite sizes were also obtained from Rietveld refinement performed in *Profex*, using the *BGMN* algorithm.

X-ray photoelectron spectroscopy (XPS) measurements were carried out using a *ThermoFisher ESCALAB Xi* spectrometer. Prior to analysis, the samples were affixed to a conductive adhesive tape to ensure stable electrical contact. In order to minimise surface charging effects, a charge neutralisation system was employed during measurements. The X-ray source utilised an aluminum anode (Al Kα radiation, 1486 eV) with an irradiation area of 650 × 100 μm. Instrument calibration was performed using the characteristic photoelectron lines of Ag $3d_{5/2}$, Au $4f_{7/2}$, and Cu $2p_{3/2}$, with binding energies of 368.2 eV, 83.9 eV, and 932.6 eV, respectively.

The reducibility of the Fe_3O_4 and cobalt-promoted Fe_3O_4 pretreated (unreduced) samples was analysed by H_2-TPR in an *AutoChem-III 2930* tool (Micromeritics Instrument Corporation) equipped with an external *Cirrus*™ *3* mass spectrometer (MKS Instruments). Prior to analysis, the samples were kept at 110 °C for several hours in static air. For the analysis, approx. 150 mg of the sample was placed in the sample tube between two pieces of quartz wool. The sample was then dried by heating to 200 °C (heating rate 10 °C/min) for 1 h using He (Linde, 99.9996%) with a flow of 50 mL/min (STP), and then cooled to 35 °C. Helium flow was changed to 50 mL/min (STP) flow of a 10 vol% H_2/Ar mixture (Air Products, 99.99%), and the sample was heated to 800 °C (heating rate 10 °C/min) for 0.5 h. Hydrogen consumption was monitored by following the signal at *m/z* 2. Other signals were also recorded (m/z 4, 12, 16, 18, 28, 29, 32, and 44). The amount of H_2 consumed was calculated based on the H_2 peak area. Calibration was performed using the *AutoChem III 2930* loop (0.5185 cm^3) by performing five injections of 10 vol% H_2/Ar at 110 °C, with a He carrier flow of 50 mL/min (STP) with an empty sample tube. The total amount of H_2 consumed was obtained from the sample's integrated profile area and the average peak area of the five calibration injections at m/z 2.

The interaction of CO_2 with the reduced Fe_3O_4 and cobalt-promoted Fe_3O_4 was investigated by CO_2-TPD. The samples were obtained as described in Section 2.1 by reduction of the pretreated samples at 400 °C (heating rate 3 °C/min) for 22 h using a H_2 flow of 50 mL/min (STP). The CO_2-TPD experiment was performed in an *AutoChem-III 2930* tool (Micromeritics Instrument Corporation) equipped with a *Cirrus*™ *3* mass spectrometer (MKS Instruments). The samples were kept dry at 110 °C for several hours in static air before the analysis. For the CO_2-TPD analysis, about 120 mg of sample was placed into the sample tube between two pieces of quartz wool. The sample was treated in helium (Linde, 99.9996%) using 50 mL/min (STP) at 200 °C, 10 °C/min, for 1 h, and then cooled to 35 °C. A reduction step was then performed using 50 mL/min (STP) of a 10 vol% H2/Ar mixture (Air Products, 99.99%) from 35 to 400 °C, at 10 °C/min, and 0.5 h hold time, followed 0.5 h purge under a helium flow of 50 mL/min (STP). The sample was then cooled to 35 °C and saturated with 50 mL/min of a gas mixture comprised by 40 mL/min (STP) of 5 vol% CO_2/He (Woikoski, 99.99%) and 10 mL/min (STP) of He. The saturated sample was flushed for 0.5 h with 50 mL/min (STP) of He to remove weakly adsorbed CO_2. Finally, the sample was heated from 35 to 800 °C (heating rate 10 °C/min, hold time 0.5 h) using 50 mL/min (STP) of He. Desorption was monitored by following signals at *m/z* 2, 12, 14, 16, 18, 22, 28, 29, 30, 32, and 44. Carbon dioxide desorption was monitored by following MS signal at m/z 44. Since CO_2 mass spectrum contains a fragment at m/z 28, the MS signal at m/z 28 for carbon monoxide was assumed to be equivalent to the recorded MS signal at *m/z* 28 minus the contribution of CO_2 to the MS signal at m/z 28. The contribution of CO_2 to m/z 28 was obtained by multiplying the TPD recorded signal at m/z 44 by the ratio between the signals at m/z 28 and m/z 44 of CO_2 obtained from CO_2 signal calibration. The calibration of the CO_2 signals was performed between the CO_2-TPD analyses using the *AutoChem-III 2930* instrument's loop (calibrated loop volume 0.5185 cm^3) with five loop injections of 5 vol% CO_2/He at 110 °C, with a He carrier flow of 50 mL/min (STP), and an empty sample tube. The total amount of CO_2 adsorbed was obtained using the sample's integrated profile area and the average area of the five calibration injections at m/z 44.

Carbon deposition on spent catalysts was quantified via combustion analysis using a *Euro Vector EA 3000* CHN analyser.

3. Results and discussion

3.1. *Catalyst characterisation*

The thermogravimetric curves of Fe_3O_4, $Co(NO_3)_2{\bullet}6H_2O$ and cobalt-promoted catalyst precursor ($Co(NO_3)_2$ on Fe_3O_4) are presented in Fig. S1 in the Supplementary Information. Within the temperature range of 30 to 600 °C, Fe_3O_4 exhibited minimal weight loss, indicating high thermal stability. In contrast, $Co(NO_3)_2{\bullet}6H_2O$ underwent substantial multi-step weight loss, with dehydration observed up to approximately 150 °C and nitrate decomposition occurring between 150 and 300 °C. Cobalt-promoted catalyst precursor ($Co(NO_3)_2$ on Fe_3O_4) exhibited weight loss between 150 and 200 °C, which is indicative of cobalt nitrate decomposition. The results indicate that the selected temperature range of 400–550 °C for catalyst calcination and reduction is sufficient to fully decompose $Co(NO_3)_2$.

The effect of the pretreatment procedure on catalyst phase composition was investigated by XRD and XPS. X-ray diffractograms of catalysts are illustrated in Fig. 1. Although quartz sand was separated from the catalysts before analysis, SiO_2 (quartz, PDF 01–075-6052) was detected for some of the catalysts. Due to the Co concentration nearing the XRD detection limit, there were no peaks associated with Co

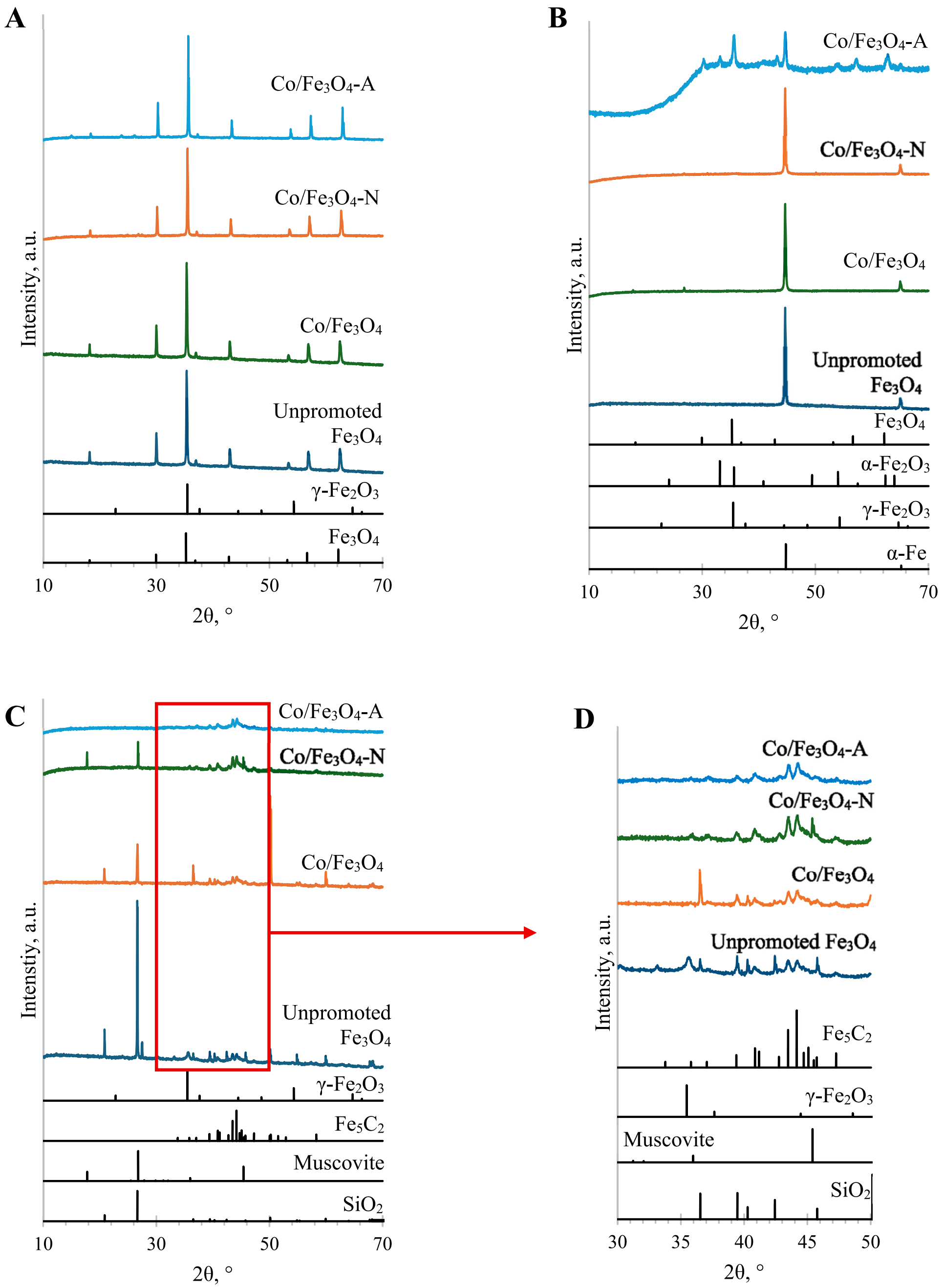

Fig. 1. XRD patterns of catalysts before reduction (A); after reduction (B) and after CO_2 hydrogenation (C) and (D).

detected in the catalysts.

α-Fe (Iron; PDF 01–071-4409) was detected in unpromoted Fe_3O_4 after reduction in H_2. Similarly, α-Fe was detected in Co/Fe_3O_4 after reduction in H_2. (Fig. 1B).

For the Co/Fe_3O_4-N, the XRD patterns after calcination in N_2 showed Fe_3O_4 (magnetite; PDF 01–071-6336), from which α-Fe was formed after the reduction in H_2.

The XRD pattern of Co/Fe_3O_4-A after calcination in air showed diffraction signals which can be associated with γ-Fe_2O_3 (maghemite; PDF 00–039-1346). However, since maghemite can be distinguished from magnetite only by a few additional peaks, the possible presence of Fe_3O_4 in the sample could not be ruled out. After reduction in H_2, the diffraction pattern of Co/Fe_3O_4-A showed reflections attributed to γ-Fe_2O_3, α-Fe_2O_3 (hematite; PDF 01–086-0550) and α-Fe. As before, the presence of Fe_3O_4 in the sample could not be ruled out.

Fe_3O_4 oxidation is known to proceed through metastable γ-Fe_2O_3, whose structure closely resembles the structure of Fe_3O_4. Thus, the Fe_3O_4 to γ-Fe_2O_3 transformation is primarily compositional [28]. In contrast, the subsequent γ-Fe_2O_3 to α-Fe_2O_3 conversion requires structural rearrangement and is strongly influenced by factors such as particle size and heteroatom incorporation [29]. Given the relatively short calcination step of Co/Fe_3O_4-A (30 min at 550 °C), only γ-Fe_2O_3 was formed under these conditions, whereas the slower γ-Fe_2O_3 to α-Fe_2O_3 transformation proceeded partially during the prolonged reduction (22 h at 400 °C).

XRD patterns of spent catalysts showed reflections attributed to Fe_5C_2 (Hägg carbide; PDF 04–006-5691). Additional diffraction signals corresponding to γ-Fe_2O_3 were observed for the unpromoted Fe_3O_4 catalyst after CO_2 hydrogenation (Fig. 1C and D).

Crystallite sizes were calculated from XRD data using both the Scherrer equation and Rietveld refinement (Table 1). During the Rietveld refinement, crystallite sizes for the Fe and Fe_2O_3 phases in Co/Fe_3O_4-A catalyst after reduction, as well as for the Fe_5C_2 phase in all catalysts after CO_2 hydrogenation, were constrained to default values and are therefore reported identically without standard uncertainties. For the minor phases (Fe and Fe_2O_3), this was due to their low weight fractions. For the primary Fe_5C_2 phase, constraining the size parameters was necessary because its complex, heavily overlapping diffraction pattern and low peak intensities prevented the stable refinement of peak profile shapes.

Table 1
Crystallite size calculated by Rietveld refinement and Scherrer formula.

Sample	Detected iron phases	Crystallite size (Rietveld), nm	Crystallite size (Scherrer Equation), nm
Fe_3O_4 before reduction	Fe_3O_4	136 ± 7	63.8
Co/Fe_3O_4 before reduction	Fe_3O_4	142 ± 7	66.4
Co/Fe_3O_4-N before reduction	Fe_3O_4	173.7 ± 6	76.2
Co/Fe_3O_4-A before reduction	γ-Fe_2O_3 Fe_3O_4	302 ± 30 123 ± 6	111.9*
Fe_3O_4 after reduction	Fe	89.1 ± 4.8	59.0
Co/Fe_3O_4 after reduction	Fe	75.5 ± 2.7	55.0
Co/Fe_3O_4-N after reduction	Fe	76.7 ± 3.0	55.8
Co/Fe_3O_4-A after reduction	Fe γ-Fe_2O_3 α-Fe_2O_3	42.4** 19.7 ± 0.5 42.4**	33.6 22.5 46.1
Fe_3O_4 after CO_2 hydrogenation	γ-Fe_2O_3 Fe_5C_2	16.2 ± 0.7 42.4**	23.0 49.9
Co/Fe_3O_4 after CO_2 hydrogenation	Fe_5C_2	42.4**	47.6
Co/Fe_3O_4-N after CO_2 hydrogenation	Fe_5C_2	42.4**	42.1
Co/Fe_3O_4-A after CO_2 hydrogenation	Fe_5C_2	42.4**	44.4

[*] Calculated from peaks which correspond to both maghemite (Fe_3O_4) and magnetite (γ-Fe_2O_3).

[**] Results constrained to default values.

Most of the crystallite sizes estimated using the Scherrer equation were smaller than those obtained from Rietveld refinement. This discrepancy arises because the Scherrer approach assumes that diffraction peak broadening originates exclusively from finite crystallite size and does not account for macrostrain or other structural defects, whereas Rietveld refinement considers the full diffraction pattern and enables separation of different peak-broadening contributions [30,31].

After reduction in H_2, the unpromoted Fe_3O_4 catalyst exhibited the largest crystallite size, whereas the phases detected in Co/Fe_3O_4-A had the smallest crystallite sizes. This indicates that the prior calcination of Co/Fe_3O_4-A in air has not induced significant sintering of the particles before the reduction step. Furthermore, after CO_2 hydrogenation, the crystallite size of Fe_5C_2 was within the range of 49.9–42.1 nm (Scherrer Equation), with the smallest values observed for calcined catalysts (Co/Fe_3O_4-N and Co/Fe_3O_4-A). These results demonstrate that cobalt acts as an effective structural stabiliser, preventing the agglomeration of the iron phases during both the reduction and CO_2 hydrogenation.

XPS analyses were performed to investigate catalyst surface composition. The Fe 2p spectrum of unpromoted Fe_3O_4 catalyst after reduction in H_2 is shown in Fig. 2. The deconvolution of the Fe $2p_{3/2}$ region showed simultaneous presence of $Fe^{(0)}$, Fe^{2+} and Fe^{3+} species, indicating the tendency of the catalyst surface to oxidise.

The obtained Fe 2p spectra of cobalt-promoted catalysts after calcination and after reduction in H_2, and their deconvolution results are shown in Fig. 3. Characterising the chemical states of Fe and Co via XPS is challenging due to complex spectra and significant overlap between the Fe 2p region (700–740 eV) and Co LMM Auger transitions (~713 eV), as well as the Co 2p region (770–815 eV) and Fe LMM Auger transitions (~784 eV) [32]. Due to the low cobalt content in our catalysts, the Co LMM Auger peak had a negligible effect on the Fe 2p region. Conversely, the Co 2p region was obscured by Fe LMM Auger transition and background noise, making it impossible to quantify Co or determine its oxidation state.

The XPS spectra of Co/Fe_3O_4 and Co/Fe_3O_4-N (both, before and after reduction) showed Fe $2p_{3/2}$ and Fe $2p_{1/2}$ doublet peaks at approximately 711 eV and 724–725 eV, respectively, consistent with mixed-valence Fe^{2+}/Fe^{3+} states. A weak satellite at 716–719 eV in Co/Fe_3O_4 and Co/Fe_3O_4-N (after calcination in N_2) confirmed the presence of Fe^{2+} and Fe^{3+} species. This suggests that Fe_3O_4 is likely the dominant oxide on the surface.

In contrast, the doublet peaks attributed to Fe $2p_{3/2}$ and Fe $2p_{1/2}$ were shifted toward higher binding energies for the air-treated Co/Fe_3O_4-A sample (both, before and after reduction), suggesting the presence of Fe_2O_3. A satellite peak at 720.0 eV in Co/Fe_3O_4-A (after reduction) confirmed the presence of Fe^{3+} species.

The deconvolution of the Fe $2p_{3/2}$ region revealed the coexistence of Fe^{2+} and Fe^{3+} surface species for all samples. For Co/Fe_3O_4 and Co/Fe_3O_4-N after reduction in H_2, an additional low-binding-energy component corresponding to metallic Fe was detected. The XPS results are generally consistent with the XRD findings; however, XPS results also indicate that the surface of the samples is oxidised.

The H_2-TPR profiles (Fig. 4) and peak deconvolution curves (Fig. S2-S5) demonstrate that despite a low cobalt loading (Co:Fe = 5:100), the addition of the promoter significantly enhances the overall reducibility of the iron catalysts through a hydrogen spillover effect [8]. For the unpromoted Fe_3O_4, a minor low-temperature reduction peak at ~ 380 °C was observed; this can be attributed to the reduction of a thin surface passivation layer of Fe_2O_3 back to Fe_3O_4, resulting from the oxidation of magnetite upon contact with ambient air [33]. This initial step was followed by a broad, demanding high-temperature peak extending to 800 °C, representing the bulk reduction of Fe_3O_4 through FeO to metallic iron [34,35]. For cobalt-promoted catalysts, this high-

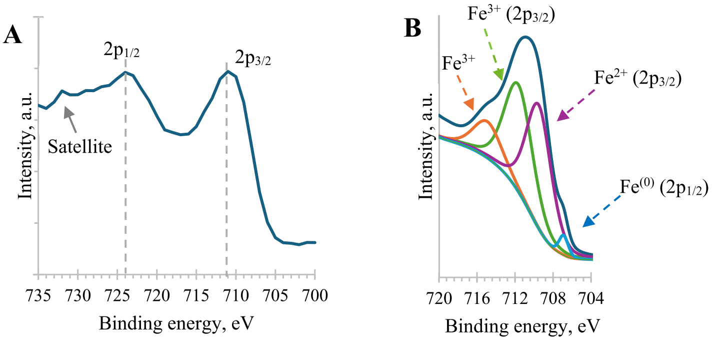

Fig. 2. Fe 2p XPS spectrum of unpromoted Fe_3O_4 catalyst after reduction in H_2 and deconvolution of Fe $2p_{3/2}$ peak.

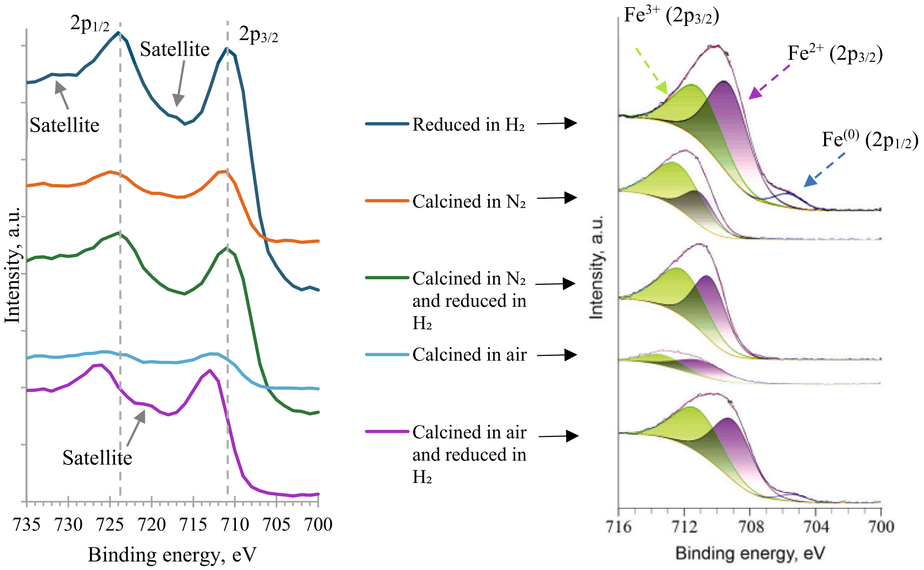

Fig. 3. Fe 2p XPS spectra and deconvolution of Fe $2p_{3/2}$ peak of cobalt-promoted catalysts.

temperature reduction shifted noticeably to lower temperatures, as easily reduced cobalt species dissociate H_2 into highly reactive atomic hydrogen to facilitate iron reduction.

The specific pretreatment conditions dictated the initial phase composition and these distinct low-temperature reduction events. The uncalcined Co/Fe_3O_4 sample displayed early reduction shoulders (~200–400 °C). The rise/peak at ~200 °C can be associated with nitrate decomposition. This is also confirmed by the TG profile of the cobalt-promoted catalyst precursor ($Co(NO_3)_2$ on Fe_3O_4, Fig. S1). Smaller peaks at 300–400 °C can be associated with the reduction of highly dispersed cobalt [36]. Calcination of Co/Fe_3O_4-N in an inert N_2 atmosphere resulted in a broadened mid-temperature peak (~ 400–450 °C); while this feature likely obscures the minor reduction of any surface passivation layer formed during sample handling, its significant broadening and shift to higher temperatures are indicative of reduction of $CoFe_2O_4$ spinels or highly interacting Co-Fe solid solutions formed via strong solid-state interactions. In contrast, the air-calcined Co/Fe_3O_4-A exhibited a distinct peak near 450 °C, attributed to the concurrent reduction of γ-Fe_2O_3 to Fe_3O_4 and the reduction of $CoFe_2O_4$ spinels [37].

Evaluating the surface basicity of the prepared catalysts through selective CO_2 chemisorption is crucial, given that these basic sites are known to govern the initial RWGS reaction and subsequently alter the final product distribution [38]. The CO_2-TPD and CO desorption profiles (Fig. 5), interpreted alongside XRD findings, reveal that the catalyst's surface acidity and the CO_2 activation pathways are heavily dependent on the final iron phase composition. The cobalt promotion and catalyst pretreatment conditions profoundly altered the surface chemistry. For the unpromoted Fe_3O_4, uncalcined Co/Fe_3O_4 and N_2-calcined Co/Fe_3O_4-N, XRD confirmed complete reduction to metallic α-Fe. Correspondingly, their CO_2-TPD profiles are dominated by low-to-moderate temperature desorption peaks (<250 °C), representing weak and medium basic sites characteristic of fully reduced metallic surfaces. Notably, even this small amount of cobalt (Co:Fe = 5:100) was sufficient to subtly enhance the moderate basic sites (~ 180 °C) and consolidate the CO dissociation peak around 450 °C, suggesting the promoter

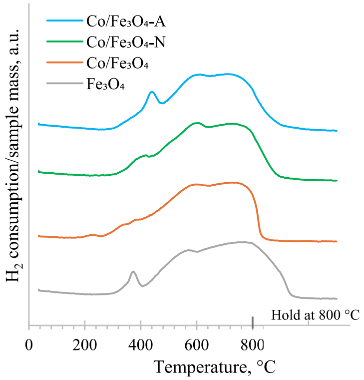

Fig. 4. H_2-TPR profiles (from MS signal at *m/z* 2) of unreduced Fe_3O_4 and cobalt-promoted Fe_3O_4 samples. Profiles were offset vertically for clarity.

facilitates a more uniform active surface for CO_2 activation.

In contrast, the air-calcined Co/Fe_3O_4-A exhibited large high-temperature CO_2 and CO desorption peaks (500–700 °C). Since XRD confirmed that the catalyst was only partially reduced, comprising γ-Fe_2O_3, α-Fe_2O_3 and α-Fe (Fig. 1 and Table 1), and considering the negligible cobalt content, these intense high-temperature features can be attributed to unreduced iron oxides rather than cobalt species. The presence of these oxides creates highly localised, strong basic sites and active metal-oxide interfaces that tightly bind and vigorously dissociate CO_2. The calcination atmosphere dictates the extent of iron reduction, thereby dictating whether CO_2 activation occurs via a purely metallic surface or a highly active metal-oxide interfacial pathway.

The quantitative analysis of catalyst reducibility and surface basicity is summarised in Table 2. For the unpromoted Fe_3O_4, uncalcined Co/Fe_3O_4, and N_2-calcined Co/Fe_3O_4-N, the primary iron phase before reduction is Fe_3O_4. The experimental values for these samples (17.1 to 18.4 mmol/g) closely align with these theoretical benchmarks, confirming deep, near-complete bulk reduction to metallic α-Fe at 800 °C. The minor deviations, specifically the slightly higher consumption observed for the unpromoted Fe_3O_4, can be attributed to the reduction of surface hydroxyl groups or residual moisture. In contrast, for the air-calcined sample, as revealed by XRD, the primary iron phase before reduction is γ-Fe_2O_3, which theoretically requires higher H_2 consumption for complete reduction. The experimentally obtained H_2 consumption value is lower than the theoretical, indicating incomplete reduction of Co/Fe_3O_4-A. The CO_2 desorption capacities varied significantly depending on the catalyst composition and pretreatment. The unpromoted Fe_3O_4 exhibited the lowest surface basicity. The introduction of cobalt in the uncalcined and N_2-calcined samples generated a moderate increase in basicity, whereas the air-calcined Co/Fe_3O_4-A catalyst demonstrated an exceptionally high CO_2 desorption capacity of 115 μmol/g. This increase provides quantitative evidence for the formation of highly localised, strong basic sites at the preserved metal-oxide interfaces.

In order to assess how cobalt promotion and catalyst pretreatment influence coke/carbon formation and deposition, all catalysts after CO_2 hydrogenation were analysed using CHN elemental analysis (Table S1). Results showed that the least amount of carbon was deposited on the surface of the unpromoted catalyst (2.7 wt%). In contrast, cobalt-promoted catalysts showed significantly higher carbon contents, ranging from 7.0 to 7.7 wt%, with the highest value observed for Co/Fe_3O_4-N. These results indicate that cobalt promotion increases the carbon formation and deposition on the catalyst surface.

3.2. Catalytic performance: Effect of reaction temperature on product distribution

For all catalysts, an increase in CO_2 conversion was observed with the elevation of the reaction temperature. With increasing reaction temperature from 280 °C to 320 °C, CO_2 conversion rose by approximately 15.1% for unpromoted Fe_3O_4 and by 7.3–8.8% for cobalt-promoted catalysts. Although CHN elemental analysis indicated coke/carbon formation and deposition on the surface of cobalt-promoted

Table 2
H_2 consumption and CO_2 desorption capacities for the catalysts.

Sample	H_2 consumption, mmol/g_{cat}		CO_2 desorbed, μmol/g_{cat}
	Experimental	Theoretical	
Fe_3O_4	18.4	17.3	47
Co/Fe_3O_4	17.6	17.2	65
Co/Fe_3O_4-N	17.1	17.2	59
Co/Fe_3O_4-A	17.4	18.7	115

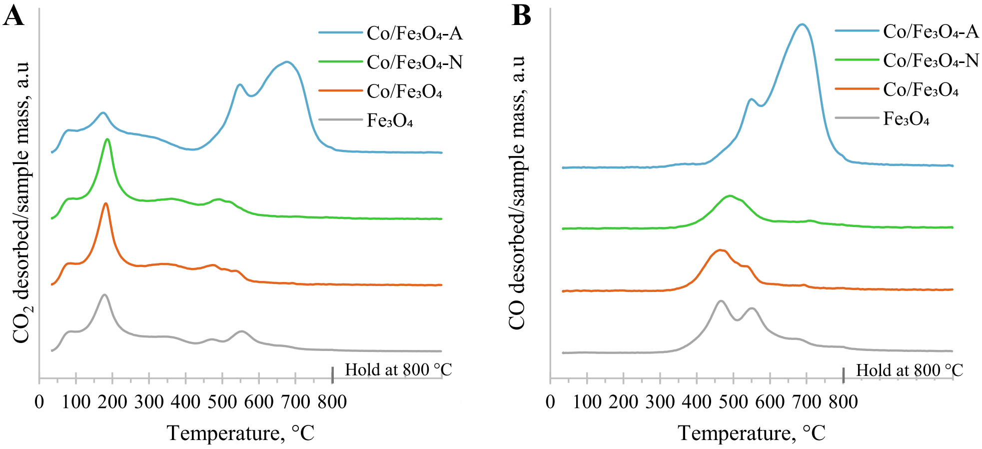

Fig. 5. CO_2-TPD profiles of reduced Fe_3O_4 and cobalt-promoted Fe_3O_4 samples after CO_2 adsorption at 35 °C: desorbed CO_2 from MS signal at m/z 44 (A), desorbed CO from adjusted MS signal at m/z 28 (B). Profiles were offset vertically for clarity.

catalysts (Table S1), all evaluated catalysts exhibited good time on stream stability across all tested temperatures (Fig. S6 – S9). No significant performance degradation was observed during the time on stream analysis, indicating a strong resistance to thermal degradation under the tested reaction conditions.

The reaction temperature affected the RWGS and FTS rates (and thus product selectivity) differently for unpromoted and cobalt-promoted catalysts (Fig. 6).

For unpromoted Fe_3O_4, with the elevation of the reaction temperature, CO selectivity decreased, while hydrocarbon selectivity increased significantly (Fig. 6A). The observed decrease in CO selectivity at elevated temperatures could be explained by secondary conversion of initially formed CO with increasing temperature (increased FTS activity). Although total hydrocarbon selectivity, including C_{2+} fractions, rose with increasing reaction temperature, the highest selectivity toward C_{5+} hydrocarbons was observed at 300 °C. In contrast to conventional FTS, CO_2 hydrogenation usually requires a higher H_2 concentration, while the concentration of CO intermediates is lower. This creates a relatively high H/C ratio on the catalyst surface, which in turn promotes methane formation and suppresses hydrocarbon chain growth [71]. With increasing CO_2 conversion (increased RWGS activity), the surface H/C ratio decreases, thus leading to increased chain growth probability.

For cobalt-promoted catalysts, CO selectivity remained high ($> 49\%$) across all temperatures, indicating that the RWGS pathway is predominant and relatively unaffected by changes in reaction temperature compared to competing pathways leading to CH_4 and C_{2+} hydrocarbons (Fig. 6B – 6D).

CH_4 selectivity for Co/Fe_3O_4 and Co/Fe_3O_4-N increased as the temperature rose from 280 °C to 300 °C, but decreased slightly at 320 °C. In contrast, Co/Fe_3O_4-A showed a continuous increase in CH_4 selectivity, reaching 16.0% at 320 °C. This indicates that at higher temperatures, CH_4 formation competes more effectively with FTS reactions, thereby reducing the yield of long-chain hydrocarbons.

The most significant temperature-induced changes observed for cobalt-promoted catalysts were associated with the formation of C_2-C_4 and C_{5+} hydrocarbons. As the temperature rose, C_2-C_4 hydrocarbon formation increased rapidly, while C_{5+} hydrocarbon selectivity decreased. With increasing reaction temperature from 280 °C to 320 °C, C_2–C_4 selectivity increased by approximately 6.0% for Co/Fe_3O_4, 6.4% for Co/Fe_3O_4-N, and 6.7% for Co/Fe_3O_4-A. The most pronounced temperature-induced changes were observed for C_{5+} hydrocarbons. Conversely, C_{5+} selectivity decreased significantly with temperature: from 19.2% to 12.6% for Co/Fe_3O_4, from 33.6% to 22.5% for Co/Fe_3O_4-N, and from 36.8% to 23.2% for Co/Fe_3O_4-A. The hydrocarbon distribution in FTS reactions is described by the Anderson–Schulz–Flory model, where the chain-growth probability (α) determines the product chain lengths. Increasing the reaction temperature decreases α, thereby reducing the probability of long-chain growth and shifting selectivity toward shorter hydrocarbons. These shorter chain hydrocarbons are thermodynamically favoured at higher temperatures [39].

Wang et al. [40] also investigated the CO_2 hydrogenation performance of K-promoted Fe-Co bimetallic catalysts at 250 °C and 300 °C, 20 bar with H_2/CO_2 ratio of 2. Similar to our study, they also observed that the addition of cobalt improved selectivity toward hydrocarbons (especially C_{5+}) compared to the K-promoted catalyst without cobalt. With the elevation of reaction temperature from 250 °C to 300 °C, they observed an increase in CO_2 conversion from 10.2% to 33.7% for the FeK_2 catalyst and from 17.2% to 46.8% for the cobalt-promoted $Fe_{12}CoK_2$ catalyst. At the same time, a sharp decrease in CO selectivity was observed for both catalysts (from 67.7% to 10.6% for FeK_2 and from 25.8% to 4% for $Fe_{12}CoK_2$). However, the catalytic performance of cobalt-promoted catalysts observed by Wang et al. differed from that of

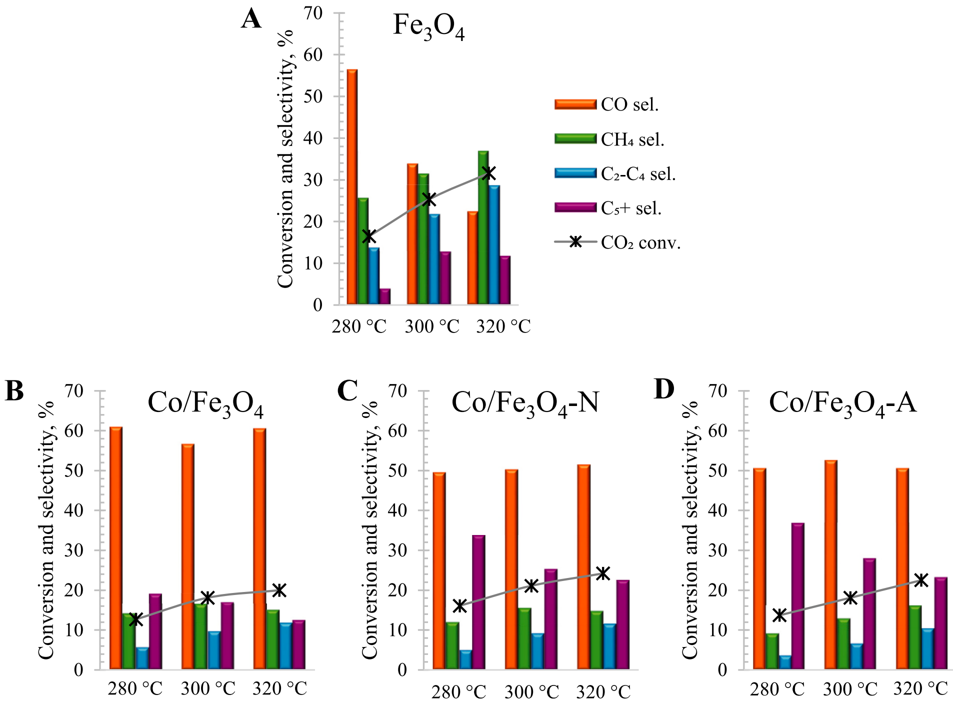

Fig. 6. The influence of reaction temperature on the catalytic performance of unpromoted (A) and cobalt-promoted Fe_3O_4 (B, C, D).

cobalt-promoted catalysts in our study. Our cobalt-promoted catalysts demonstrated a lower CO_2 conversion level and higher CO selectivity. Besides, the CO selectivity for cobalt-promoted catalysts remained almost unchanged across all tested temperatures. The observed differences might be related to catalyst Co loadings (Co:Fe = 5:100 in our study vs 1:12 reported in [40]), the presence of K, as well as differences in reaction conditions.

The process of CO_2 hydrogenation to hydrocarbons produces

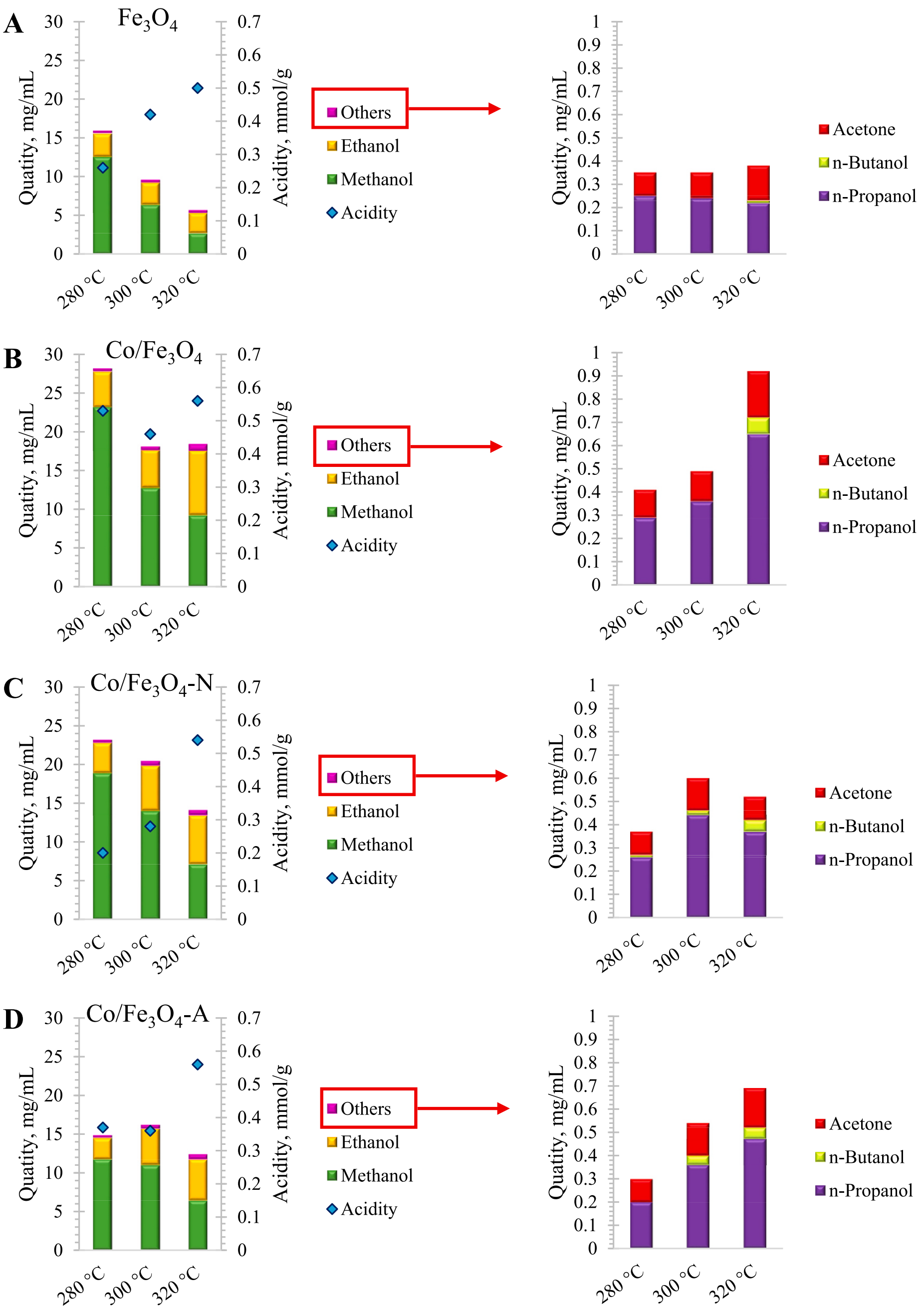

Fig. 7. The influence of reaction temperature on the aqueous phase product quantity and composition of minor oxygenate products (others) over unpromoted (A) and cobalt-promoted Fe_3O_4 (B, C, D).

substantial wastewater. Water is produced via both the RWGS (Eq. 1) and the FTS (Eq. 2) reactions. This wastewater contains various oxygenated compounds, such as alcohols, acids, aldehydes, and ketones, necessitating appropriate treatment. Limiting the formation of by-products is essential, as these compounds reduce the selectivity of target products and pose both environmental and economic challenges. The water-soluble oxygenates represented less than 2% of total product selectivity (Table 1S). For all catalysts, methanol was the main oxygenate; other observed products were *n*-alcohols up to *n*-butanol and acetone.

Fig. 7 demonstrates that increasing the reaction temperature produces similar trends in oxygenate selectivity across all catalysts studied. As the temperature increased from 280 °C to 320 °C, the methanol concentration decreased rapidly. The lowest methanol production (2.7 mg/mL) was observed at 320 °C for unpromoted Fe$_3$O$_4$. Among cobalt-promoted catalysts, the lowest methanol production (6.4 mg/mL) was observed at 320 °C for Co/Fe$_3$O$_4$-A. According to the literature, at temperatures above 280 °C, the thermodynamics and equilibrium of CO$_2$ hydrogenation favour CH$_4$ formation over methanol [41]. For all catalysts studied, CH$_4$ formation therefore competes more effectively with both FTS reactions and methanol formation.

An increase in temperature from 280 °C to 320 °C resulted in a more rapid rise in the concentration of C$_{2+}$ alcohols in the aqueous phase. Notably, *n*-butanol formation was observed with Co/Fe$_3$O$_4$-N at 280 °C, whereas at 320 °C, *n*-butanol was detected in the aqueous phase for all catalysts. Previous studies demonstrate that cobalt-containing iron catalysts possess high activity for CO dissociation and C-C coupling. These catalysts also promote hydrogenation steps, thereby enhancing the formation of longer-chain oxygenated products at elevated temperatures. This tandem mechanism contrasts with low-temperature methanol pathways, which are less favourable under these conditions [42].

Acetone was present in the aqueous phase at all reaction temperatures and for all catalysts examined. As with other C$_{2+}$ oxygenates, its concentrations in the aqueous phase increased with increasing temperature. During CO$_2$ hydrogenation, acetone formation occurs as a secondary reaction. This process is feasible only when C$_3$ intermediates are generated within the system, and oxidising conditions exist [42].

3.3. Catalytic performance: Effect of catalyst pretreatment on product distribution

Promoted iron-based catalysts experience multiple phase transformations during both activation and the CO$_2$-FTS reaction. Pretreatment with various gases can alter the composition of Co and Fe phases and, consequently, the catalytic activity during the target reaction.

The catalyst precursor was divided into three portions for different pretreatments: direct H$_2$ reduction (Co/Fe$_3$O$_4$), N$_2$ calcination followed by H$_2$ reduction (Co/Fe$_3$O$_4$-N), and air calcination followed by H$_2$ reduction (Co/Fe$_3$O$_4$-A). The influence of catalyst pretreatment on product distribution during CO$_2$ hydrogenation was assessed at 280 °C (Fig. 8). At this temperature, C$_{2+}$ product selectivity exceeds that observed at 300 °C and 320 °C for all catalysts (Fig. 6).

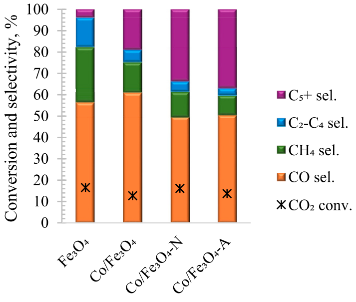

Fig. 8. The influence of pretreatment procedure on the catalytic performance of unpromoted and cobalt-promoted Fe$_3$O$_4$ at 280 °C.

None of the catalysts exhibited sufficiently strong CO$_2$ activation or H$_2$ dissociation to promote deep hydrogenation pathways. The RWGS reaction was the predominant pathway during CO$_2$ hydrogenation at 280 °C with these catalysts, as evidenced by CO selectivity up to 61% observed with Co/Fe$_3$O$_4$. The H$_2$O generated during the RWGS stage can negatively impact the formation of the active iron carbide phase and promote its oxidation back to Fe$_3$O$_4$ [43].

The catalytic performance data, evaluated alongside the XRD analysis of the spent catalysts, provide a clear mechanistic picture of how cobalt promotion and pretreatment strategies govern product selectivity during CO$_2$ hydrogenation. The unpromoted Fe$_3$O$_4$ benchmark catalyst showed the highest CO$_2$ conversion (16.5%) but exhibited high selectivity toward light hydrocarbon fraction with minimal C$_{5+}$ formation (Fig. 8). The XRD pattern of spent Fe$_3$O$_4$ catalyst showed γ-Fe$_2$O$_3$ alongside the active Fe$_5$C$_2$ (Hägg carbide) phase, indicating water-induced oxidation during the reaction. The oxidation of active carbidic sites prematurely terminates C-C chain growth, thereby driving the selectivity toward shorter hydrocarbons. In contrast, the XRD patterns of spent cobalt-promoted catalysts showed only the active Fe$_5$C$_2$ phase with no detectable γ-Fe$_2$O$_3$. Before CO$_2$ hydrogenation, reduced Fe$_3$O$_4$, Co/Fe$_3$O$_4$, and Co/Fe$_3$O$_4$-N contained α-Fe as the main bulk crystalline phase. This indicates that even at low loading, cobalt protects the Fe$_5$C$_2$ phase from water-induced oxidation. Consequently, cobalt promotion suppressed CH$_4$ formation and enhanced C$_{5+}$ hydrocarbon selectivity for all cobalt-promoted catalysts. H$_2$-TPR analysis (Fig. 4) demonstrated that the addition of cobalt improves bulk iron reducibility through the hydrogen spillover effect.

Furthermore, the selected pretreatment strategy significantly influenced the CO$_2$ hydrogenation performance of cobalt-promoted catalysts. While the uncalcined Co/Fe$_3$O$_4$ catalyst strongly favoured the RWGS pathway, yielding the highest CO selectivity, calcination significantly enhanced catalytic performance. Although the system remained within the RWGS regime in the presence of calcined cobalt-promoted catalysts, N$_2$-calcined Co/Fe$_3$O$_4$-N achieved the highest CO$_2$ conversion (16.1%) and the lowest CO selectivity (49.5%) at 280 °C. Air-calcined Co/Fe$_3$O$_4$-A demonstrated a marginally higher CO$_2$ conversion (13.7%) compared to uncalcined Co/Fe$_3$O$_4$ (12.7%). The CO selectivity of Co/Fe$_3$O$_4$-A was similar to that of Co/Fe$_3$O$_4$-N, while its C$_{2+}$ hydrocarbon selectivity (40.4%) during the CO$_2$ hydrogenation process was the highest among all catalysts evaluated. Given that XRD detected metallic Fe as the sole phase for unpromoted Fe$_3$O$_4$, uncalcined Co/Fe$_3$O$_4$ and N$_2$-calcined Co/Fe$_3$O$_4$-N prior to the CO$_2$-FTS, it can be concluded that the catalytic performance is strongly influenced by the formed cobalt phase and resulting cobalt-iron interactions.

Fig. 6 demonstrates that the main difference between the uncalcined (Co/Fe$_3$O$_4$) and calcined (Co/Fe$_3$O$_4$-N and Co/Fe$_3$O$_4$-A) cobalt-promoted catalysts is their hydrocarbon selectivity, especially for C$_{5+}$. The specific Co phases present on the catalyst surface influenced the degree of C$_{5+}$ selectivity enhancement. Consequently, catalyst pretreatment plays a crucial role in determining the final product distribution. The uncalcined Co/Fe$_3$O$_4$ exhibited the lowest C$_{5+}$ selectivity among cobalt-promoted catalysts. For the preparation of all cobalt-promoted Fe$_3$O$_4$ catalysts, Co(NO$_3$)$_2$ was employed as the precursor. When Co(NO$_3$)$_2$ on Fe$_3$O$_4$ is subjected to a H$_2$ atmosphere at 400 °C, metallic Co is expected to be the predominant phase formed [44]. Given that Fe$_3$O$_4$ serves as the support, the formation of a Co-Fe alloy is also theoretically possible; however, a significant extent of Co-Fe alloying generally requires higher temperatures [45]. Thus, the dominant cobalt phase in the Co/Fe$_3$O$_4$ catalyst most likely is metallic Co, and the observed low catalytic activity may be attributed to its susceptibility to oxidation, especially when exposed to H$_2$O, which reduces its activity. This phenomenon could account for the reduced catalytic performance of Co/Fe$_3$O$_4$ during hydrocarbon formation.

The calcined catalysts Co/Fe_3O_4-N and Co/Fe_3O_4-A exhibited enhanced selectivity for C_{5+} hydrocarbons, indicating that their surfaces, in addition to metallic Co, most likely contain other cobalt-based compounds that contribute to this increased selectivity. Pretreatment of Co/Fe_3O_4-N in a N_2 atmosphere at 450 °C, followed by reduction in H_2, likely leads to the formation of cobalt ferrite spinel ($CoFe_2O_4$) on the surface, as metallic Co formation is restricted under N_2 conditions [38].

Given that Co/Fe_3O_4-A also exhibited high C_{5+} selectivity, it is likely that cobalt in this catalyst is also not present as metallic Co or as cobalt oxides (Co_xO_y). Unlike Co/Fe_3O_4-N, this catalyst showed a significantly lower content of oxygen-containing compounds in the aqueous phase, which is most likely due to the formation of a cobalt ferrite phase distinct from stoichiometric $CoFe_2O_4$. XRD of the catalyst before reduction indicated the presence of γ-Fe_2O_3 and partially α-Fe_2O_3; it appears that these phases exhibit a stronger synergistic effect with cobalt than those observed for the other catalysts. According to a literature study [46], nonstoichiometric cobalt ferrite ($Co_xFe_{3\text{-}x}O_4$) can form when an Fe^{3+}-rich zone and Co^{2+} are available.

We further assessed the distribution of aqueous-phase products generated during CO_2 hydrogenation in the presence of the selected catalysts at 280 °C (Fig. 9). Previous studies have identified iron carbides as the active phase in FTS for the production of various chemicals, including alcohols. Furthermore, the incorporation of cobalt into iron-based catalysts enhances catalytic performance in CO_2 hydrogenation and increases alcohol selectivity [47,48].

Analysis of the aqueous phase revealed that the formation of water-soluble oxygenates was a minor reaction pathway for all tested catalysts, accounting for 1.6% or less of the total product selectivity (Table S2). The aqueous phase composition was dominated by short-chain alcohols – primarily methanol, followed by ethanol. Despite the low overall yields, the catalyst pretreatment procedures significantly influenced the extent of oxygenate formation. The uncalcined Co/Fe_3O_4 catalyst exhibited the highest oxygenate selectivity (1.6%), the largest total quantity of oxygenates in aqueous phase (~28 mg/mL) and the highest aqueous phase acidity (~0.53 mmol/g). This indicates that without a thermal pretreatment step to drive robust Co-Fe structural integration, the catalyst surface is more prone to early chain termination, releasing intermediates as short-chain alcohols and organic acids. As discussed previously, Co/Fe_3O_4 catalyst most likely contains metallic Co, which is susceptible to oxidation. From the literature, it is known that cobalt oxides can promote the formation of oxygenates. Co^{2+}/Co^{3+} oxide phases preferentially promote associative formate intermediates under hydrogenation conditions, in contrast to metallic phases that favour dissociative C-O bond cleavage pathways [49]. Conversely, air calcination strongly suppressed these oxygenate pathways. The Co/Fe_3O_4-A catalyst yielded the lowest overall oxygenate selectivity (0.5%) and total quantity of oxygenates in aqueous phase (~15 mg/mL).

The observed trends in aqueous phase oxygenate formation directly correlate with the surface basicity identified via CO_2-TPD. The uncalcined Co/Fe_3O_4 catalyst possesses moderate basic sites that permit the premature desorption of oxygenated intermediates, resulting in the highest yield of short-chain alcohols and acids. Similarly, the unpromoted Fe_3O_4 and N_2-calcined Co/Fe_3O_4-N also possess moderate basic sites and exhibit high selectivity toward water-soluble oxygenates (1.3% and 1.2%, respectively). In contrast, the air-calcined Co/Fe_3O_4-A catalyst, as established by CO_2-TPD, possesses strong basic sites. These localised sites bind oxygenated intermediates tightly, preventing their early desorption and instead forcing their complete deoxygenation to C_{2+} hydrocarbons.

4. Conclusions

The results demonstrate that the introduction of a minor amount of cobalt (Co:Fe = 5:100) into iron-based catalysts fundamentally alters their structural evolution, surface chemistry and catalytic behaviour during CO_2 hydrogenation. Characterisation revealed that cobalt acts as a highly effective structural stabiliser, preventing the agglomeration of iron phases and maintaining smaller crystallite sizes both during reduction and throughout the reaction. Furthermore, H_2-TPR analysis confirmed that even at low loading, cobalt significantly enhances the reducibility of the bulk iron.

Crucially, the pre-treatment environment dictates the final catalyst properties. Uncalcined (Fe_3O_4 and Co/Fe_3O_4) and N-calcined (Co/Fe_3O_4-N) catalysts reduced fully to metallic α-Fe, generating moderate surface basicity. Air calcination resulted in an incompletely reduced catalyst containing iron oxides (γ-Fe_2O_3 and α-Fe_2O_3), which generated highly localised, strong basic sites and active metal-oxide interfaces capable of massive high-temperature CO_2 dissociation.

The addition of minor amounts of cobalt fundamentally transforms the catalyst's stability and product selectivity. Cobalt enhances bulk iron reducibility through hydrogen spillover and hinders the water-induced oxidation of the Fe_5C_2 phase. Catalytically, these structural and chemical modifications led to distinct reaction pathways. N_2 calcination followed by H_2 reduction yields the most balanced catalytic performance. In comparison, air calcination promotes higher C_{5+} selectivity but reduces CO_2 conversion due to a more oxidised Fe^{3+} rich surface. Direct H_2 reduction produces catalysts that are easily oxidised during reaction, resulting in increased oxygenate and acid formation and decreased selectivity for long-chain hydrocarbons. The results indicate that increasing the reaction temperature enhances CO_2 conversion while shifting selectivity toward CH_4, shorter hydrocarbons, and oxygenates. Within the 280–300 °C range, reaction temperature exerts a stronger influence on catalytic performance than the specific catalyst pretreatment. While pretreatment defines the starting phase, temperature dictates the thermodynamic boundaries and kinetic rates that ultimately determine the product distribution and the specific types of oxygenates formed.

These findings highlight that trace cobalt promotion, coupled with

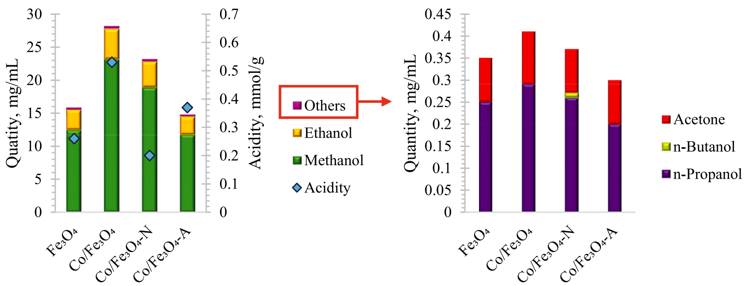

Fig. 9. The influence of pretreatment procedure on the aqueous phase product quantity and composition of minor oxygenate products (others) of unpromoted and cobalt-promoted Fe_3O_4 at 280 °C.

tailored calcination strategies, offers a powerful tool for steering catalysts' CO_2 hydrogenation performance.

Funding

This research has been supported by the EU Recovery and Resilience Facility within Project No 5.2.1.1.i.0/2/24/I/CFLA/003 "Implementation of consolidation and management changes at Riga Technical University, Liepaja University, Rezekne Academy of Technology, Latvian Maritime Academy and Liepaja Maritime College for the progress toward excellence in higher education, science and innovation" academic career doctoral grant (ID 1092).

CRediT authorship contribution statement

Agija Stanke: Writing – review & editing, Writing – original draft, Investigation, Funding acquisition, Formal analysis, Data curation, Conceptualization. **Agris Berzins:** Writing – review & editing, Formal analysis. **Jorge A. Velasco:** Writing – review & editing, Writing – original draft, Investigation, Formal analysis, Data curation. **Kristaps Sarsuns:** Writing – review & editing, Investigation, Formal analysis, Data curation. **Riikka L. Puurunen:** Writing – review & editing, Supervision. **Kristine Lazdovica:** Writing – review & editing, Writing – original draft, Supervision, Investigation, Conceptualization.

Declaration of competing interest

The authors declare that they have no known competing financial interests or personal relationships that could have appeared to influence the work reported in this paper.

Data availability

Data will be made available on request.

Acknowledgments

The Bioeconomy and Raw Materials research infrastructures at Aalto University were used for the H_2-TPR and CO_2-TPD experiments in this study.

Appendix A. Supplementary data

Supplementary data to this article can be found online at https://doi.org/10.1016/j.fuproc.2026.108467.

References

[1] X. Du, M.N. Khan, G.C. Thakur, Machine learning in carbon capture, utilization, storage, and transportation: a review of applications in greenhouse gas emissions reduction, Processes 13 (2025), https://doi.org/10.3390/pr13041160.

[2] E. Hanson, C. Nwakile, V.O. Hammed, Carbon capture, utilization, and storage (CCUS) technologies: evaluating the effectiveness of advanced CCUS solutions for reducing CO2 emissions, Results Surf. Interfaces 18 (2025), https://doi.org/10.1016/j.rsurfi.2024.100381.

[3] S. Saeidi, S. Najari, V. Hessel, K. Wilson, F.J. Keil, P. Concepción, S.L. Suib, A. E. Rodrigues, Recent advances in CO2 hydrogenation to value-added products — current challenges and future directions, Prog. Energy Combust. Sci. 85 (2021) 100905, https://doi.org/10.1016/j.pecs.2021.100905.

[4] C. Panzone, R. Philippe, A. Chappaz, P. Fongarland, A. Bengaouer, Power-to-Liquid catalytic CO2 valorization into fuels and chemicals: Focus on the Fischer-Tropsch route, J. CO_2 Util. 38 (2020) 314–347, https://doi.org/10.1016/j.jcou.2020.02.009.

[5] M. Albrecht, U. Rodemerck, M. Schneider, M. Bröring, D. Baabe, E.V. Kondratenko, Unexpectedly efficient CO2 hydrogenation to higher hydrocarbons over non-doped Fe2O3, Appl. Catal. B 204 (2017) 119–126, https://doi.org/10.1016/j.apcatb.2016.11.017.

[6] M. Tavares, G. Westphalen, J.M. Araujo Ribeiro de Almeida, P.N. Romano, E. F. Sousa-Aguiar, Modified Fischer-Tropsch synthesis: a review of highly selective catalysts for yielding olefins and higher hydrocarbons, Front. Nanotechnol. 4 (2022), https://doi.org/10.3389/fnano.2022.978358.

[7] J. Liang, J. Liu, L. Guo, W. Wang, C. Wang, W. Gao, X. Guo, Y. He, G. Yang, S. Yasuda, B. Liang, N. Tsubaki, CO2 hydrogenation over Fe-CO bimetallic catalysts with tunable selectivity through a graphene fencing approach, Nat. Commun. 15 (2024), https://doi.org/10.1038/s41467-024-44763-9.

[8] F. Yuan, G. Zhang, J. Zhu, F. Ding, A. Zhang, C. Song, X. Guo, Boosting light olefin selectivity in CO2 hydrogenation by adding CO to fe catalysts within close proximity, Catal. Today 371 (2021) 142–149, https://doi.org/10.1016/j.cattod.2020.07.072.

[9] R. Satthawong, N. Koizumi, C. Song, P. Prasassarakich, Light olefin synthesis from CO2 hydrogenation over k-promoted Fe-CO bimetallic catalysts, Catal. Today 251 (2015) 34–40, https://doi.org/10.1016/j.cattod.2015.01.011.

[10] R. Satthawong, N. Koizumi, C. Song, P. Prasassarakich, Bimetallic Fe-Co catalysts for CO2 hydrogenation to higher hydrocarbons, J. CO_2 Util. 3–4 (2013) 102–106, https://doi.org/10.1016/j.jcou.2013.10.002.

[11] L. Guo, Y. Cui, H. Li, Y. Fang, R. Prasert, J. Wu, G. Yang, Y. Yoneyama, N. Tsubaki, Selective formation of linear-alpha olefins (LAOs) by CO2 hydrogenation over bimetallic Fe/CO-Y catalyst, Catal. Commun. 130 (2019), https://doi.org/10.1016/j.catcom.2019.105759.

[12] J.X. Liu, P. Wang, W. Xu, E.J.M. Hensen, Particle size and crystal phase effects in Fischer-Tropsch catalysts, Engineering 3 (2017) 467–476, https://doi.org/10.1016/J.ENG.2017.04.012.

[13] J. Zhu, S. Shaikhutdinov, B.R. Cuenya, Structure-reactivity relationships in CO2 hydrogenation to c2+ chemicals on Fe-based catalysts, Chem. Sci. (2024), https://doi.org/10.1039/d4sc06376g.

[14] Q. Wang, K. Hu, R. Gao, L. Zhang, L. Wang, C. Zhang, Hydrogenation of carbon dioxide to value-added liquid fuels and aromatics over Fe-based catalysts based on the Fischer–Tropsch synthesis route, Atmosphere (Basel) 13 (2022), https://doi.org/10.3390/atmos13081238.

[15] D.B. Bukur, X. Lang, Y. Ding, Pretreatment effect studies with a precipitated iron Fischer–Tropsch catalyst in a slurry reactor, Appl. Catal. A Gen. 186 (1999) 255–275, https://doi.org/10.1016/S0926-860X(99)00148-9.

[16] T. Riedel, H. Schulz, G. Schaub, K.-W. Jun, J.-S. Hwang, K.-W. Lee, Fischer–Tropsch on iron with H2/CO and H2/CO2 as synthesis gases: The episodes of formation of the Fischer–Tropsch regime and construction of the catalyst, Top. Catal. 26 (2003) 41–54, https://doi.org/10.1023/B:TOCA.0000012986.46680.28.

[17] E. Patanou, N.E. Tsakoumis, R. Myrstad, E.A. Blekkan, The impact of sequential H2-CO-H2 activation treatment on the structure and performance of cobalt based catalysts for the Fischer-Tropsch synthesis, Appl. Catal. Gen. 549 (2018) 280–288, https://doi.org/10.1016/j.apcata.2017.10.007.

[18] E. Kraleva, H. Lund, J. Weiß, S. Bartling, H. Atia, Z. Cherkezova-Zheleva, D. Paneva, S. Wohlrab, U. Armbruster, Effect of pretreatment conditions on a benchmark iron catalyst for CO2 hydrogenation to light olefins, Appl. Catal. A Gen. 683 (2024), https://doi.org/10.1016/j.apcata.2024.119857.

[19] I.C. ten Have, B.M. Weckhuysen, The active phase in cobalt-based Fischer-Tropsch synthesis, Chem Catal. 1 (2021) 339–363, https://doi.org/10.1016/j.checat.2021.05.011.

[20] S. Yan, Y. Wang, G. Chen, W. Ma, Y. Chen, X. Wang, K. Zeng, Y. Yao, H. Sun, H. Yang, H. Chen, Transition metal-promoted Fe-based catalysts for photothermal catalytic CO2 hydrogenation, Catal. Sci. Technol. 15 (2025) 856–866, https://doi.org/10.1039/D4CY01271B.

[21] Y. Gao, W. Yi, J. Yang, K. Jiang, T. Yang, Z. Li, M. Zhang, Z. Liu, B. Wu, Effect of calcination atmosphere on the performance of Cu/Al2O3 catalyst for the selective hydrogenation of furfural to furfuryl alcohol, Molecules 29 (2024), https://doi.org/10.3390/molecules29122753.

[22] M. Zainul Anwar, R. Triandi Tjahjanto, U. Hasanah, Synthesis and activation study of iron (Fe) based Fischer Tropsch (FT) catalyst using sol-gel method, J. Pure Appl. Chem. Res. 8 (2019) 217–224, https://doi.org/10.21776/ub.jpacr.2019.008.03.480.

[23] M. Oschatz, T.W. van Deelen, J.L. Weber, W.S. Lamme, G. Wang, B. Goderis, O. Verkinderen, A.I. Dugulan, K.P. de Jong, Effects of calcination and activation conditions on ordered mesoporous carbon supported iron catalysts for production of lower olefins from synthesis gas, Catal. Sci. Technol. 6 (2016) 8464–8473, https://doi.org/10.1039/C6CY01251E.

[24] M. Akbari, A.A. Mirzaei, M. Arsalanfar, Microemulsion based synthesis of promoted Fe–Co/MgO nanocatalyst: influence of calcination atmosphere on the physicochemical properties, activity and light olefins selectivity for hydrogenation of carbon monoxide, Mater. Chem. Phys. 249 (2020), https://doi.org/10.1016/j.matchemphys.2020.123003.

[25] R. Roknabadi, A.A. Mirzaei, H. Atashi, Assessment of composition and calcination parameters in Fischer-Tropsch synthesis over Fe-Mn-Ce/γ -Al_2O_3nanocatalyst, Oil Gas Sci. Technol. Rev. IFP Energies Nouvelles 76 (2021), https://doi.org/10.2516/ogst/2020089.

[26] M. Feyzi, M. Irandoust, A.A. Mirzaei, Effects of promoters and calcination conditions on the catalytic performance of iron-manganese catalysts for Fischer-Tropsch synthesis, Fuel Process. Technol. 92 (2011) 1136–1143, https://doi.org/10.1016/j.fuproc.2011.01.010.

[27] A. Stanke, K. Lazdovica, A. Gaile, L. Laipniece, Fischer-Tropsch synthesis product selectivity over silica-supported iron-based catalyst: effect of K/Fe ratio, Fuel 387 (2025), https://doi.org/10.1016/j.fuel.2025.134399.

[28] F. Genuzio, A. Sala, T. Schmidt, D. Menzel, H.J. Freund, Phase transformations in thin iron oxide films: Spectromicroscopic study of velocity and shape of the reaction fronts, Surf. Sci. 648 (2016) 177–187, https://doi.org/10.1016/j.susc.2015.11.016.

[29] S.S. Pati, L. Herojit Singh, J.C. Mantilla Ochoa, E.M. Guimarãesa, M.J.A. Sales, J.A. H. Coaquira, A.C. Oliveira, V.K. Garg, Facile approach to suppress γ-Fe_2O_3 to

α-Fe_2O_3 phase transition beyond 600 °C in Fe_3O_4 nanoparticles, Mater. Res. Express 2 (2015), https://doi.org/10.1088/2053-1591/2/4/045003.

[30] L. Kumar, P. Kumar, A. Narayan, M. Kar, Rietveld analysis of XRD patterns of different sizes of nanocrystalline cobalt ferrite, Int. Nano Lett. 3 (2013) 8, https://doi.org/10.1186/2228-5326-3-8.

[31] S.A. Hassanzadeh-Tabrizi, Precise calculation of crystallite size of nanomaterials: a review, J. Alloys Compd. 968 (2023) 171914, https://doi.org/10.1016/j.jallcom.2023.171914.

[32] H. Liu, G. Wei, Z. Xu, P. Liu, Y. Li, Quantitative analysis of fe and co in co-substituted magnetite using XPS: the application of non-linear least squares fitting (NLLSF), Appl. Surf. Sci. 389 (2016) 438–446, https://doi.org/10.1016/j.apsusc.2016.07.146.

[33] Y. Yuan, S. Huang, H. Wang, Y. Wang, J. Wang, J. Lv, Z. Li, X. Ma, Monodisperse Nano-Fe_3O_4 on α-Al_2O_3 catalysts for Fischer–Tropsch synthesis to lower olefins: promoter and size effects, ChemCatChem 9 (2017) 3144–3152, https://doi.org/10.1002/cctc.201700792.

[34] C.G. Visconti, M. Martinelli, L. Falbo, A. Infantes-Molina, L. Lietti, P. Forzatti, G. Iaquaniello, E. Palo, B. Picutti, F. Brignoli, CO2 hydrogenation to lower olefins on a high surface area k-promoted bulk fe-catalyst, Appl. Catal. B 200 (2017) 530–542, https://doi.org/10.1016/j.apcatb.2016.07.047.

[35] R. Gao, X. Chen, C. Deng, L. Xu, L. Zhang, C. Zhang, K.W. Jun, T. Zhao, Y. Yang, Selective synthesis of C2–C4 olefins via CO_2 hydrogenation over spinel-structured Fe–CO bimetal catalysts, Int. J. Hydrogen Energy 146 (2025), https://doi.org/10.1016/j.ijhydene.2025.06.198.

[36] W. Zhang, P. Anguita, J. Díez-Ramírez, C. Descorme, J.L. Valverde, A. Giroir-Fendler, Comparison of different metal doping effects on Co3O4 catalysts for the total oxidation of toluene and propane, Catalysts 10 (2020) 865, https://doi.org/10.3390/catal10080865.

[37] P. Li, Z. Li, J. Cui, C. Geng, Y. Kang, C. Zhang, C. Yang, N-doped graphene/CoFe2O4 catalysts for the selective catalytic reduction of NOx by NH3, RSC Adv. 9 (2019) 15791–15797, https://doi.org/10.1039/C9RA02456E.

[38] L. Guo, Y. Cui, H. Li, Y. Fang, R. Prasert, J. Wu, G. Yang, Y. Yoneyama, N. Tsubaki, Selective formation of linear-alpha olefins (LAOs) by CO2 hydrogenation over bimetallic Fe/CO-Y catalyst, Catal. Commun. 130 (2019) 105759, https://doi.org/10.1016/j.catcom.2019.105759.

[39] J. Chen, C. Yang, Thermodynamic equilibrium analysis of product distribution in the Fischer-Tropsch process under different operating conditions, ACS Omega 4 (2019) 22237–22244, https://doi.org/10.1021/acsomega.9b03707.

[40] W. Wang, E. Toshcheva, A. Ramirez, G. Shterk, R. Ahmad, M. Caglayan, J. L. Cerrillo, A. Dokania, G. Clancy, T.B. Shoinkhorova, N. Hijazi, L. Cavallo, J. Gascon, Bimetallic Fe-Co catalysts for the one step selective hydrogenation of CO_2 to liquid hydrocarbons, Catal. Sci. Technol. 13 (2023) 1527–1540, https://doi.org/10.1039/d2cy01880b.

[41] N.S. Featherstone, E. van Steen, Meta-analysis of the thermo-catalytic hydrogenation of CO_2, Catal. Today 423 (2023), https://doi.org/10.1016/j.cattod.2022.11.012.

[42] G. Cui, Y. Lou, M. Zhou, Y. Li, G. Jiang, C. Xu, Review of mechanism investigations and catalyst developments for CO_2 hydrogenation to alcohols, Catalysts 14 (2024), https://doi.org/10.3390/catal14040232.

[43] P. Thüne, P. Moodley, F. Scheijen, H. Fredriksson, R. Lancee, J. Kropf, J. Miller, J. W.H. Niemantsverdriet, The effect of water on the stability of iron oxide and iron carbide nanoparticles in hydrogen and syngas followed by in situ x-ray absorption spectroscopy, J. Phys. Chem. C 116 (2012) 7367–7373, https://doi.org/10.1021/jp210754k.

[44] C. Ehrhardt, M. Gjikaj, W. Brockner, Thermal decomposition of cobalt nitrato compounds: Preparation of anhydrous cobalt(II)nitrate and its characterisation by infrared and raman spectra, Thermochim. Acta 432 (2005) 36–40, https://doi.org/10.1016/j.tca.2005.04.010.

[45] S. Waseem Ullah, D.F. khan, S. Burki, M.U. Khan, H. Yin, Modeling, simulations, predictions, calculations and thermodynamic assessments of Cobalt-Ferric binary alloys system using calphad method and pbine database, J. Heterocyclics (2020) 3–6, https://doi.org/10.33805/2639-6734-109.

[46] J. Rodewald, J. Thien, T. Pohlmann, M. Hoppe, F. Timmer, F. Bertram, K. Kuepper, J. Wollschläger, Formation of ultrathin cobalt ferrite films by interdiffusion of Fe3O4/CoO bilayers, Phys. Rev. B 100 (2019) 155418, https://doi.org/10.1103/PhysRevB.100.155418.

[47] W. Wang, X. Guo, Y. Wang, S. Lin, X. Gao, J. Liang, J. Zhang, J. Xie, H. Jiang, F. Cao, Y. Chen, G. Yang, T. Frauenheim, M. Wang, T. Xing, Y. Lu, Q. Liu, K. S. Novoselov, N. Tsubaki, M. Wu, Transformation of CO2 to c2+ alcohols by tailoring the oxygen bonding via Fe-based tandem catalyst, Nat. Commun. 16 (2025), https://doi.org/10.1038/s41467-025-62727-5.

[48] A. Kostyniuk, B. Likozar, State-of-the-art advancements in the thermocatalytic conversion of CO2 into ethanol and higher alcohols: recent progress in catalyst development and reaction mechanisms, Chem. Eng. J. 503 (2025), https://doi.org/10.1016/j.cej.2024.158467.

[49] K. Li, X. Li, L. Li, X. Chang, S. Wu, C. Yang, X. Song, Z.J. Zhao, J. Gong, Nature of catalytic behavior of cobalt oxides for CO2 hydrogenation, JACS Au 3 (2023) 508–515, https://doi.org/10.1021/jacsau.2c00632.

Agija Stanke dzimusi 1989. gadā Rīgā. Rīgas Celtniecības koledžā ieguvusi restauratora kvalifikāciju (2011). Rīgas Tehniskajā universitātē (RTU) ieguvusi dabaszinātņu bakalaura (2019) un maģistra (2021) grādu ķīmijā. Patlaban ir RTU Dabaszinātņu un tehnoloģijas fakultātes Ķīmijas un ķīmijas tehnoloģijas institūta pētniece. Zinātniskās intereses saistītas ar oglekli saturošu izejvielu termoķīmisko pārveidi augstvērtīgos produktos.

Agija Stanke was born in 1989 in Riga. She obtained a Restorer Qualification (2011) from Riga Building College. She obtained a Bachelor's degree (2019) and a Master's degree (2021) in Natural Sciences in Chemistry from Riga Technical University (RTU). Currently, she is a researcher at the Institute of Chemistry and Chemical Technology of the Faculty of Natural Sciences and Technology of RTU. Her research interests focus on the thermochemical transformation of carbon-containing raw materials into high-value products.